Dark Matter
at the International Linear Collider

Dissertation
zur Erlangung des Doktorgrades
an der Fakultät für Mathematik, Informatik und
Naturwissenschaften
Fachbereich Physik
der Universität Hamburg

vorgelegt von
Moritz Habermehl

Hamburg
2018

Gutachter der Dissertation:	Dr. Jenny List Prof. Dr. Dieter Horns
Zusammensetzung der Prüfungskommission:	Prof. Dr. Caren Hagner Dr. Jenny List Prof. Dr. Dieter Horns Prof. Dr. Gudrid Moortgat-Pick Prof. Dr. Peter Schleper
Vorsitzende der Prüfungskommission:	Prof. Dr. Caren Hagner
Datum der Dissertation:	20.11.2018
Vorsitzender Fachpromotionsausschuss Physik:	Prof. Dr. Wolfgang Hansen
Leiter des Fachbereichs Physik:	Prof. Dr. Michael Potthoff
Dekan der Fakultät MIN:	Prof. Dr. Heinrich Graener

Abstract

The International Linear Collider (ILC) is a planned electron-positron collider with polarised beams and centre-of-mass energies of up to 500 GeV. By performing high-precision measurements of Standard Model observables and searches for new particles it can complement the potential of the Large Hadron Collider (LHC).

One of the most prominent open questions in physics is the nature of dark matter. Weakly Interacting Massive Particles (WIMPs) are possible candidates for dark matter, which can be searched for at colliders. In this thesis, the expected sensitivity to a WIMP signal at the ILC is explored in a Monte Carlo study. The WIMPs are assumed to be produced in pairs together with a photon from initial state radiation, through which the process can be identified.

A detector simulation at $\sqrt{s} = 500\,\text{GeV}$ is performed for the International Large Detector (ILD) concept, including beam-induced backgrounds and the luminosity spectrum. In comparison to previous studies many aspects of the analysis are treated in a more realistic way: e.g. the cuts in the event generation have been updated, a complete description of the reconstruction in the crucial forward region has been added and the systematic uncertainties of the luminosity spectrum have been fully treated for the first time.

In order to provide a model-independent WIMP search, the approach of effective operators is chosen to describe the new interaction. The photon energy spectra for different signal hypotheses and the distribution of the Standard Model background are used to calculate the expected 5σ discovery reach as well as the 2σ exclusion limits. For the example of a vector operator, energy scales of up to 3 TeV can be tested for WIMP masses $\lesssim 250\,\text{GeV}$ assuming 20 years of operation. With beam polarisation the sensitivity can be increased and with the help of data sets taken with different polarisation configurations the effect of the systematic uncertainties can be significantly reduced. The role of the forward acceptance for the suppression of the Bhabha scattering background is quantified.

With two different approaches, estimates for the sensitivity at other centre-of-mass energies than the 500 GeV of the full simulation can be calculated. This allows to provide results for the full ILC programme, e.g. energy scales of up to 1.4 TeV can be probed with an initial stage of the ILC at a centre-of-mass energy of 250 GeV, while energy scales of up to 4.5 TeV could be probed at $\sqrt{s} = 1\,\text{TeV}$.

Zusammenfassung

Der International Linear Collider (ILC) ist ein geplanter Elektron-Positron-Collider mit polarisierten Strahlen und Schwerpunktsenergien von bis zu 500 GeV. Hochpräzissionsmessungen von Observablen des Standardmodells und Suchen nach neuen Teilchen bilden eine Ergänzung zum Potenzial des Large Hadron Colliders (LHC).

Eine der bedeutesten offenen Fragen in der Physik ist die Natur der Dunklen Materie. Weakly Interacting Massive Particles (WIMPs) sind mögliche Kandidaten für Dunkle Materie, welche an Beschleunigern gesucht werden können. In dieser Arbeit wird die erwartete Sensitivität für ein WIMP-Signal am ILC in einer Monte-Carlo-Studie untersucht. Es wird angenommen, dass die WIMPs paarweise produziert werden, zusammen mit einem Photon aus Abstrahlung im Anfangszustand, durch das der Prozess identifiziert werden kann.

Bei $\sqrt{s} = 500\,\mathrm{GeV}$ wird unter Einbezug von strahlinduzierten Untergründen und des Luminositätsspektrums eine Detektorsimulation für das Konzept des International Large Detectors (ILD) durchgeführt. Im Vergleich zu früheren Studien werden viele Aspekte realistischer beschrieben: z.B. wurden die Schnitte in der Ereignisgenerierung verbessert, eine vollständige Beschreibung der Rekonstruktion in der wichtigen Vorwärtsregion wurde hinzugefügt und die systematischen Unsicherheiten des Luminositätsspektrums wurden zum ersten mal vollständig behandelt.

Um die WIMP-Suche modellunabhängig durchzuführen, wird für die Beschreibung der neuen Wechselwirkung der Ansatz effektiver Operatoren ausgewählt. Mit den Photonenergiespektren für verschiedene Signalhypothesen und der Verteilung des Standardmodell-Untergrunds werden die erwartete 5σ-Entdeckungsreichweite und 2σ-Ausschlussgrenzen berechnet. Werden 20 Jahre Betrieb angenommen, können z.B. für einen Vektoroperator Energiebereiche bis zu 3 TeV für WIMP-Massen $\lesssim 250\,\mathrm{GeV}$ getestet werden. Mit Strahlpolarisation kann die Sensitivität gesteigert werden und mithilfe von Datensätzen mit unterschiedlichen Polarisationskonfigurationen kann der Effekt der systematischen Unsicherheiten maßgeblich reduziert werden. Die Rolle der Akzeptanz in der Vorwärtsregion für die Unterdrückung des Bhabhastreuungs-Untergrunds wird quantifiziert.

Mit zwei unterschiedlichen Ansätzen können genäherte Sensitivitäten bei anderen Schwerpunktsenergien als die 500 GeV der vollen Simulation berechnet werden, wodurch Ergebnisse für das volle ILC-Programm gegeben werden können. Z.B. können in einer Anfangsphase mit $\sqrt{s} = 250\,\mathrm{GeV}$ Energiebereiche bis zu 1.4 TeV untersucht werden, während bei $\sqrt{s} = 1\,\mathrm{TeV}$ Energiebereiche bis zu 4.5 TeV untersucht werden.

Contents

Chapter 1

Introduction

The description of nature at the smallest scales is the subject of particle physics. An important tool to study the particles are accelerators where their interactions can be tested in collisions.

Our theoretical understanding of particle physics is based on the description provided by the Standard Model of particle physics. Four decades after the formulation of the Standard Model, almost all observed processes on particle level can be successfully described by this model. Yet, it cannot be the final theory in physics because a connection to general relativity, our description of large scales, is missing. Also, a number of phenomena observed in nature is lacking an explanation. A prominent example is dark matter, which is the motivation for this thesis.

So far, the existence of dark matter is known from a number of astronomical and cosmological observations, which cannot be explained by ordinary matter and hence indicate that there is an additional component. It is called dark matter, because it interacts gravitationally, like matter, but is not visible through light. The known particles of the Standard Model do not offer a candidate which could account for its observed abundance.

All the observations make clear that there is something we do not understand. Either the description of gravity is wrong or there must be some form of matter, which behaves distinctly different from the known matter. Whereas approaches to find a modified formulation of gravity put the established description of gravity in question and try to give an alternative approach, this analysis is a response to the hypothesis of an additional type of matter.

Weakly Interacting Massive Particles (WIMPs) are possible candidates for dark matter with masses in the GeV to TeV range. WIMPs will be the main topic of investigation in this thesis. Among the other proposed particles for cold dark matter are the sterile neutrinos and the light (sub-eV to eV) axions and other weakly interacting *slim* particles (WISPs). Also non-particle dark matter is under study, for example primordial black holes.

So far, dark matter has only been observed in gravitational interactions. Whether non-gravitational interactions between dark matter and Standard Model particles exist, can be tested in collider searches. If a dark matter candidate is discovered at a collider, only a verification with direct or indirect detection can show that the new particle is *the* dark matter.

With the unprecedented centre-of-mass energies of the Large Hadron Collider, new phase space is being accessed to look for answers to the open questions in physics. An alternative approach to search for new physics are high precision measurements at e^+e^--colliders, like the planned International Linear Collider (ILC). In this way, for example, the nature of dark matter could be revealed at a collider. Searches for dark matter at the ILC are complementary to searches at the LHC because they directly probe the coupling to leptons rather than couplings to quarks and gluons.

The centre-of-mass energy of the ILC can be tuned between 250 GeV and 500 GeV and is upgradable to 1 TeV. Both the electron and position beams are foreseen to be polarised to at least ±80% and ±30%, respectively. The ILC will have one interaction region which will accommodate the two foreseen detectors in a push-pull scheme. The presented study is performed for the International Large Detector (ILD) concept.

The study presented in this thesis is a generic search for a new particle which has the properties of WIMPs. The chosen approach is highly model-independent, both by looking for WIMP pair production in association with a photon from initial state radiation (ISR) and by computing the sensitivity in the framework of effective operators.

This work is based on a full detector simulation of the ILD concept at a centre-of-mass energy of 500 GeV. Simulations of the beam-beam interactions and the resulting luminosity spectrum are included. The Standard Model background processes of neutrino pair production and Bhabha scattering are taken into account. Crucial detector requirements are a high tracking efficiency to distinguish the signal photon from charged leptons, a good photon identification in the electromagnetic calorimeter, and hermeticity in the forward region to suppress the Bhabha scattering background.

After a cut-based event selection the signal and background events are used to calculate the potential to discover a WIMP in the mass range of $1 - 250\,\mathrm{GeV}$ or, alternatively, expected exclusion limits for different assumptions on the effective operator, the beam polarisation and the integrated luminosity. With an extrapolation of the obtained exclusion limits, estimates of the sensitivity are given for the entire centre-of-mass energy range of the ILC.

This analysis is a complete update of a previous WIMP study with the mono-photon signature at a centre-of-mass energy of $500\,\mathrm{GeV}$ based on a full ILD detector simulation [1, 2]. Short-comings like the incompleteness of the phase space of the generated Bhabha scattering data sample or inadequate cuts in the signal definition have been corrected. The ISR treatment in the event generation has been improved. Furthermore, the event samples profit from a more realistic beam background level and updated reconstruction algorithms, especially the improved treatment of the BeamCal reconstruction in the forward region. Completely new features are the evaluation of the main systematic uncertainty induced by the luminosity spectrum (see section 7.5) and an extrapolation of the results to other ILC centre-of-mass energies (see sections 8.3 and 8.4).

In [1, 2] the WIMP signal was interpreted using a different general approach, which is based on cosmological observables. In [3] the same Monte Carlo data was reinterpreted using the framework of effective operators, i.e. the same approach followed in the study presented here.

In the following chapter 2 an introduction to cosmology and particle physics in the context of dark matter is given. The ILC and the detector concept ILD are described in chapter 3. In chapter 4 an overview of the different tools in the ILD simulation chain is presented, including the simulation of the beam-beam interactions, the event generation, the simulation of the detector response and the event reconstruction.

In chapter 5 the setup of the event generation is presented and the quality of the photon reconstruction is evaluated. In chapter 6 the criteria of the event selection are described and the efficiency to suppress the background is discussed. The sensitivity calculation is subject of chapter 7, where also WIMP expected exclusion limits with a focus on the effects of polarisation, integrated luminosity and systematic uncertainties are presented. The expected sensitivity for the whole ILC programme can be found in chapter 8.

Chapter 2

Dark Matter in the Context of Cosmology and Particle Physics

Dark matter is one of the big puzzles linking cosmology and particle physics. In this chapter, our current knowledge about this mysterious new form of matter is summarised, thereby laying the foundations for the work presented in this thesis.

First, the existence of dark matter is motivated with a presentation of astronomical observations, which hint towards a new mass component. In section 2.2 the Standard Model of particle physics is presented to provide the basic foundation for this collider study. It will be shown that the Standard Model does not contain a particle which can explain the observed effects. Instead, WIMP dark matter, which is introduced in section 2.3, is assumed in this analysis. The framework for the interpretation of the data is addressed in section 2.4. Finally, the potential of the different search channels is discussed in section 2.5.

2.1 Observational evidence

Dark matter is a form of matter which has been postulated to explain astrophysical oberservations at all distance scales, starting in our own galaxy and reaching up to cosmic scales. With the precise recording of the cosmic microwave background [4, 5] evidence for dark matter from the early universe was added. This makes the understanding of its underlying nature one of the most important open questions in physics.

In general, the observations cannot be explained by the stars, gas and dust, i.e. by baryonic matter alone and indicate that there has to be an additional mass component. The problem was first encountered in the 1930s, when the motions in the Milky Way [6] or those of the galaxies in the Coma cluster [7] could not be explained by the mass of the known matter.

2.1.1 Rotatation curves of galaxies

With the observation that rotation curves of spiral galaxies like our Milky Way are flat in the 1970s more signs were found that the assumed mass from known matter can only account for a part of the galaxies' masses [8, 9].

The dynamics within spiral galaxies show a clear indication for an additional mass component. The distribution of the missing mass can be illustrated by drawing the orbital speed of visible stars and gas as a function of the radius r, i.e. the distance of the object to the galactic centre. Measurements of star light extends out to approximately 10 kpc and further out gas can be surveyed, e.g. via the 21 cm line of hydrogen. In figure 2.1 the rotation curve for the spiral galaxy NGC 3198 is shown as an example.

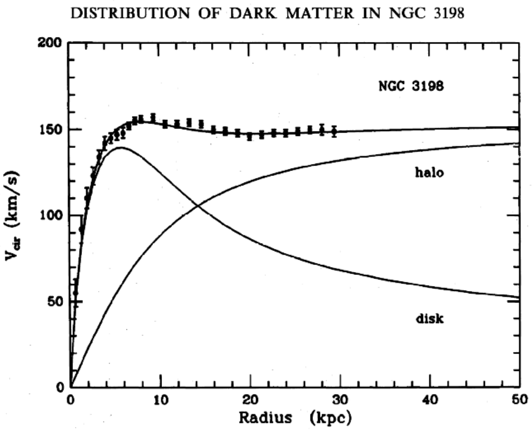

Figure 2.1: Rotation curve of the spiral galaxy NGC 3198. The observed flatness (uppermost line) can be explained by a combination of the known mass (*disk*) and dark matter (*halo*). Taken from [10].

The observation of a flat rotation curve in the outer region of galaxies cannot be explained by the gravitational potential formed by the visible mass. The expected velocity distribution is denoted *disk* in figure 2.1 and falls off as $1/\sqrt{r}$. The discrepancy has to be compensated by an additional (invisible) component with an increasing mass distribution that extends into the halo of the galaxy and is thus called *halo* in the figure.

2.1.2 Galaxy cluster mergers

The historically first indications for dark matter came from dynamical observations. A second category of observations, which are canonically explained by dark matter, are measurements of gravitational lensing, for example in dwarf spheroidal galaxies in the galactic halo or in objects further away, like galaxy clusters.

Evidence for invisible, non-baryonic matter also comes from the observation of the collision of galaxy clusters. One example of a galaxy cluster merger is the system 1 E 0657-558. In the optical image, shown in figure 2.2a, the galaxies of the two clusters can be seen. The X-ray image of the same region (in figure 2.2b) shows two components clearly offset from the optical structures. The distinct shape of the western (right) X-ray feature gave rise to the name *bullet cluster*.

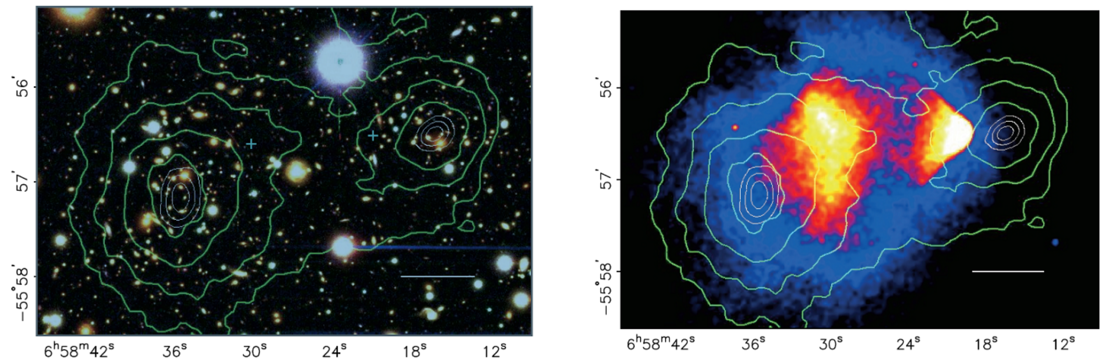

(a) (b)

Figure 2.2: (a) Optical (Magellan telescope) and (b) X-ray (Chandra X-ray Observatory) images of the "bullet cluster" 1 E 0657-558. The green contours show the mass concentrations of the two clusters, which are clearly offset from the peaks in the X-ray emission. Taken from [11].

The distances between the galaxies are so large, that they did not collide, but travelled through each other. The largest component of the baryonic mass, the gas, on the other hand, interacts and gets excited and is hence visible in X-rays. It is slowed down by its interaction and is hence offset from the optical counterparts towards the centre of the system.

From gravitational lensing, using optical data from the Magellan telescope and the Hubble Space Telescope, the mass distribution in the system is deduced and drawn as counters in the images [11]. Both peaks are clearly offset from the centres of the gas clouds, indicated by the blue plus signs in figure 2.2a. This means that the largest mass component must be non-baryonic, behaving like collisionless particles.

2.1.3 Cosmic microwave background

With the presented astrophysical observations there is clear evidence for dark matter in today's universe. With cosmological models the abundance of dark matter in the early universe can be calculated, where an important source of information is the cosmic microwave background (CMB).

The CMB radiation is a relic of the early universe: Due to its expansion the universe cools down and approximately 380,000 years after the big bang the temperatures allowed electrons to combine with baryons to form atoms. There were no longer charged particles the photons could interact with and thus they started to propagate freely, i.e. they decoupled. Today, the red-shifted photons coming from this surface of last scattering can be detected in the microwave range.

The sky map of the CMB recorded with the Planck satellite is shown in figure 2.3a. The CMB is highly isotropic with a relative temperature difference of only 10^{-5}. As these photons travelled freely since the time of decoupling, the density distribution of the universe at that time is imprinted on the photon energy distribution. The angular scales of the small anisotropies are visualised in figure 2.3b. The best model to describe the observations is the Λ Cold Dark Matter (ΛCDM) model, which hence has been established as the standard model of cosmology. The Λ reflects the necessity of a cosmological constant to explain the expansion of the universe to explain the dark energy, which makes up the largest share of the energy density of the universe. The second largest component can be explained by cold (i.e. non-relativistic) dark matter (see below, equation 2.4).

One important feature of the universe, which can be deduced from the position of the first peak in figure 2.3b, is that the curvature of the universe is compatible with being flat Euclidean space. Thus, the total energy density of the universe is close to the critical density at present time (denoted by the subscript 0)

$$\rho_{critical,0} = \frac{2H_0^2}{8\pi G} \tag{2.1}$$

with the Hubble constant $H_0 = 70.4\,\mathrm{km/(Mpc\cdot s)}$ and the gravitation constant G. A conventionally introduced variable is the energy density of a certain component in units of the critical energy density

$$\Omega_{i,0} = \rho_{i,0}/\rho_{critical,0} \tag{2.2}$$

where i can stand for radiation r, matter m (with the two components baryonic b

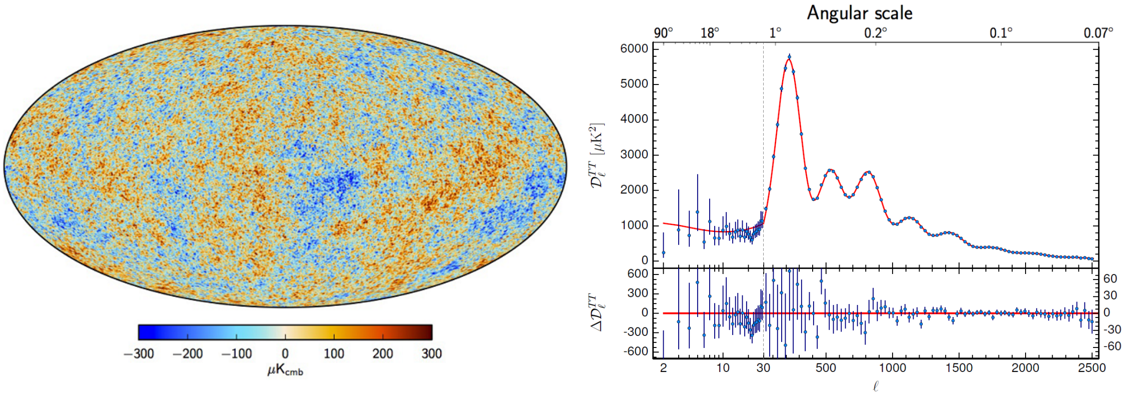

(a)

(b)

Figure 2.3: (a) Sky map of the anisotropies of the CMB temperature. The dipole from the relative motion of the earth and the Milky Way foreground have been removed. (b) CMB temperature deviations at different angular scales with fit. (a) taken from [5], (b) adapted from [5].

and cold dark matter CDM) and dark energy Λ. This leads to the relation

$$\Omega_{m,0} + \Omega_{\Lambda,0} = \Omega_{tot,0} \approx 1 \tag{2.3}$$

where the radiation density has been neglected since it is very small in the present universe. The different components can be obtained from fits assuming the ΛCDM model to the data from the Planck measurements [12]

$$\begin{aligned} \Omega_b h^2 &= 0.02226 \pm 0.00023 \\ \Omega_m h^2 &= 0.1415 \pm 0.0019 \\ \Omega_\Lambda &= 0.692 \pm 0.012 \end{aligned} \tag{2.4}$$

where h relates to the Hubble constant as $h = H_0 \frac{1}{100} \frac{\mathrm{s \cdot Mpc}}{\mathrm{km}}$. With $\Omega_b h^2 = 0.02226$ only about 16% of the mass in the universe ($\Omega_m h^2 = 0.1415$) can be explained by baryonic matter and the rest is dark matter.

The small fraction of $\Omega_b h^2$ with respect to $\Omega_m h^2$ can be understood from model calculations of the structure formation: In the transition of radiation domination to matter domination (shortly) before the decoupling of the photons, structure formation begins. The seen structures can be explained by some kind of matter which does not interact with photons and baryons and hence its fluctuations can begin to grow. The structure formation can be better explained by cold dark matter (i.e. non-relativistic at decoupling) which is thus favoured over hot dark matter.

2.1.4 Conclusions from the observations

The observed abundance of dark matter could not be explained by searches for astrophysical sources. In scans of galactic halos for non-luminous matter, like brown dwarfs, neutron stars and black holes, via gravitational lensing not enough of these objects were found [13]. Primordial black holes with an abundance that could explain dark matter are also ruled out with constraints from microlensing [14].

In this way, particle dark matter is favoured. The different presented observations draw a consistent picture and a number of properties of this new particle (or particle*s*) can be deduced:

- First of all it needs to be dark, meaning that it does not couple to photons.
- It clearly also needs to be massive. Its mass, together with its annihilation cross-section have to reproduce the relic density, if thermal production is assumed (see section 2.3.2).
- It needs to be sufficiently stable, meaning that its lifetime has to be in the order of the age of the universe.
- It has to be non-baryonic: As shown in equation 2.4 the disagreement between $\Omega_b h^2$ and $\Omega_m h^2$ is much larger than the uncertainties and hence these values clearly indicate that the baryonic matter cannot account for the matter density observed in the CMB data.
- No interaction with itself or known matter is noticeable, which means it can at most be weakly interacting.
- It has to be non-relativistic (cold), already at the time of structure formation.

The listed properties could be concluded from observations at large scales. In order to understand what dark matter is made of, the physics of small scales is addressed in the following by giving an introduction to the Standard Model of particle physics. At the end of section 2.2 it will be shown that particle content of the Standard Model does not provide a candidate to explain the observed abundance of dark matter either.

2.2 The Standard Model of particle physics

The Standard Model of particle physics is a theory describing the fundamental building blocks of matter, the particles, and their interactions. The smallest structure according to the Standard Model are the elementary particles, which are described as point-like objects without any substructure. The interactions are explained in terms of fundamental forces: the electromagnetic force, the weak force and the strong force. Only gravity is not included in the formulation. Gravity is described in the theory of General Relativity, which has a completely different structure than the quantum field theories the Standard Model is based on.

2.2.1 Elementary particles in the Standard Model

A number of elementary particles are fermions with a spin of 1/2, others are bosons with spin 0 or 1. The particles with a spin of 1/2 form *matter*. There are two kinds, leptons and quarks, which in turn have two-sub groups each: there are up-type and down-type quarks, and the leptons are categorised as charged leptons and neutrinos. All of those sub-groups come in three families or generations, shown in table 2.1, and each particle has an anti-particle with the same mass but opposite quantum numbers. The anti-particle is either indicated by a bar, e.g. $\bar{f}$ for an anti-fermion, or by its charge, e.g. e^+ for the positron, the “anti-electron”. Whether the neutrino is a Majorana particle (ν and $\bar{\nu}$ are different states of the same particle) or a Dirac particle (ν and $\bar{\nu}$ are different particles, as it is the case for the other fermions) remains an open question.

As can be seen from the quantum numbers in table 2.1, the particles of the different generations share the same quantum numbers and they only differ in mass. Charged fermions of the second and third generation are unstable and decay into particles of the first generation.

The three fundamental forces described by the Standard Model (electromagnetism, weak and strong force) are mediated by the bosons with spin 1, i.e. an interaction can be understood as an exchange of the corresponding boson. All charged particles undergo electromagnetic interactions, described by quantum electrodynamics (QED), which is mediated by photons (see section 2.2.2.1). Particles with a color charge (the quarks) interact with the strong force, mediated by 8 gluons, carrying color themselves. In the following, *charge* will be used for the electric charge and *colour charge* will be explicitely written out. The strong force is described in quantum chromodynamics (QCD) (see section 2.2.2.4).

fermions	family			quantum numbers			
	1	2	3	Q	T_w^3	Y	colour
leptons	$\begin{pmatrix}\nu_e\\ e\end{pmatrix}_L$	$\begin{pmatrix}\nu_\mu\\ \mu\end{pmatrix}_L$	$\begin{pmatrix}\nu_\tau\\ \tau\end{pmatrix}_L$	0	+1/2	−1	-
				−1	−1/2	−1	
	e_R	μ_R	τ_R	−1	0	−2	
quarks	$\begin{pmatrix}u\\ d'\end{pmatrix}_L$	$\begin{pmatrix}c\\ s'\end{pmatrix}_L$	$\begin{pmatrix}t\\ b'\end{pmatrix}_L$	+2/3	+1/2	1/3	r, g, b
				−1/3	−1/2	1/3	
	u_R	c_R	t_R	+2/3	0	4/3	
	d_R	s_R	b_R	−1/3	0	−2/3	

Table 2.1: The Standard Model fermions with their quantum numbers: charge Q in units of the electron charge, the third component of the weak isospin T_w^3, the hypercharge Y and the colour charge r, g, b (for red, green and blue).

In table 2.1 also the chirality of the particles is specified, which has the two eigenstates *left-handed* (L) and *right-handed* (R). The charged fermions have been observed in both chirality states, but neutrinos only left-handed. All left-handed fermions take part in interactions of the weak force. Here the messenger particles are the charged $W^\pm$ and the neutral Z.

The weak force and the electromagnetic force are unified in the electroweak theory or the Glashow-Salam-Weinberg model [15–17] (see section 2.2.2.3), which lead to the first general formulation of the Standard Model, to which QCD was added later [18]. The masses are generated through the Higgs mechanism, which gives rise to the Higgs boson, the only scalar elementary particle of the Standard Model. An overview of the bosons can be found in table 2.2.

Higgs boson (spin = 0)		mass	charge
		125.09 GeV	0
gauge bosons (spin = 1)	interaction		
photon (γ)	electromagnetic	0	0
$W^\pm$	weak	80.39 GeV	±1
Z		91.19 GeV	0
8 gluons (g)	strong	0	0

Table 2.2: The bosons of the Standard Model. The mass values are taken from [19].

2.2.2 The gauge principle

One of the key ingredients of the Standard Model is the gauge principle, which is introduced with the simple example of quantum electrodynamics. This discussion mainly follows [20, 21].

2.2.2.1 The QED Lagrangian

Within the formalism of the Standard Model, the particles are represented as quantum fields and their dynamics and interactions are formulated as a Lagrangian. A fermion is described by a complex spinor $\psi(x)$ with the space-time coordinates x.

The Dirac Lagrangian of a free electron is

$$\mathcal{L}_{Dirac} = i\bar{\psi}(x)\gamma^{\mu}\partial_{\mu}\psi(x) - m\bar{\psi}(x)\psi(x) \tag{2.5}$$

with the Dirac γ^{μ}-matrices and the electron's mass m. The expression is invariant under global phase transformations $\psi \to e^{i\theta}\psi$, but if the phase is a function of space and time, i.e. if the phase transformation is *local* $\psi \to e^{i\theta(x)}\psi$, the Lagrangian is modified. In order to make the Lagrangian invariant under local phase transformations, the derivative is replaced by the covariant derivative

$$\partial_{\mu} \to D_{\mu} = \partial_{\mu} + ieA_{\mu}(x) \tag{2.6}$$

where $A_{\mu}(x)$ is a new field, which has to be massless, because a mass term $(-\frac{1}{2}m_A^2 A_{\mu}A^{\mu})$ would not leave the Lagrangian invariant. A vector field like $A_{\mu}(x)$ is called a gauge field and the transformation in equation 2.6 is a gauge transformation. This gauge field transforms under the gauge transformation as:

$$A_{\mu} \to A'_{\mu} + \frac{1}{e}\partial_{\mu}\theta(x) \tag{2.7}$$

The additional term in the Lagrangian describes the interaction of the gauge field with the fermions. Here A_{μ} can be interpreted as the electromagnetic potential and is directly associated with the mediator of electrodynamics, the massless photon, and e is the coupling strength, i.e. the elementary charge.

For the new field A_{μ} the kinetic term

$$-\frac{1}{4}F_{\mu\nu}F^{\mu\nu} \tag{2.8}$$

is required in the Lagrangian. It is expressed with the electromagnetic field tensor $F_{\mu\nu} = \partial_\mu A_\nu - \partial_\nu A_\mu$. With equations 2.6 and 2.8 the full Lagrangian of quantum electrodynamics becomes

$$\mathcal{L}_{QED} = \underbrace{i\bar{\psi}\gamma^\mu \partial_\mu \psi}_{\text{kinetic term fermion}} - \underbrace{m\bar{\psi}\psi}_{\text{mass term fermion}} - \underbrace{e\bar{\psi}\gamma^\mu A_\mu \psi}_{\text{interaction term}} - \underbrace{\frac{1}{4}F_{\mu\nu}F^{\mu\nu}}_{\text{kinetic term boson}} \tag{2.9}$$

where the dependence on x is not explicitely spelled out.

2.2.2.2 The Standard Model gauge structure

In the Standard Model, all particle interactions, i.e. forces, are described by local gauge theories with an underlying symmetry, like illustrated above for QED. From the principle that a local phase transformation according to the respective symmetry has to keep the Lagrangian invariant, the interactions between the fermions and the mediators, the gauge bosons, are naturally generated. A symmetry is always associated with the conservation of a quantity [22] and hence also the symmetry of QED leads to a conserved quantum number, namely the electric charge.

The local gauge transformation can be written as unitary matrices and the set of unitary transformations form a mathematical group. In the Standard Model formalism symmetries are expressed in the form of gauge groups of the following types:

- $U(n)$: *Unitary* group with dimension n, i.e. a group with unitary $n \times n$ matrices
- $SU(n)$: *Special Unitary* group, forming a sub-group of $U(n)$, with unitary $n \times n$ matrices with determinant 1.

The QED transformation $\psi \to e^{i\theta(x)}\psi$ is equal to a multiplication of ψ with a unitary matrix U(1), which is hence the gauge group of electrodynamics. The full Standard Model gauge structure is

$$SU(3)_C \otimes SU(2)_L \otimes U(1)_Y \, . \tag{2.10}$$

Electromagnetic interactions, as described above in section 2.2.2.1, are unified with the weak interactions to the electroweak theory. The symmetry group of the electroweak theory is $SU(2)_L \otimes U(1)_Y$. $SU(3)_C$ is the symmetry of the strong interaction.

The elements of $U(1)$ commutate and hence $U(1)$ is Abelian. $SU(2)$ and $SU(3)$ are Lie groups, meaning that the commutator of any two generators $\mathcal{G}_i$ of the group is $[\mathcal{G}_i, \mathcal{G}_j] = i\sum_{k=1}^{n} f^{ijk}\mathcal{G}_k$ with the dimension n. The Levi-Civita tensors f^{ijk} form the (totally antisymmetric) structure constants of the group.

2.2.2.3 Electroweak theory

In order to explain the masses of the mediators Z and $W^{\pm}$, the electroweak symmetry $SU(2)_L \otimes U(1)_Y$ has to be spontaneously broken, as will be explained below. The generator of $SU(2)_L$ is the weak isospin, denoted $\vec{T}$ and $U(1)_Y$ is the group of hypercharge (Y) transformations, both $\vec{T}$ and Y being conserved before the symmetry breaking. The subscript of $SU(2)_L$ indicates that the gauge transformations only apply to left-handed particles, which are grouped into (weak isospin) doublets and the right-handed particles are singlets, as indicated in table 2.1.

The motivation for the new quantity Y is that isospin doublets, e.g.

$$\begin{pmatrix} \nu_e \\ e \end{pmatrix}_L , \tag{2.11}$$

should only differ in T_3 but all other quantum numbers must be the same. Y is defined such that the charge Q can be expressed with the two new quantum numbers

$$Q = \frac{1}{2}Y + T_3 \tag{2.12}$$

which means that both e_L^- and ν_e have $Y = -1$ and only differ in T_3. The right-handed fermions, e.g. e_R^+, must have $T = 0$ and $T_3 = 0$, because they transform into themselves under weak isospin rotations.

In electroweak interactions the type of quark, i.e. its flavor, can change. This is reflected by the weak eigenstates of the down-type quarks, written as d_L' in table 2.1, which differ from the mass eigenstates d_L, i.e. they are a linear combination of the mass eigenstates

$$d_L^{j\,\prime} = \sum_{j=1}^{3} V_{CKM}^{ij} d_L^j \tag{2.13}$$

with the Cabibbo-Kobayashi-Maskawa matrix and the indices i, j indicating the quark generation.

Similarly to the modification of the derivate in $\mathcal{L}_{QED}$, the covariant derivate, which is introduced to make the Lagrangian gauge invariant under $SU(2)_L \otimes U(1)_Y$

is

$$D_\mu = \partial_\mu - ig'YB_\mu - ig\vec{T}\cdot\vec{W}\,. \tag{2.14}$$

In this way, four gauge fields are introduced: B_μ is related to the hypercharge and the coupling strength of $U(1)_Y$ is g', W^i_μ, with 1=1,2,3, are related to the weak isospin and the coupling strength of $SU(2)_L$ is g.

In the introduction to the local gauge invariance of QED (section 2.2.2.1) the gauge bosons were required to be massless, but the gauge bosons of the weak interactions are clearly massive (see table 2.2). The origin of the mass is explained by the *Higgs mechanism*, a spontaneous breaking of the electroweak symmetry [23, 24].

A new complex $SU(2)$ doublet of scalar fields, the Higgs field, is introduced:

$$\Phi = \begin{pmatrix} \Phi^+ \\ \Phi^0 \end{pmatrix} = \frac{1}{\sqrt{2}} \begin{pmatrix} \Phi_2 + i\Phi_1 \\ \Phi_4 + i\Phi_3 \end{pmatrix} \tag{2.15}$$

which carries weak isospin and hypercharge (and hence has to be a doublet). The Higgs field has four degrees of freedom incorporated by the real fields $\Phi_{1\ldots4}$. The Lagrangian of the Higgs field

$$\mathcal{L}_{Higgs} = (\partial_\mu\Phi)^\dagger(\partial_\mu\Phi) - V(\Phi) \tag{2.16}$$

contains the Higgs potential

$$V(\Phi) = \mu^2\Phi^\dagger\Phi + \lambda(\Phi^\dagger\Phi)^2\,. \tag{2.17}$$

Whereas the Higgs self coupling λ is positive, the parameter μ can be chosen to be negative, which results in a non-zero ground state or vacuum expectation value. Instead the minima lie on a circle given by $\sqrt{-\mu^2/\lambda}$. As a consequence the ground state has to be “chosen”, meaning that the symmetry (in which $V(\Phi) = V(-\Phi)$ would hold) is spontaneously broken. Furthermore, a negative μ^2 can be associated with a mass.

The symmetry breaking of $SU(2)_L \otimes U(1)_Y$ has the consequence that weak isospin and hypercharge are no longer conserved. On the other hand, $U(1)_{QED}$ is not broken and hence electric charge is still conserved and also the photon remains massless after symmetry breaking. The other electroweak gauge bosons acquire a mass by the mixing with the vacuum value of the Higgs field. In this way, three of the four degrees of freedom are absorbed, whereas the remaining one gives rise to the massive Higgs boson.

The photon γ and the neutral Z are a mixture of the neutral gauge particles of weak isospin W^3 and weak hypercharge B, and the charged bosons mix to form $W^\pm$ in the following way

$$\begin{aligned} \gamma &= B\cos\theta_W + W^3\sin\theta_W \\ Z &= -B\sin\theta_W + W^3\cos\theta_W \\ W^\pm &= 1/\sqrt{2}(W^1 \mp iW^2) \end{aligned} \tag{2.18}$$

where θ_W is called the electroweak mixing angle (or Weinberg angle). It also gives a relation between the QED and electroweak coupling strengths:

$$e = g'\cos\theta_W = g\sin\theta_W\,. \tag{2.19}$$

2.2.2.4 Quantum chromodynamics

Whereas the leptons do not carry colour charge, the quarks come in three colours, called *red*, *green* and *blue*. This colour charge is the source of the strong force. The corresponding symmetry is $SU(3)_C$, where C stands for *chroma*, i.e. colour. Similarly, to the procedure of the other interactions, the derivate is modified in order to allow local gauge invariance

$$\mathcal{D}_\mu = \partial_\mu + ig_3\vec{\lambda}\cdot\vec{G_\mu} \tag{2.20}$$

with the coupling constant g_3 and the 8 Gell-Mann matrices $\vec{\lambda}$. This gives rise to 8 gauge fields $\vec{G_\mu}$, which can be directly identified with the massless gluons.

2.2.2.5 The Standard Model Lagrangian

In order to summarise this introduction to the gauge structure of the Standard Model, the gauge part of the Standard Model Lagrangian is given:

$$\mathcal{L}_{\text{gauge}} = \underbrace{-\frac{1}{4}B_{\mu\nu}B^{\mu\nu}}_{U(1)_Y} \underbrace{-\sum_{a=1}^{3}\frac{1}{4}W^a_{\mu\nu}W^{a,\mu\nu}}_{SU(2)_L} \underbrace{-\sum_{a=1}^{8}G^a_{\mu\nu}G^{a,\mu\nu}}_{SU(3)_C} \tag{2.21}$$

with the gauge field tensors

$$\begin{aligned} B_{\mu\nu} &= \partial_\mu B_\nu - \partial_\nu B_\mu \\ W^a_{\mu\nu} &= \partial_\mu W^a_\nu - \partial_\nu W^a_\mu - g \sum_{b=1,c=1}^{3} \epsilon^{abc} W^b_\mu W^c_\nu \\ G^a_{\mu\nu} &= \partial_\mu G^a_\nu - \partial_\nu G^a_\mu - g_3 \sum_{b=1,c=1}^{8} f^{abc} G^b_\mu G^c_\nu \,. \end{aligned} \tag{2.22}$$

$W_\mu^{1..3}$ represent the three fields of the weak interactions and $G_\mu^{1..8}$ are the gluon fields. ϵ^{abc} and f^{abc} are the structure constants of the respective group, as introduced in section 2.2.2.2.

2.2.3 Physics beyond the Standard Model

The Standard Model is a very successful theory to describe the phenomena of particle physics as they have been observed in experiments. It also had the power to predict undiscovered particles, like the Higgs boson. Now, after its discovery, the set of particles predicted by the Standard Model is complete, but our understanding of physics is far from being complete. There are a number of phenomena which cannot be explained by the Standard Model, like the gravitational force or the challenge to stabilise the Higgs mass (usually refered to as the *hierarchy problem*) and, in particular, the nature of dark matter.

The Higgs mass receives contributions from quantum loop corrections. Assuming that the Standard Model is valid up to the Planck energy scale, i.e. $\sim 10^{19}$ GeV, these corrections are orders of magnitude higher than the Higgs mass. Hence, the cancellations of contributions from tree level and loops are apparently "fine-tuned" to result in a much smaller mass than the single contributions, which gives rise to the hierarchy problem.

Another shortcoming of the description of the Standard Model is that the Grand Unificiation is not possible. As described in section 2.2.2.2, one of the great successes of the Standard Model was the unification of the electromagnetic and the weak force into the electroweak theory. A unification with QCD, however, seems to be impossible, because the coupling strengths do not unify when they are evoluted to higher energies.

Also an experimental observation on particle level shows a clear discrepancy with the expectations of the Standard Model, namely the neutrino oscillations which indicate that the neutrinos have to be massive, whereas they are predicted to be massless by the Standard Model (e.g. reviewed in [25]).

All of these puzzles of the Standard Model show that it cannot be the final theory of the fundamental structures, and physics beyond the Standard Model is needed.

2.2.3.1 Dark matter is physics beyond the Standard Model

By comparing the properties a dark matter particle has to fulfill with those of the Standard Model particles, most of the particles are directly ruled out. As summarised in section 2.1.4, a dark matter candidate must not couple to the photon (i.e. it does not interact electromagnetically) and it is non-baryonic (i.e. it does not participate in the strong force). This leaves only the neutrinos as potential dark matter particle. They are massive, long-lived and interact only weakly and hence clearly contribute to the non-baryonic part of the matter. But they represent hot dark matter and hence are not *the* dark matter, i.e. there must be something else to explain the abundance and the behaviour of *cold* dark matter.

Nevertheless, neutrinos play a crucial role in this study, because at a collider neutrino pair production can lead to the same signature as a dark matter event, which means that neutrino pair production is an irreducible background.

2.2.3.2 Dark matter candidates

The possible mass range of the dark matter components is huge. Attempts to constrain it have led to lower limits in the range of $m_{\text{dark matter}} > 10^{-21}\,\text{eV}$ [26] and upper limits from microlensing of $m_{\text{dark matter}} < 10^{44}\,\text{GeV}$ [14].

Whereas some ideas to explain dark matter solely try to solve the dark matter problem (like MACHOs [27], WIMPzillas [28]), in other proposed models for physics beyond the Standard Model several of the shortcomings are addressed.

If there is new physics at much lower scales than the Planck scale, the hierarchy problem could be solved. For example in supersymmetric models the correct Higgs mass is obtained with less fine-tuning, i.e. in a more natural way [29]. With new particles the renormalisation group equations would be modified, such that the Grand Unification of the forces is possible. In many supersymmetric models the lightest new particle is a dark matter candidate.

Another example for dark matter candidates arising from an approach, which addresses one of the other open questions are Axions [30]. They originate from a theory which can also solve the strong CP problem. This problem is the lack of an explanation for the unnaturally small CP-violating term in the QCD Lagrangian.

With the discovery that neutrinos are not suitable dark matter candidates [31–33], the concept of Weakly Interacting Massive Particles (WIMPs) as candidates for dark matter, was born [34, 35]. As discussed below, WIMPs are particles arising from a number of different models for physics beyond the Standard Model. In this work the focus is on WIMP dark matter, which is thus introduced in more detail.

2.3 Weakly Interacting Massive Particles

WIMPs are proposed new particles, which (as reflected by their name) are massive and interact at the scale of the electroweak force. The mass ranges from GeV to a few TeV. In order to be a candidate for dark matter, a WIMP it has to be stable and reproduce the observed abundance[i].

2.3.1 Motivation for WIMP dark matter

One way to motivate WIMPs are models, which solve the hierarchy problem. The divergent quadratic corrections in the Higgs mass terms could be circumvented if there was new physics at a scale not much higher than the heaviest known elementary particles, i.e. at the electroweak scale [29]. If such physics beyond the Standard Model incorporates a dark matter particle in the range of GeV to a few TeV, which was thermally produced in the early universe (see further section 2.3.2), its thermally averaged annihilation cross-section has to be in the order of $\langle \sigma_{ann} v \rangle \approx 3 \times 10^{-26}\,\mathrm{cm}^3\mathrm{s}^{-1}$ to obtain the right abundance today, which is the cross-section range of electroweak forces [29], hence this particle would be a weakly interacting massive particle.

One key requirement of a successful theory to describe WIMP dark matter is an explanation for the particle's stability. In general, either the couplings are very weak or some symmetry is required to protect the WIMP. The first option is not discussed here, because it would also make the detection in any of the channels almost impossible. For the latter case, examples for a new conserved quantum numbers are given by R-parity in Supersymmetry [36, 37], T-parity in Little Higgs [38, 39] and KK-parity [40, 41] in universal extra dimension theories [42]. In this thesis a generic WIMP search is conducted, independent of a specific model.

---

[i] If the WIMP abundance of a model is too low, but all the other properties are fulfilled, there must be yet another source of dark matter.

2.3.2 Thermal relic of the early universe

For the WIMP properties discussed above, it is assumed that the WIMPs were in thermal equilibrium with other Standard Model particles in the early universe [43]: Initially, when the temperature was much higher than the WIMP mass, they were constantly produced by annihilation of Standard Model particles and annihilated through the inverse reaction (e.g. $\chi\chi \leftrightarrow e^+e^-$ or ZZ or other Standard Model particle pairs)[ii], such that their comoving number density was constant with time, as illustated in figure 2.4. When the temperature decreased through the expansion of the universe, the WIMP production started to be suppressed and the thermal equilibrium number density dropped. Without the production of WIMPs, their number density decreased in the expanding universe until they were so thinned out that they stopped annihiliating, meaning that the interactions upholding the thermal equilibium "froze out". As a consequence, the (comoving) number density remains constant after the freeze-out. Depending on the annihilation cross-section the fraction of remaining WIMPs differs: the larger the cross-section the lower the fraction (depicted by the dashed lines in figure 2.4).

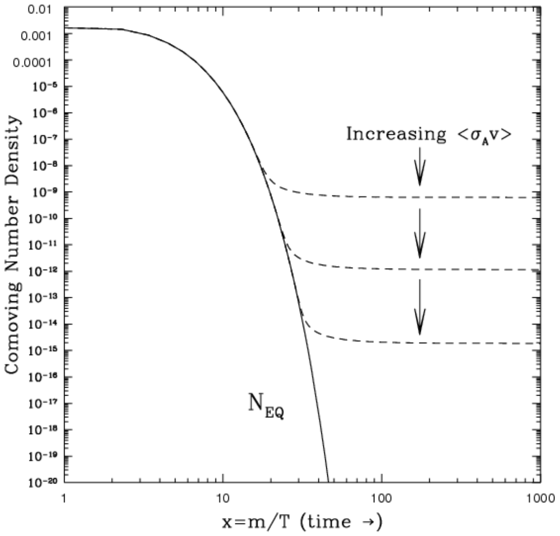

Figure 2.4: Comoving WIMP number density as a function of time (given in mass over temperature, which decreases with time). At high temperatures the WIMPs are in thermal equilibrium. Once their production stops, the WIMPs continue annihilating and their number density decreases, until they "freeze out". With increasing annihilation cross-section the remaining fraction of WIMPs is smaller, depicted by the three dashed lines. Taken from [44].

The WIMP relic density can be calculated by starting with the two equations [29]

$$\frac{\mathrm{d}n}{\mathrm{d}t} = -3Hn - \langle\sigma_{ann}v\rangle(n^2 - n_{eq}^2) \tag{2.23}$$

[ii] χ will be used as symbol for the WIMP throughout this thesis.

and

$$\frac{\mathrm{d}s}{\mathrm{d}t} = -3Hn \tag{2.24}$$

which describe the evolution with time of the WIMP number density n and the entropy (s) conservation, respectively. H is the Hubble constant and $\langle \sigma_{ann} v \rangle$ is the thermally averaged annihilation cross-section. The two equations are related with the parameter $Y = n/s$ and the WIMP relic density can be expressed as a function of the present WIMP abundance Y_0 and the WIMP mass m_χ

$$\Omega h^2 = 2.755 \times 10^8 Y_0 m_\chi / \mathrm{GeV} \tag{2.25}$$

(See e.g. [29] for a full derivation.)

2.3.3 Approaches to search for WIMPs

Three fundamentally different methods to search for WIMPs can be employed: *direct detection*, *indirect detection* and *collider searches*. Whereas in the first two approaches one tries to discover a reaction of the WIMPs abundant in the universe, in collider experiments the aim is to produce dark matter particles in the laboratory. In figure 2.5 the different kinds of reactions between WIMPs and Standard Model particles in the three complementary ways to search for dark matter are visualised.

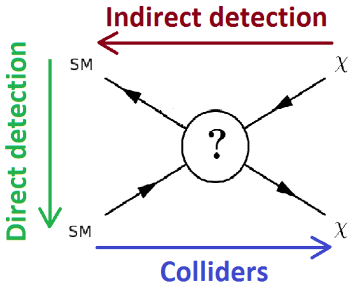

Figure 2.5: Visualisation of the respective reaction between Standard Model (SM) and dark matter (χ) particles tested in direct, indirect and collider searches.

In direct detection experiments scattering processes of Standard Model and dark matter particles are tested. The assumption is that a dark matter particle travels through the detector and interacts *directly* with the detector material. For a visualisation of the reaction in direct searches the diagram in figure 2.5 has to be read from top to bottom. When reading the diagram from right to left, the hypothesis that Standard Model particles can be annihilation products of WIMPs is visualised. The astrophysical observation of the decay products would be an *indirect* evidence for dark matter. In a collider search the reverse process is assumed and the figure has to be read from from left to right.

A discovery of a signal in any search would put the ideas of *modified newtonian dynamics* [45] and their adaptations to relativity [46] under pressure even before an astrophysical proof that it is dark matter.

An introduction to the main principles of the three different types of searches is given in the following and a review can be found e.g. in [47].

2.3.3.1 Direct detection

In direct detection experiments one looks for elastic WIMP-nucleus scattering, meaning that, if a dark matter particle travels through the detector and transfers energy to the detector material, this could be measured as a nucleus recoil. See [48] for a review on direct detection experiments.

The experiments are earth-bound and usually located underground, to suppress the background of cosmic rays. One of the limiting factors is that the detector material has to be radiopure to keep the background of radioactivity low. The aimed key characteristics are a low energy treshold, very low background and good background discrimination. The measurement is a rate in the detector, which means that a large volume is favoured. The techniques used to measure the recoil are via scintillation light, heat (phonons) and ionisation (in time projection chambers).

In figure 2.6 exclusion limits on the cross-section of spin-independent WIMP-nucleon scattering from a selection of experiments is shown, including data from XENON1T [49], LUX [50] and PandaX-II [51]. *Spin-independent* means that protons and neutrons in the nuclei contribute equally to the scattering process [48]. In the WIMP mass range of 10 GeV to 1 TeV cross-sections down to $10^{-46} - 10^{-47}\,\text{cm}^2$ or $10^{-7} - 10^{-8}\,\text{fb}$ could be excluded.

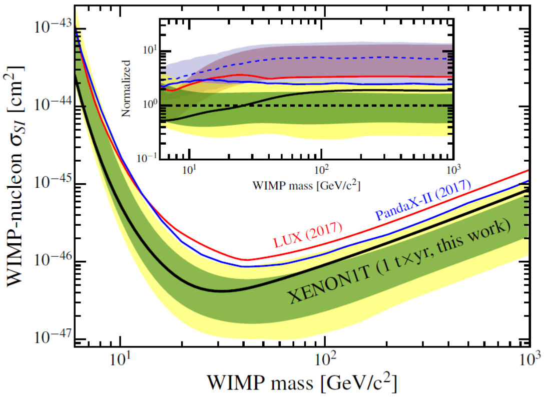

Figure 2.6: 90% confidence level upper limit on the spin-independent WIMP-nucleon cross-section σ_{SI}. Taken from [49].

2.3.3.2 Indirect detection

In indirect searches, signs of dark matter annihiliation as excess in the fluxes of photons, anti-particles and neutrinos are searched for.

Gamma rays which are promptly generated at the WIMP annihilation, i.e. emitted from charged annihiliation products, keep their directional information. This allows to look for sources with an expected high abundance of dark matter, like the galactic centre and dwarf spheroidals by using the Fermi-LAT satellite [52] and earth-bound cherenkov detectors (reviewed in [53]). Other potential sources of photons include the annihilation radiation of positronium (511 keV line) [54] and secondary emission, like synchrotron and inverse Compton scattering.

The main challenge for indirect detection is the ambiguity that an observed excess could also stem from an astronomical source. For example different gamma ray sources, like galactic emission, point sources and isotropic distributions have to be understood. In general, large uncertainties are induced through the astrophysical foregrounds and backgrounds and, in the case of charged particles, their diffuse propagation.

The source of anti-matter particles, like positrons, anti-protons or anti-deuterons, could be WIMPs annihilating into pairs of Standard Model particles. The charged particles (especially positrons) loose energy when they travel through the galactic magnetic field and hence they allow to probe only the local Milky Way halo.

Here, one measurement which was also interpreted as possible signal is presented in more detail. At the Alpha Magnetic Spectrometer (AMS) on the International Space Station the positron fraction in the energy range of $0.5 - 350\,\mathrm{GeV}$ was observed [55] and extended to 500 GeV [56], which is shown together with data from other experiments [57–62] in figure 2.7. The fraction first rises with energy and flattens above 200 GeV. As discussed in [56], dark matter was suggested to be the origin of this apparent excess, but a second canonical explanation was that pulsars could produce the observed signature.

As WIMPs are expected to accumulate in the centre of the sun, also high-energetic neutrinos can be looked for (reviewed in [63]). Depending on the assumed model they could either be produced directly in WIMP annihilation or in the decay of produced Standard Model particles, like heavy quarks or tau leptons.

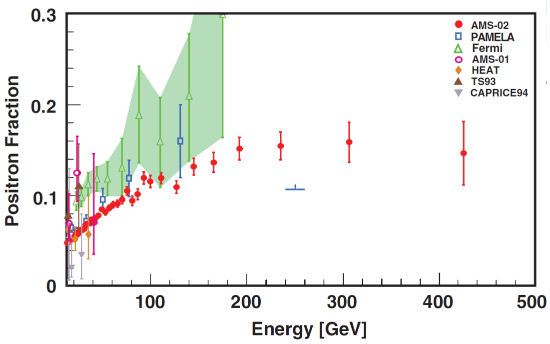

Figure 2.7: Positron fraction in the energy range up to 500 GeV as measured with AMS and other experiments. Taken from [56].

2.3.3.3 Collider searches

The main difference of collider searches to direct and indirect detection, is the assumption that the WIMPs are produced in the particle collision rather than looking for astrophysical WIMPs. This allows to test the particle hypothesis in the laboratory.

The main advantage over the other search channels is that in a collider experiment the initial state is known. The identity of the colliding particles is evident and hence the WIMP interaction with these specific particles is tested. The energy transfer is comparably well known, and different centre-of-mass energies can be examined. With the potential of polarised beams the chirality of the interaction and hence the type of mediator can be studied. Additionally, other signatures of a new theory could potentially be seen. In this way, collider searches can complement direct and indirect detection with the unique feature of a controlled environment.

If WIMPs are produced in a collider experiment, they can only be detected indirectly. The detectors of collider experiments are not designed to observe dark matter itself. The signature of a signal event is the missing energy and momentum which is carried away by the invisible dark matter particles. Thus, a pure production of WIMPs would not be noticed. In order to identify such an event, an additional particle (or several) has to be produced in association with the WIMPs.

A number of different analyses are performed to search for WIMPs at colliders. As reviewed in [64] for the LHC, they range from tests of full theories (like the models listed in section 2.3.1) with more complex, i.e. model-specific, signatures to generic searches with a simpler signature. An example for the study of a model-specific analysis is given in [65], where a supersymmetric model with its full spectrum and complete decay chains and branching ratios is studied with at the LHC and the ILC. A large fraction of the most recent studies at the LHC follow generalised approaches. An initial outline for the run 2 prospects focuses on simple detector signatures without a detailed description of the underlying model [66].

In [66] generic signals are described, which have in common that dark matter is produced in pairs. In order to enable a detection of events with these invisible particles, the production of additional (Standard Model) particles are assumed. The general process is visualised by the pseudo Feynman diagram in figure 2.8a (left)[iii]. Like all Feynman diagrams in the following, it is read from left to right. In the simplest cases one additional particle is assumed, which leads to the *mono-X* signature, where X can stand for many different particles, like electroweak bosons, a photon, a gluon, quarks and leptons.

At the LHC also the mediator of dark matter production is searched for directly. If the coupling between the WIMPs and the Standard Model particles is mediated in an s-channel, an enhancement of di-quark production will occur at the same time. Thus, precision measurements of di-jet events can set strong limits on the coupling of the new mediator to the Standard Model [68].

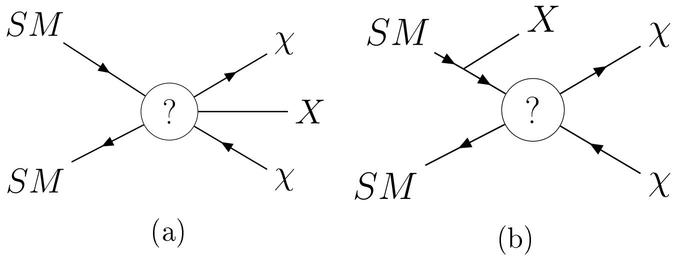

Figure 2.8: Pseudo Feynman diagrams of the mono-X channel.

In collider searches, the most general way is to extend the assumed reaction of Standard Model particles producing a WIMP pair by initial state radiation (ISR), which is visualised in figure 2.8b. In this way no further assumptions on the new process are made, because the incoming fermion (f) can always emit ISR. In any model that allows the reaction $f\bar{f} \rightarrow \chi\chi$ also the reaction $f\bar{f} \rightarrow \chi\chi$+ISR is possible, which makes it the simplest extension to the process shown in figure 2.5. The ISR, however, is not emitted independently of the hard interaction, e.g. the maximum energy of the ISR is restricted by the mass of the other produced particles. As a consequence the photon energy range depends on the WIMP mass, which is further discussed in section 5.1.2.

Many different particles can be emitted as ISR. The emission of an ISR photon has by far the largest cross-section at a lepton collider. The analysis presented here exploits this *mono-photon* channel.

The high model-independence together with the high cross-section of processes

---

[iii] Feynman diagrams in figures 2.8, 5.1, 5.2, 5.3, 5.4 are drawn using [67].

with a detectable ISR particle are the motivations to search for WIMP pair production with an associated ISR photon in this analysis. The signature of the search is thus a photon in an otherwise “empty” detector.

Analogously to the di-jet precision measurements at the LHC, the mediator can be tested in di-lepton production at the ILC. In this analysis the focus is on the mono-photon signature, but precision measurements of the di-lepton cross-section could complement the study.

2.4 Interpretation framework

A number of different theories and concepts have been developed to explain the existence and abundance of dark matter, but so far there is no experimental evidence for any of them to be realised in nature. If one were to test individual full models it would hence be undetermined which to select. Instead, the general approach of effective field theories is chosen.[iv]

2.4.1 Effective field theory

Many processes of different full theories can lead to the same observables in a collider experiment, which allows to categorise them and describe them effectively. The theoretical framework used in this analysis are effective operators [70, 71] (ILC specific), [72–77] (with a focus on different experiments, selection). The underlying idea is to construct a minimal effective Lagrangian by integrating out the mediator, as visualised in figure 2.9. This implies that the mass of the considered mediator has to be well above the momentum transfer in the process, which is the fundamental assumption in effective theories. As a consequence, effective operators provide a good description in an energy regime where any new physics decouples.

Compared to using a specific model, the description of WIMP interactions in the effective field theory has a high model independence. A broad range of phenomena are covered, because heavy fields in the Lagrangian, describing the short range interaction, are replaced by light fields in order to obtain the general form of the effective Lagrangian of the interaction

$$\mathcal{L}_{eff,int} = \sum_{d,i} \frac{\alpha_i}{\Lambda^{d-4}} \mathcal{O}_i \tag{2.26}$$

[iv] In the first ILC study [1,2] a different general approach was used, which is based on cosmological observables [69].

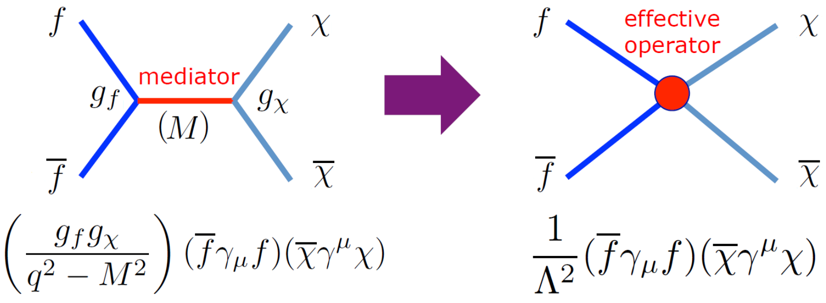

Figure 2.9: Visualisation of the difference between full and effective field theory description, for the example of WIMP pair production from two Standard Model fermions with an exchange of a mediator in the s-channel. Instead of looking at all free parameters (mediator mass and couplings) the process is treated as an effective four-point interaction. The free parameter Λ has units of energy.

with mass dimension d, operators of the light field $\mathcal{O}_i$ and dimensionless parameters α_i [78]. Here the interpretation is restricted to dimension 6 and it is assumed that WIMPs and Standard Model particles only interact through one operator, which means that one of the parameters α_i is equal to 1 whereas all others are 0 and hence $\mathcal{L}_{eff,int} = \frac{1}{\Lambda^2}\mathcal{O}$.

The only parameter that remains, Λ, can be called the energy scale of new physics and is a function of the mediator mass and the coupling to the Standard Model fermions g_f and the coupling to the WIMPs g_χ:

$$\Lambda = M_{mediator}/\sqrt{g_f g_\chi} \tag{2.27}$$

In order to allow perturbative calculations, the two couplings have to be small, e.g. $< \sqrt{2\pi}$. This means that the condition of a high $M_{mediator}$ is transfered to a required high Λ. Hence, an effective Lagrangian can only describe processes at centre-of-mass energies below Λ and effective field theories are not suitable to describe the resonant enhancement in the case of mediator masses in the range of the centre-of-mass energy. The resulting limit would be too conservative and for mediator masses below the resonance the limits are too aggressive [79]. As shown later (in the results chapters 7 and 8), the testable energy scales at the ILC are significantly higher than the centre-of-mass energy and hence effective operators can be used.

2.4.1.1 Effective operators used in this analysis

In this analysis, the mono-photon data is analysed using three example operators, called *vector*, *axial-vector* and *scalar* operator. The approach and the nomenclature follow [70]. The three considered operators are only examples, more operators can be built, but this selection covers a large variety of the phenomenological spectrum. In table 2.3 the properties of the operators are shown.

	four-fermion operator	$\sigma_{LR} = \sigma_{RL}$	$\sigma_{LL} = \sigma_{RR}$
vector	$(\overline{f}\gamma^\mu f)(\overline{\chi}\gamma_\mu\chi)$	$\neq 0$	0
axial-vector	$(\overline{f}\gamma^\mu\gamma^5 f)(\overline{\chi}\gamma_\mu\gamma_5\chi)$	0	$\neq 0$
scalar	$(\overline{\chi}\chi)(\overline{f}f)$	0	$\neq 0$

Table 2.3: Effective operators used in this analysis.

All of the operators describe an s-channel exchange of mediators. It is worth noting that in each case either only the opposite (σ_{LR} and σ_{RL}) or equal (σ_{LL} and σ_{RR})[v] helicity combinations give a non-zero cross-section.

Whether dark matter consists of Majorana or Dirac particles is an open question. The following discussion and the basic concept of this analysis are compatible with either assumption. In this setup the WIMP is assumed to be a spin-1/2 Dirac fermion.

In [70] the double-differential cross-sections are given for the energy E_γ and the polar angle θ_γ of the ISR photon. For convenience dimensionless quantities are used: $z = \frac{2E_\gamma}{\sqrt{s}}$, $\cos\theta_\gamma$ and $\mu = \frac{M_\chi}{\sqrt{s}}$, with the centre-of-mass energy $\sqrt{s}$ and the WIMP mass M_χ.

The double-differential cross-section for the vector type (V) and incoming particles with opposite polarisation is [70]:

$$\frac{d^2\sigma_{V,LR}}{dz d\cos\theta} = \frac{d^2\sigma_{V,RL}}{dz d\cos\theta} =$$
$$\frac{\alpha}{12\pi^2}\frac{(\sqrt{s})^2}{\Lambda^4}\frac{1}{z\sin^2\theta}\sqrt{\frac{1-z-4\mu^2}{1-z}}\left(1-z+2\mu^2\right)\left[4(1-z)+z^2(1+\cos^2\theta)\right] \quad (2.28)$$

The cross-section for electrons and positrons with equal polarisation vanishes: $\sigma_{V,LL} = \sigma_{V,RR} = 0$.

---

[v] Where L stands for 100% left-handed and R for 100% right-handed incoming electron and positron.

And for an axial-vector (AV) type the formula is similar, but for inverse polarisation dependence [70]:

$$\frac{d^2\sigma_{AV,RR}}{dzd\cos\theta} = \frac{d^2\sigma_{AV,LL}}{dzd\cos\theta} = \frac{\alpha}{12\pi^2}\frac{(\sqrt{s})^2}{\Lambda^4}\frac{1}{z\sin^2\theta}\left(\frac{1-z-4\mu^2}{1-z}\right)^{3/2}(1-z)[4(1-z)+z^2(1+\cos^2\theta)] \quad (2.29)$$

and $\sigma_{AV,LR} = \sigma_{AV,RL} = 0$.

For the third assumption tested in this analysis, the scalar mediator, the cross-section for incoming particles with equal polarisation is [70]:

$$\frac{d^2\sigma_{S,RR}}{dzd\cos\theta} = \frac{d^2\sigma_{S,LL}}{dzd\cos\theta} = \frac{\alpha}{8\pi^2}\frac{(\sqrt{s})^2}{\Lambda^4}\frac{1}{z\sin^2\theta}\left(\frac{1-z-4\mu^2}{1-z}\right)^{3/2}(1-z)[2(1-z)+z^2] \quad (2.30)$$

and $\sigma_{S,LR} = \sigma_{S,RL} = 0$.

2.4.1.2 LEP exclusion limits

The lepton collider with the highest energy so far was the Large Electron-Positron Collider (LEP) at CERN, which was in operation from 1989 to 2000. At LEP no excess in mono-photon events was seen.

In [72] the effective operators presented in section 2.4.1.1 were used to calculate exclusion limits for LEP with centre-of-mass energies from 180-209 GeV. The analysed mono-photon signal, is based on data from DELPHI and corresponds to an integrated luminosity of 650 pb^{-1} [72]. The exclusion limits with a 90% confidence level are shown in figure 2.10. The testable energy scale is in the range of a few 100 GeV for WIMP masses up to ~80 GeV and for higher WIMP masses the sensitivity decreases. The maximum testable masses are $\lesssim$100 GeV, i.e. just below the centre-of-mass energy. In section 8.6.2 limits on the sensitivity are compared to results of this work.

2.4.2 The alternative approach of simplified models

At the LHC also effective operators were used for WIMP searches [80–82], but the limits did not exceed the centre-of-mass energy and hence effective field theory turned out to be an inadequate approach to describe the full claimed phase space

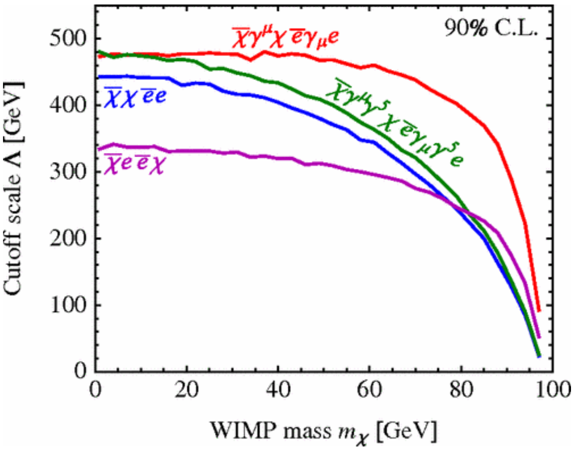

Figure 2.10: Lower exclusion limits for LEP on the Λ parameter as a function of the WIMP mass for a vector (red), axial-vector (green), scalar, s-channel (blue) and scalar, t-channel (purple) effective operators. Taken from [72].

region [83, 84]. The interpretation framework used for general WIMP searches at the LHC are simplified models [79, 85, 86].

Instead of an effective four-point interaction the idea in the approach of simplified models is to describe the new process with generic mediators. In s-channel WIMP production there are three free parameters instead of one for effective operators (Λ): the mediator mass, the coupling to the Standard Model particles and the coupling to the WIMP. In this way, the setup of simplified models is slightly more complex but they still provide a rather general description.

2.4.2.1 Example of an LHC limit

According to the *LHC dark matter working group* [87] the recommended way [88] to present results obtained in the framework of simplified models is in two dimensions: as a function of mediator mass and WIMP mass. The other two free parameters, the couplings, are fixed for a certain presentation of the results. The generic values for the couplings to WIMPs q_{DM} and to Standard Model fermions q_{SM} are chosen to be $q_{DM} = 1$ and $q_{SM} = 0.25$. The rather strong limits on the di-jet production are reflected in the small value for the Standard Model coupling.

In figure 2.11 CMS results [89] as an example for LHC exclusion limits are presented. For ATLAS analogous studies are conducted [90]. In [89] data taken at $\sqrt{s} = 13\,\text{TeV}$ corresponding to $12.9\,\text{fb}^{-1}$ is analysed assuming a vector operator. The shown exclusion region is restricted to mediator masses which are at least twice the WIMP mass, i.e. to the lower right half of the graph. For the assumed coupling strengths mediator masses up to 700 GeV are excluded for WIMP masses up to 300 GeV.

In section 8.6.3 ILC and LHC results are compared, where simplified models are

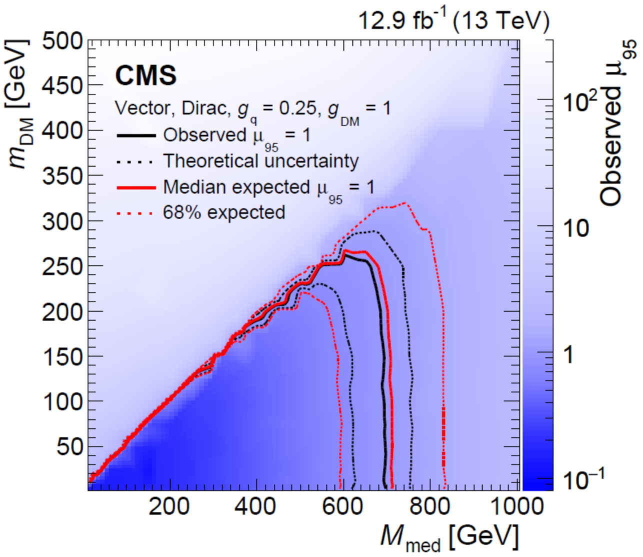

Figure 2.11: CMS exclusion limits assuming a vector operator for WIMP masses up to 500 GeV and mediator masses up to 1 TeV. Taken from [89].

used. The ILC exclusion limits obtained with effective operators are translated into limits on the mediator mass. For a vector and axial-vector operator the relation is $\Lambda = M_{med}/\sqrt{q_{DM}q_{SM}}$. In the conversion of the ILC results it is assumed that the coupling to leptons is 0.25, analogously to the assumption for the LHC results that the coupling to the quarks is 0.25.

2.5 Interplay between different experiments

The three search strategies of direct detection, indirect detection and collider searches are highly complementary. The tested energy transfer between dark matter and Standard Model particles is at different scales, especially between direct detection and the other two approaches. Additionally, the experimental conditions offer different advantages and challenges. The discovery of a suitable new particle at a collider will remain only a dark matter *candidate*, until it is identified by astrophysical observations and can only solve the dark matter puzzle if the correct abundance can be inferred. The discovery of a signal in direct or indirect searches on the other hand, will probably not allow to learn as much about the underlying physics as in collider experiments with their controlled environment.

A comparison of limits obtained by the three channels is only possible for specific models because a certain running of the coupling has to be assumed to relate the different scales of energy transfer and the different Standard Model particles involved.

Comparison of direct detection and collider searches

A confrontation of LHC limits with direct detection results shows, that depending on the assumptions on the underlying process either of the channels can lead to a better sensitivity [75, 84]. Additionally to the different energy scale in direct detection, the exclusion limits on the cross-section of WIMPs and nuclei cannot be generally translated to limits on the interaction of WIMPs and leptons. Especially if WIMPs are *leptophilic* [91], i.e. mainly couple to leptons, direct detection cross-section limits would be weaker than in other models.

In [71] two examples for different assumptions on the coupling are tested in a comparison of the expected ILC sensitivity to direct detection limits, obtained within the framework of effective operators, to direct detection limits. In the first case all Standard Model particles couple to the WIMP with the same strength. If a “Yukawa-like”, i.e. mass-dependent, coupling is assumed, the expected ILC bounds are more pessimistic.

In [78] an approach is presented to identify phase space which can be tested at future lepton colliders and is not yet excluded by other experiments, including data from direct detection experiments, from the LHC and from Planck. In figure 2.12 the allowed region in the plane of WIMP particle mass and energy scale Λ is shown in light yellow, assuming a model with a Majorana WIMP. A different approach to test whether a certain model point is excluded is the CheckMATE [92] programme. With information from ILC Monte Carlo of a preliminary version of this work is also included to test the compatibility of dark matter models with the expected ILC sensitivity [93].

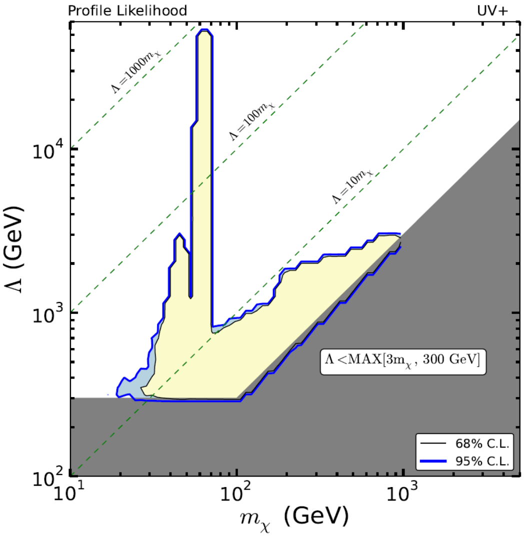

Figure 2.12: Allowed phase space in the plane of WIMP mass and the energy scale of the effective operators Λ, resulting from a likelihood analysis with data from direct detection experiments, LHC and Planck. Taken from [78].

Comparison of lepton and hadron colliders

Also the comparison of different collider searches are model-dependent. In the dark matter searches at the LHC the coupling of the WIMP to quarks and gluons is probed, whereas at electron-positron colliders the coupling to leptons is tested. This complementarity also means, that without a full theory or strong assumptions on how couplings to leptons relates to the couplings to quarks and gluons, any limits on couplings to hadrons from LHC data do not give a unique prediction how the testable phase space at the ILC is restricted.

Besides the different type of incoming particles, which might have a coupling to WIMPs, a number of fundamental differences of lepton and hadron colliders can be identified. The colliding particles at hadron colliders are composite, whereas they are elementary at a lepton collider. This means that the four-momentum of the initial state is known at the ILC, hence the energy carried away by the WIMPs is reflected in missing four-momentum. In addition, the environment at a lepton collider is cleaner, i.e. the detectors have a comparably low activity, because there are no beam remnants and no colour strings between the produced particles. Also the systematic uncertainties from parton density functions are absent. The lower cross-sections of electroweak reactions compared to QCD reactions also means that the background levels are lower and the ILC will operate without pile-up and no trigger. As a consequence, also unexpected exotic events are not discarded.

The programme of dark matter collider searches comprises studies at the running machines LHC and Belle [94] and at previous accelerators like LEP. Whereas the searches at the LHC is limited to couplings of dark matter to hadrons, the lepton colliders Belle and LEP have rather low centre-of-mass energies and low luminosities, respectively. A lepton collider at the energy frontier with unprecedented luminosities can complement the existing approaches.

Chapter 3

The International Linear Collider

In this chapter the International Linear Collider (ILC), a proposed electron-positron collider, is presented. In the first section of this chapter the advantages of the ILC over other planned projects are discussed. In section 3.2 an overview of the accelerator is given, followed by a summary of the key goals of the physics programme in section 3.3. Two possible operation scenarios are presented in section 3.4. In section 3.5 the luminosity spectrum and the several beam-induced background processes are described. The ILD detector concept, used for this analysis, is introduced in section 3.6.

The mature technology of accelerator and detector concepts is presented in the Technical Design Report volume 1 through 4 [95–99]. The description of the accelerator and the detector concept are based on the Technical Design Report, volume 3.II [98] (accelerator) and volume 4 [99] (detector), if not stated otherwise.

3.1 Comparison to other planned high-energy electron-positron colliders

The proposed high-energy lepton colliders have two fundamentally different designs: The Compact Linear Collider (CLIC) [100] is linear like the ILC and the Future Circular Collider (FCC-ee) [101, 102] and the Circular Electron Positron Collider (CEPC) [103, 104] are based on storage rings. Whereas new phase space in the WIMP search can be explored at all the experiments, they have a different potential to meet the key requirements of the analysis, which are a high centre-of-mass energy, high luminosities and polarised beams.

Because of the increase of the synchrotron radiation with energy [105]

$$\Delta E_{\mathrm{synch}} \propto \frac{1}{R} \cdot \frac{E^4}{m^4} \tag{3.1}$$

the acceleration of electrons with their rather small mass m in circular machines is only feasible up to moderate energies. So the centre-of-mass energies of the CEPC (240-250 GeV) and FCC-ee (up to 350 GeV) are smaller than those of the planned linear colliders. Whereas the maximum centre-of-mass of a circular machine is basically fixed by the circumference of the ring, one of the advantages of a linear collider is the possibility of a staged construction, meaning that the operation starts at a lower centre-of-mass energy with shorter linacs, which are successively extended. At CLIC the first stage is supposed to be at 380 GeV and with the final extension 3 TeV can be reached. In order to reduce the costs of the first stage, the ILC is currently assumed to start operation at 250 GeV [106], whereas in the Technical Design Report [95–99] the centre-of-mass energies range from 200 to 500 GeV. By extending the main linear accelerators (linacs) an upgrade to 1 TeV is possible. The higher centre-of-mass energies and the potential of extentions is a clear advantage of the linear machines CLIC and ILC for the WIMP search.

For the second requirement of a high luminosity the circular machines are advantageous. At a linear collider a high luminosity can only be achieved by highly collimated beams, which lead to beamstrahlung (see section 3.5). Beam polarisation on the other hand is more difficult to realise at circular machines. At CLIC the electron polarisation is supposed to be 80% and in an upgrade positron polarisation might be added. At the ILC both beams are planned to be longitudinallly polarised. In the baseline design the electron polarisation is at least 80% and the positron polarisation 30%, upgradable to 60%.[i] If new particles are observed, the polarisation of both beams allows the determination of the chirality of the new interaction.

In this analysis the ILC is taken as an example for a future linear collider. The higher possible centre-of-mass energies make the linear machines more suitable for a WIMP search. In the results chapters 7 and 8 the role of the centre-of-mass energy in comparison to the integrated luminosity will be discussed. There, also the benefit of polarised beams will be shown.

---

[i] 80% polarisation means that the remaining 20% of the particles are equally split over the two chiral states.

3.2 Overview of the accelerator

In figure 3.1 the general layout of the baseline design of the ILC for up to 500 GeV is shown. The footprint of the machine has a total length of 34 km [107, 108]. A possible candidate site is near Kitakami in the Iwate prefecture, situated in the north of Honshu, Japan's main island. One interaction point is foreseen, where two multi-purpose detectors, the Silicon Detector (SiD) and the International Large Detector (ILD), will be operated in a push-pull setup.

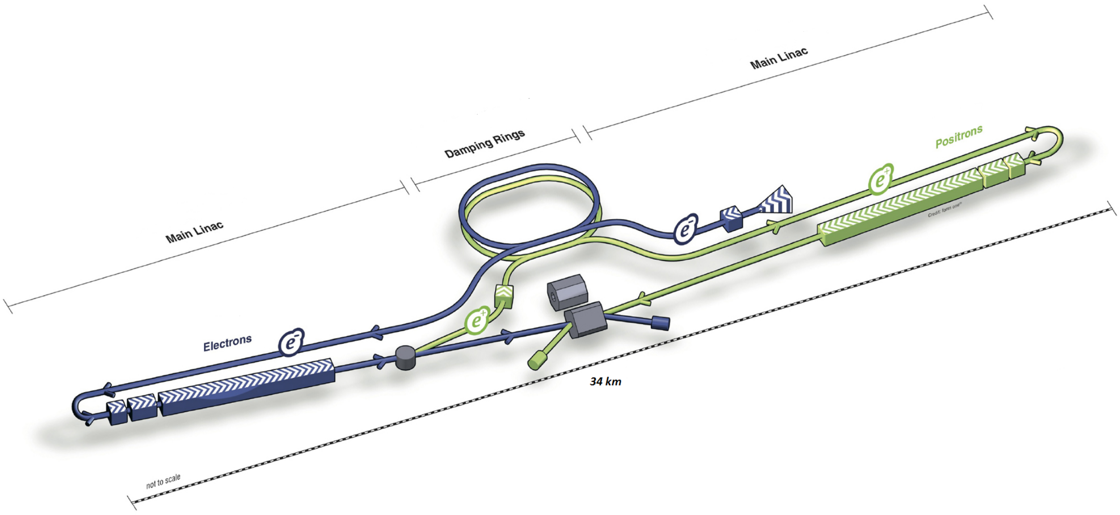

Figure 3.1: Schematic view of the ILC baseline design for centre-of-mass energies up to 500 GeV.

The electrons are generated in a polarised source, based on a GaAs photocathode illuminated by a laser. In a normal-conducting linac the particles are bunched and pre-accelerated to 76 MeV and consecutively to 5 GeV in a superconducting linac.

The positron source is based on a helical undulator. After the main linac the electron beam is guided through the magnetic structure in order to emit photons which produce e^+e^- pairs at the impact on a target. With a 147 m[ii] undulator 30% polarisation are supposed to be achieved. For an upgrade to 60% a longer magnetic structure is needed and space for a 220 m undulator and a photon collimater is kept.

After being accelerated to 5 GeV, the particles are injected into a damping ring, where electrons and positrons share a common tunnel with a circumference of 3.2 km.

[ii] For a 250 GeV machine a longer (231 m) undulator is required because of the lower electron beam energy [106].

The ring is located in the central region of the accelerator, horizontally offset from the detector hall by 100 m. The two straight sections of the ring house radio frequency cavities and damping wigglers. In this way the beam emittance is lowered, which is a prerequisite for the required high instantaneous luminosity.

After the damping ring the electrons and positrons are transported to the opposite ends of the machine from where they are accelerated further in the main linacs with a length of 12.5 km[iii] on both sides for a centre-of-mass energy of 500 GeV. The acceleration is based on the TESLA technology with superconducting radio-frequency (1.3 GHz) niobium cavities, operated at 2 K. The anticipated average gradient is 31.5 MV/m. Trains with 1312 bunches are accelerated at a rate of 5 Hz. The pulse length is 1.6 ms.

The beam delivery systems comprise the last 2.2 km on each side of the interaction point, where the beams are focused to allow an instantaneous luminosity of $1.3 \cdot 10^{34}\,\mathrm{cm}^{-2}\mathrm{s}^{-1}$ at a centre-of-mass energy of 500 GeV. The electron and positron bunches are brought to collisions with a crossing angle of 14 mrad.

3.3 Physics goals

Before turning to the physics goals of the ILC it is worthwhile to highlight that a lepton collider is complementary to hadron colliders like the LHC. Compared to a hadron collider the background level is lower and the events are cleaner. The lower event rates allow for a triggerless operation and there is no pile-up of multiple events. Also hadrons from the underlying event and the large systematic uncertainties on the proton structure function are absent. All of this allows for high precision measurements at lepton colliders, whereas the LHC operates at higher centre-of-mass energies.

A complete presentation of the physics case of the ILC can be found in [96], which has been updated both from a phenomenological point of view [109] and with a focus on the experiment [110]. The overview is complemented with a summary of the programme at a 250 GeV machine [111] and a discussion about the potential to discover new particles at the ILC in [112] .

As stated in [110], the physics programme of the ILC covers a broad range of aspects, like precision electroweak measurements, studies of the W and Z boson couplings and tests of QCD. The three key aspects are high-precision measurements

---

[iii] In the Technical Design Report [98] the linacs were only 11 km long, resulting in a total length of 31 km, which was modified in the 4th ILC change request [107].

of the properties of the Higgs boson and the top quark and searches for new particles beyond the Standard Model.

The measurements of the Higgs boson and the top quark can be seen as the guaranteed programme of the ILC. The outcome of the searches for physics beyond the Standard Model is unclear, but even in the case that no new particles are found, precision measurements can be sensitive to indirect effects of new physics at higher mass scales [113]. Similarly, in [112] it is shown that new phenomena can be discovered at the ILC independent of whether new particles will be found at the LHC and what their mass scale is. Especially the complementarity of the tested couplings in the case of the WIMP search means that new phase space can be explored at the ILC.

3.4 Operation scenarios

The exact scheme for running the ILC will depend on the status of LHC measurements and the operation will be adapted to new results, obtained both at the LHC and ILC as well as other particle physics experiments.

For the time being, three operation scenarios for a 20 years programme of the ILC are given in [114], assuming the baseline machine with centre-of-mass energies up to 500 GeV and stages at centre-of-mass energies of 250, 350 and 500 GeV. Figure 3.2a visualises the sequence of operation energies for the scenario H20 with integrated luminosities of $2000\,\mathrm{fb}^{-1}$ for $\sqrt{s} = 250\,\mathrm{GeV}$, $200\,\mathrm{fb}^{-1}$ for 350 GeV and $4000\,\mathrm{fb}^{-1}$ for 500 GeV. The ILC is supposed to start operation at 500 GeV and would collect $500\,\mathrm{fb}^{-1}$ in the initial four years. In order to obtain a realistic estimate of the time needed to accumulate the targeted integrated luminosities the time for machine upgrades and for ramp-up, i.e. a smaller initial instantaneous luminosity, are taken into account, as can be seen in the figure. With a luminosity upgrade after eight years, which requires a shut-down for a one and a half years, the time needed to collect the integrated luminosities is 20 years.

With a polarisation of both beams, the particles can be brought to collision with four different polarisation configurations: $\mathrm{sgn}(P(e^-),P(e^+))$=(−,−), (−,+), (+,−) and (+,−), where "−" denotes left-handed and "+" denotes right-handed chirality. For 500 GeV the proposed sharing between the different beam polarisations is 40% for $\mathrm{sgn}(P(e^-),P(e^+))$=(−,+) and (+,−) each and 10% for each of the equal-sign combinations with $|P_{e^-}| = 80\%$ and $|P_{e^-}| = 30\%$. In table 3.1 the integrated luminosity per beam helicity configuration for the H20 scenario is shown. The main

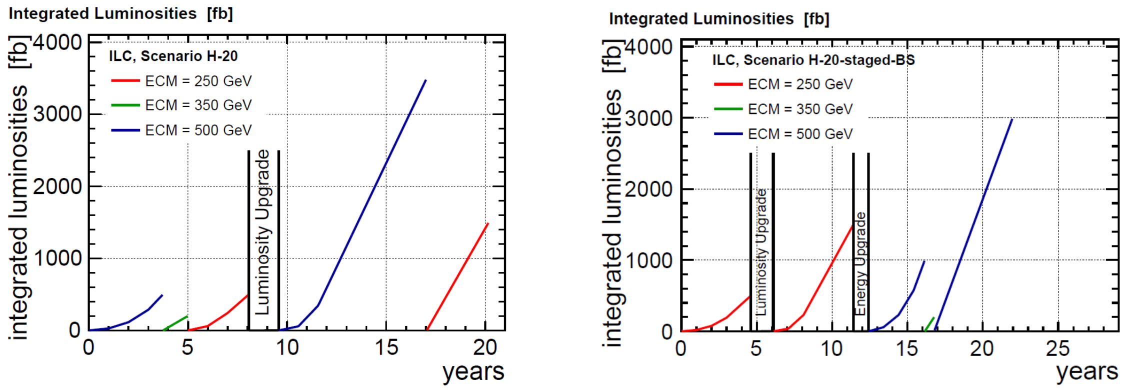

(a)

(b)

Figure 3.2: The integrated luminosity as a function of time for a machine with an initial maximum centre-of-mass energy of (a) 500 GeV [114] and (b) 250 GeV [111].

results of the WIMP analysis will be given for the H20 scenario (see chapters 7 and 8). At 350 GeV also a different scenario (I20) with a larger data set corresponding to 1700 fb^{-1} will be considered.

In a staged scenario with an initial centre-of-mass of 250 GeV a possible running scenario can be seen in figure 3.2b [111]. If the beams are focused more strongly, the instantaneous luminosity can be increased, which means that the proposed programme only has to be slightly longer, in order to reproduce the final integrated luminosities of the H20 scenarios.

	$(-,+)$	$(+,-)$	$(-,-)$	$(+,+)$	total
$\sqrt{s}$	$[\mathrm{fb}^{-1}]$	$[\mathrm{fb}^{-1}]$	$[\mathrm{fb}^{-1}]$	$[\mathrm{fb}^{-1}]$	$[\mathrm{fb}^{-1}]$
250 GeV	1350	450	100	100	2000
350 GeV	135	45	10	10	200
500 GeV	1600	1600	400	400	4000

Table 3.1: Integrated luminosity per centre-of-mass energy and beam helicity in the running scenario H20.

3.5 Luminosity spectrum and beam-induced backgrounds

Despite the cleanliness of the ILC compared to hadron colliders, also events at high energy lepton colliders suffer from background processes and uncertainties on the collision energy.

In order to provide a high instantaneous luminosity at unprecedented centre-of-mass energies, the particle bunches have to be highly collimated. As a consequence strong beam-beam effects induce background processes and lead to a tail in the distribution of centre-of-mass energies. First the parameters of the colliding bunches are introduced (section 3.5.1), followed by a description of the luminosity spectrum (section 3.5.2) and background processes (section 3.5.3).

3.5.1 Parameters of the beam delivery system

The instantaneous luminosity is given by [115]

$$\mathcal{L}_{inst} = \frac{n_b N^2 f_{rep}}{4\pi \sigma_x \sigma_y} \tag{3.2}$$

where n_b is the number of colliding particle bunches with N particles per bunch, the repetition rate f_{rep}, and the horizontal (x) and vertical (y) beam sizes σ, where Gaussian beam profiles are assumed. The beam size is related to the emittance ϵ and the beta function at the interaction point β^*: $\sigma = \sqrt{\epsilon\beta^*}$.

The beam parameters for a centre-of-mass energy of 500 GeV are summarised in table 3.2. The emittance is given as a product with the Lorentz factor γ. The waist is the distance of the last quadrupole focal points to the interaction point. Intuitively one would propose that the focal points should coincide with the interaction point, but the luminosity is optimized when the waist in vertical direction is slightly in front of the interaction point as to maximize the pinch effect from beam-beam interactions, explained below.

horizontal beam size at IP	σ_x	474	nm
vertical beam size at IP	σ_y	5.9	nm
horizontal emittance	$\gamma\epsilon_x$	10	10^{-6} m rad
vertical emittance	$\gamma\epsilon_y$	0.035	10^{-6} m rad
horizontal beta function at IP	β_x^*	11	mm
vertical beta function at IP	β_y^*	0.48	mm
number of particles in bunch	N	2	10^{10}
waist shift in vertical direction	waist$_y$	250	μm

Table 3.2: Parameters of the beam delivery system for the baseline design and a centre-of-mass energy of 500 GeV.

3.5.2 Luminosity spectrum

These beam parameters lead to a certain distribution of centre-of-mass energies, the luminosity spectrum. The two characteristic regions of the spectrum are the peak around the nominal centre-of-mass energy and the tail towards lower energies.

Underlying to the luminosity spectrum are the beam energy spectra, the energy distributions of the individual electron and positron beams. The beam spectra for baseline parameters and a centre-of-mass energy of 500 GeV are shown in figure 3.3. The spread around the nominal centre-of-mass energy is a consequence of the different arrival time of the particles along the length of the bunch in the alternating accelerating field. The energy spread of the electrons is broadened when they propagate through the undulator of the positron source [116]. The wider distribution is clearly visible in the zoom of the peak region in figure 3.3b.

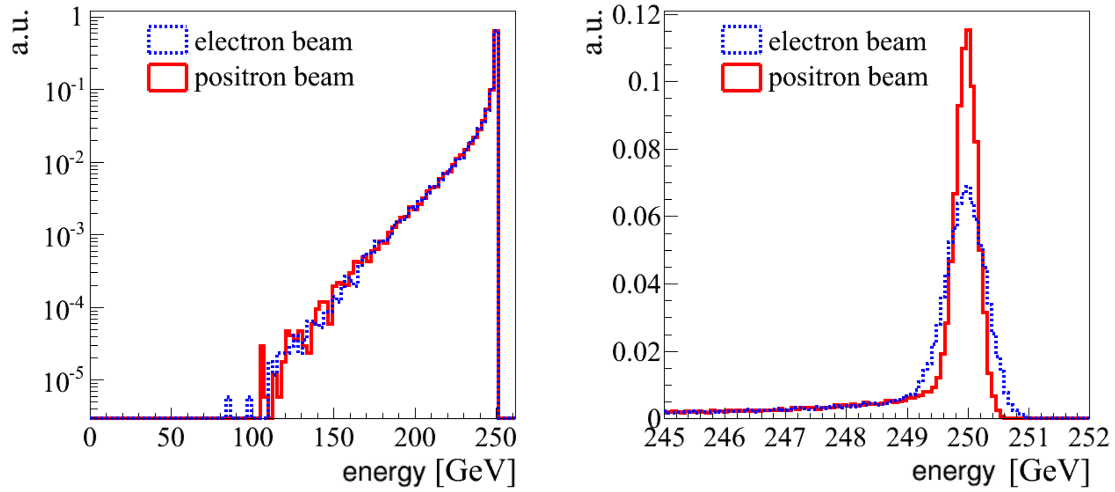

(a) (b)

Figure 3.3: Beam energy spectra of the electron (blue, dotted) and positron (red, solid) beams at the interaction point for baseline parameters and a centre-of-mass energy of 500 GeV, generated with GUINEAPIG (see section 4.2).

The tail to lower energies is a consequence of the nanometer-sized beams. The small beam sizes and the high particle energies lead to strong electromagnetic fields. The field of one bunch acts on the approaching bunch of opposite charge. The bunches attract each other and the individual particles are accelerated towards the centre of the oncoming bunch, which is called *pinch effect*. The result is that the bunches are focused further and hence the instantaneous luminosity

$$\mathcal{L}_{inst} = \frac{n_b N^2 f_{rep}}{4\pi\sigma_x\sigma_y} H_D \tag{3.3}$$

is increased, which is described by the enhancement factor H_D [117].

But on the other hand the individual particles propagate on bent trajectories and hence emit photons, known as beamstrahlung, visualised in figure 3.4. The electrons and positrons, which lost energy due to the photon emission, populate the tail of the beam energy spectra and the beamstrahlung radiation produces background processes discussed below.

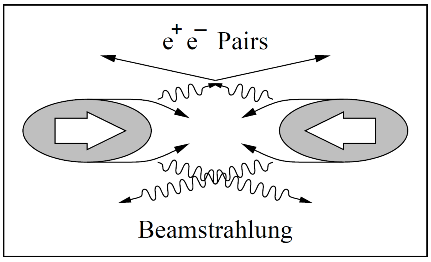

Figure 3.4: Visualisation of the pinch effect. The emitted beamstrahlung photons cause the tail in the luminosity spectrum and lead to backgrounds like the e^+e^- pairs. Taken from [117].

The further away the particles are from the beam axis, the stronger the pinch effect. As a consequence of this spatial dependence of the energy distribution, the energy distributions of the two beams are correlated, which has to be considered when the luminosity spectrum is modelled (see section 4.3).

The shape of the beams is driven by an optimal balance of high instantaneous luminosity and low average energy loss per particle δE. With flat beams the energy loss, which is inversely proportional to the *sum* of the vertical and horizontal beam sizes ($\delta E \propto \frac{1}{(\sigma_x+\sigma_y)^2}$), is lowest for a given high instantaneous luminosity, which in turn is inversely proportional to the *product* of the beam sizes (recall equation 3.3).

3.5.3 Beam-induced background processes

The various background processes induced by the beamstrahlung photons are described in the following. The beamstrahlung photons are strongly focused in the forward region with polar angles of less than 1 mrad and fly along the outgoing beam axis. Consequently, they are no detector background themselves.

3.5.3.1 Electron-positron pairs

Electron-positron pairs can be created coherently from a beamstrahlung photon in the strong electromagnetic field [118]. Also in the scattering process of two photons, electron-positron pairs can be created. This incoherent production is dominant at ILC energies. Three cases can be distinguished: The Breit-Wheeler process [119] is the scattering of two real beamstrahlung photons, the Bethe-Heitler process [120] describes the interaction of one real photon and one virtual photon and the interaction of two virtual photons is called Landau-Lifshitz process. As beamstrahlung does not play a role at lower centre-of-mass energies, the Breit-Wheeler and Bethe-Heitler processes are an additional challenge high-energy lepton colliders will have to face.

The pair particles are created under a small angle, but in contrast to the photons, they are deflected in the electromagnetic field of the bunch. The particle with the charge of the originating bunch is deflected towards the bunch centre and the oppositely charged component gets a relatively large transverse momentum which can be high enough to hit the detector. A dedicated design of the detector magnet system can guide the particles towards the outgoing beam pipe (see section 3.6.4) but a pollution of the very forward instruments cannot be circumvented.

As a consequence, pair particles lead to a background, mainly in the forward region of the detector, where they deteriorate the identification of products of the main e^+e^- interactions (see section 3.6.5), and to a smaller extend particles backscattering from the forward calorimeters can reach the central part of the detector [121]. On the other hand, the geometrical pattern of the pair particles depends on the parameters of the beam delivery system, which hence can be fitted to the observed background (see section 7.5.4).

3.5.3.2 Hadrons from photon-photon interactions

Hadrons are also produced incoherently in the scattering processes of two photons with an average number of 1.05 per bunch crossing at a centre-of-mass energy of 500 GeV [122]. Hadron pairs are produced with a significantly lower rate than electron-positron pairs. The resulting jets, though, can *not* easily be distinguished from the product of the main e^+e^- interaction. Within the ILC working groups this background is often referred to as a *low-p_T hadron overlay*. *Low-p_T* because the transverse momenta are at the low end of typical e^+e^- to hadron interactions, but are still in the same range, *overlay* because the photon reactions happen independently of, but simultaneously to, the e^+e^- interaction. This means that also WIMP events may contain hadrons and a certain detector activity has to be allowed in order to keep the signal events (see chapter 6).

3.5.3.3 Synchrotron radiation and muons

Additional beam-induced background comprises synchrotron radiation [123] and muons [124]. The non-Gaussian tails of the beams passing slightly off-axis through the focusing quadrupoles generate synchrotron radiation photons. In the interaction of the beam halo and collimators upstream of the detector muons are created.

3.6 International Large Detector

The International Large Detector (ILD) concept, which is described in detail in the ILC Technical Design Report volume 4 [99], is based on the particle flow approach, explained in section 3.6.1. An overview of the detector components is given in section 3.6.2, followed by the definition of the detector coordinate systems in section 3.6.3 and a short summary of the magnetic system in section 3.6.4. A more detailed description is given for the very forward calorimeter BeamCal (section 3.6.5) and the electromagnetic calorimeter (section 3.6.6), which play a central role in the mono-photon study.

3.6.1 The particle flow concept

The ILD detector concept is optimised for the particle flow approach where individual particles and their four-momenta are reconstructed. In this way the energy measurement of the single particles can be taken from the sub-detector with the best possible energy resolution, rather than measuring the jet energy using purely calorimeter information. Thus, the momenta of charged particles can be measured in the tracking detectors, which have a better momentum resolution than the calorimeters (see table 3.3). Only the energies of photons and neutral hadrons are obtained from the measurements in the calorimeters.

One of the implications for the detector design is the need for a high granularity of the calorimeters to allow the reconstruction of individual particles and match clusters with tracks.

component	detector	energy resolution
charged particles ($X^{\pm}$)	tracker	$10^{-4} \cdot E_{X^{\pm}}^{2}$
photons (γ)	ECAL	$0.15 \cdot \sqrt{E_{\gamma}}$
neutral hadrons (h^{0})	HCAL	$0.55 \cdot \sqrt{E_{h^{0}}}$

Table 3.3: Typical energy resolution for different sub-detectors. Adapted from [125].

3.6.2 Overview of the detector components

The colours in the following overview of the main detector components refer to figure 3.5. The most central component is the vertex detector, followed by a hybrid tracking system, with a time-projection chamber (TPC, yellow) as the main tracker and several layers of silicon tracking inside and outside of it. The calorimeter system has two parts, an electromagnetic (ECAL, blue) and hadronic (HCAL, green) system. Outside of the coil (light purple), there is an iron return yoke as muon system and tail-catcher calorimeter (brown). The main calorimeter systems constist of an approximately cylindrical *barrel* and two *endcaps*.

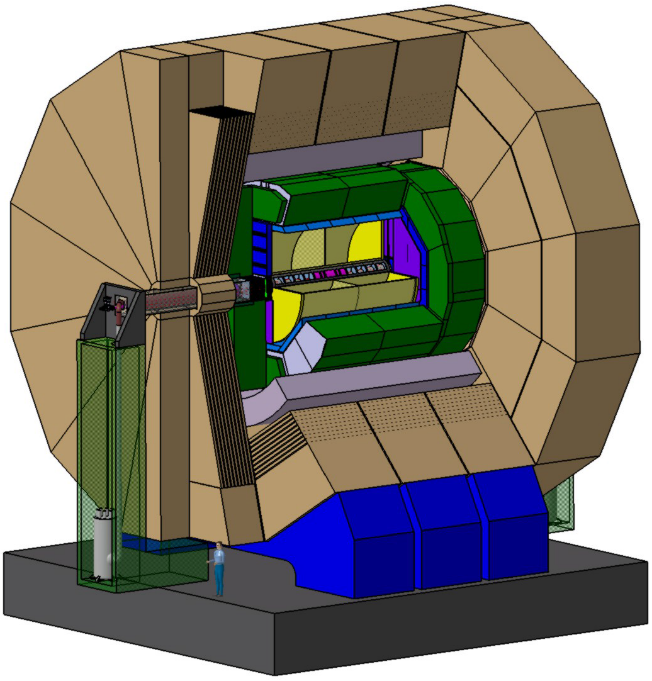

Figure 3.5: Schematic view of the ILD detector concept.

With three further calorimeters on either side in the forward region, LumiCal, LHCal and BeamCal, shown in figure 3.6, the calorimeter system almost covers 4π of solid angle. LumiCal serves as luminosity monitor, with LHCal the hadronic coverage is extended to low angles and BeamCal is clostest to the beam pipes.

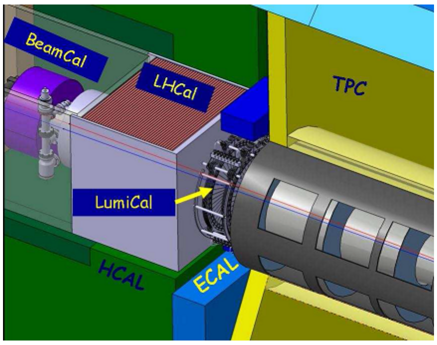

Figure 3.6: Forward region of ILD with the calorimeters BeamCal, LHCal and LumiCal. The interaction region lies outside of the image to the right.

The crucial detector components for the WIMP search are described in more detail: The mono-photon analysis mainly depends on the electromagnetic calorimeter (section 3.6.6), where the photons deposit the largest fraction of their energy. The most forward detector BeamCal, on the other hand, plays an important role for the suppression of the Bhabha background (section 3.6.5).

Other detector components play a more indirect role for the WIMP search. The tracking system is needed to discriminate photons from other electromagnetic particles. The high tracking efficiency of the TPC allows to identify a neutral cluster in ECAL as a photon. In the very forward region no tracking information is available and photons cannot be distinguished from electrons, which is also reflected in a minimum polar angle in the signal definition (see section 5.3). The hadronic calorimeter und muon systems are needed to veto against hadronic events and muon events, respectively. The high granularity of the calorimeters allows a good cluster reconstruction. Because of the clear identification hadronic background is not considered in the WIMP search.

3.6.3 Coordinate systems of the detector

The main detector coordinate system [126] has its origin at the nominal interaction point. The z-axis lies between the axes of the beams and it points close to the flight direction of the electron beam. It is a right-handed coordinate system and the y-axis points upwards. The crossing angle is in the horizontal plane and the incoming (outgoing) beams are in negative (positive) x-direction, as shown in figure 3.7.

As visualised by the sketch of the BeamCal position in figure 3.7, the forward instruments BeamCal, LumiCal and LHCal are centred around the outgoing beams. This means that their geometry can be best described in coordinate systems which are tilted by 7 mrad with respect to the ILD coordinates. In the following, this coordinate system is called *BeamCal coordinate system*. A conversion between the

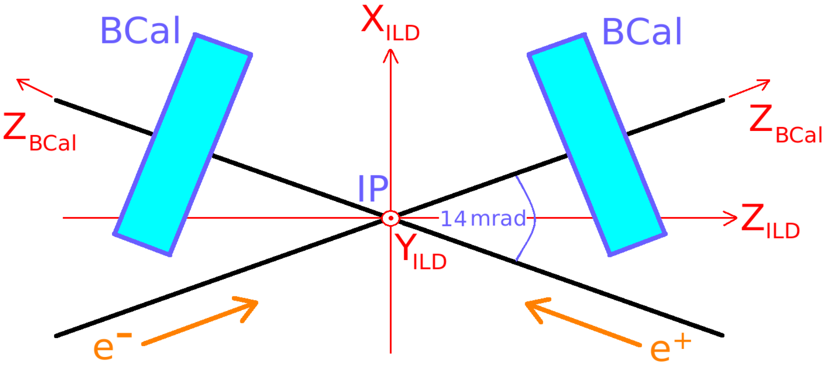

Figure 3.7: Topview of the ILD and BeamCal coordinate systems. The z axis of the forward instruments is tilted by 7 mrad with respect to ILD coordinates.

general ILD and the BeamCal coordinate systems corresponds to a Lorentz boost, as it is described in section 4.5.

3.6.4 The magnetic system

The magnetic system consists of a superconducting coil which provides a field of 3.5 T. In order to allow for an association between tracks and clusters, a prerequisite for particle flow reconstruction, the ECAL and HCAL are *inside* the magnetic coil.

In this study an additional *anti-DID* magnetic field is assumed, which is not part of the baseline design. Before turning to this setup, the *DID* field is explained.

Due to the crossing angle the main solenoid field causes a small vertical angle of the colliding electrons and positrons at the interaction point, resulting in a small (1°) spin rotation and hence a misalignment of the spin. This misalignment can be compensated by the detector-integrated dipole (DID) [127], a pair of coils wound on the detector solenoid, creating a sine-like transverse field.

A drawback of this additional coils is an increase of the field seen by the outgoing beams as well as the electron-positron pairs created by beamstrahlung photons (see section 3.5.3.1). The low energy pair particles are dispersed, resulting in an enhancement of this background.

In an alternative approach, following [128], the polarity of the additional coils is reversed, giving rise to the name *anti-DID*. This results in an effective alignment with *outgoing* beams, instead of an effective alignment of the field with the incoming beams. In this way the trajectories of the low energy pair particles are optimised and their majority is directed into the holes of the outgoing beams.

3.6.5 BeamCal in the forward region

BeamCal is instrumented directly outside the beam pipes and hence is the most forward calorimeter system. Measured from the outgoing beampipe (i.e. in BeamCal coordinates) it covers a polar angle range of 5.6−42.9 mrad. The purpose of BeamCal is threefold: reconstruction of (high energy) electrons with best possible hermeticity down to the lowest angles to suppress SM backgrounds, shielding of accelerator components from the beam-induced background and using this latter background to supply beam diagnostics information.

BeamCal [121] is an electromagnetic tungsten-sandwich sampling calorimeter with 40 layers building up a cylindrical volume. Each layer is made of a 3.5 mm thick tungsten absorber and a 0.3 mm sensor[iv]. The pad size is approximately $8 \times 8\,\mathrm{mm}^2$.

In figure 3.8 one layer of the calorimeter is shown. At the centre, a round hole is cut out for the outgoing beam. To the left (in negative x direction) the hole extends to a key hole shaped second opening spanning 40 degrees in ϕ to leave space for the incoming beam. The sensitive area starts at polar angles given in the BeamCal coordinate system of $\theta > 5.6\,\mathrm{mrad}$ for $|\phi| < 160°$ and $\theta > 18.9\,\mathrm{mrad}$ above.

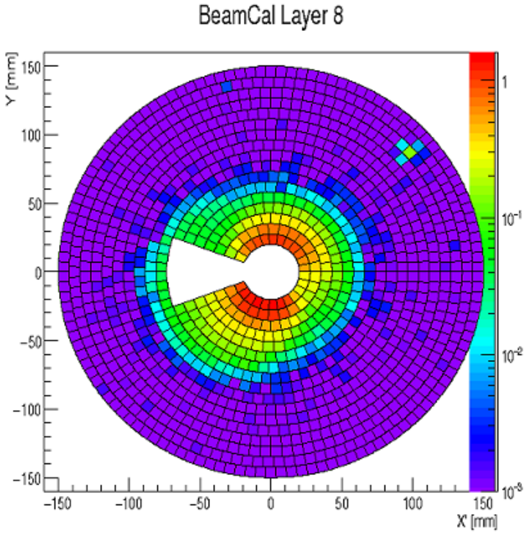

Figure 3.8: BeamCal layer with energy depositions from pair background and a high energetic electron.

In figure 3.8 it can be seen that the energy depositions of electron-positron pairs in BeamCal increase considerably towards the central round hole for the outgoing beam, as expected for the anti-DID magnetic field (see section 3.6.4). The pads in the upper right corner with activity clearly above the level of the neighbouring

---

[iv] The studies to select the sensor material are ongoing. Diamond is implemented in the simulation. [129]

pads contain the energy deposition of a high energetic electron, which, with its comparably high polar angle, can be easily reconstructed. Particles closer to outgoing beam pipe are more difficult to reconstruct. The reconstruction of BeamCal hits is described in detail in section 4.6.2.

While the beam-induced processes are a significant background in the particle reconstruction, the measurement of their energy deposition in the forward detectors contribute to monitoring and controlling the beams. With the help of a fast feedback [130] the beam parameters can be improved such that the instantaneous luminosity is enhanced. The measurements of the beam-induced background in the forward detectors serve as input to the beam parameter determination [130], which is used to evaluate the effect of the shape of the luminosity spectrum on the systematic uncertainties of the WIMP exclusiton limits, described in section 7.5.

3.6.5.1 Redesign of the forward region

The detector geometry used for the simulation was re-visited during the progress of this thesis. Because the ILC detectors share the same interaction region, it is beneficial for the design of the beam delivery system if both have the same focal distance of the final quadrupole magnet (L*). The new value for L* is 4.1 m [108,131] which is 30 cm less than the previous length at ILD (4.4 m).

As a consequence the forward region had to be redesigned. The modification that has the largest impact on this study is the new position of BeamCal. It was moved closer to the interaction point by 40 cm, which leads to larger background rates [132] and the identification of Bhabha leptons might degrade.

In the detector simulation performed for this analysis the z position of BeamCal is still 359.5 cm, i.e. the one from before the redesign (as shown in figure 3.9). The influence of the new design on the WIMP study is discussed in section 7.3.1.2.

3.6.6 The electromagnetic calorimeter system

The main components of the electromagnetic calorimeter system are the ECAL barrel and the two endcaps. The barrel has a length of 2.35 m on both sides of the interaction point and an inner radius of 1.84 m. Tungsten as an absorber allows a compact design and with 30 readout layers the outer radius is 2.03 m. Thus, the transition region from barrel to endcap is at $\cos\theta = 0.8$.

Besides the main components there are the ECAL rings (or plugs) on both sides in the forward region, bridging the interspace between LumiCal and the ECAL end-

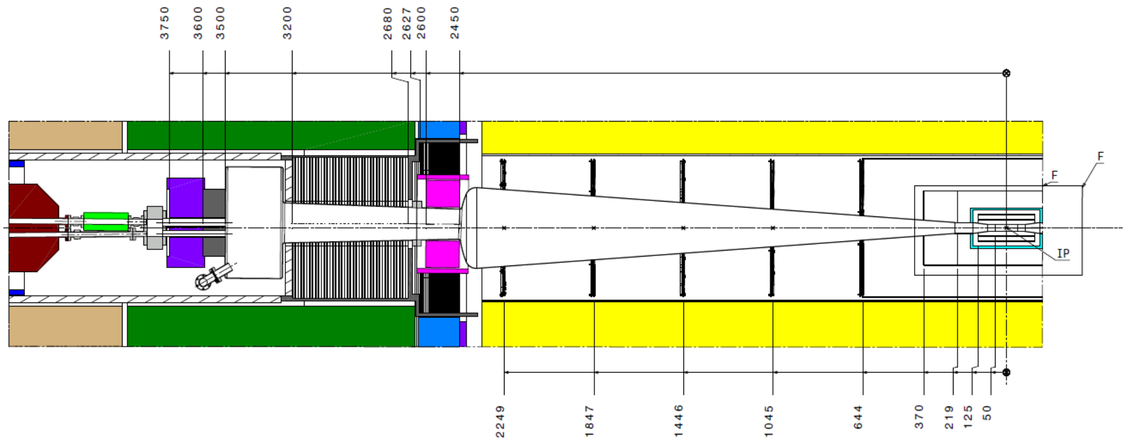

Figure 3.9: The central and forward region of the ILD detector concept, from the final quadrupole, partially shown on the left, to the interaction point on the far right. Dimensions are in mm and correspond to the detector simulation used for the WIMP analysis. The two separate beam pipes for incoming and outgoing beams are visible to the left and it can be clearly seen that the purple BeamCal is centred around the upper (outgoing) beam pipe.

caps enabling 4π coverage. The shape of the rings is sketched in figure 3.10. In section 5.5.3 the influence of the ϕ-dependent transition region between the endcap and the ring (resulting from the square shape of the ring) on the photon reconstruction will be discussed.

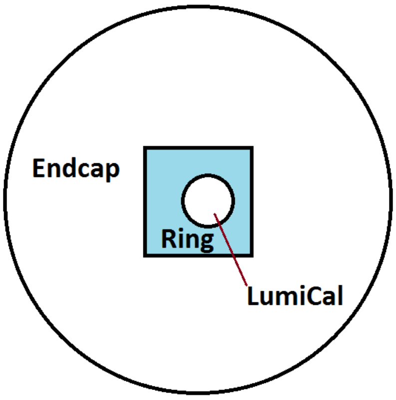

Figure 3.10: Sketch of one ECAL endcap with the ECAL ring, leaving space for LumiCal.

The high granularity with pixel sizes of $5 \times 5\,\mathrm{mm}^2$ allows for pattern recognition and separation of close-by showers, i.e. particles, which is a prerequisite for particle flow. One proposed design are silicon pin diodes. An alternative approach are $5\,\mathrm{x}\,45\,\mathrm{mm}^2$ scintillator strips, which are arranged in alternative directions to approximately achieve an effective granularity of $5 \times 5\,\mathrm{mm}^2$.

The downside of the high granularity is a limited energy resolution. Compared to the energy resolution of other developed electromagnetic calorimeters, like $\sigma_E/E \approx 2.8\%/\sqrt{E} \oplus 0.3\%$ at CMS [133] or $\sigma_E/E \approx 0.066\%/\sqrt{E} \oplus 1.34\%$ at Belle II [134], the energy resolution observed in test beam studies of prototypes for ILD are about an order of magnite higher. The resolution for the scintillator-based design is $12.5\%/\sqrt{E([\mathrm{GeV}])} \oplus 1.2\%$ [135] and for the Si-ECAL design, which is used in the simulation of the WIMP study, can be fitted to [136]

$$\sigma_E/E = 16.53\%/\sqrt{E([\mathrm{GeV}])} \oplus 1.07\% \tag{3.4}$$

Whether the energy resolution is good enough for the WIMP analysis will be evaluated in section 7.3.3. The high granularity on the other hand is beneficial for the photon ID (see section 4.6.1) and for a good angular position.

Chapter 4

The Simulation Tools

The effort to build the ILC can only be justified by detailed physics analyses based on Monte Carlo simulations with a realistic description of both the detector and the accelerator environment. In addition to an evaluation of the physics potential, the studies help to identify the key requirements for the machine design and they contribute to the optimisation of the detectors.

This chapter provides a description of the simulation tools needed for a Monte Carlo study of a physics channel at the ILC, with a focus on the required settings and algorithms for the WIMP search. The necessary tasks are performed using a number of different programmes. The chain of steps is introduced in the first section 4.1 and the individual programmes are described in the following sections.

4.1 The simulation chain

The required tasks to perform a Monte Carlo simulation can be divided into two parts. First the beam-beam interactions are simulated and in a second step the actual Monte Carlo events are produced.

The accelerator environment is modelled using GuineaPig [137] (section 4.2). One result of these beam-beam interaction simulation are the beam energy spectra which are required for a realistic description of the centre-of-mass energy distribution in the event generation. In the second preparational step the luminosity spectrum is parametrised with the programme Circe2 [138] (see section 4.3).

The production of Monte Carlo events comprises three steps: the event generation using Whizard [139] (see section 4.4), the simulation of the interaction of the generated particles with the detector material using Mokka [140] (see section 4.5) and the event reconstruction in the Marlin framework [141] (see section 4.6).

In the scope of this thesis a new setup in both the beam energy spectrum modelling (see section 4.3) and the event generation (see section 4.4) was developed.

All the software for detector simulation and event reconstruction is collected in the framework ILCSoft [142] and the file format for the simulation and reconstruction is LCIO [143]. In figure 4.1 the structure of the LCIO event data model with its four groups of classes is shown.

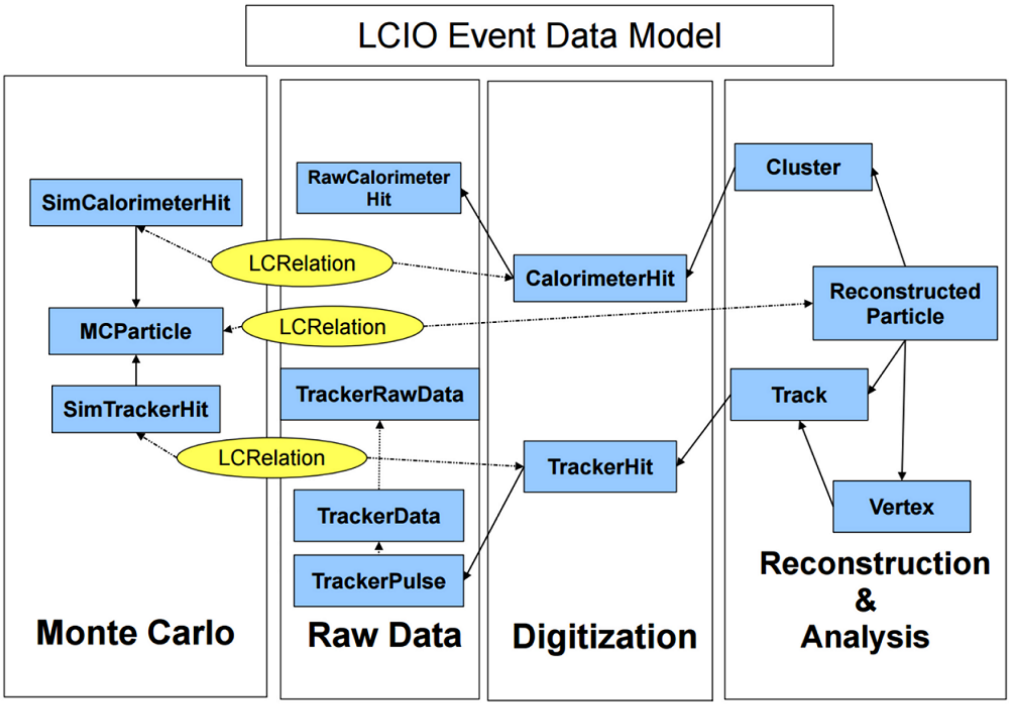

Figure 4.1: LCIO event data model. Taken from [144].

In the *Monte Carlo* group output from the event generation and the simulation are available. The *MCParticle* class corresponds to the information on generator level, i.e. the output of the event generator Whizard which is given in the StdHep [145] format and copied into the LCIO event files. The *SimCalorimeterHit* and *SimTrackerHit* result from the simulation with the detector material with Mokka.

In the *Raw Data* classes data from beam tests or future running experiments could be included. This means that for real data the same reconstruction framework can be used.

In the third step the simulated data is *digitised*, meaning that the hits are smeared and noise is included. In this way, the Monte Carlo data is close to real data. In the last step the hits are combined with the help of pattern recognition and reconstruction algorithms to eventually form *Reconstructed Particles.* The Marlin framework is used for these two last steps. In a Monte Carlo simulation all underlying information on the true generated particles and the simulated hits which they created is available and via *LCRelations* they are linked to the reconstructed objects.

Reconstruction algorithms which are of special importance for the WIMP analysis are presented in more detail: The photon reconstruction [125, 146] is introduced in section 4.6.1, and the reconstruction of the forward calorimeter BeamCal [129], which was adapted to the parameters of the ILC and ILD in the context of this thesis, is described in section 4.6.2.

4.2 Simulation of the beam-beam interaction using GuineaPig

For the modelling of the beam energy spectra GuineaPig [137] (*Generator of Unwanted Interactions for Numerical Experiment Analysis - Programme Interfaced to Geant*) is used. The beam-beam interactions in e^+e^- collisions are simulated, the luminosity is calculated and beam-induced backgrounds (see section 3.5.3) are generated. The relevant output files for the event generation contain pairs of colliding beam electrons and positrons. In appendix A the format of the output is shown. The energy distributions of the colliding particles, i.e. the beam energy spectra, are shown in figure 3.3 on page 54. The luminosity spectrum is obtained from $\sqrt{s} = 2\sqrt{E_{e^-}E_{e^+}}$ with the energies of the individual pairs of electrons and positrons. In figure 4.2 luminosity spectra are shown for a nominal centre-of-mass energy of 500 GeV as the red thin lines.

Each GuineaPig run corresponds to one interaction of an electron and a positron bunch. As explained in [137], the technical approach to simulate the collision effects is to replace the beam particles by *macro-particles* (80,000 in this study) and to cut the beams in longitudinal slices. The individual slices interact consecutively with all the slices of the other beam. From the charge distribution within the slices the forces on all macro-particles are calculated and their trajectories are bent accordingly. The beamstrahlung photons, which are emitted as a result, as well as pair-produced electrons and positrons are created and the trajectories of these particles are also modelled, taking the electromagnetic field of the beams into account.

In the WIMP analysis GuineaPig simulations are used twice: for the event generation and for the evaluation of the systematic uncertainty induced by the luminosity spectrum. The latter will be discussed in detail in section 7.5.

For the event generation the GuineaPig files from the central ILD production for the *Detailed Baseline Design* (DBD)[i] are used [147]. The corresponding GuineaPig steering file is shown in appendix B.

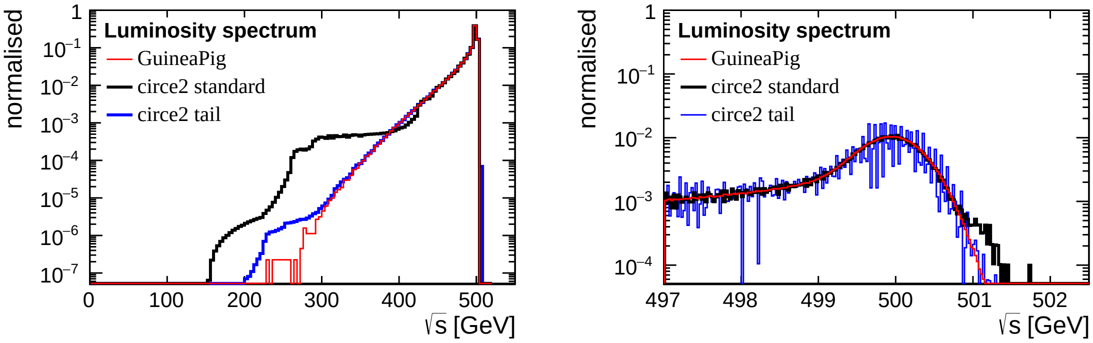

(a) (b)

Figure 4.2: Comparison of the luminosity spectrum simulated with GuineaPig for the DBD (red) and two CIRCE2 parametrisations. The black curve corresponds to the approach used in the data sets of this analysis. With this fit the region around the nominal centre-of-mass energy is well described. In the tails of the distribution the large bin widths of the parametrisation lead to steps. The second parametrisation (blue) gives a better description of the tails, but the peak region shows strong fluctuations.

4.3 Luminosity spectrum modelling using CIRCE2

As the next step the GuineaPig output has to be linked to the event generation with Whizard. Whereas the standard procedure with Whizard 1 was the *Lumi-linker* parametrisation [148], Whizard 2 offers three options to read in the luminosity spectrum. A list of pairs of energies of colliding electrons and positrons can be read in directly, or alternatively a one-dimensional (Circe1 [149]) or a two-dimensional parametrisation (Circe2 [138]) can be used.

An accurate description of the luminosity spectrum is important for the WIMP search because the exact knowledge of the initial state is crucial for a precise determination of the missing four momentum. Hence the different possibilities were studied in the context of this thesis.

---

[i] The DBD data sets were used to study the physics case presented in the Technical Design Report [96].

The intermediate step of a parametrisation has several advantages compared to directly reading in the GuineaPig output. First of all the number of colliding pairs in the existing data is finite. In a test run, where the pairs were directly read in, the GuineaPig output was looped over several times. This means the existing number of colliding pairs, which corresponds to one bunch train, is insufficient to generate statistically independent events. Producing the numbers needed for a large scale event production (with more iterations in the cross-section calculation and larger event numbers than in the test run) would be very CPU-intensive. With a parametrisation the cross-section calculation in Whizard is also significantly faster.

In Circe1 a simplified description is used, where the correlation between the energy distributions of the two beams (as explained in section 3.5.2) is ignored and hence a one-dimensional spectrum is returned. For centre-of-mass energies in the range of a few 100 GeV correlations of the two beams start to play a role and a two-dimensional parametrisation, like the one offered by Circe2, is required for a good description of the spectrum [138].

As a consequence, Circe2 is used as interface between the beam-beam interaction simulation and the event generation in the WIMP analysis. Circe2 is a stand-alone tool that is also a subpackage of Whizard. The parametrisation is performed in a separate step by running circe2_tool prior to the event generation. See appendix C for the steering files. The energies of pairs of colliding electrons and positrons are read in from the GuineaPig output and put in a two-dimensional grid with 100×100 pixels. The input comprises approximately 4 million e^+e^- collisions from 20 bunch crossing simulations.

With the steep distribution of the beam energy spectra the entries of the grid initially vary over many orders of magnitude and a significant fraction of the pixels is empty. Subsequently, the pixel sizes are adapted to the variance of their entries in several iterations. In figure 4.3 it is shown how the weights become more and more similar for increasing number of iterations. The varying pixel sizes are not shown.

In order to find the optimal description of the luminosity spectrum steering parameters were varied and the final values for two different parametrisations are shown in table 4.1. As can be seen in figure 4.3f a similar level of weights over the full range of the grid can be obtained with 10 iterations which is used for the parametrisation in the WIMP study. More iterations lead to an overestimation of the weights in the tails, visible as the rise towards the lower left corner.

In order to remove statistical fluctuations a Gaussian smearing is applied. Neighboring pixels are averaged with the weight $\frac{1}{\sqrt{2\pi\sigma^2}}\exp(-\frac{|x-x_0|^2}{2\sigma^2})$, where $|x - x_0|$ is

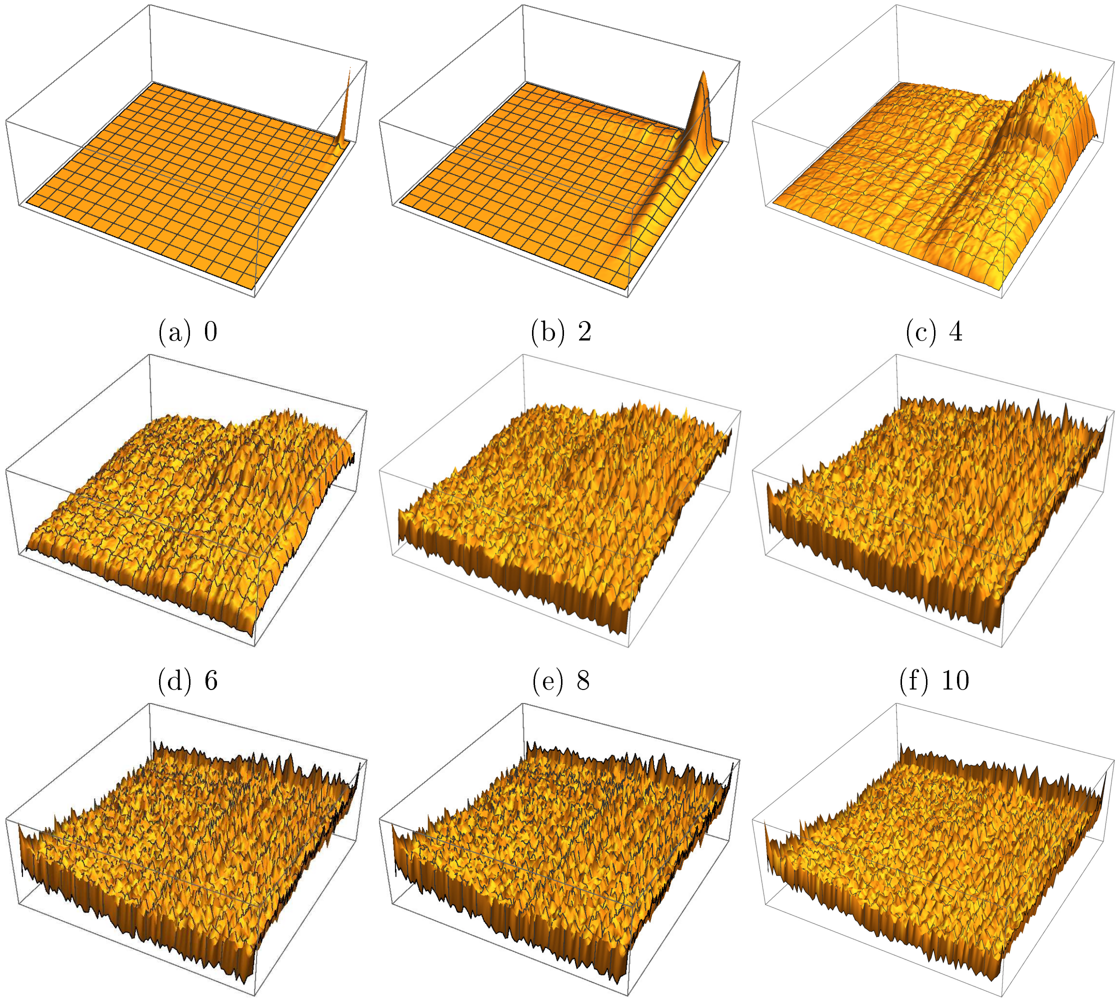
(a) 0 (b) 2 (c) 4 (d) 6 (e) 8 (f) 10 (g) 12 (h) 15 (i) 20

Figure 4.3: Visualisation of the grid adaptation to minimise the variance of the weights in several iterations (0,2,4,6,8,10,12,15,20). Before the adaptation very few bins around the nominal beam energies have high weights and most other bins are almost empty. After 10 iterations the level of weights is similar over the full grid. For higher values the weights in the tail regions start to become larger than the general level. Analogously to [150].

measured in pixels and σ is set by the parameter `smooth` in the CIRCE2 steering. In figure 4.4 several settings of `smooth` are shown for 10 iterations. With `smooth` $= 5$ the fluctuations are eliminated and this value is chosen for the parametrisation used in the event generation for the WIMP study.

The luminosity spectrum from this "standard" parametrisation is compared to the underlying distribution of GUINEAPIG pairs in figure 4.2 (black curve). The choice of a high number of iterations in this setup describes the peak region best and

parametrisation	`iterations`	`smooth`	visualisation	
standard	10	5	black curves in fig. 4.2	fig. 4.4c
tail	2	1	blue curves in fig. 4.2	fig. 4.5

Table 4.1: Settings for the parameters `iterations` and `smooth` in different CIRCE2 runs. The values for the parametrisation used in this analysis ("standard") are `iterations`=10 and `smooth`=5.

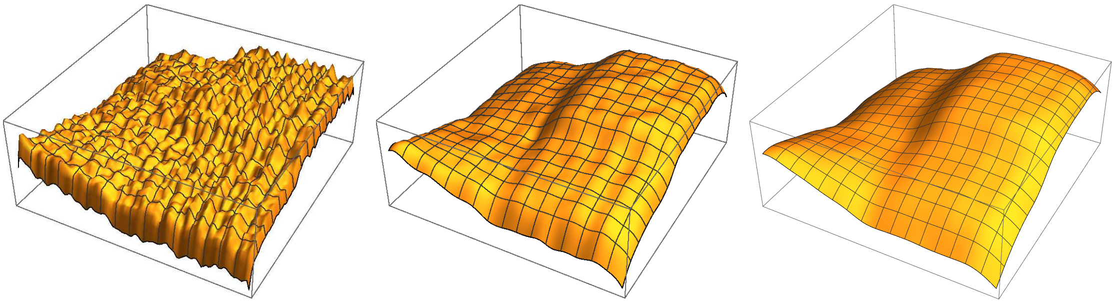
(a) (b) (c)

Figure 4.4: Distribution of the weights for 10 iterations and different choices of the parameter `smooth` (1,3,5) in the CIRCE2 parametrisation.

the bins become large where the statistics is low. As a consequence, the individual bins are visible as steps in the tail regions, where the data hence is not well described (see figure 4.2a). Using this parametrisation with a focus on the region around the nominal centre-of-mass energy is justified because it gives a good description of the largest fraction of the luminosity spectrum and the processes in this analysis are not very sensitive to the tails.

A second setup ("tail") with a focus on a good description of the tail rather than the peak was also created but not used for the generation of the events in this analysis. It should be used for physics channels which are highly sensitive to the tail of the luminosity spectrum, like the top mass measurement in a cross-section scan at the pair production threshold [151]. The steps in the distribution are avoided by using only 2 iterations, instead of 10. Since the bin entries are not at the same level, large values of `smooth` would artificially broaden the peak and hence the distribution can only be smoothed with a σ of 1. The distribution of weights is shown in figure 4.5 and the spectrum is drawn as the blue curve in figure 4.2. The steering files for both parametrisations can be found in appendix C.

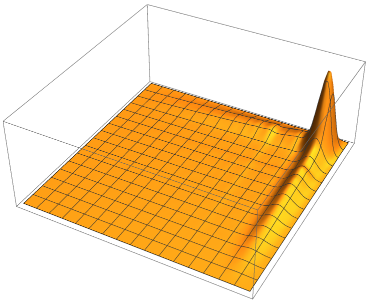

Figure 4.5: Distribution of the weights in the second available parametrisation which gives the best description of the tail.

4.4 Event generation using Whizard

After the preparational steps of generating the luminosity spectrum with GuineaPig and its parametrisation with Circe2 the events are generated using Whizard (*W, HIggs and Z And Respective Decays*) [139]. Whizard is a multi-purpose event generator that covers all necessary steps, like computation of the cross-sections and distributions of observables. The tree-level matrix elements are calculated using O'Mega (*Optimized Matrix Element Generator*) [152].

In section 2.2.2.5 the Lagrangians describing the interactions of the Standard Model of particles were presented. The interactions can also be expressed by the Feynman rules derived from the Lagrangian, from where the matrix elements can be calculated [153]. The simple reaction $e^+e^- \to \chi\chi$ would correspond to a tree-level diagram and the considered signal process with an ISR photon $e^+e^- \to \chi\chi\gamma$ is one order higher. The cross-section for this process is divergent for vanishing energy (soft singularity) and for vanishing polar angle (collinear singularity) [153], and hence a special treatment of ISR is required.

For the WIMP study dedicated data sets were produced in the scope of this thesis. The setup will be presented in sections 5.3 and 5.4. The environment of the ILC is treated realistically by taking into accout the beam energy spectrum (as discussed above in section 4.3), the beam polarisations, and initial state radiation (ISR). The modelling of the ISR photons is of great relevance for the mono-photon analysis and the chosen approach will be discussed in section 5.4.1.

Whizard allows to set cuts on the kinematics of *all* particles, including the ISR photons, which is crucial to reduce CPU time. The cuts of the preselection on generator level are presented in section 5.3.2. The events used in this analysis were generated using Whizard 2.4.4 and the steering files can be found in appendix D.

4.5 Detector simulation using Mokka

As the next step the passage of the generated particles through the detector is simulated. A full detector simulation of the ILD detector concept is performed using the Geant4-based [154–156] programme Mokka [140], which offers a detailed description of the ILD concept. Mokka version 08-00-03 was used, which is contained in ILCSoft version 01-16-02. The implemented detector model is `ILD_o1_v05` which is based on the Technical Design Report Volume 4 [99].

For the study of the BeamCal efficiency, single electrons are generated directly by Mokka using its functionality `particle gun` (see section 4.6.2.3).

In Whizard the events are generated in a head-on collision. The crossing angle of the two beams of 14 mrad (see section 3.6.3) is realised with Mokka during the detector simulation by applying a Lorentz boost. With the crossing being in the horizontal plane the momenta in the y and z directions are not affected, but the momentum in the horizontal direction becomes

$$\widetilde{\vec{p}_x} = \beta\sqrt{p_x^2 + p_y^2 + p_z^2 + m^2} + \gamma\vec{p}_x \tag{4.1}$$

with $\beta = \tan\alpha$, $\gamma = \sqrt{1 + \tan^2\alpha}$ and the half crossing angle $\alpha = 7\,\text{mrad}$. The particle energy increases or decreases according to the modification of p_x.

4.6 Event reconstruction using Marlin

Marlin (*Modular Analysis and Reconstruction for the LINear collider*) [141] is used to digitise the hits and energy depositions in the detector and reconstruct particle candidates. The software is organised in modules, called *processors*, which perform the different steps like digitisation, tracking and cluster formation.

The beam-induced background events are simulated separately of the main events. They originate from the same bunch crossing and hence occur simultaneously, but are created independently, because the colliding particles are different. This allows that the simulated detector hits from the main events and those of the beam-induced background are overlaid in the reconstruction. The low-p_T hadron events (see section 3.5.3.2) are randomly taken from a pool of simulated events. The e^+e^- pairs (see section 3.5.3.1) are taken into account in the BeamCal reconstruction (see section 4.6.2).

Marlin version 01-09 (ILCSoft version 01-17-11) was used for this analysis.

In the following sections, two aspects of the reconstruction are presented which are of particular importance for the WIMP search. A new approach to the photon reconstruction [146] compared to the previous analysis [1,2] is used (see section 4.6.1). And a new reconstruction of the forward detector BeamCal [129] was tested and implemented in the general ILD reconstruction (see section 4.6.2).

4.6.1 Photon reconstruction in the Pandora Particle Flow Algorithm

In the reconstruction, the particle flow algorithm is implemented in the Pandora Particle Flow Algorithm (PandoraPFA) software package [125]. PandoraPFA 02-09-01 was used in the WIMP analysis. The input are the calorimeter hits and reconstructed tracks. The particle candidates reconstructed using PandoraPFA are called `Particle Flow Objects` (`PFOs`). The reconstruction consists of several steps, like the cluster formation and association with the tracks. In the main clustering step of PandoraPFA the calorimeter hits are merged to form clusters with a cone-based approach.

In PandoraPFA the reconstructed particle candidates are categorised in several groups with particles codes following the scheme of the particle data group (`PDG`, [157]). Hadrons with an assigned track are reconstructed as charged pions (`PDG`=±211), without a track as neutrons (`PDG`=2112). This means that for example a proton, which is correctly reconstructed as a charged hadron is asigned the `PDG` of a pion. `PFOs` with electromagnetic clusters are categorised as electrons (`PDG`=±11), if they have an asigned track, or as photons (`PDG`=22) if they pass the criteria listed below. Muons are categorised separately (`PDG`=±13). Objects created by the vertex finder have the `PDGs` 310 or ±3122.

Before the main clustering step a dedicated photon reconstruction algorithm is applied [146]. This algorithm is a complete revision of the approach used for the mass production for the Technical Design Report in 2012. As shown in [146] the photon reconstruction is significantly improved. Also the photon splitting, observed in [1, 2], is eliminated to a large extend, as will be shown in section 5.5.1. The algorithm comprises several steps itself, visualised by the flow chart in figure 4.6 and explained in the following.

photon clustering: First clusters are formed from ECAL hits using a cone clustering algorithm. The clusters are either seeded with a projection of a recon-

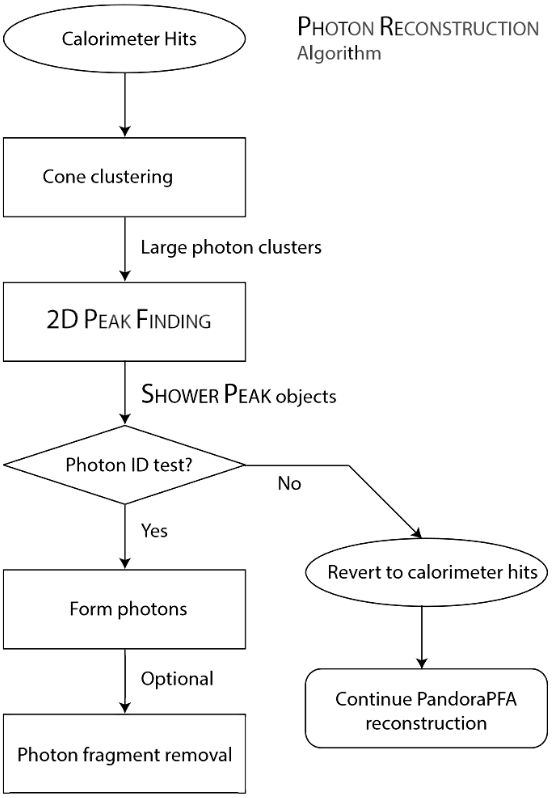

Figure 4.6: Flow chart illustrating the steps of the photon reconstruction within the PANDORAPFA. The optional photon fragment removal is switched on in this analysis. Based on [158].

structed track and thus reconstructed as a charged `PFO` or, in the absence of a track, with high energy calorimeter hits to form a neutral `PFO`. The parameters are such that large clusters are preferably formed, according to the general approach within PANDORAPFA to rather break clusters up than merge them in the following steps.

photon candidates: In this step the previously formed large clusters are split up to form photon candidate clusters. The energy depositions are projected on a two-dimensional plane perpendicular to the direction of the initial large cluster. The electromagnetic shower topology with its narrow cone translates into a sharp peak in the projection. Individual photons are found by a dedicated peak finding algorithm which allows good separation of close-by photons.

photon ID test: The formed shower peak objects are now tested to be compatible with an electromagnetic shower by applying a set of discriminating variables, like longitudinal and transverse shower profile and distance to tracks. If a shower peak fails the test, its hits are passed back to the main clustering step of PANDORAPFA.

fragment removal: The fragment removal comprises two steps, one for ECAL and one for HCAL fragments.

An ECAL fragment is a cluster which does not have a typical electromagnetic shower structure and is lower in energy than the “main” photon cluster. Fragments which are peripheral to the electromagnetic shower core are looped over. A photon-fragment pair is merged if they pass several cuts making them compatible with the profile of a single photon. If several fragments pass the test individually with the same photon, the one closest in space is merged.

In the second step energy depositions in HCAL are assessed. In the main photon clustering algorithm only ECAL hits are considered, but high energetic electromagnetic showers may not be fully contained in ECAL and leak into HCAL. If a neutral HCAL cluster is close to the photon cluster and more than 50% of the hits in HCAL are within a cone fitted to the ECAL cluster, the HCAL cluster is considered as fragment and merged with the photon cluster.

4.6.2 BeamCal reconstruction

The forward region, and in particular BeamCal (introduced in section 3.6.5), plays a central role in the discrimination of mono-photon events from Bhabha scattering, because the Bhabha leptons predominantly have small polar angles. At the same time the reconstruction of particles in the very forward detector BeamCal is challenging because of the high occupancy due to pair background induced by beamstrahlung (see section 3.5.3.1). With these high background levels a reconstruction of all hits in BeamCal is not desired, in contrast to the rest of the detector. Therefore the BeamCal reconstruction is not part of the PANDORAPFA and hence the reconstructed particles form their own class called `BeamCalRecoParticle`.

Different patterns of the energy deposition of overlay and energetic particles can be exploited to distinguish between the two. From the main electron-positron interaction individual outgoing particles are expected to hit BeamCal typically with rather high energies. The overlay on the other hand consists of many particles with low energies. As a consequence the longitudinal distribution of beam-induced background differs from energetic particles like electrons from Bhabha scattering, because the depth of the peak of the deposition depends on the energy: The beam-induced background deposits its energy mainly in the first layers of the calorimeter. Particles with a higher energy start depositing energy later and travel further within the detector storing a significant amount of energy in consecutive layers. How the algorithm makes use of these different patterns is shown in section 4.6.2.3.

4.6.2.1 Introducting more realism in the BeamCal reconstruction

In the previous WIMP study [1, 2] the Marlin processor BCalReco [121] was used. Instead of a reconstruction of the BeamCal, the efficiency to tag a particle hitting BeamCal was calculated, taking into account its energy on generator level and the expected overlay from beamstrahlung electron-positron pairs in the particular BeamCal region.

The new reconstruction algorithm BeamCalClusterReco [129] was initially developed for CLIC. It takes the hits of the main events and the overlay into account and performs a full reconstruction. As a consequence, also *fakes* can be created, i.e. reconstructed objects from overlay hits. This means that the new BeamCal reconstruction allows a more realistic description of the detector performance in the forward region.

The beam-induced electron-positron pairs are generated with GuineaPig (see section 4.2) and simulated separately from hard interaction events. The files used here are from the DBD production [147]. The approach in BeamCalClusterReco comprises several steps. First the events from the hard interaction are overlaid with the pair background, for which BeamCalClusterReco offers several methods (described in section 4.6.2.2). In the following steps several cuts are applied to reject calorimeter hits which are likely to stem from overlay. To begin with, the average expected energy deposition from beam-induced overlay is subtracted in each pad. The parameters for the subsequent identification of potential high-energetic objects were tuned in the scope of this thesis, to get a suitable description for the ILC environment and the ILD detector layout. See section 4.6.2.3 for the selection of the parameters and section 4.6.2.4 for the efficiency of the BeamCal reconstruction.

The BeamCalClusterReco algorithm offers two reconstruction methods. The *clustering* algorithm is prefered over the *shower fitting* algorithm because of its simple and robust functionality. The latter method might yield better precision of the spatial coordinates, but the main goal within this analysis is the tagging of high-energetic leptons potentially coming from Bhabha scattering, but not their exact reconstruction.

4.6.2.2 Methods to overlay the pair background

In BeamCalClusterReco there are four methods to overlay the background during the BeamCal reconstruction: “Pregenerated”, “Gaussian”, “Averaged” and the one used for the WIMP study: “Parametrised”.

With the option “Pregenerated” a background sample which is randomly selected from a pool of simulated background bunch crossings is overlaid directly. For the other three options the background energy depositions in each read-out cell (called *pads*) are created randomly according to parametrisations describing how the energy in the individual BeamCal pads deposited by the overlay is distributed over different bunch interactions, e.g. they calculate the average expected value.

In the “Gaussian” method a Gaussian distribution is used as fit function. When BeamCal is read out after *several* bunch crossings the distributions can be well described by a Gaussian, but when the pads are read out more frequently the distributions suffer from fluctuations. At the ILC it is foreseen that BeamCal is read out after each bunch crossing and hence this method is not applied.

With the “Averaged” option the input files to the previous reconstruction algorithm [121] can be read in, which hence allows backward compatibility. It is also based on a Gaussian distribution.

In the “Parametrised” option a Gaussian distribution is combined with a $1/x$ function to describe the energy distribution: $\frac{A}{x}\exp(\frac{x-B}{C})^2$ which gives the best description of the energy distribution in the case of single bunch crossings. While a Gaussian function describes the distribution well for pads in the centre (where the deposited energy simply fluctuates around a certain non-zero value) and in the outer region with rare and low depositions (and is hence reproduceable with a Gaussian distribution centred around 0), there is a transition region where in most cases little energy is deposited but also a substantial number of bunch crossings with large energy depositions exist.

Prior to the event reconstruction the parameters for the three options “Averaged”, “Gaussian” and “Parametrised” are obtained by taking the energy distribution in each pad from the pool of bunch crossing simulations and fit with the corresponding distribution. The fit parameters are stored in a root file which is accessed during reconstruction to create the energy depositions of the overlay.

4.6.2.3 Tuning of the parameters in the BeamCal reconstruction

As a preparation for the BeamCal reconstruction the MOKKA `particle gun` is used to simulate two data sets containing only one electron per event with a fixed energy of either 50 or 200 GeV. The simulated electrons cover the full angular range of BeamCal. The rather low energy of the 50 GeV electrons make a reconstruction in the inner part of BeamCal challenging and thus they are used to tune the parameters of the BeamCalClusterReco algorithm. The performance will also be evaluated for the 200 GeV electrons (see section 4.6.2.4).

The focus on the optimisation of the reconstruction is on two parameters which define minimum energy threshold to consider a pad in the reconstruction (`SigmaCut` and `ETPad`) and on the parameters `StartLookingInLayer` and `MinimumTowerSize`, which define settings for accepted patterns of pads. The four parameters were tuned by testing several hundred different combinations of values to study the optimal settings which lead to the highest cluster reconstruction efficiency and lowest fake rates. The meaning of the four parameters and the chosen values are presented below.

In figures 4.7 and 4.8 it is shown how the efficiency to reconstruct 50 GeV electrons varies for different values of the parameters. For each tuned parameter the efficiency and the fake rate are shown as a function of the polar angle in BeamCal coordinates (see section 3.6.3) for the chosen value (black crosses) together with examples of one smaller and one larger value. The other parameters are set to the final values, such that the black distributions are the same in all respective graphs. In figures 4.7b and d the green (and black) curves are outside of the plotted range.

SigmaCut and ETPad: After the subtraction of the average energy expected from overlay (see above in section 4.6.2.1), pads are only considered in the cluster formation if they fulfill two conditions: The remaining energy in the pad must be higher than two times the standard deviation of the energy distribution which is also obtained from the root file (reflected in the steering file by: `SigmaCut` $= 2$). This means that the initial energy in a pad has to be larger than the mean plus 2 standard deviations.

Additionally, a global threshold of 0.01 GeV for the energy in each pad is applied (`ETPad` $= 0.01$). Whereas the first condition differs from pad to pad the latter is global.

StartLookingInLayer: As explained at the beginning of section 4.6.2, the depths of the energy deposition of overlay and high-energetic particles differ. Hence a large fraction of the overlay can be suppressed when ignoring the first layer without loosing much of the information on the high-energetic lepton. In the algorithm this is enabled by the setting `StartLookingInLayer` $= 2$.

MinimumTowerSize: With the last tuned parameter `MinimumTowerSize` the minimum number of pads with same radius r and azimuthal angle ϕ (in BeamCal

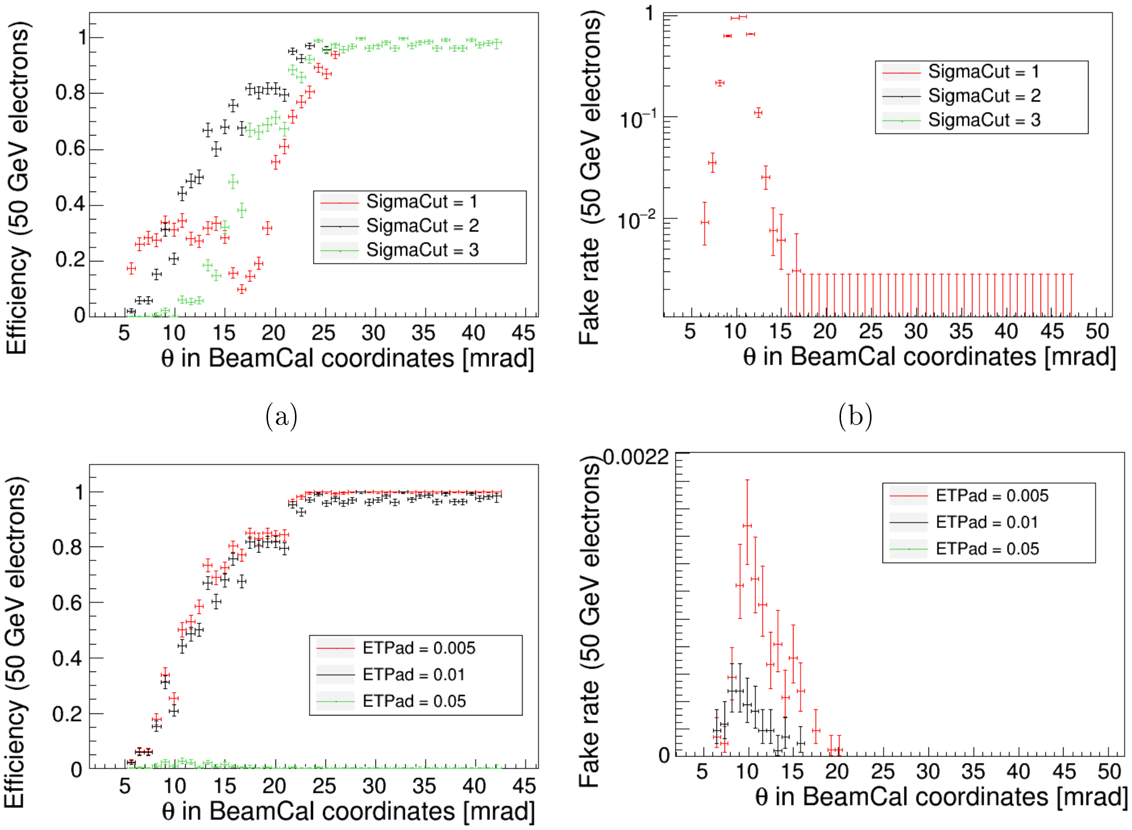

(a) (b)

(c) (d)

Figure 4.7: (a) and (c): Efficiency to reconstruct 50 GeV electrons in BeamCal as a function of polar angle (in the BeamCal coordinate system) for different values of the tuned parameters `SigmaCut` (a) and `ETPad` (c). In (b) and (d) the corresponding fake rates are shown. The black curves are for the settings used in this analysis.

coordinates) is set which are required to form a *tower* of pads. The best value was found to be six. This means that r/ϕ towers with less than six pads, which passed the previous thresholds, are ignored. After selecting the tower with the highest energy, neighboring towers are added to form a *cluster* until no more towers are directly next to the cluster. If there are towers not combined to the cluster, among the remaining towers again the one with the highest energy is chosen and combined with neighboring towers to a second cluster. This procedure is repeated until no towers remaining.

The best value for a fifth value (`ETCluster`) was tested, which defines a threshold energy to consider a formed cluster as a reconstructed particle. Several values were tested and `ETCluster` = 0.5 (corresponding to 36 GeV) was found to be the optimal minimum value for a cluster.

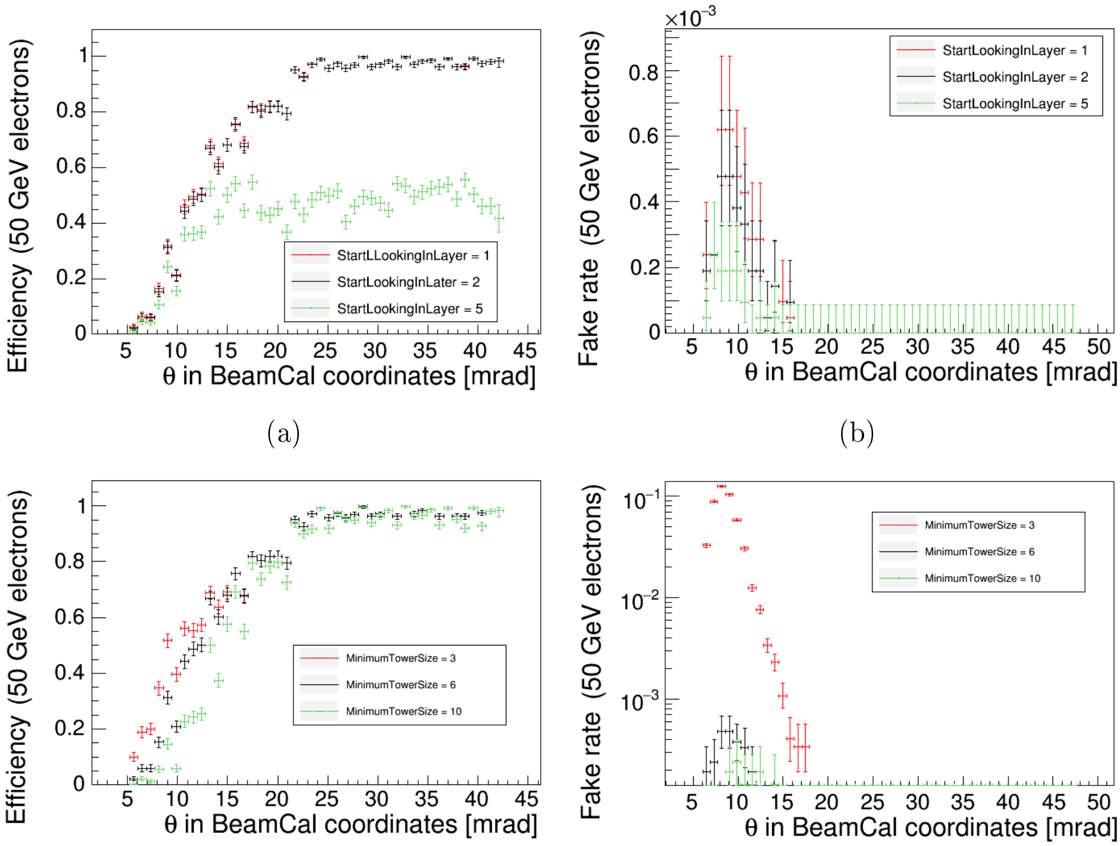

(a) (b)

(c) (d)

Figure 4.8: Efficiencies (a,c) and fake rates (b,d) for different values of the tuned parameters `StartLookingInLayer` (a,b) and `MinimumTowerSize` (c,d).

The input collection to the reconstruction is supposed to be the list of simulated BeamCal hits. Instead, the digitised hits were used in this study. As a consequence, energy-related parameters (`ETCluster` and `ETPad`) have to be adjusted, if the simulated hits are used. As will be shown in section 4.6.2.4 the performance of the algorithm is good nevertheless.

A summary of the tuned parameters together with the key settings of the steering for the BeamCalClusterReco algorithm are shown in table 4.2. For the energy calibration the digitised hits are assumed as input.

4.6.2.4 BeamCal reconstruction efficiency

The most realistic approach to overlay the beam-induced background (see section 4.6.2.2) would be to read in the background directly (by using the "Pregenerated" option), but in order to save CPU time a parametrisation is prefered. In

BackgroundMethod	background parametrisation	Parametrised
UseConstPadCuts	the cluster algorithm is used	false
LinearCalibrationFactor	energy calibration	72
ETCluster	minimum cluster energy	0.5
SigmaCut		2
ETPad		0.01
StartLookingInLayer		2
MinimumTowerSize		6

Table 4.2: Settings of the BeamCalClusterReco steering. The optimal set of values was found by testing alternative settings for the first four parameters and by scanning over the last four.

order to test the performance of the different methods, the reconstruction efficiencies for 50 GeV electrons are compared in figure 4.9. The parametrisation have a very similar performance to the "Pregenerated" option and can hence be used. The very similar behaviour for settings shows that the more realistic overlay description of the "Parametrised" method has no direct effect on the reconstruction efficiency.

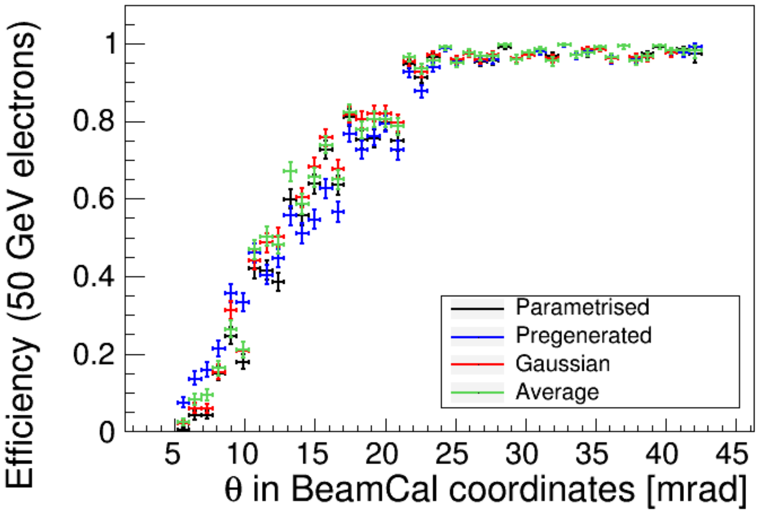

Figure 4.9: Efficiency to reconstruct 50 GeV electrons in BeamCal as a function of polar angle (in the BeamCal coordinate system) for the four different overlay methods.

In figure 4.10 the two generatead lepton energies of 50 GeV and 200 GeV are compared. With the rather strong conditions for cluster formation, electrons at 50 GeV have a lower reconstrution efficiency than at 200 GeV. Above 20 mrad the efficiency is close to 100% in both cases. The step-like drop around 20 mrad is due to the keyhole shaped clearance for the incoming beam pipe (see figure 3.8 on page 61). Its coverage of 40° is reflected in the efficiency (which is the integral over all ϕ angles) of approximately 90% for the 200 GeV electrons in that range. For the

50 GeV electrons the efficiency steadily decreases and below 12 mrad only less than half of the particles can be reconstructed in the increasing occupancy due to the pair overlay. The efficiency of the 200 GeV electrons only drops in the innermost part of BeamCal. This high reconstruction efficiency can also be expected for a large fraction of Bhabha leptons, which have typical energies around half the centre-of-mass energy of 500 GeV. But the efficiencies for 50 GeV shows that also Bhabha events with significantly lower energetic leptons can be identified.

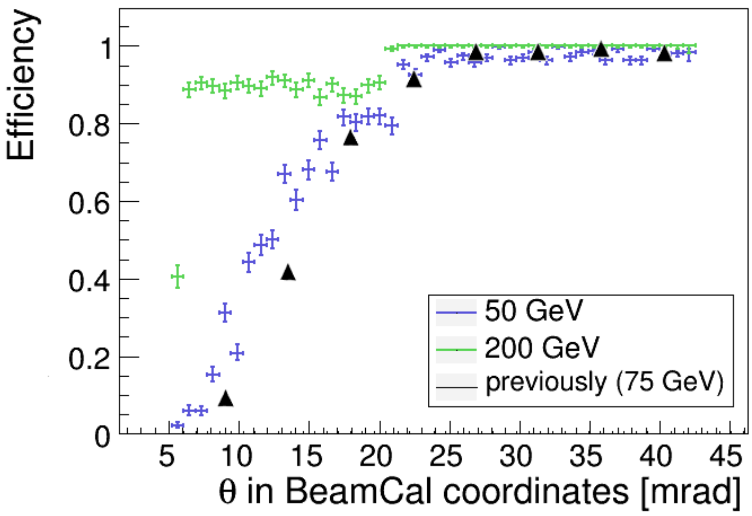

Figure 4.10: Efficiency to reconstruct electrons in BeamCal. The green (blue) line is obtained with the BeamCalClusterReco processor for 200 GeV (50 GeV) electrons. The previous reconstruction algorithm (black triangles) [121] shows a worse performance for 75 GeV electrons.

The black triangles in figure 4.10 show the reconstruction efficiency for 75 GeV electrons using the previous standard reconstruction [121]. The shape of the curve is very similar to the one the 50 GeV electrons but the overall efficiency is worse despite the higher energy. This proves that BeamCalClusterReco is not only more realistic but also more efficient than BCalReco.

Chapter 5

Strategy of the Mono-Photon Analysis

This chapter is dedicated to the characteristics of this WIMP search, from an introduction to the physics of the mono-photon channel to the Monte Carlo event production, based on the simulation tools which have been introduced in the previous chapter 4.

After a presentation of the background processes and the phase space of initial state radiation in section 5.1, the concept of this analysis is outlined in section 5.2. In section 5.3 the criteria for the signal definition are explained and with the discussion of the deduced phase space restrictions on generator level, the foundation for the presentation of the event samples is laid. The technical approach of event generation and the event samples are presented in section 5.4. Finally, the quality of the photon reconstruction in these data sets is evaluated in section 5.5.

5.1 The mono-photon channel: photons from initial state radiation

In this analysis the signal consists of a photon in an otherwise "empty" detector. The tested underlying process of this mono-photon final state is WIMP (χ) pair production with a photon from initial state radiation (ISR) recoiling against the invisible particles, depicted as pseudo Feynman diagram in figure 5.1. The lack of knowledge of the underlying process is reflected by the question mark in a circle.

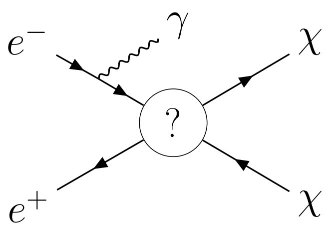

Figure 5.1: Pseudo Feynman diagram of WIMP pair production at an e$^+$e$^-$ collider with associated ISR emission.

5.1.1 Background processes

A number of Standard Model processes can lead to the same signature as WIMPs produced in association with a photon. Background processes to the mono-photon channel either contain only invisible particles in the final state (apart from the photon) or the photon is the only particle which is reconstructed.

Neutrino pair production with an ISR photon is the only Standard Model process in the first category. This irreducible background is indistinguishable from WIMP pair production on an event-by-event basis. On the other hand, the photon spectra differ (see section 5.1.2). Figure 5.2 shows the Feynman diagrams for the different production channels of neutrino pair production, discussed below.

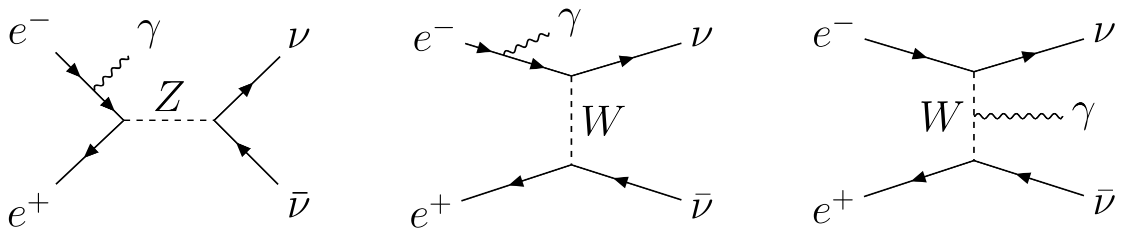

Figure 5.2: Tree-level Feynman diagrams for the radiative neutrino pair production. Via the first process with an s-channel exchange of a Z boson pairs of all neutrino generations can be produced. The t-channel exchange of a W boson is the dominant production channel, which is only possible for electron neutrinos and left-handed electrons and right-handed positrons.

Most Standard Model processes either contain jets or charged particles, which makes it comparably easy to distinguish them from a WIMP event. But in principle, any process with a photon in the final state can contribute to the second category of reducible background, provided that all other particles escape detection. Bhabha scattering with an associated photon from initial or final state radiation can mimic a mono-photon event, because the distribution of the momentum of the produced electron peaks in the direction of flight of the incoming electron (and analogously for the positron) and hence the outgoing leptons potentially escape detection through the beam pipe. Other processes that are likely to fulfill the signal criteria of a photon in an "empty" detector, like production of photons, showed to have a minor effect [1, 2] and are not included in this analysis. Hence, the two considered background processes are neutrino pair production and Bhabha scattering. Feynman diagrams for radiative Bhabha scattering are shown in figure 5.3.

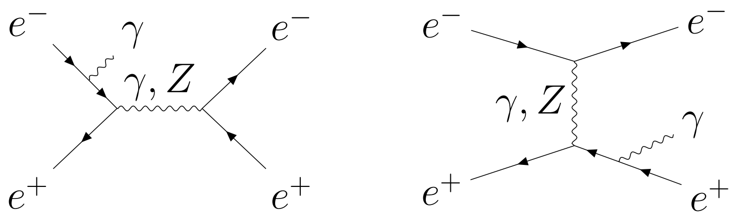

Figure 5.3: Main reducible background process: Bhabha scattering with s-channel and t-channel production and photons from initial and final state radiation.

The beam polarisation at the ILC is one of the major advantages for this study compared to other collider-bound WIMP searches, because it can help to lower the background. Pairs of all neutrino generations (ν_e, ν_μ, ν_τ) can be produced in the s-channel via a Z boson, as shown in the left-hand Feynman diagram in figure 5.2. The other two processes shown in the figure, involving a t-channel exchange of a W boson, are only allowed for electron neutrinos. These processes with a W boson exchanged in the t-channel give the largest contribution to the neutrino cross-section, but is highly polarisation dependent (for more details see section 5.4.2). Only left-handed electrons and right-handed positrons can take part in this scattering process. In this way, the beam polarisation can be used to enhance or suppress the background rate. How polarisation influences the exclusion limits will be discussed in section 7.2.2.

In the case of the Bhabha scattering process polarisation only has a minor effect, because at the ILC energies the photon exchange dominates. For the suppression of this background process the best possible hermeticity in the forward region of the detector is required (see section 7.3.1).

5.1.2 Photon phase space

Even though ISR photons are predominantly emitted at low angles and with low energies, a substantial fraction of photons can have a transverse momentum high enough to hit the detector and lead to the mono-photon signature. Clearly, several ISR photons can be emitted in an event, as depicted in figure 5.4, and furthermore it is possible that several photons have polar angles high enough to interact with the detector. These higher orders are taken into account in this analysis. The details on the photon treatment in the event generation can be found in section 5.4.1.

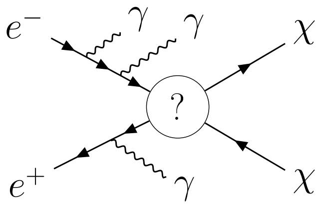

Figure 5.4: Pseudo Feynman diagram for WIMP pair production with several ISR photons.

In the case of ISR in association with WIMP pair production the photon energy spectrum depends on the WIMP mass. The higher the WIMP mass the lower the maximum possible photon energy (see figure 5.5). The spectrum of photons emitted in association with particles with negligible mass, like neutrinos, extends up to half the centre-of-mass energy. The endpoint for massive particles is given by

$$E_\gamma = \frac{\sqrt{s}}{2}\left(1 - \frac{4M_\chi^2}{(\sqrt{s})^2}\right) \tag{5.1}$$

Due to the high background level this endpoint is not resolvable, which will be shown in figure 7.1a. But the WIMP mass dependent shape of the photon spectrum is used for the calculation of expected exclusion limits of the sensitivity (see further section 7.6.1).

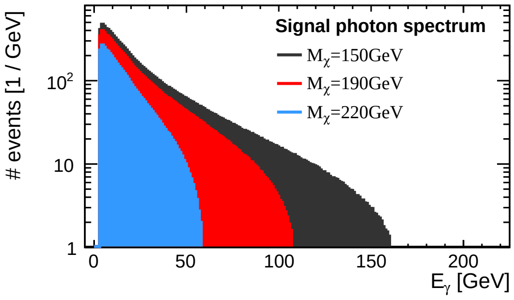

Figure 5.5: Photon spectrum for different assumed WIMP masses and the vector operator. With increasing WIMP mass the endpoint moves to smaller energies.

5.2 General principles of this analysis

Input to the calculation of WIMP exclusion limits are the photon energy spectra of the signal and the background. The background distributions are obtained by neutrino and Bhabha scattering events after a full detector simulation, following all the steps explained in chapter 4, and an event selection, addressed in chapter 6. The

WIMP events, on the other hand, are *not* simulated directly. Instead the selected neutrino events are reweighted to WIMP events, as explained in the following.

5.2.1 Strategy to obtain the signal events

Being highly model independent is one of the strengths of the mono-photon WIMP search and different model assumptions are tested. Repeating the full chain of event generation and detector simulation for each signal hypothesis would be very CPU-intensive. Instead the neutrino events, which are indistinguishable from WIMP events on an event-to-event basis, are used to obtain the signal events. For this, the photon energy spectrum of the selected neutrino events is converted into a WIMP photon spectrum by reweighting the neutrino events according to the ratio of the polarised cross-sections of WIMP pair production in the particular model $d\sigma_{\chi\chi\gamma,pol}/dE_\gamma$ and the Standard Model neutrino pair production $d\sigma_{\nu\bar{\nu}\gamma}/dE_\gamma$. All neutrino events are combined to an unpolarised data set to obtain the largest statistics. WIMP events for different polarisation configurations are obtained by applying the weights

$$w_{signal,pol} = \frac{d\sigma_{\chi\chi\gamma,pol}/dE_\gamma}{d\sigma_{\nu\bar{\nu}\gamma}/dE_\gamma} \tag{5.2}$$

More details can be found in section 7.1.2.

5.2.2 Choice of the centre-of-mass energy

For the Monte Carlo simulation 500 GeV is chosen out of the possible centre-of-mass energies at the ILC. The WIMP search can be carried out at any energy, but these for these studies higher centre-of-mass energies are generally favoured because of two reasons. Production of particles is possible to almost half the centre-of-mass energy and hence a broader WIMP mass range can be tested. For many processes also smaller couplings can be tested with higher centre-of-mass energies[i]. This is the motivation to perform the study at the highest centre-of-mass energy of the baseline design as presented in the Technical Design Report [99]. Extrapolations of the results to other centre-of-mass energies are discussed in sections 8.3 and 8.4, which allow to give WIMP exclusion limits also for the initial stage in a running scenario with a lower initial centre-of-mass energy [106].

---

[i] In the case of a mediator mass in the centre-of-mass energy range of the collider, a production at the resonance leads to the largest discovery potential.

5.3 Signal definition and cuts on generator level

In section 2.4.1.1 the cross-sections for the effective operators, which will be used to describe the WIMP data, are given. In a collider search it is not feasible to investigate the full angular range and all kinematically possible z values of equations 2.28, 2.29 and 2.30, because in a real experiment one cannot simply look for a single photon in an empty detector. An event selection is required to compensate for reconstruction deficits and features of the detector, and avoid regions in paramter space with high background levels.

The events are selected in two steps. First, events have to contain a photon which fulfills the signal definition comprising several cuts (explained in the following). Subsequently these signal-like events have to meet three conditions which ensure low detector activity to meet the requirement of low detector activity (see chapter 6).

5.3.1 Signal definition

An event is considered signal-like if it contains a photon with an energy in the range $2\,\mathrm{GeV} < \mathrm{E}_\gamma < 220\,\mathrm{GeV}$, a polar angle in the range $7^\circ < \theta_\gamma < 173^\circ$ and a minumum transverse momentum which is ϕ-dependent: $p_{T,\gamma} > 1.92\,\mathrm{GeV}$ for $|\phi_\gamma| > 35^\circ$ and $p_{T,\gamma} > 5.65\,\mathrm{GeV}$ for $|\phi_\gamma| \leq 35^\circ$. For convenience, the $p_{T,\gamma}$ conditions are expressed in the coordinate system of the forward calorimeter BeamCal (BeamCal coordinates, see section 3.6.5). If an event contains several reconstructed photons, the one with the largest transverse momentum is tested. The criteria are summarised in the central column of table 5.1, together with preselection cuts on generator level (see section 5.3.2). The motivation for the cuts is discussed in the following sections.

	signal definition	**preselection**
distinguish from charged electromagnetic particles	$\lvert\cos(\theta_\gamma)\rvert < 0.992546$ $(\Leftrightarrow 7^\circ < \theta_\gamma < 173^\circ)$	$\lvert\cos(\theta_\gamma)\rvert < 0.9975$ $(\Leftrightarrow 4.05^\circ < \theta_\gamma < 175.95^\circ)$
ensure identification of Bhabha scattering events	$p_{T,\gamma} > 1.92\,\mathrm{GeV}$ for $\lvert\phi_\gamma\rvert > 35^\circ$ $p_{T,\gamma} > 5.65\,\mathrm{GeV}$ for $\lvert\phi_\gamma\rvert \leq 35^\circ$ (in BeamCal coordinates)	$p_{T,\gamma} > 1\,\mathrm{GeV}$
distinguish from noise	$\mathrm{E}_\gamma > 2\,\mathrm{GeV}$	-
avoid Z return	$\mathrm{E}_\gamma < 220\,\mathrm{GeV}$	-

Table 5.1: Criteria for the signal definition and the corresponding preselection cuts at the event generation.

5.3.1.1 Distinguish photon from charged leptons

The detector signature of photons consists of energy depositions in ECAL which is, in practice, indistinguishable from an electron or positron signature. But in contrast to the leptons, the neutral photon leaves no hits in the tracker. The angular range suitable for photon identification is hence constrained to detector regions where tracking instruments are installed in front of ECAL.

In the very forward region no tracking is instrumented: The Forward Tracking Disks start at 5.13°. An efficient track reconstruction is possible above 7° [99] ($|\cos\theta_\gamma| < 0.992546$), which is hence applied as the minimum polar angle.

5.3.1.2 Suppression of Bhabha scattering background

A minimum transverse momentum of the photon is applied to suppress the Bhabha scattering background. In order to identify a Bhabha event, at least one electron or positron has to be reconstructed in the detector. Thus, they must not escape through the beam pipe, which implies that they have a larger polar angle than the inner rim of the most forward detector, BeamCal. As visualised in figure 5.6 the probability for a lepton produced in Bhabha scattering to hit the detector can be considerably enhanced by requiring a photon with a certain transverse momentum, which is balanced by the lepton system. The peak of transverse momentum distribution of the lepton which is on the side of the photon emission is shifted to $|p_{T,\gamma}|$. The other electron or positron distribution is not affected and peaks at zero.

With the inner rim of BeamCal being ϕ-dependent, the largest signal region is obtained if the $p_{T,\gamma}$ cut is ϕ-dependent as well. The shape of the inner rim of BeamCal can be easiest described in the BeamCal coordinate system (see section 3.6.5). In figure 5.7 the radii of the two openings are shown. The higher threshold has to be applied for the clearance of the incoming beam at $|\phi| > 160°$. In order to take a safety margin of one BeamCal pad into account, this region is extended to $|\phi| > 145°$. As the two forward regions are mirror symmetric (see figure 3.7 on page 60), the azimuthal range is the same on both, the electron and the positron, side.

The round opening for the outgoing beam pipe has a radius of 20.01 mm. The opening for the incoming beam extends to 73.54 mm from the BeamCal centre, i.e. the centre of the round opening. The minimum transverse momentum corresponding to a polar angle outside of this dead area can be calculated using $p_T = E \cdot \frac{r_i}{z_{BeamCal}}$, where E is the particle energy, $z_{BeamCal} = 3595\,\mathrm{mm}$ is the dis-

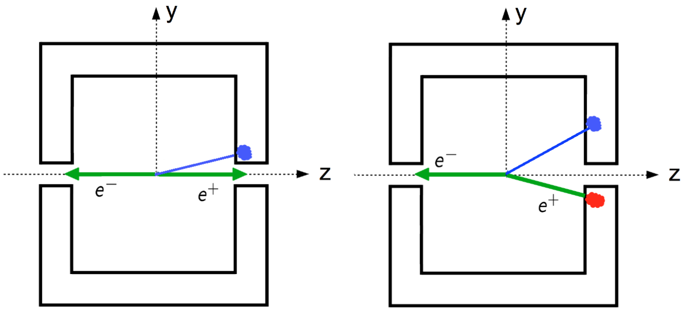

(a) (b)

Figure 5.6: Sketch of a Bhabha event with an associated photon in a simplified detector. (a) Without constraints on the photon, the electron and positron distributions peak at low angles and they are likely to escape detection. (b) With the condition of a minimum transverse momentum of the photon, one lepton is likely to have a sizeable angle and the event can be distinguished from a mono-photon event.

tance of BeamCal to the interaction point and r_i is the extend of the dead area with a safety margin of 7.65 mm, corresponding to the size of one pad: $r_{outgoing} = (20.01 + 7.65)\,\mathrm{mm}$ and $r_{incoming} = (73.54 + 7.65)\,\mathrm{mm}$.

With a lepton energy of $E = 250\,\mathrm{GeV}$ one obtains $p_{T,e} > 1.92\,\mathrm{GeV}$ for $|\phi| < 145°$ and $p_{T,e} > 5.65$ above.[ii] As this cut is not applied on the lepton but on the photon which counter-balances the p_T, the ϕ-dependence are mirrored and the photon minimum transverse momenta are 1.92 GeV for $|\phi| > 35°$ and 5.65 for $|\phi| \leq 35°$.

5.3.1.3 Energy restrictions

The energy threshold of 2 GeV is applied to reject reconstructed photon candidates which might be the result of noise in the detector. Photons with energies below the minimum transverse momentum cut can occur because the $p_{T,BeamCal}$ is tested in the BeamCal coordinate system and the corresponding $p_{T,ILD}$ in the detector coordinate system may be smaller. With a small $p_{T,ILD}$ also the energy could be close to zero. By chosing this cut close to the minimum p_T only few additional events are cut away.

With the criterion of the maximum energy of 220 GeV on the other hand, a phase

---

[ii] By assuming half the centre-of-mass energy (250 GeV) the values for $p_{T,min}$ are conservative. Due to the energy carried away by the photon, the lepton energy is lower, which also leads to a slightly lower required transverse momentum.

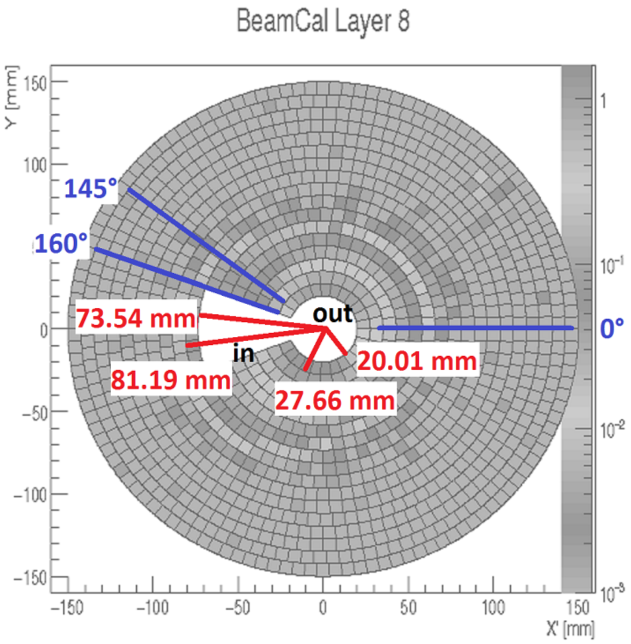

Figure 5.7: Visualisation of the dimensions of the inner rim of BeamCal. With a safety margin of one pad, the cut is designed such that a lepton hits the detector outside of 27.66 mm on the right-hand side and 81.19 mm in the region of the left opening (above $\phi = 145°$).

space region with high background rates can be rejected. At any centre-of-mass energy above the Z boson mass, the emission of initial state radiation can reduce the energy and Z bosons may be produced on-shell. This *radiative return to the Z boson* leads to a significant cross-section increase of processes that are mitigated by the Z boson. The corresponding photon energy is given by

$$E_{\gamma,return} = \frac{(\sqrt{s})^2 - M_Z^2}{2\sqrt{s}} \tag{5.3}$$

or 241.7 GeV for $\sqrt{s} = 500$ GeV.

All considered background processes can be produced via a Z boson in the s-channel. In figure 5.8a the photon energy spectrum of the full Standard Model background for unpolarised beams is shown. All cuts of the signal definition despite the maximum energy are applied. The increase towards lower energies reflects the typical ISR spectrum. The peak around the highest energies is explained by the radiative return.

In this figure *reconstructed* events are shown for the first time. The additional features at high energies are the result of a mis-calibration of the very forward ECAL component, see section 5.5.3 for more details. The visible features at lowest energies are explained in section 6.1.4. With a centre-of-mass energy well above the Z boson mass the photon distribution is less dominated by the peak corresponding to the radiative return than at LEP.

In figure 5.8b the photon energy distribution in association with neutrino pair production for completely right-handed electrons and left-handed positrons is depicted. The effect of the radiative return to the Z boson is most pronounced in this helicity configuration, because the otherwise dominant t-channel production is suppressed due to the polarisation of the beams.

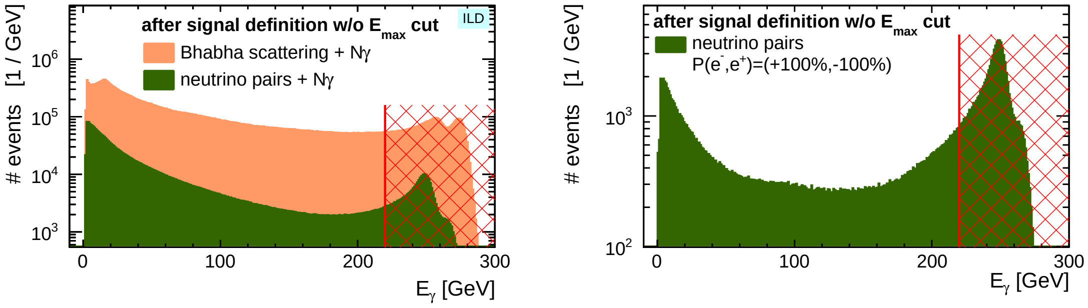

(a) (b)

Figure 5.8: Energy spectrum of the reconstructed signal-like photons, (a) all background processes with unpolarised beams, (b) neutrino pair production with $P_{e^-} = +100\%$, $P_{e^+} = -100\%$. In the analysis events with $\mathrm{E}_\gamma > 220\,\mathrm{GeV}$ are discarded to avoid the large background rates induced by the radiative return to the Z boson.

The high background rates around the radiative return energy are avoided by applying the maximum energy cut, visualised by the red lines in figure 5.8. As can be seen in the figure the rise of the background level extends well below $\mathrm{E}_\gamma = 241.7\,\mathrm{GeV}$ and hence a safety margin is applied by choosing $\mathrm{E}_{\gamma,return} < 220\,\mathrm{GeV}$ ($\approx 90\%$ of $\mathrm{E}_{\gamma,return}$) as one of the signal criteria.

5.3.1.4 Comparison of the signal definition to the previous analysis

In [1,2] the signal definition was based on an energy threshold rather than a minimum transverse momentum. With $10\,\mathrm{GeV} < \mathrm{E}_\gamma < 220\,\mathrm{GeV}$ and $|\cos\theta_\gamma| < 0.98$ ($11.5° < \theta_\gamma < 168.5°$) the signal definition had a severe shortcoming: The resulting minimum transverse momentum

$$p_{T,\gamma,\mathrm{min}} = E_{\gamma,\mathrm{min}} \cdot \sin\theta_{\mathrm{min}} = 1.99\,\mathrm{GeV} \tag{5.4}$$

(in the main detector coordinates) allowed Bhabha scattering events with both leptons escaping detection through the beam pipe which makes them indistinguishable from signal-like events. With real data this would have led to an increase of the

Bhabha background which was not observed in [1,2], because very forward leptons were not generated (see section 5.3.2.2).

The $p_{T,e}$ distribution of the Bhabha lepton from which the photon is recoiling peaks at $p_{T,\gamma}$ and consequently values in the range of the minimum photon transverse momentum will also occur for the leptons. The polar angle of these leptons is $\theta_e = \sin^{-1}(\frac{p_T}{E_e})$. It is smallest for the largest energies, the beam energy $E_e = 250\,\mathrm{GeV}$, and for smallest transverse momenta, $p_{T,min} = 1.99\,\mathrm{GeV}$. The resulting polar angle is $\theta_e = 8\,\mathrm{mrad}$, which is sketched in figure 5.9 as a black circle. The circle is centred around the z-axis of the detector and hence offset from the BeamCal centre. It can be clearly seen that the opening for the beam pipes extends to larger polar angles on the left and the right. If the lepton momentum points towards one of these regions highlighted in yellow, it escapes detection. The other lepton of the Bhabha final state is not constrained by the signal definition, so it predominantly has a vanishing polar angle and hence neither interacts with the detector material. This illustrates how the signal definition in [1,2] did not prevent electron and positron from Bhabha scattering events to escape detection.

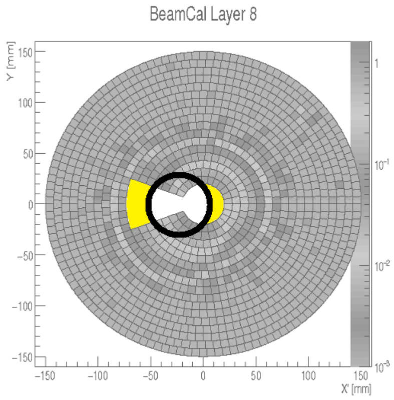

Figure 5.9: Sketch of the polar angle of Bhabha electrons or positrons projected on a BeamCal layer as it follows from the minimum transverse momentum of the photon calculated using the signal definition in [1,2].

A second advantage of a minimum transverse momentum over a minimum energy is that it leads to a larger signal region. This is reflected in the fiducial cross-section of the irriducible neutrino background, $\sigma_{unpolarised} = 4534.1\,\mathrm{fb}$ (see table 6.3) which is 58% higher than in [1,2] (2863.0 fb).

5.3.2 Phase space restrictions on generator level

In order to save CPU time, the phase space of the event samples is already adjusted to the signal definition at the event generation. One of the photons in the matrix element γ_i has to fulfill criteria which are similar to the signal definition cuts but loose enough to account for shifts of position and energy in the reconstruction compared to generator level, due to detector effects and the boost of the crossing angle. The signal photon preselection cuts are $p_{T,\gamma_i} > 1\,\mathrm{GeV}$ and $|\cos(\theta_{\gamma_i})| < 0.9975$.

The cuts on generator level are summarised in table 5.2 and compared to the signal defining conditions in table 5.1 on page 89. Additional cuts have to be applied to avoid divergences in the cases of several emitted photons (see section 5.3.2.1) and Bhabha scattering (see section 5.3.2.2). In the WHIZARD steering (see apendix D) the conditions are given after the `cuts` keyword.

signal photon preselection	$\lvert\cos(\theta_{\gamma_i})\rvert < 0.9975$ $(4.05° < \theta_{\gamma_i} < 175.95°)$ $p_{T,\gamma_i} > 1\,\mathrm{GeV}$
additional matrix element photons	$\lvert\cos(\theta_\gamma)\rvert < 0.9999755$ $(0.4° < \theta_\gamma < 179.6°)$ $p_{T,\gamma} > 0.1\,\mathrm{GeV}$ $\Theta_{\gamma\gamma} > 0.15°$, all pairs of photons
Bhabha scattering	$M_{inv,e_{in}^{+/-},e_{out}^{+/-}} < -1\,\mathrm{GeV}$ $M_{inv,e_{out}^{-},e_{out}^{+}} > 1\,\mathrm{GeV}$ $M_{inv,e_{out}^{+/-},\gamma_i} > 4\,\mathrm{GeV}$, signal-like photon $M_{inv,e_{out}^{+/-},\gamma} > 1\,\mathrm{GeV}$, all photons

Table 5.2: Phase space restrictions on generator level. All cuts with subscript γ_i have to be fulfilled by one photon simultaneously, cuts with γ have to be fulfilled by all matrix element photons.

5.3.2.1 Cuts on additional photons

In events with more than one photon several conditions are applied to avoid a divergence of the cross-section. One of the photons has to fulfill both the preselection cuts. On all additional photons looser cuts are applied: $p_{T,\gamma} > 0.1\,\mathrm{GeV}$ and $0.4° < \theta_\gamma < 179.6°$ ($|\cos(\theta_\gamma)| < 0.9999755$). Furthermore, a minimum angular separation of all photon-photon pairs is required. The choice of $\Theta_{\gamma\gamma} > 0.15°$ corresponds approximately to the $5 \times 5\,\mathrm{mm}^2$ cell size of ECAL (see section 3.6.6). More details on the event generation with several photons and a discussion of the implications of the cuts can be found in section 5.4.1.

5.3.2.2 Bhabha scattering: additional cuts

A number of additional cuts have to applied in the generation of Bhabha scattering events. As discussed in [159,160], the cross-section of the radiative Bhabha scattering process takes very large values for the following cases of parallel four-momenta

$$\underbrace{q3||p1 \quad q3||p2}_{\text{I}} \qquad \underbrace{q1||q2}_{\text{II}} \qquad \underbrace{q3||q1 \quad q3||q2}_{\text{III}} \qquad \underbrace{p1||q1 \quad p2||q2}_{\text{IV}} \tag{5.5}$$

where $q3$ is the four-momentum of the photon, and p_i and q_i are the four momenta of the incoming and outgoing electrons ($i = 1$) and positrons ($i = 2$), respectively (as visualised in figure 5.10). The Roman numerals refer to the discussion of the four different cases below.

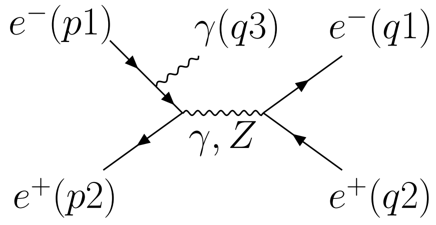

Figure 5.10: Example Feynman diagram of Bhabha scattering. p_i and q_i are the particles' four-momenta.

In cases where Bhabha scattering events can mimic the mono-photon signature, these divergences have to be avoided by defining a suitable signal definition, similarly to the requirement of the maximum photon energy to remove the large background rates close to the radiative return to the Z boson (see section 5.3.1.3).

I - photon parallel to incoming particles: The first case in equation 5.5 is equivalent to a vanishing photon polar angle, which implies that the peak of the transverse momentum distribution of the outgoing electron and positron is at zero and thus a large fraction of leptons escape detection through the beam pipe. On the other hand, in the case of a hard non-collinear ISR photon the Bhabha scattering process has an asymmetric reference frame and the peak of the lepton distribution is shifted to a similar transverse momentum as the photon. So with the minimum photon transverse momentum criterion in the signal definition (see section 5.3.1.2) the first constellation leading to a large cross-section is avoided.

Not all of the cases leading to high cross-sections can be addressed by the signal definion. But some of the "divergences" have to be circumvented by setting cuts in WHIZARD, in order to allow a convergence of the cross-section calculation and to safe computation time. Ideally, no potential background to the mono-photon signal is cut away.

In the event generation with WHIZARD, cuts are applied on two variables: the invariant mass of two particles $M = \sqrt{2q_iq_j(1 - \cos\Theta_{ij})}$ and the negative square of four-momentum transfer $Q^2 = -q^2 = -(p_i - q_j)^2 = 4p_iq_j \sin^2(\Theta_{ij}/2)$. In the

WHIZARD steering (see appendix D) the four-momentum transfer is also expressed as M which, in this case, is the signed square root: $M = -\sqrt{|Q|}$. In order to avoid cases II-IV of equation 5.5 suitable M cuts are applied.

II - collinear outgoing electron and positron: In this case $M_{e^-_{out},e^+_{out}}$ becomes minimal and e^+_{out} and e^-_{out} are collinear to each other. In the event generation the cut $M_{e^-_{out},e^+_{out}} > 1\,\mathrm{GeV}$ is applied to speed up the matrix element calculation. The deviation of the cross-section without this cut is several orders of magnitude below the uncertainty given by O'MEGA, which means that the cut has no effect on the generated phase space and can be safely applied.

III - photon parallel to outgoing leptons: The third case comprises photons parallel to e^-_{out} or e^+_{out}, which means that these mass singularities occur for final state radiation. The signal-like photon γ_i hits the detector in a region where tracking is instrumented which is ensured by the maximum $|\cos(\theta)|$ of the signal definition (see section 5.3.1.1). Hence, an electron or positron close to that photon is identified as a charged particle and the event would be discarded. In order to avoid the generation of events which would not fulfill the selection criteria, a rather large cut of $M_{e^{+/-}_{out},\gamma_i} > 4\,\mathrm{GeV}$ is applied. In this way, the initial data set becomes significantly smaller, but the background after the event selection is not affected.

On the other hand, the additional photons in multi-photon events may well hit the detector in the forward region where a close-by lepton cannot be identified as charged particle. Therefore the cut for all other photons is weaker: $M_{e^{+/-}_{out},\gamma} > 1\,\mathrm{GeV}$. With this unavoidable cut the contribution of soft and collinear final state radiation is not taken into account and the cross-section has a theory uncertainty, which is expected to have a smaller effect than the analogous case of initial state radiation (see section 5.4.1.2) and is therefore neglected.

IV - $\mathbf{e^-_{out}}$ parallel to $\mathbf{e^-_{in}}$ (or $\mathbf{e^+_{out}}$ and $\mathbf{e^+_{in}}$): The cross-section increases sharply for vanishing p_T transfer in the Bhabha scattering. The case of both the outgoing electron and positron being parallel to their incoming counterpart is avoided by the required photon p_T and the resulting unsymmetric reference frame. Thus, a large fraction of the critical phase space is avoided by the transverse momentum cuts on the photon in the signal definition.

In events with a photon transverse momentum in concordance with the signal definition, the lepton angles can nevertheless be so small that the cross-section calculation is divergent. Thus the additional cut $M_{e^{+/-}_{in},e^{+/-}_{out}} < -1\,\mathrm{GeV}$ on the four-momentum transfer of all possible pairs of incoming and outgoing leptons is applied in WHIZARD. In figure 5.11b it is shown that with this cut the complete angular

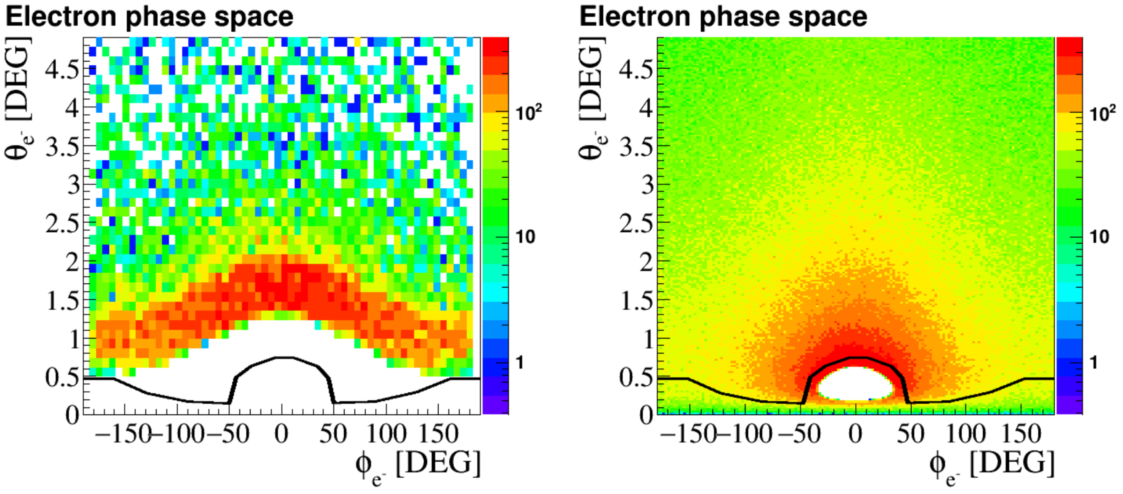

(a) (b)

Figure 5.11: Polar angle versus azimuthal angle of the generated electrons in Bhabha scattering events after applying the crossing angle boost. The invariant mass cut between incoming and outgoing electron and postitron is (a) $M_{e_{in},e_{out}} < -4\,\mathrm{GeV}$ and (b) $< -1\,\mathrm{GeV}$. The black line corresponds to the inner rim of BeamCal. The unpopulated parameter space extends to within the detector for the test sample with $M_{e_{in},e_{out}} < -4\,\mathrm{GeV}$, whereas the lower cut only leaves angles within the outgoing beam pipe empty.

range of leptons which hit the detector is generated. Only leptons with very low lepton angles are not included.

As shown by the angular distribution of events in a test sample with a harder cut of 4 GeV (figure 5.11a) the omitted phase space is substantially bigger and the inner part of BeamCal is not covered. This cut was used in [1,2], which led to a too optimistic estimate of the Bhabha scattering background. Due to this incompleteness of the generated phase space the deficient signal definition (see section 5.3.1.4) was not reflected in the selection efficiency.

The data set with the updated cut of $M_{e_{in},e_{out}} < -1\,\mathrm{GeV}$ provides a complete description of the instrumented angular range and hence gives a realistic description of the detector activity, which is crucial to optimise the event selection (see chapter 6).

On the other hand, by applying the required minimum $M_{e_{in},e_{out}} < -1\,\mathrm{GeV}$, events might be cut away, which would fulfill the signal definition and survive all selection criteria. So the background level could be higher than assumed in this study and the exclusion limits might be worse. A requirement of a realistic description of Bhabha scattering at a future linear collider is hence a setup which also takes the possible configuration of a photon in the detector and both outgoing leptons with vanishing transverse momentum into account, e.g. following [161].

In section 7.3.1 it will be shown that the WIMP exclusion limits would be worse by about 10%, even if the Bhabha scattering cross-section was five times higher. This means that the effect of the description of the Bhabha scattering phase space, which cannot reflect reality completely, is moderate.

5.3.2.3 Motivation to use Whizard for Bhabha scattering

The problematic phase space caused by the divergencies can be better described by dedicated Bhabha scattering generators [161–164]. Whizard is nevertheless prefered because of two reasons. First, it provides a detailed description of a lepton collider environment. Second, the steering can be well adjusted to the requirements of the WIMP study to produce one photon or several with sizeable transverse momentum. For this, the possibility to apply cuts directly on the photons is an important prerequisite, which is not provided by most other generators.

For example, in the steering of Bhwide [162], developed for Bhabha scattering with sizeable angles, cuts on the photon are not possible, which means that the efficiency to select signal-like events would be close to zero. In a test run of Bhwide, the produced statistics of 10^8 events did not contain a single event with a hard photon according to the signal definition.

With Bhlumi [163,164] Bhabha scattering events for luminosity measurements can be produced. The angular range is restricted to $\theta \lesssim 10^\circ$, which would contain most of the interesting phase space. But again the number of photons and their distribution are not steerable and only cuts on momentum transfer can be set.

5.4 The event samples of the WIMP study

The event samples were exclusively produced in the context of this analysis, with the dedicated preselection cuts, as discussed before in section 5.3.2, and the special treatment of the ISR photons, presented in the following.

All processes are generated with a centre-of-mass energy of 500 GeV and 100% polarisation of both beams. For the neutrino pair production the two possible cases are generated: $P(e^-, e^+) = (-1, +1)$ and $(+1, -1)$. Bhabha scattering is generated with all four polarisation combinations. In order to obtain data samples with a different polarisation level, the events are reweighted as described in section 5.4.2.2.

All three neutrino generations (ν_e, ν_μ, ν_τ) are generated in a combined data set, using aliases in the WHIZARD steering files (see appendix D). This follows the general approach for ILC Monte Carlo samples to produce processes with indistinguishable final states together.

5.4.1 Modelling of initial state radiation

For modelling ISR photons, WHIZARD offers a dedicated parametrisation that comprises all orders of soft and soft collinear photons and the first three orders of hard collinear photons [165, 166]. With this parametrisation the cross-sections of the considered processes are calculated with high accuracy. However, available tools in WHIZARD do not give a realistic distribution of the photon polar angle.

In the ISR parametrisation, the four-momentum loss of the emitting beam particles is written out as one entry per beam in the list of stable Monte Carlo particles. The motivation is to keep momentum conservation rather than producing physical particles. Nevertheless, the particle data group (PDG, [157]) particle code of these pseudo particles is 22 as for photons. The four-momentum of these objects corresponds to the sum of all emitted ISR photons from the respective beam. As a consequence, the angle and energy are unphysical and evidently the number of photons is wrong.

A different way to produce individual ISR photons (with a non-vanishing transverse momentum) is to include them in the matrix element of the considered process. In the previous study [1, 2] the ISR photons were modelled using both approaches. However, because the non-physical photons from the ISR routine were not restricted to zero polar angle, the phase space of the two approaches was not clearly separated. This means, that double counting occured, when a pseudo photon with incorrect description was used in the analysis in the case it passed the selection criteria. Furthermore, if the photons produced with this parametrisation are not constrained to zero polar angle, the energy might not be conserved in the event. Therefore non-collinear photons should only be described by including them in the matrix element.

The strategy to describe ISR photons followed in this analysis is also a combination of both approaches, but by restricting the elements from the ISR parametrisation to zero transverse momentum, the case that they hit the detector and mimic a physical photon is excluded. In this way, double counting is avoided by construction. In order to also cover the case of events with several photons that interact with the detector, event samples with different numbers of photons in the matrix element are produced (see the next section 5.4.1.1). By using the ISR parametrisation in addition, the cross-section is corrected for the contribution of soft collinear ISR photons and the most accurate cross-section can be obtained.

5.4.1.1 Number of photons in the events

The two considered processes, neutrino pair production and Bhabha scattering, are generated in several sub-processes with an increasing number of photons included in the matrix element. Higher orders are ignored once the cross-section for $e^+e^- \to \nu\bar{\nu}$+Nγ ($e^+e^- \to e^+e^-$+Nγ) is more than four orders of magnitude smaller than the cross-section of the leading order $\nu\bar{\nu}$+1γ (e^+e^-+1γ). The maximum number of photons is 4 in the case of neutrino pair production and 3 for Bhabha scattering. The cross-sections for the processes with different numbers of photons are shown in figure 5.12, together with the uncertainties induced by the arbitrariness of the p_T cut, discussed in the following.

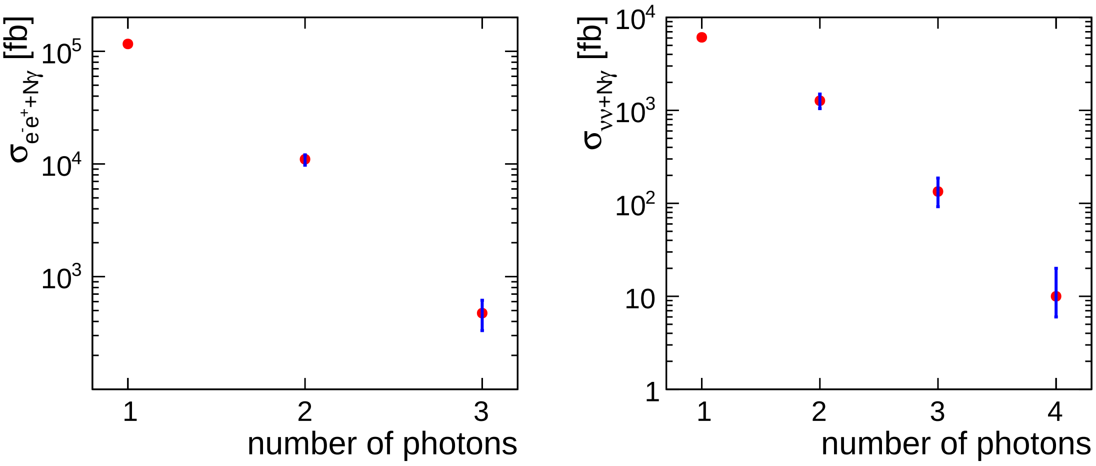

(a) (b)

Figure 5.12: Unpolarised cross-section for (a) Bhabha scattering and (b) neutrino pair production for different numbers of photons in the matrix element with the theory uncertainties.

5.4.1.2 Theory uncertainty of the cross-section

With the preselection cuts (see section 5.3.2) one photon in the event is hard and non-collinear. Such photons are well modelled when included in the matrix element calculation. Additional matrix element photons are predominantly softer and more collinear and are not constrained by the signal photon preselection.

Whereas the ISR parametrisation gives a good description of soft collinear photons, no full description of soft photons with only a small polar angle existed in WHIZARD at the time of the event production[iii]. Therefore a minimum transverse momentum cut on the matrix element photons is required to avoid infrared and collinear divergences. The exact value is arbitrary and the cross-section depends on the choice.

The reasoning behind the idea of generating samples with different photon numbers is that they have different signatures in the detector. Hence the chosen value of $p_{T,\gamma} > 0.1\,\text{GeV}$ is supposed to describe a rough threshold below which the photons will not be detected in ECAL (introduced in section 3.6.6). At high angles this p_T cut simply acts a an energy threshold and towards lower angles the minimum energy rises to account for the larger beam-induced background which makes it harder to reconstruct soft photons in the very forward region (see section 4.6.2). With a second cut on all photons the generated phase space is restricted to angles where detector components are instrumented: With $0.4^\circ < \theta < 179.6^\circ$ ($|\cos(\theta_\gamma)| < 0.9999755$) the BeamCal opening is cut out and photons which would escape through the beam pipe are not generated. For simplicity, this cut only ensures that photons lie outside the round beam pipe of the outgoing beam, but the keyhole shaped opening for the incoming beam is not cut out.

The lack of a complete descripton of the ISR photon phase space, which leads to the discussed arbitrariness of the cuts, is reflected in an uncertainty on the cross-section, which will be refered to as *theory* uncertainty in the following. It is evaluated by changing the p_T cut to 50% and 200% of the value in the event generation (0.05 and 0.2 GeV, respectively). The cross-sections calculated with these values are taken as upper and lower theory uncertainties (see table 5.3). Whereas the effect for single sub-processes is rather large, it is a few per cent for the sum over all photons: The theory uncertainty on the neutrino pair production cross-section is $+3.8\%$ -3.6% and for Bhabha scattering $+0.9\%$ -1.1%.

The effect of this uncertainty on the WIMP exclusion limits is evaluated (see section 7.6.4). In the standard setting of the sensitivity calculation, they are not included because ISR at the ILC is purely QED and hence can be calculated with great precision (see section 7.4.4).

[iii] A more realistic ISR treatment within WHIZARD is currently under development.

	cross-section [fb]					
$p_{T,\gamma,min}$	$\nu\bar{\nu}\gamma$	$\nu\bar{\nu}\gamma\gamma$	$\nu\bar{\nu}\gamma\gamma\gamma$	$\nu\bar{\nu}\gamma\gamma\gamma\gamma$	combined	uncertainty
0.05 GeV		1497 (+18%)	187 (+40%)	16 (+60%)	7799	+3.8%
0.1 GeV	6099	1270	134	10	7513	
0.2 GeV		1044 (−18%)	92 (−31%)	6 (−40%)	7241	−3.6%
	$e^+e^-\gamma$	$e^+e^- + \gamma\gamma$	$e^+e^-\gamma\gamma\gamma$		combined	uncertainty
0.05 GeV		12046 (+9.4%)	759 (+23%)		129028	+0.9%
0.1 GeV	116223	11013	616		127852	
0.2 GeV		9756 (−11.4%)	474 (−23%)		126453	−1.1%

Table 5.3: Unpolarised cross-sections for neutrino pair production (Bhabha scattering) with 1-3 (1-4) photons in the matrix element. One photon has to fulfill the preselection criteria. For the other photons a minimum transverse momentum is required to avoid divergences. The standard cut of $p_{T,\gamma} > 0.1\,\text{GeV}$ is varied and the difference of the combined cross-sections is taken as a theory uncertainty.

5.4.2 The produced number of events

In table 5.4 the main features of the produced event samples for neutrino pair production and Bhabha scattering are summarised. The shown uncertainties on the cross-sections are obtained in the matrix element calculation performed by O'Mega (see section 4.4). They are well below the theory uncertainties shown in table 5.3.

The cross-section of the neutrino pair production with $P_{e^-} = +1$, $P_{e^+} = -1$[iv] corresponds to the s-channel exchange of a Z boson, shown as the left Feynman diagram in figure 5.2. In the case of reversed polarisation the other two processes in the figure contribute in addition which leads to a ~15 times higher cross-section. The process with a photon emitted by the W boson contributes with a similar scale as the s-channel process and the largest contribution by far is the process with a W boson mediator and a photon from ISR.

5.4.2.1 Luminosity weights

The targeted integrated luminosity of the neutrino events were $500\,\text{fb}^{-1}$, which correspond to the initial four years of ILC operation in the H20 scenario (see section 3.4). In order to compensate occasional job failures when running the simulation and reconstruction, 20% more events were generated. The integrated luminosity corresponding to the final numbers of reconstructed events, listed in table 5.4, are well above $500\,\text{fb}^{-1}$.

The integrated luminosity of the Monte Carlo samples $\mathcal{L}_{MC}$ differs from the ILC

[iv] As defined in section 3.4, "−" ("+") denotes left- (right-) handed chirality.

	process	σ [fb]		N$_{events}$	$\mathcal{L}_{MC}$ [fb^{-1}]
neutrino pair production					
$P_{e^-} = -1,\ P_{e^+} = +1$					
	$\nu\bar{\nu}\gamma$	22925.0	±31.4		
	$\nu\bar{\nu}\gamma\gamma$	4653.5	±9.0		
	$\nu\bar{\nu}\gamma\gamma\gamma$	481.1	±1.5		
	$\nu\bar{\nu}\gamma\gamma\gamma\gamma$	33.6	±0.3		
	combined	28093.1	±32.7	14 745 059	524.9
$P_{e^-} = +1,\ P_{e^+} = -1$					
	$\nu\bar{\nu}\gamma$	1431.5	±2.5		
	$\nu\bar{\nu}\gamma\gamma$	438.6	±1.0		
	$\nu\bar{\nu}\gamma\gamma\gamma$	62.0	±0.2		
	$\nu\bar{\nu}\gamma\gamma\gamma\gamma$	5.5	±0.03		
	combined	1937.6	±2.7	1 161 407	599.4
Bhabha scattering					
$P_{e^-} = -1,\ P_{e^+} = -1$					
	$e^+e^-\gamma$	112691.6	±71.4		
	$e^+e^-\gamma\gamma$	10616.5	±11.7		
	$e^+e^-\gamma\gamma\gamma$	60.3	±1.1		
	combined	123911.1	±72.4	2994007	24.2
$P_{e^-} = -1,\ P_{e^+} = +1$					
	$e^+e^-\gamma$	120805.9	±77.4		
	$e^+e^-\gamma\gamma$	11598.3	±12.7		
	$e^+e^-\gamma\gamma\gamma$	66.6	±1.2		
	combined	133070.8	±78.4	2994006	22.5
$P_{e^-} = +1,\ P_{e^+} = -1$					
	$e^+e^-\gamma$	118393.2	±74.3		
	$e^+e^-\gamma\gamma$	11208.8	±11.7		
	$e^+e^-\gamma\gamma\gamma$	63.3	±1.1		
	combined	130234.7	±75.2	2994006	23.0
$P_{e^-} = +1,\ P_{e^+} = +1$					
	$e^+e^-\gamma$	112694.1	±69.2		
	$e^+e^-\gamma\gamma$	10618.2	±11.1		
	$e^+e^-\gamma\gamma\gamma$	60.4	±1.1		
	combined	123916.5	±70.1	2994007	24.2

Table 5.4: List of the Monte Carlo event samples. Integrated luminosity and number of events refer to simulated and reconstructed events.

luminosity considered in the analysis $\mathcal{L}_{ILC}$. In order to obtain data corresponding to a certain $\mathcal{L}_{ILC}$ the Monte Carlo events are weighted according to

$$w_{\mathcal{L}} = \frac{\mathcal{L}_{ILC}}{\mathcal{L}_{MC}} \tag{5.6}$$

$\mathcal{L}_{MC}$ for the different processes is shown in the last column of table 5.4.

Because of the large cross-section in the case of Bhabha scattering only 3 million events for each polarisation configuration were produced and the available data sets correspond to about 22-24 fb^{-1} each. This means, for example, that the events have to be weighted with a factor of 5.3 to obtain a data set for unpolarised beams and an integrated luminosity of 500 fb^{-1}. After the events selection it will be shown in chapter 6 that the surviving Bhabha scattering events are very few compared to the neutrino events and hence the fluctuations induced by these weights have a negligible effect on the background photon energy distribution.

5.4.2.2 Polarisation weights

A second weight is applied to go from the 100% polarised Monte Carlo samples to electron (positron) polarisation values P_{e^-} (P_{e^+}) feasible in the experiment:

$$w_{pol} = \frac{1}{4}(1 \pm P_{e^-})(1 \pm P_{e^+}) \tag{5.7}$$

The standard choice in this analysis is $P_{e^-} = \pm 80\%$ and $P_{e^+} = \pm 30\%$, according to the ILC baseline design. Different polarisation setups, like no beam polarisation or higher percentages are used to study the influence of beam polarisation (see section 7.2).

In general all four fully polarised cross-sections σ_{LL}, σ_{LR}, σ_{RL} and σ_{RR} contribute to the cross-section with a level of polarisation P_{e^-} and P_{e^+} below 100%:

$$\begin{aligned}\sigma_{P_{e^-}P_{e^+}} = \frac{1}{4}[&(1 - P_{e^-})(1 - P_{e^+})\sigma_{LL} + (1 - P_{e^-})(1 + P_{e^+})\sigma_{LR} \\ &+(1 + P_{e^-})(1 - P_{e^+})\sigma_{RL} + (1 + P_{e^-})(1 + P_{e^+})\sigma_{RR}]\end{aligned} \tag{5.8}$$

5.4.3 Photon phase space

In figure 5.13 the distribution of ISR photons in association with neutrino pair production is shown. Energy and polar angle θ are the values from the event generation, i.e. without the effects of the detector interaction and reconstruction. Despite the applied cuts (see section 5.3.1), the general pattern of the ISR photon spectrum can be recognised: The number of photons steeply decreases for both higher energies and larger polar angles.

The minimum polar angle cut of the preselection on generator level (see section 5.3.2) of 4.04° (i.e. 175.6°) is clearly visible. The second population in both

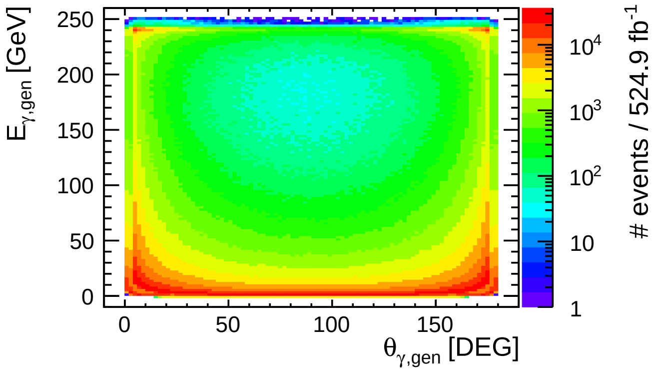

Figure 5.13: The phase space of ISR photons is characterised by an energy distribution which peaks at low values and a polar angle distribution which increases towards the forward regions.

lower corners correspond to the additional photons with smaller minimum energy and angles (see section 5.3.2.1).

For a particular process the ISR photon spectrum is influenced by the cross-section at different centre-of-mass energies. In the case of neutrino pair production the smaller peaks around 240 GeV can be explained by the radiative return to the Z boson, which is discussed in section 5.3.1.3.

5.5 Quality of the photon reconstruction

This section contains a discussion of the quality of the photon reconstruction in the produced events. The observables of the reconstructed photons are compared to the underlying events on generator level. The data set of neutrino events is used for this analysis, because it is a clean photon sample, which only contains $1-4$ (matrix element) photons apart from overlay and detector background. The events with $(P_{e^-}; P_{e^+}) = (-100\%; +100\%)$ are taken because of the larger statistics compared to the other polarisation combination.

5.5.1 Efficiency of the photon reconstruction

The photon reconstruction in the events of the previous WIMP study [1,2] suffered from fractured electromagnetic clusters. With the used version of the PandoraPFA algorithm (v00-03-01) true clusters from photons in many cases were split up into several clusters and tagged as reconstructed photons. As a consequence, in [1, 2] the clusters had to be merged after the main reconstruction by applying a cone algorithm.

The photon reconstruction in this analysis relies on the approach [146] presented in section 4.6.1, which is only available from PandoraPFA v02-00-00. Figure 5.14

shows the number of reconstructed photons associated to one generated photon. Generated photons are only considered if they were included in the matrix element, if they fulfill $E_\gamma > 2\,\text{GeV}$ and $7° < \theta_\gamma < 173°$, and if they have a maximum number of 1 daughter particle to exlude photons that converted into electron-positron pairs. The reconstructed photons do not have to fulfill any cuts, they only must have a truth link to a generated photon.

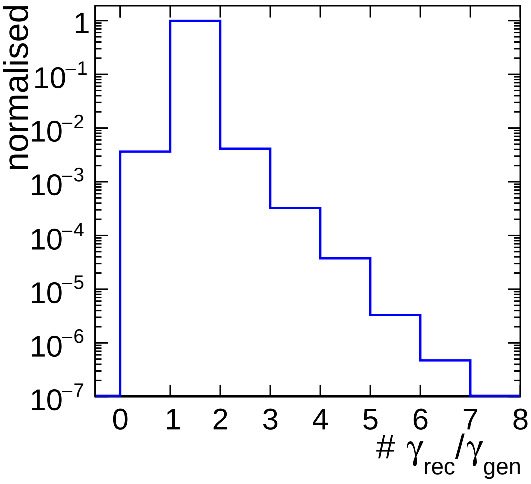

Figure 5.14: Number of reconstructed photons associated to a generated photon.

As depicted in figure 5.14, more than 99% of the generated photons have exactly one associated reconstructed photon. In only 0.4% of the cases the photon is not reconstructed as a photon but as a neutral hadron (`PFO`=2112). Also in 0.4% of the cases the hits of one photon are split up into two clusters that both passed the tests to be compatible with a photon. The rates of more reconstructed photons are steadily decreasing. This shows that the correct assignment of calorimeter hits works well with the new photon reconstruction provided by PandoraPFA.

In figure 5.15 the average number of reconstructed photons N_{rec} per generated photon N_{gen} is shown as a function of the energy and the polar angle, together with the corresponding distributions from [1, 2]. It can be clearly seen that the overall level of photon splitting in the new data set is considerably lower. In both cases the splitting increases with photon energy but the average number of reconstructed photons for the highest energies is only 1.02 compared to 3.5. The values below 1 can be explained by the slightly reduced photon reconstruction efficiency at low energies (see figure 5.27 in [158]).

The angular dependence looks similar in both cases, but at a different overall scale. The spike around $\cos(\theta) = 0.75$ can be explained by the detector geometry: The angular range corresponds to the transition region of the ECAL barrel and

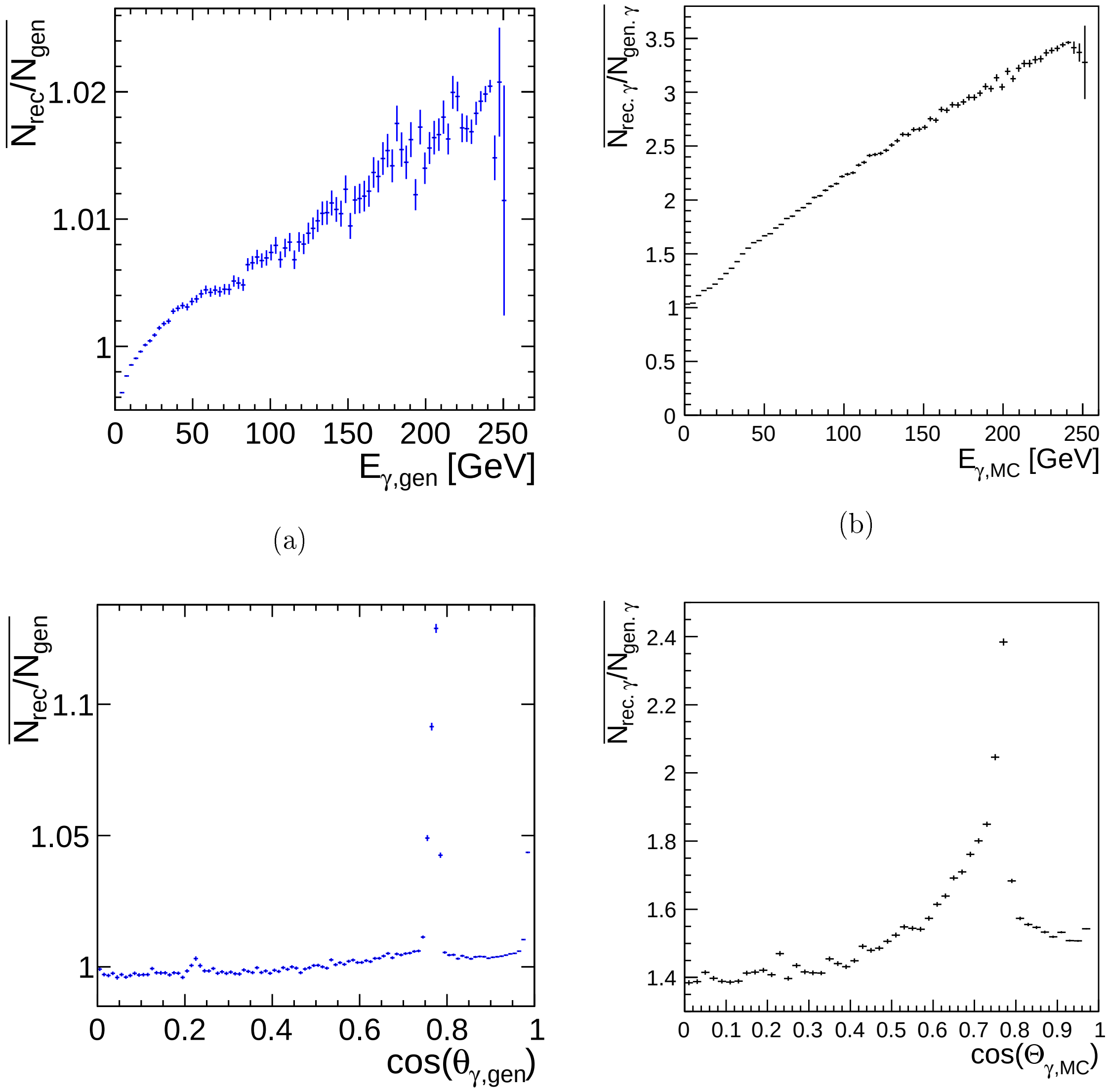

(a)

(b)

(c)

(d)

Figure 5.15: Number of reconstructed photons per generated photon as a function (a,b) of the energy and (c,d) $\cos(\theta)$ of the generated photon. The distributions on the left-hand side (a,c) are from this analysis which are compared to the case of [1,2] (b,d). Note the different vertical scales.

endcaps (see section 3.6.6). If a photon deposits energy in both components, the cluster algorithms often fail to merge the two parts of the cluster. With the new approach this peak is not only lower but also significantly narrower. At the largest values of $\cos(\theta)$ the distribution increases a second time, because of the issues at the transition of ECAL endcap and ring. Due to a cut of $\cos(\theta) < 0.98$ in the old sample, this region is only partially included in the right-hand figure. In [1,2] ratios close to 1 ($0.995 - 1.01$) could be obtained after the cluster merging procedure.

With the low level of photon splitting in the new data set the photon candidates from the reconstruction can be directly used in the analysis, as opposed to the procedure of cluster merging in the old approach.

5.5.2 Photon energy reconstruction

Prior to the event reconstruction the energy calibration of the calorimeters was performed centrally by the ILD collaboration with a dedicated procedure of the PandoraPFA package [167]. In several iterations the constants for the conversion of *SimCalorimeterHit* energy deposits into *CalorimeterHit*[v] and particle energies is determined using events containing single photons at an energy of 10 GeV. No energy dependence of this constant is taken into account.

The energy reconstruction and resolution is analysed with the distribution of reconstructed energy divided by generated energy for all photons generated in the matrix element. If several reconstructed photons are associated with an underlying photon by a truth link (i.e. if $\gamma_{\text{rec}}/\gamma_{\text{gen}} > 1$ in figure 5.14), the one with the highest transverse momentum is chosen.

In figure 5.16 the distribution for all events is shown and in figures 5.17, 5.18, 5.19 for different energy ranges and detector regions. The data is fitted with Gaussian distributions and the red lines on the graphs represent the fit ranges which are restricted to the region around the maximum where the data is well described by the fit function.

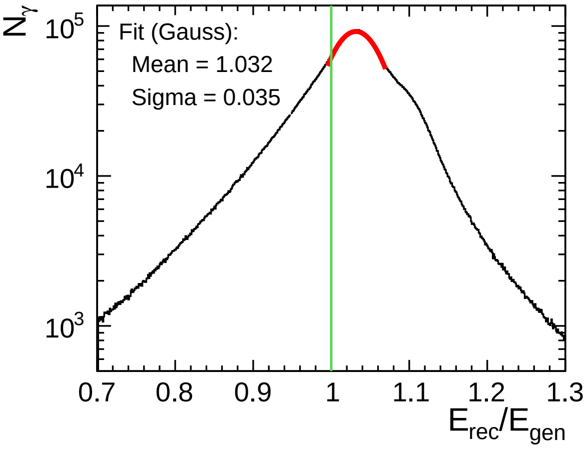

Figure 5.16: Reconstructed energy of the photon divided by the generated photon energy. A fit with a Gaussian distribution shows that the reconstructed energy is on average 3% too high. The uncertainty on the mean is $3 \cdot 10^{-5}$.

---

[v] which are classes of the LCIO event data model, see figure 4.1

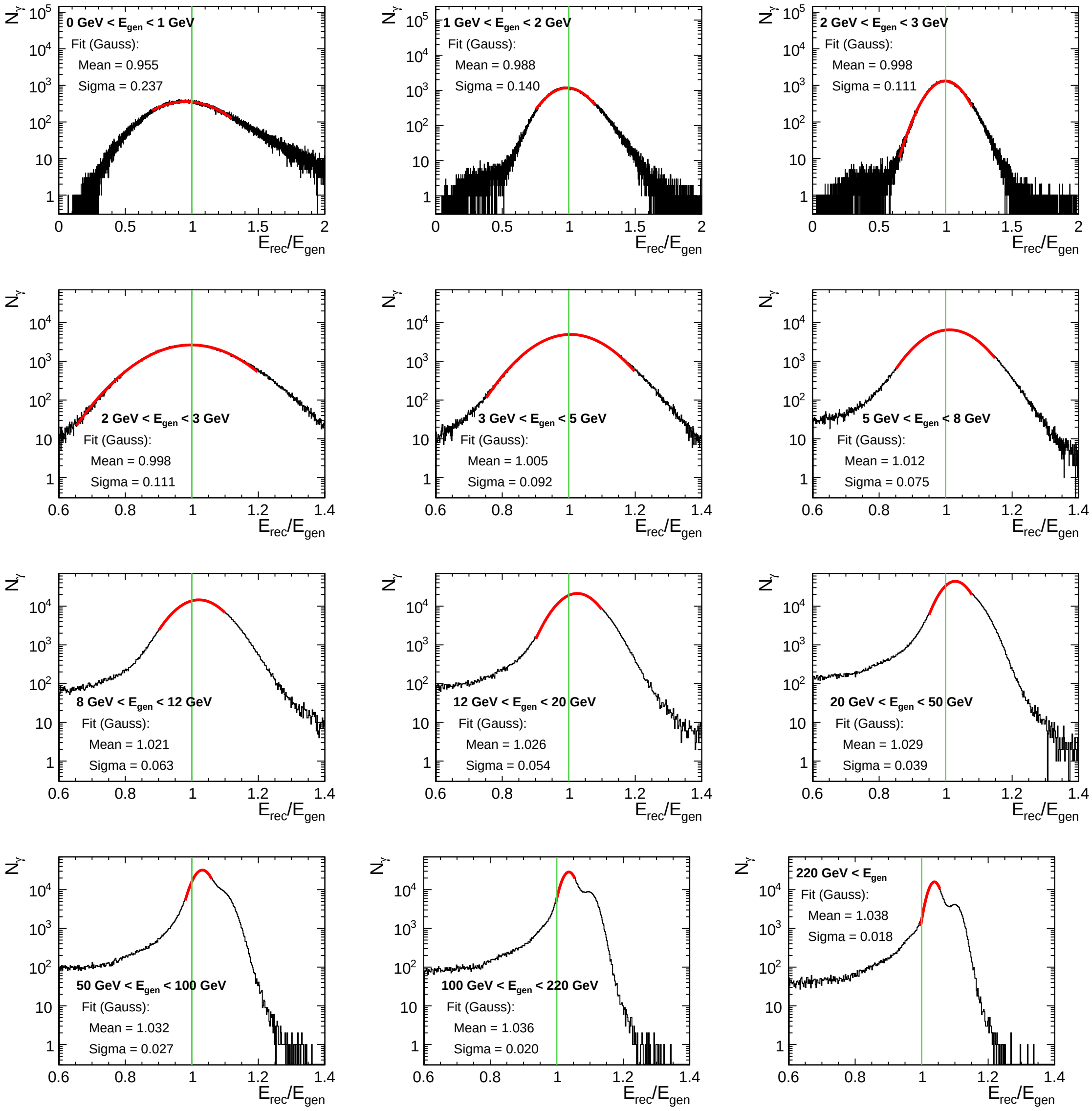

Figure 5.17: Reconstructed energy over generated energy for different generated energies. Note the shown range in the uppermost three graphs is larger.

As can be seen in figure 5.16 the mean reconstructed energy is 3% higher than the generated energy. In figure 5.17 the ratio of reconstructed and generated energy is depicted for different generated energy ranges. As expected from the general energy dependence of the energy resolution $\sigma_E \propto 1/\sqrt{E}$ (see also section 3.6.6), the distribution gets narrower for increasing energy. The width of the fitted Gaussian distributions (σ) approximately reproduces the test beam ECAL resolution of $16.53\%/\sqrt{E(GeV)} \oplus 1.07$ [136], e.g. for $E = 1.5\,\text{GeV}$ ($75\,\text{GeV}$) the test beam formula yields $\sigma = 0.145$ ($\sigma = 0.030$) and the fit result in the range $1\,\text{GeV} < E_{gen} < 2\,\text{GeV}$

(50 GeV< E_{gen} <100 GeV) is 0.140 (0.027).

The fitted mean values, however, show a significant deviation from 1, the expected value, and increase with rising energy. For low energies the reconstructed energy is a few per cent too low and at the highest energies the deviation to higher energies is almost 4%. It is notable that also the reconstructed energies around 10 GeV do not fit, even though 10 GeV photons were used for the energy calibration. The uncertainties on the mean are in the range 10^{-5} to 10^{-4} which shows that the Gaussian distribution describes the selected region well.

The energy reconstruction in the different ECAL components (barrel, endcaps and rings - see also section 3.6.6) is evaluated by looking at the corresponding polar angle ranges. In figure 5.18 the ratio of reconstructed and generated photon energy is shown for the barrel ($41.5° < \theta < 138.5°$), the transition region from barrel to endcap ($37.5° \leq \theta \leq 41.5°$ and $138.5° \leq \theta \leq 142.5°$) and for the endcap ($13° < \theta < 37.5°$ and $142.5° < \theta < 167°$).

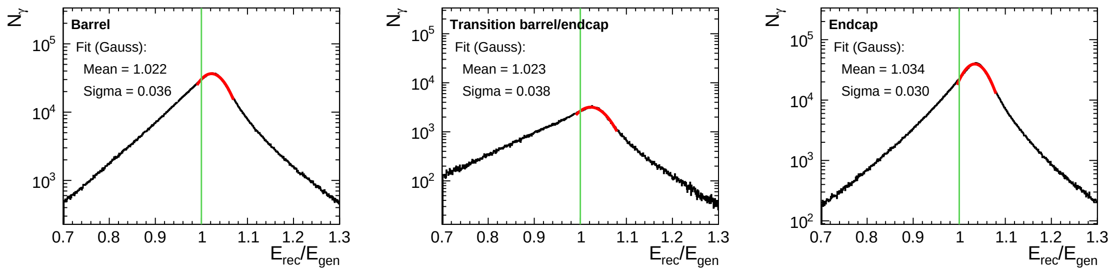

(a) (b) (c)

Figure 5.18: Reconstructed energy over generated energy of photons in the ECAL barrel (a), transition region from barrel to endcap (b) and in the endcap (c).

In all distributions the mean is larger than one. The mean in the endcap is larger and the width is smaller than in the barrel which can be explained by a larger fraction of high-energetic photons in the forward region (see figure 5.13 for the correlation of photon energy and polar angle). The complicated geometry in the transition regions makes the reconstruction more difficult, which is reflected in the larger width in figure 5.18b. Apart from the wrong energy scale, the reconstruction in barrel and endcaps is hence as expected. The photon reconstruction in the ECAL ring, however, suffers from deficits which are discussed in the following.

5.5.3 Reconstruction imperfections in the ECAL ring

In the very forward region several reconstruction imperfections can be identified. In figure 5.19 the ratio of reconstructed and generated photon energy is shown for the transition region from endcap to ring ($9° \leq \theta \leq 13°$ and $167° \leq \theta \leq 171°$) and the ring ($6° < \theta < 9°$ and $171° < \theta < 174°$). See figure 5.21a for a sketch of the ECAL forward region.

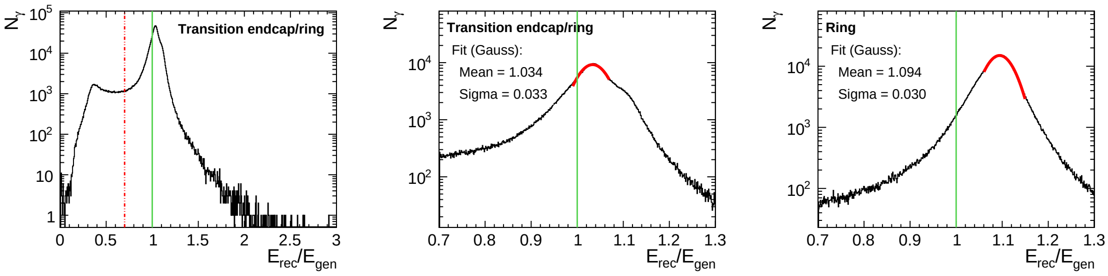

(a) (b) (c)

Figure 5.19: Reconstructed energy over generated energy of photons (a,b) in the transition region from ECAL endcap to ring and (c) in the ring. The events left of the red dashed line in (a) are further studied in figure 5.21.

Due to an insufficient calibration the average of the reconstructed energy is considerably too high (∼10%). As shown in figure 5.13 photons with higher energies mainly populate the forward region. As a consequence the distribution of the photons with the highest energies suffers most from this energy shift.

This can be clearly seen in figure 5.20, which shows a close-up of the highest energies of figure 5.8b. Due to the mis-calibration the photon energy distribution extends well above half the centre-of-mass energy of 250 GeV. The excess at photon energies corresponding to the radiative return to the Z boson is shifted to higher values than the expected value (241.68 GeV), which is indicated by the purple dashed line in figure 5.20. This is a consequence of the energy dependence of the photon energy response, which is not taken into account in the energy calibration (visible in figure 5.17), and the resulting shift in the average reconstructed energy by several per cent, as shown in figure 5.16. The additional feature of a shoulder around $110\% \times 241.68\,\text{GeV} = 266\,\text{GeV}$ is caused by the shift of ∼10% seen in the second peak in the distribution for the highest energies in figure 5.17 and more clearly isolated in figure 5.19c. Note that these events are discarded in the event selection because of the maximum photon energy cut (visualised by the red solid line in figure 5.20).

In the transition region from endcap to ring the distribution of reconstructed

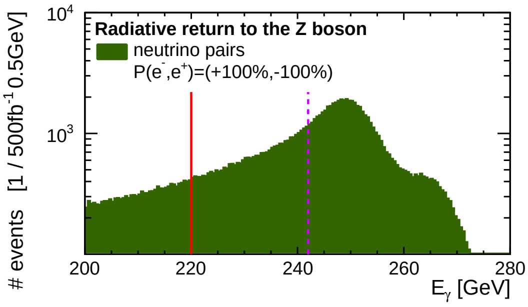

Figure 5.20: Energy distribution of the reconstructed signal-like photons around the peak corresponding to the radiative return to the Z boson. The peak is shifted to higher energies than the value calculated with equation 5.3, visualised by the dashed purple line.

over generated energy has a significant tail to lower entries, which is clearly visible in figure 5.19a. In order to better understand the origin of this reconstruction failure, the ϕ-dependence is looked at for polar angles of the transition region of endcap and ring ($9.3° < \theta < 12°$), shown in figure 5.21b, together with a control region in the endcap with $20° < \theta < 30°$ (figure 5.21c). The number of events with a reconstructed energy below 70% of the generated energy (indicated by the red dashed line in figure 5.19a) are divided by the total number of events in the angular region.

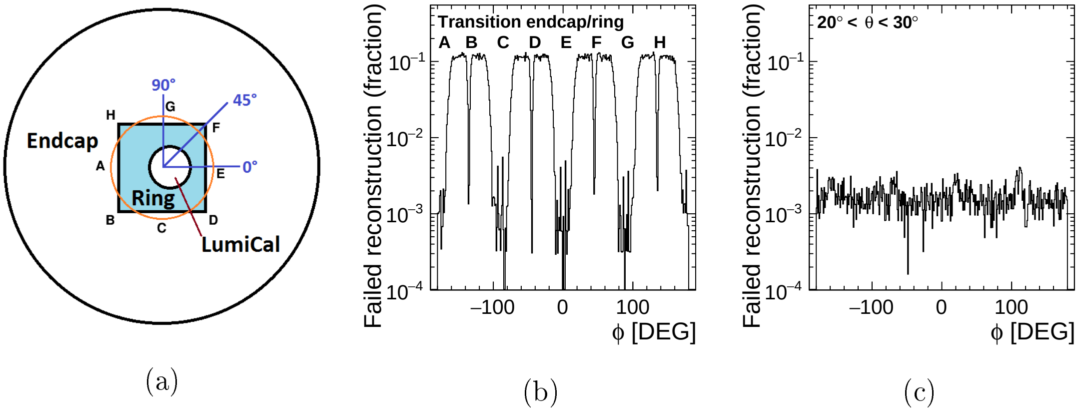

(a) (b) (c)

Figure 5.21: (a) Sketch of the ECAL ring in the centre of the endcap. (b) and (c) Number of events with a reconstructed energy below 70% of the generated energy as a function of ϕ for the polar angle ranges $9.3° < \theta < 12°$ (b) and $20° < \theta < 30°$ (c) divided by the total number of photons in the ϕ and θ bin.

The fraction of low reconstructed energies around azimuthal angles of $\phi = 0°$, 45°, 90°, 135°, 180°, 225°, 270° and 315° is at a similar level as in the control region. The distinct pattern in the transition region can be explained by the square shape of this transition region and the annular shape of the region looked at (indicated by the orange circle in figure 5.21a). At $\phi = 0°$, 90°, 180° and 270° (45°, 135°, 225° and 315°) the cluster is fully contained in the endcap (ring) and the reconstruction algorithm works normally and the fraction of failed reconstruction is at the per mille level, i.e. the same as in the control region (figure 5.21c). In the ϕ ranges in between these values the level of wrongly reconstructed photon rises by two orders of magnitude to $\sim$10%. Here, the cluster is split over the two ECAL components which is likely to lead to the observed excess at low values in figure 5.19a.

5.5.4 Conclusions for the WIMP study

In order to evaluate the quality at the presented detail, large statistics are needed in all the investigated ranges of parameters. Therefore the reconstruction imperfections could only be discovered with the final data samples, i.e. when it was too late to correct the energy calibration in the event production. The ECAL was calibrated assuming a linear energy response, which turns out to be an oversimplification. With a re-calibration of the digitiser with parameters of a non-linear response the observed energy shifts could be eliminated in future productions. In an updated reconstruction version (ILCSoft v02-00) the wrong calibration of the ECAL ring has been fixed.

For the WIMP study the reconstructed photons are used without compensating for the reconstruction deficits. The next step is the event selection, described in chapter 6. In order to evaluate the impact of reconstruction imperfections the event selection is re-done using information on the events from the generator level, hence from before the detector simulation and the photon distributions are compared to the selected events from the full reconstruction (see section 6.2). With these events the sensitivity calculation is repeated (see section 7.3.2). The limits are very close to the ones from the full reconstruction, which shows that the influence of the reconstruction deficits can be neglected.

Chapter 6

Selection of Events

In this chapter the event selection is described and the efficiencies to suppress the background are presented. In section 6.1 solely information of the reconstructed events is used, which means, this is closest to an analysis with real data. At the end of this chapter (section 6.2) the impact of the shortcomings in the photon reconstruction (see section 5.5) is evaluated by using information from the generator level for the photon energy and polar angle.

6.1 Event selection in the full reconstruction

The signature of a WIMP event is a photon in an “empty” detector. The two characteristics of this signature are addressed in different ways. The first part is the signal definition, a number of cuts a reconstructed photon has to fulfill (see section 5.3.1). This chapter is about the second part of the event selection, the requirement of low detector activity, which can be addressed after the detector simulation and event reconstruction where overlay and noise are modelled. Because of these effects a certain activity in the detector has to be allowed.

Signal-like events with only little detector activity besides the photon are selected by requiring the following three criteria: There must be no charged particles with large transverse momenta (see section 6.1.1), the visible energy in the detector has to be small (see section 6.1.2) and finally, there must be no electrons and positrons detected in the forward region or, more technically speaking, no clusters may be reconstructed in the forward detector BeamCal (see section 6.1.3). The efficiencies to select the two considered kinds of background events, neutrino pair production and Bhabha scattering, will be shown in tables 6.2 and 6.3 in section 6.1.4.

6.1.1 Suppression of events with charged particles

A mono-photon WIMP event does not contain charged particles. Hence, selecting events with no charged particles would be a strong veto against many Standard Model processes, like Bhabha scattering. On the other hand, signal events have to be kept if they are overlaid with charged hadrons from beam-induced photon-photon interactions (see section 3.5.3.2).

In figure 6.1 the transverse momentum distribution of reconstructed electrons and positrons and in figure 6.2 of all other charged particles in signal-like events is shown. As visible in the left-hand graphs the distribution has a tail to values around half the centre-of-mass energy (250 GeV). The right-hand graphs show a zoom on the lowest values, where most of the charged particles are located. Over the full range there are more high-energetic charged particles in the Bhabha scattering events. In the case of neutrino pair production the distributions also fall off more steeply. This contrary pattern for the two types of background makes the transverse momentum cuts suitable criteria to suppress the reducible background.

In the lower graphs, the origin of the charged particles is visualised. With the help of the MC truth link, three categories are formed: particles that originate from overlay, daughter particles of a matrix element photon (i.e. photons which converted into a pair of charged particles) and the remaining particles.

The distributions show a clear separation in energy depending on the origin in both cases, electrons (figure 6.1a) and other charged particles (figure 6.2a). Whereas the low energetic particles mainly come from overlay, the other two categories dominate at higher energies. At the transition between the two domains a kink in the distribution is visible at around 5 GeV, the end of the overlay distribution.

A second kink around 8 GeV is visible in the case of charged particles in figure 6.2b. The additional contribution below 8 GeV are mis-identified electrons reconstructed in the forward detector LHCal, for which all reconstructed clusters are categorised as hadrons. The peaks around 40 and 150 GeV in figure 6.2c also stem from mis-identified electrons hitting the detector at the transitions of barrel and endcaps.

The minimum p_T cuts have to be chosen such that a large fraction of reducible background is rejected, while most neutrino events are kept. As the distribution of overlay particles falls off sharply around 5 GeV, this value was first tested as the maximum transverse momentum. But lower cuts were found to be beneficial. With $p_{T,max} = 5\,\text{GeV}$ more neutrino events could be kept, but the higher rate of Bhabha

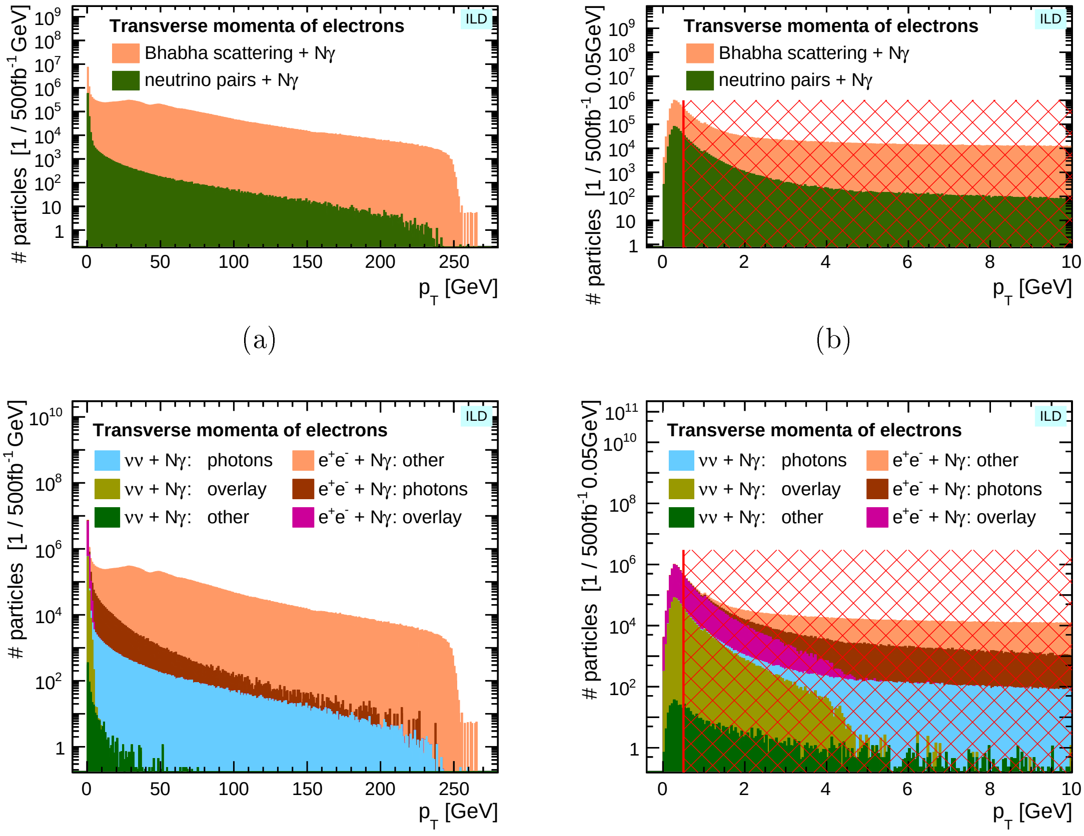

(a) (b)

(c) (d)

Figure 6.1: Distribution of the transverse momentum of electrons and positrons in events that fulfill the signal definition. In (b,d) a zoom of the peak region at low p_T is shown. In (c,d) the type of true underlying particles on generator level is visualised. Events with a transverse momentum of an electron or positron above 0.5 GeV, i.e. right of the red lines, are discarded.

scattering events could not be recovered by the other cuts. Thus, 3 GeV is chosen as the maximum p_T of charged particles, indicated by the red lines in figure 6.2.

In figure 6.1d it can be seen, that a fraction of the hadrons from the overlay are mis-identified as electrons, hence also electrons have to be allowed in a WIMP event. As only a small fraction of overlay particles are reconstructed as electrons a lower threshold of $p_{T,max} = 0.5\,\text{GeV}$ is applied, which is beneficial to suppress Bhabha scattering events.

At higher energies the dominating contribution in neutrino events are pairs of particles created from a photon. In the case of Bhabha scattering the situation is clearly completely different: the outgoing electrons and positrons dominate the

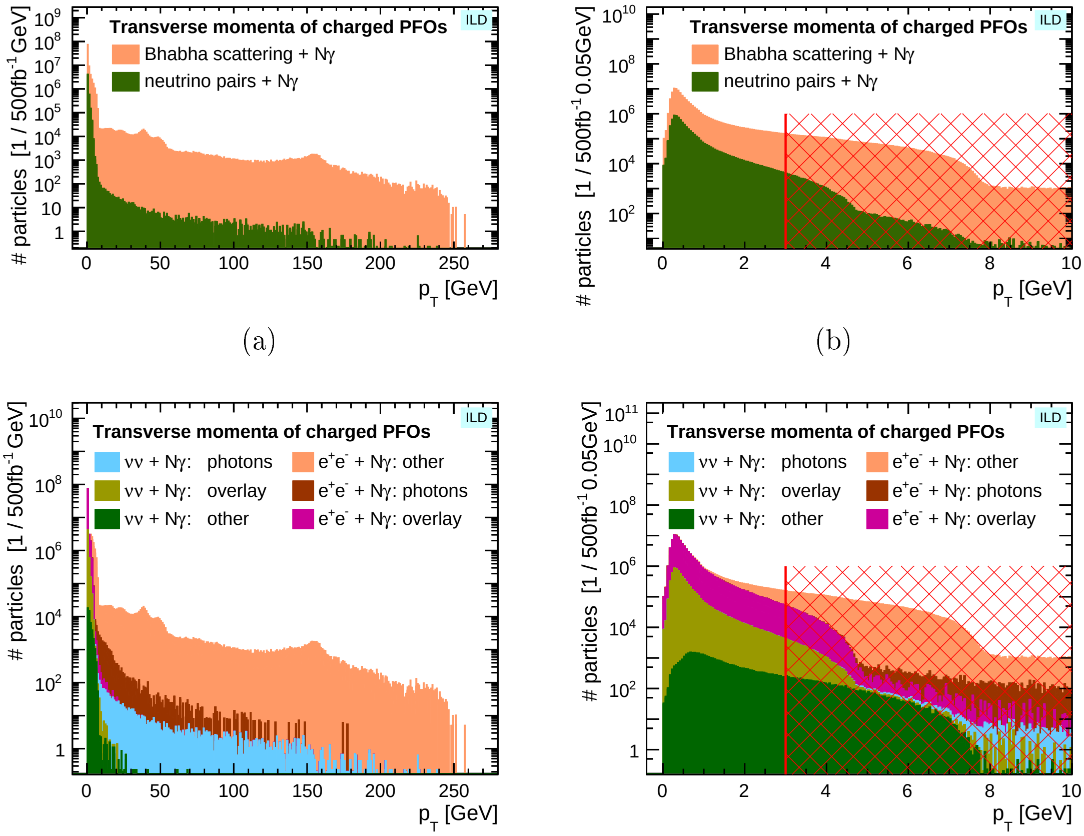

(a) (b)

(c) (d)

Figure 6.2: Distribution of the transverse momentum of all other charged particles in events that fulfill the signal definition. (c,d) Visualisation of the type of underlying particles on generator level. Events with a charged p_T above 3 GeV, i.e. right of the red lines, are discarded.

distribution in figure 6.1 and due to electrons mis-identified as hadrons also in figure 6.2. As a consequence of this contrast, these cuts reject more than half of the Bhabha scattering events, whereas only a few per cent of the neutrino events are lost.

6.1.2 Small visible energy

After testing the transverse momentum of charged particles, in the next step the energy sum of charged *and* neutral particles (without the signal photon) is considered in the surviving events. Here, all particles reconstructed with PandoraPFA (see section 4.6.1) are considered, i.e. `Particle Flow Objects` (`PFOs`). The reconstructed objects in the forward detector BeamCal are treated separately in the following step (see section 6.1.3).

In figure 6.3 the energy distributions for the different particle types of `PFOs` are shown[i]. With the help of the MC truth link particles originating from overlay are identified. In the case of photons (figure 6.3a) mis-identified electrons are drawn as a separate category.

Due to the previous cuts on the transverse momentum of charged particles, the energy range of the remaining electrons, muons and pions is restricted to lower values and originate from overlay. Compared to the neutrino background the Bhabha scattering events contain large numbers of photons and neutrons, especially at higher values.

The neutrons (figure 6.3e), stemming mainly from photonuclear reactions, i.e. an interaction of photons with nuclei of the detector material, approximately follow the signal photon spectrum, including energies corresponding to the radiative return to the Z boson, because the maximum energy cut of the signal definition cleary has no effect on photons converted into neutrons. In the neutron distribution from Bhabha scattering events a drop around 80-100 GeV can be seen. Its origin is not understood, but the effect on the WIMP study is assumed to be negligible.

The photon distribution (figure 6.3a) of the neutrino events is similar to the signal photon distribution, but values above the maximum energy cut are possible for the additional photons. At high energies the photon distribution in the Bhabha scattering events is dominated by mis-identified electrons hitting the detector in the forward region, where no tracking is instrumented. They extend to higher values with a rather sharp cut-off around 275 GeV, which can be explained by underlying leptons at half the centre-of-mass energy in the ECAL ring where the reconstructed energy is $\sim$10% too high (see section 5.5.3). Due to the low polar angle they are not the photon with the highest transverse momentum in the event and are thus not selected in the signal definition.

Analogously to the p_T cuts the thresholds of allowed visible energy have to be low enough to reject Standard Model background and the higher they are the more overlay is allowed and hence more signal events are kept. One criterion to keep a high number of signal events is that only particles with an energy above 5 GeV are considered, because very soft particles are likely to stem from processes which can also occur in signal events, like the overlay of beam-induced background as shown in figure 6.3.

For the energy sum, two categories of particle types are treated differently. The

---

[i] See section 4.6.1 for an overview of all possible reconstructed particles types.

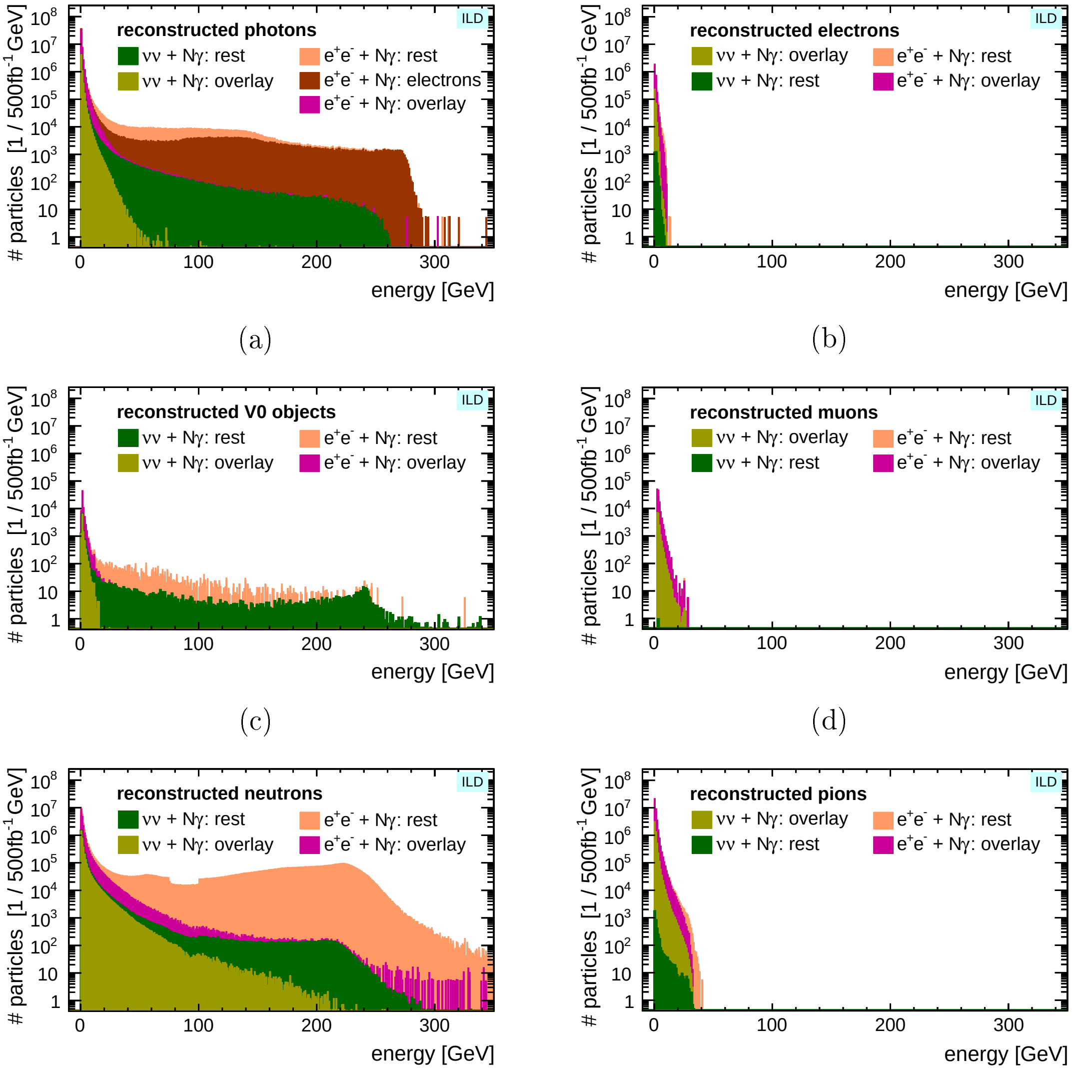

(a)

(b)

(c)

(d)

(e)

(f)

Figure 6.3: Energy distribution of different particle types in the remaining events after the p_T cuts.

energy sum of all particles, excluding the signal-like photon, has to be below 30 GeV. In order to allow higher energies of the low-p_T overlay, reconstructed hadrons (pions and neutrons) are not considered in the third criterion: The energy sum of all photons, electrons, muons and vertex finder objects[ii] has to be below 10 GeV. The criteria are summarised in table 6.1.

In figure 6.4 the energy sum of all `PFOs` (including soft particles) is shown. When applying the threshold of 5 GeV the distribution looks similar (as shown in

---

[ii] As only a fraction of the V0 objects stem from hadrons, they are not categorised as hadrons.

minimum energy of individual particles	5 GeV
maximum energy of sum of particles, all particles types	30 GeV
maximum energy of sum of particles, excluding pions and neutrons	10 GeV

Table 6.1: Criteria for the visible energy cut.

figure 6.5a), but in a test with different minimum `PFO` energies, it could be shown that a larger number of signal-like neutrinos can be kept with the threshold of 5 GeV, while the additional remaining Bhabha scattering events are rejected in the following cuts.

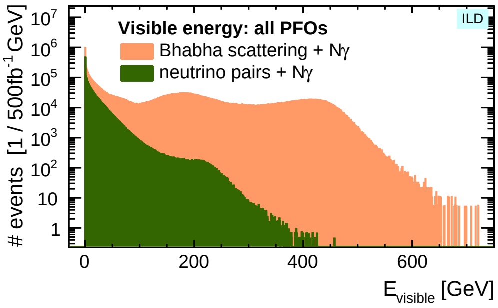

Figure 6.4: Sum of the energies of all `PFOs` in the event, without the signal photon. Events remaining after the p_T criterion are considered.

The visible energy distributions, shown in figures 6.4 and 6.5a, have higher values for the Bhabha scattering background than for the neutrino events, which is also expected from the distributions in figure 6.3. Around 200 GeV the features of the neutron distribution (figure 6.3e) are visible in the visible energy distribution of the neutrino events. In the case of Bhabha scattering there are two moderate peaks, below 200 GeV and above 400 GeV. The peak at lower energies stems from the distribution of several `PFOs` and the one at higher energies corresponds to events where almost the whole centre-of-mass energy is detected, for which a possible combination is one electron mis-identified as photon and a real photon mis-identified as neutron. The tail towards values clearly above 500 GeV can be explained by an additional contribution of overlay.

Without the energies of neutrons and pions the shape and level of the distribution look different (see figure 6.5b). Without the neutrons the plateau in the neutrino distribution is lower and corresponds approximately to the height of the photon distribution (figure 6.3a), with a sharper edge due to the peak of the V0 energies.

As shown in figure 6.5, the visible energy can be sizeable, also in the case of neutrino pair production, mainly because of the additional ISR photons. In table 6.3 it can be clearly seen that this cut suppresses more and more events with increasing number of photons, for both the neutrinos and Bhabha scattering.

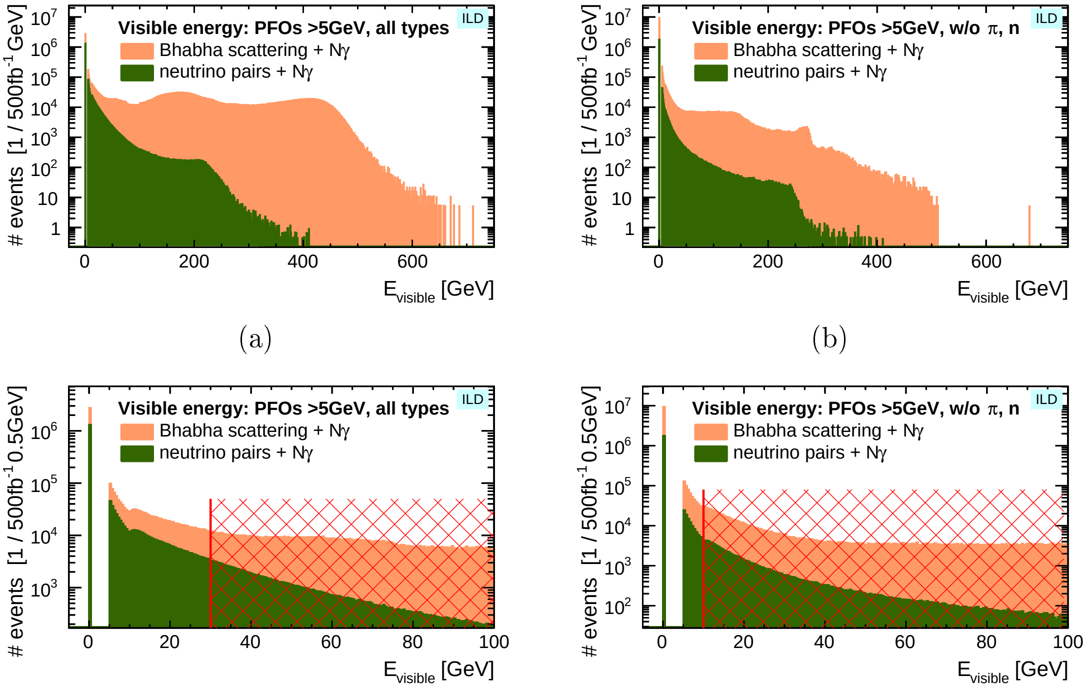

(a)

(b)

(c)

(d)

Figure 6.5: Sum of the energies of all `PFOs` above 5 GeV. (a,c) all particle types, (b,d) without reconstructed neutrons and pions. (c,d) When zooming into the low energy region the fraction of events with no `PFOs` contributing to the visible energy can be seen at $E_{visible} = 0\,\text{GeV}$.

After applying these criteria, only a quarter of the Bhabha scattering events remain. With this cut more neutrino events are rejected than in the first step of the selection, but still only a few per cent are lost.

6.1.3 No electrons in the forward region

The forward detector BeamCal (see section 3.6.5) plays a central role to suppress Bhabha scattering events. Because of the contamination with beam-induced background (see section 3.5.3.1), a high level of activity in BeamCal is allowed without reconstructing a particle. Therefore it is treated separately and energy depositions in BeamCal are not considered in the previous step of a maximum additional visible energy.

In figure 6.6 the number of clusters which passed the criteria of the BeamCal reconstruction (see section 4.6.2) is visualised. The two background types show a very distinct pattern. 98% of neutrino pair events are without a BeamCal cluster, whereas 97% of Bhabha scattering events contain one or more. The neutrino events with only one photon in the matrix element are drawn separately to visualise the fraction of *fakes*, i.e. BeamCal clusters which stem from the overlay and not from a single high-energetic particle from the hard interaction. Only 0.5% of the events with a single photon contain one BeamCal cluster and the number of events is rapidly decreasing with increasing number of clusters. For the neutrino events with more than one photon the fraction of events with BeamCal clusters is higher. This shows the effect of the additional photons in the events, which can hit BeamCal.

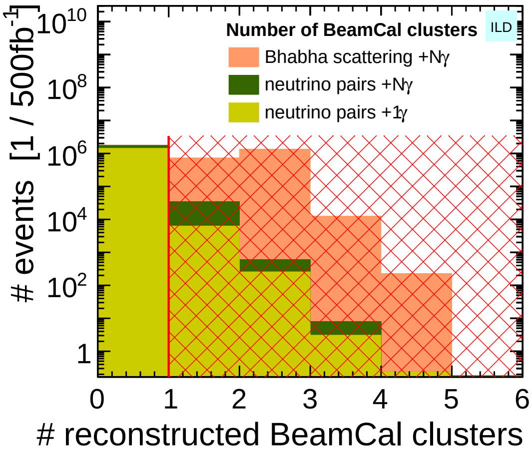

Figure 6.6: Number of clusters in BeamCal per event after the visible energy cuts. All events with non-zero clusters are rejected.

As discussed in section 4.6.2, the BeamCal reconstruction processor is tuned for high energetic electrons. As can be seen in figure 6.6, the vast majority of Bhabha scattering events contain BeamCal clusters, which confirms with Monte Carlo data of complete physics events that the tuning of the BeamCalClusterReco parameters (presented in section 4.6.2.3) was successful.

The clear distinction of reducible and irreducible background in the cluster distribution, allow for a simple criterion: Events with one or more BeamCal clusters are discarded. This leads to a significant suppression of the Bhabha background. On the other hand, the fake rates are small and lead to very little loss of neutrino events with one ISR photon (see table 6.3). The effect of the additional photons, which may also hit BeamCal and lead to a reconstructed BeamCal cluster, is reflected in the decreasing efficiency with increasing number of photons in the event.

		signal definition	low p_T of charged	low visible energy	BeamCal veto
neutrino pair production	$\mathbf{P_{e^-} = 0\%, P_{e^+} = 0\%}$				
	number of events	4534.1	3987.6	3565.4	3494.9
	selection efficiency		87.95%	78.64%	77.08%
	$\mathbf{P_{e^-} = -80\%, P_{e^+} = -30\%}$				
	number of events	5516.1	4856.1	4358.4	4279.7
	selection efficiency		88.04%	79.01%	77.58%
	$\mathbf{P_{e^-} = -80\%, P_{e^+} = +30\%}$				
	number of events	10176.8	8960.9	8048.2	7905.5
	selection efficiency		88.05%	79.08%	77.68%
	$\mathbf{P_{e^-} = +80\%, P_{e^+} = -30\%}$				
	number of events	1067.7	928.4	794.1	762.0
	selection efficiency		86.95%	74.37%	71.36%
	$\mathbf{P_{e^-} = +80\%, P_{e^+} = +30\%}$				
	number of events	1375.7	1205.0	1061.1	1032.6
	selection efficiency		87.59%	77.13%	75.06%
Bhabha scattering	$\mathbf{P_{e^-} = 0\%, P_{e^+} = 0\%}$				
	number of events	50508.2	19646.6	4260.7	113.3
	selection efficiency		38.90%	8.44%	0.22%
	$\mathbf{P_{e^-} = -80\%, P_{e^+} = -30\%}$				
	number of events	49388.8	19561.3	4259.8	113.7
	selection efficiency		39.61%	8.63%	0.23%
	$\mathbf{P_{e^-} = -80\%, P_{e^+} = +30\%}$				
	number of events	50873.1	19648.8	4260.6	112.9
	selection efficiency		38.62%	8.37%	0.22%
	$\mathbf{P_{e^-} = +80\%, P_{e^+} = -30\%}$				
	number of events	50802.9	19683.3	4261.1	113.4
	selection efficiency		38.74%	8.39%	0.22%
	$\mathbf{P_{e^-} = +80\%, P_{e^+} = +30\%}$				
	number of events	50967.8	19693.1	4261.2	113.3
	selection efficiency		38.64%	8.36%	0.22%

Table 6.2: Number of events per fb^{-1} and selection efficiencies in per cent for the signal definition and the three selection criteria with different polarisation configurations: no beam polarisation and all combinations for $|P_{e^-}| = 80\%$ and $|P_{e^+}| = 30\%$.

6.1.4 Selection efficiencies

In tables 6.2 and 6.3 event numbers corresponding to an integrated luminosity of $1\,\mathrm{fb}^{-1}$ before and after the individual steps of event selection are listed and the efficiencies are given in per cent with respect to the number of events fulfilling the signal definition. In table 6.2 the selection efficiencies are presented for unpolarised beams and all four polarisation combinations with $|P(e^-)| = 80\%$ and $|P(e^+)| =$

		signal definition	low p_T of charged	low visible energy	BeamCal veto
neutrino pair production	$\nu\bar{\nu}\gamma$				
	number of events	3607.9	3189.3	2999.4	2985.7
	selection efficiency		88.40%	83.13%	82.75%
	sel. eff., previously [1, 2]		97.68%	91.60%	89.83%
	$\nu\bar{\nu}\gamma\gamma$				
	number of events	823.8	711.8	519.1	470.5
	selection efficiency		86.40%	63.01%	57.11%
	sel. eff., previously [1, 2]		94.52%	69.28%	66.37%
	$\nu\bar{\nu}\gamma\gamma\gamma$				
	number of events	95.2	80.5	44.3	36.6
	selection efficiency		84.57%	46.54%	38.44%
	sel. eff., previously [1, 2]		92.13%	46.54%	43.50%
	$\nu\bar{\nu}\gamma\gamma\gamma\gamma$				
	number of events	7.3	6.1	2.4	1.8
	selection efficiency		82.41%	33.21%	25.01%
Bhabha scattering	$e^+e^-\gamma$				
	number of events	44519.1	18261.1	4138.8	110.8
	selection efficiency		41.02%	9.30%	0.25%
	sel. eff., previously [1, 2]		21.10%	15.99%	0.29%
	$e^+e^-\gamma\gamma$				
	number of events	5602.7	1333.4	119.5	2.5
	selection efficiency		23.80%	2.13%	0.05%
	$e^+e^-\gamma\gamma\gamma$				
	number of events	386.7	52.0	2.1	0.0
	selection efficiency		13.45%	0.55%	0.003%

Table 6.3: Number of events per fb^{-1} and selection efficiencies in per cent for different numbers of photons in the matrix element. The efficiencies are compared to the previous full simulation [1, 2]. All numbers are for unpolarised beams.

30%, and in table 6.3 for different numbers of matrix element photons in the process.

The most important result is that the suppression of the Bhabha background is two orders of magnitude larger than for neutrino pair production. Whereas the events after applying the signal definition are dominated by Bhabha scattering, the largest fraction of selected events are neutrino events. Even for right-handed electrons and left-handed positrons the number of neutrino events is more than six times higher than the selected Bhabha scattering events. This means that the event selection is very efficient: most signal-like neutrino events are kept and the reducible Bhabha background is heavily suppressed.

As shown in table 6.2, the selection efficiency of the Bhabha scattering events is almost independent of the polarisation. In the case of the neutrino data sets a polarisation dependence at the per cent level can be seen. The larger the share of right-handed electrons and left-handed positrons, the lower the efficiencies. For right-handed electrons and left-handed positrons the s-channel production has a larger contribution and the radiative return to the Z boson is more pronounced (see figure 5.8b on page 93), which means that the photons tend to have a higher energy. As the photons contribute to the visible energy, it is hence more often above the thresholds defined in the cut (sec section 6.1.2). Neutrons, which are produced in a photonuclear reaction, also lead to more events being discarded by the visible energy cuts. The distribution of electrons and positrons from pair creation are at higher energies as well and hence more events are rejected in the first step event selection, where events are tested for charged particles (see section 6.1.1). These photon products and the additional photons can also hit BeamCal and may lead to a reconstructed cluster, which is reflected in the lower efficiency also in the last step.

The main conclusion from the efficiencies in table 6.3 is that the number of discarded events increases with the number of matrix element photons. In events with several photons the additional photons (or particles stemming from interaction with the photons) may hit BeamCal or a different part of the detector. Therefore the efficiencies in all three selection steps decrease with increasing number of photons.

The effect of a larger suppression with increasing photon number is more pronounced in the case of Bhabha scattering compared to neutrino pair production. In the case of neutrinos the efficiencies of the visible energy cut and the BeamCal veto have the largest dependence on the photon number. Only if the additional photons convert into electron-positron pairs, they can increase the number of events rejected by the first cut. In the case of Bhabha scattering the additional photons can lead to a larger momentum transfer on the outgoing leptons, which are thus more likely to be detected. Depending on the kinematics this can cause a rejection in any of the three steps, which leads to the observed strong dependence of all selection efficiencies on the photon number.

The comparison of the selection efficiencies to the previous full simulation [1, 2] is addressed in section 6.1.7.

6.1.5 Photon observables after applying the signal definition

The effect of the individual steps on the photon observables is shown in figures 6.7, 6.8 and 6.9, where the photon energy, transverse momentum and polar angle distribu-

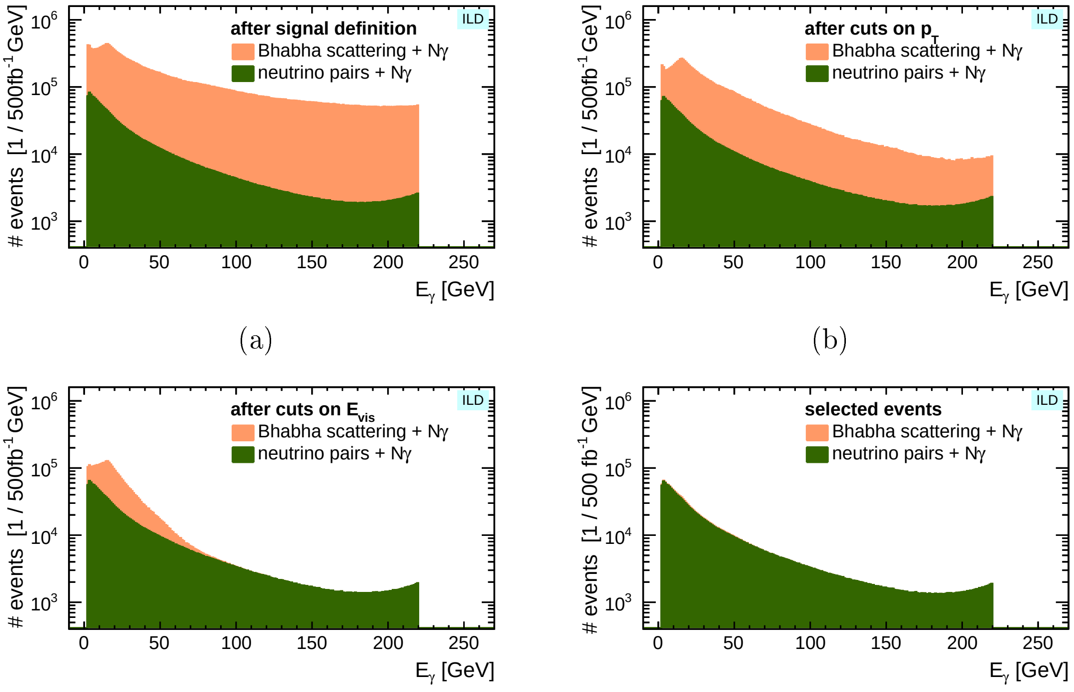

(a) (b) (c) (d)

Figure 6.7: Photon energy distribution (a) after the signal definition, (b) after the p_T cuts, (c) after the visible energy criteria and (d) after the BeamCal veto (final selection). The events correspond to 500 fb^{-1} for unpolarised beams.

tion, respectively, are depicted before and after the inividual steps. The shown photons are the ones with the highest transverse momentum in the event, i.e. the signal photons. The shown data corresponds to an integrated luminosity of 500 fb^{-1} for unpolarised beams.

The photons, shown in the top left graphs, fullfill the signal definition, as described in section 5.3.1. The observables of these signal-like photons are distributed as expected from the ISR phase space distribution depicted in figure 5.13 on page 106. The number of photons rises for low energy and transverse momentum as well as towards forward angles. At highest energies the rise towards the radiative return to the Z boson is visible in figure 6.7a. The peak around $E_\gamma = 15\,\mathrm{GeV}$ in the Bhabha scattering distribution is addressed in section 6.1.6.2.

The fraction of the produced events (shown in table 5.4 on page 104) fulfilling the signal definition varies from process to process. 62% of the produced neutrino events with left-handed electron and right-handed positron survive the cuts of the signal definition. In the neutrino data set with opposite beam polarisation a large fraction of the photons have energies around the radiative return to the Z boson, which are

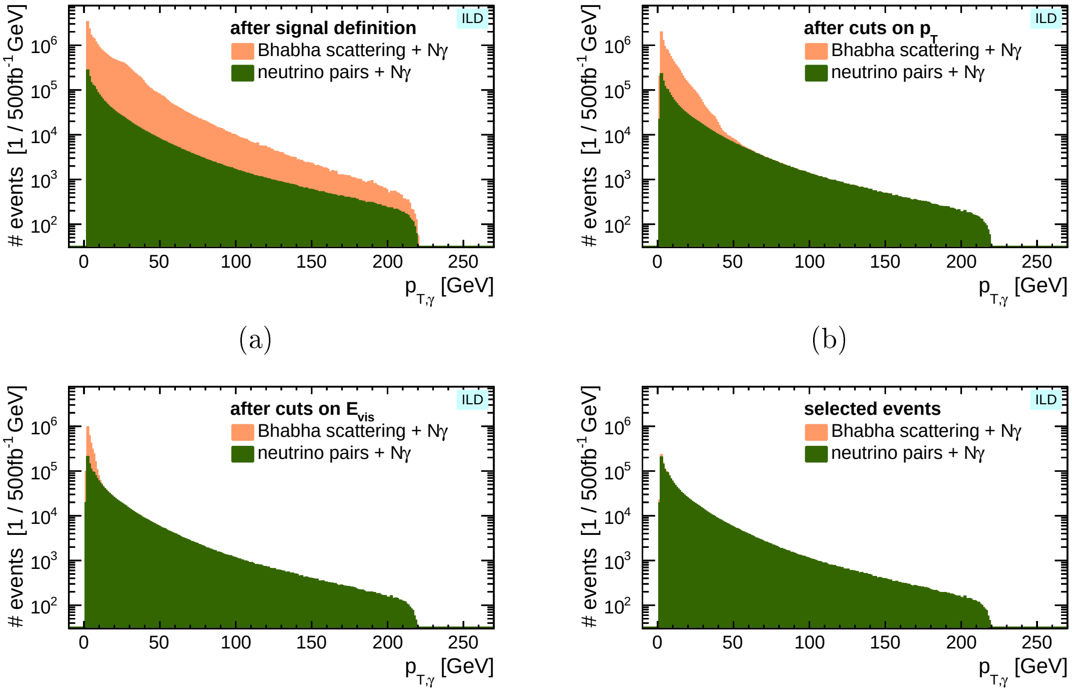

(a)

(b)

(c)

(d)

Figure 6.8: Distribution of photon transverse momentum in BeamCal coordinates, (a) after the signal definition, (b) after the p_T cuts, (c) after the visible energy criteria and (d) after the BeamCal veto (final selection).

higher than the maximum energy cut and the events are hence discarded. Here, only 41% of the produced events are signal-like. The fraction of Bhabha scattering events is at a similar level (38-40%). This means that the event selection can be tested with around 10 million unweighted neutrino events and almost 5 million Bhabha scattering events.

As can be seen in the polar angle distributions (figure 6.9), the increase in the forward regions is steeper in the case of Bhabha scattering. This different dependence on the polar angle of the cross-sections of the two background processes is also the main reason for the lower fraction of signal-like events in the Bhabha scattering data sets.

In the polar angle distribution small excesses around the transition from endcap to barrel (∼40°) are visible, which reflects the excess of reconstructed photons in those regions (see figure 5.15 on page 108). The steps in the distribution at lowest angles (shown in figure 6.10a) can be explained by the reconstruction failures in the ECAL rings and the transitions from the endcaps to the rings. The structures in these transition regions are more pronounced in the case of Bhabha scattering,

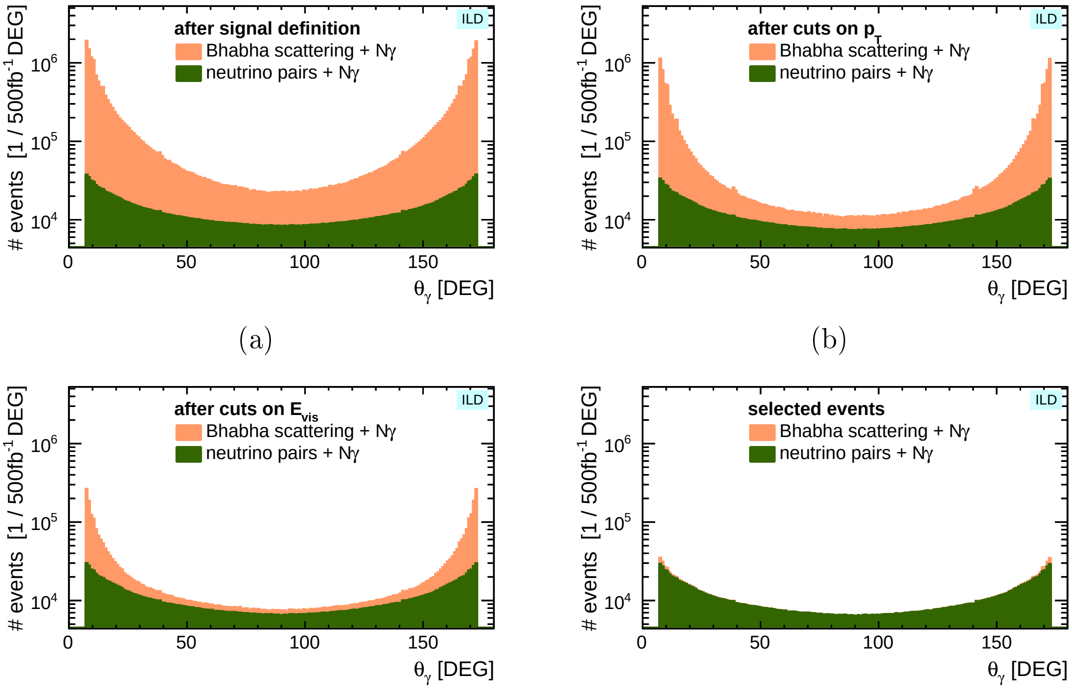

(a) (b) (c) (d)

Figure 6.9: Photon polar angle distribution (a) after the signal definition, (b) after the p_T cuts, (c) after the visible energy criteria and (d) after the BeamCal veto (final selection).

because they have a larger share of photons with higher energies and (as shown in figure 5.13 on page 106) high energetic photons are mainly in the critical forward region.

In figure 6.10b the low end of the energy distribution is shown. The smooth edge above the minimum energy cut of 2 GeV can be explained by the minimum transverse momentum cut in the signal definition which counteracts the increase of the cross-section for ISR photons towards lower energies.

The transverse momentum continues to rise to its minimum value of 1.92 GeV with an almost sharp edge (see figure 6.10c). Here, the minimum energy condition leads only to a small decrease below 2 GeV. The shown transverse momenta are in BeamCal coordinates (see section 3.6.3) which means that photons flying in the positive x-direction can have a $p_{T,BCal}$ below the minimum energy measured in ILD coordinates.

Due to the different values for different azimuthal ranges, a step at the second minimum transverse momentum cut of 5.65 GeV can be seen. In the energy distribution this can only be seen as a very small feature in the neutrino distribution.

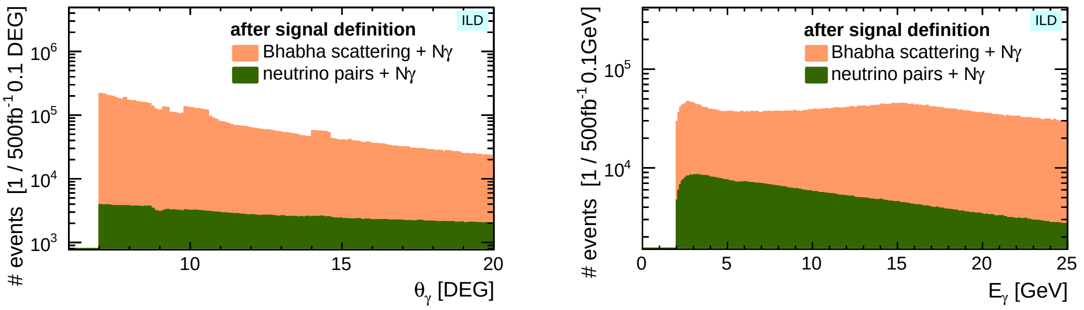

(a) Photon polar angle

(b) Photon energy

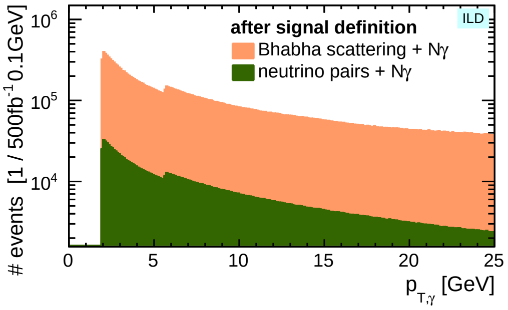

(c) Photon transverse momentum

Figure 6.10: The low end of the photon observables (a) polar angle, (b) energy and (c) transverse momentum after the signal definition.

6.1.6 Phase space of the Bhabha scattering background

The revised setup of the Bhabha scattering generation is evaluated in more detail in section 6.1.6.1 by looking at the phase space of the remaining Bhabha scattering events. The origin of the peak around 15 GeV in the energy distribution of the photon is evaluated in section 6.1.6.2 and an alternative event generation setup is discussed in section 6.1.6.3.

6.1.6.1 Bhabha scattering suppression

In figure 6.11 the effect of the different cuts on the transverse momentum distribution of the photons in Bhabha scattering events is visualised. After the p_T cuts, the number of events at higher values are suppressed by several orders of magnitude, whereas the effect at lowest values is smaller. The visible energy criteria suppress all events above $p_{T,\gamma} = 50\,\text{GeV}$ and the BeamCal veto leads to a suppression in the whole remaining range. As discussed in section 5.3.2.2 (case III) the number of generated leptons with a substantial p_T is reduced by the cut $M_{inv,e^{+/-}_{out},\gamma_i} > 4\,\text{GeV}$, i.e. with real data more events would be signal-like but then discarded by the p_T cuts.

With a higher photon transverse momentum also the transverse momentum of

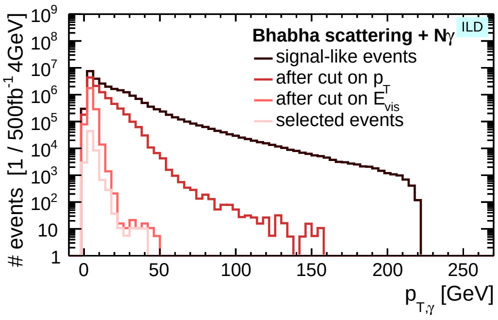

Figure 6.11: Transverse momentum of the photons from Bhabha scattering in BeamCal coordinates before and after the different cuts.

the lepton system has to be higher, which means that it is more likely that one electron or positron (or both) hit the detector. In that case they are either rejected because of a transverse momentum above 0.5 GeV (or 3 GeV if they are mis-identified as other charged particle) or they contribute to the visible energy, mainly if they are mis-identified as photons. At lowest photon transverse momenta the leptons also have a smaller polar angle and a larger fraction hits the forward region and is reconstructed as BeamCal clusters.

In figure 6.12 the phase space of the outgoing leptons in the final Bhabha scattering events is depicted. The information is obtained from generator level. The electron or positron with the highest polar angle is selected. The shown events are from the data set with both beam particles being right-handed, corresponding to an integrated luminosity of $24.2\,\mathrm{fb}^{-1}$.

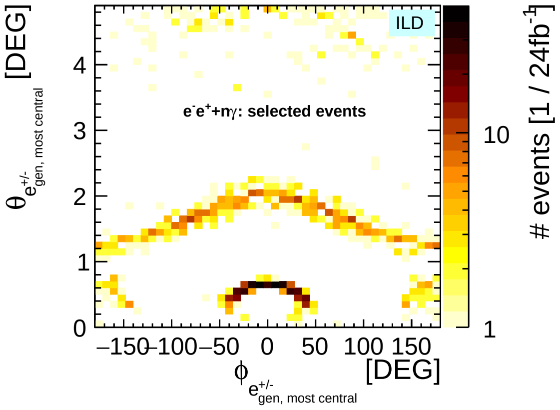

Figure 6.12: The lepton phase space of Bhabha scattering events surviving all cuts is examined on generator level: The position of the electron or positron with the highest polar angle is drawn for unweighted events from the data set with both beams being right-handed.

Several regions in the parameter space can be distinguished: the distinct features below $\theta \approx 1°$, a ϕ-dependent band in the polar angle range $1° < \theta < 2°$ and a low density of particles at higher angles. The particles below $\theta \approx 1°$ escape detection through the beam pipe. The leptons at high angles are mainly low energetic and cannot prevent the events from passing the p_T and visible energy cuts.

The range $1° < \theta < 2°$ corresponds to the transition to the forward detector

LHCal and thus a possible explanation is that the leptons scatter at its inner surface, which hinders the reconstruction. The shape of this population is ϕ-dependent, because LHCal is centred around the outgoing beam pipe.

The particles at the lowest angles can be separated into two groups at different azimuthal angle. Around ±180° the leptons escape through the beam pipe for the incoming beam and around 0°, they fly along the outgoing beam pipe. As explained in section 5.3.1.2, a cut on the minimum transverse momentum of the photon is applied to enable the reconstruction of at least one Bhabha scattering lepton in the detector. But the cut can only shift the *peak* of the lepton distribution to higher polar angles, meaning that a fraction of the leptons can escape through the beam pipes.

The highest concentration of missed leptons is in the angular range of the outgoing beam pipe. As shown in figure 5.11b this is simply the azimuthal range with most generated events. In a real experiment the distribution is expected to continue to lower polar angles, so the rates of missed leptons around the incoming beam pipe would increase. These regions in parameter space could not be generated because of a lacking suitable setup (see section 5.3.2.3).

Nevertheless, the generated outgoing leptons cover the full instrumented polar angular range (see figure 5.11b), which allows an optimisation of the event selection with a complete description of the detector activity. The setup is hence a clear improvement with respect to any previous modelling of the Bhabha scattering phase space.

With a better description of the Bhabha scattering forward region, the cross-section of the background would change, but not in a way that would influence the performance of the detector, the reconstruction and the selection criteria. Only the minimum transverse momentum cuts in the signal definition could be moved to higher values, if the Bhabha scattering background was higher, which would lead to a smaller signal region. The effect of a different background level (without changing the signal definition) is evaluated in section 7.3.1.

6.1.6.2 Features in the photon energy distribution

In figure 6.7 the energy distribution of the photons in Bhabha scattering events shows a different behaviour than the expected rise towards lowest values, which can be seen for the photons from neutrino pair production. Instead the peak is shifted to ~15 GeV because of the cuts in the WHIZARD steering (see section 5.3.2.2).

Due to the cut on the four-momentum transfer between incoming and outgoing Bhabha leptons $M_{e_{in},e_{out}} < -1\,\mathrm{GeV}$, the outgoing electron or positron has a minimum polar angle, which depends on the energies of the incoming and outgoing leptons. When assuming the nominal energy of 250 GeV for the energy of the incoming lepton, the angle between the two particles is

$$\Theta_{e_{in},e_{out}} > \cos^{-1}\left(1 - \frac{M^2_{e_{in},e_{out}}}{2 \cdot E_{e_{in}} \cdot E_{e_{out}}}\right) = \cos^{-1}\left(1 - \frac{1\,\mathrm{GeV}^2}{2 \cdot 250\,\mathrm{GeV} \cdot E_{e_{out}}}\right) \quad (6.1)$$

which is simply the polar angle θ of the outgoing particle because the beam particles have a negligible angle.

Analogously, from the condition $M_{e_{out},\gamma} > 4\,\mathrm{GeV}$ it follows that the angle between the outgoing lepton and photon is

$$\Theta_{\gamma,e_{out}} > \cos^{-1}\left(1 - \frac{M^2_{e_{out},\gamma}}{2 \cdot E_{e_{out}} \cdot E_{\gamma}}\right) = \cos^{-1}\left(1 - \frac{(4\,\mathrm{GeV})^2}{2 \cdot (250\,\mathrm{GeV} - E_{\gamma}) \cdot E_{\gamma}}\right) \quad (6.2)$$

where it is assumed that the energy of the outgoing lepton and the photon add up to the energy of the incoming beam particle: $E_{e_{out}} + E_{\gamma} = 250\,\mathrm{GeV}$. This is true if the momentum transfer in the lepton scattering is minimal, for which the cross-section is maximal and hence this gives a reasonable approximation.

Whereas the angle in equation 6.1 is the polar angle of the particle, in equation 6.2 the angle is the opening angle of the two particles' flight direction and has a polar and azimuthal component: $\Theta_{\gamma,e_{out}} = \sqrt{\theta^2_{\gamma,e_{out}} + \phi^2_{\gamma,e_{out}}}$. When assuming that the azimuthal component is zero the two angles can be added: $\theta_{\gamma,e_{out}} + \Theta_{e_{in},e_{out}}$ to obtain the polar angle of the photon, as sketched in figure 6.13.

As low photon polar angles are favoured, a peak can be expected for the minimum angle allowed by the cuts on generator level, which is $\theta_{\gamma} = 4.05°$ (see section 5.3.2). With $M_{e_{in},e_{out}} < -1\,\mathrm{GeV}$, $M_{e_{out},\gamma} > 4\,\mathrm{GeV}$ and $E_{e_{out}} + E_{\gamma} = 250\,\mathrm{GeV}$ the corresponding photon energy can be calculated: $E_{\gamma} = 15.4\,\mathrm{GeV}$, which is visible as the peak in the photon energy distribution in figure 6.7. The rather large width of the peak can be explained by two effects which were not taken into account in the simplified calculation above: The azimuthal component of the angle between lepton and photon can take any value. Secondly, due to the beam energy spectrum, the energy of the incoming particle may differ from the nominal energy. For incoming particles with a lower energy the minimum energy of a photon with $\theta_{\gamma} = 4.05°$ shifts to higher values.

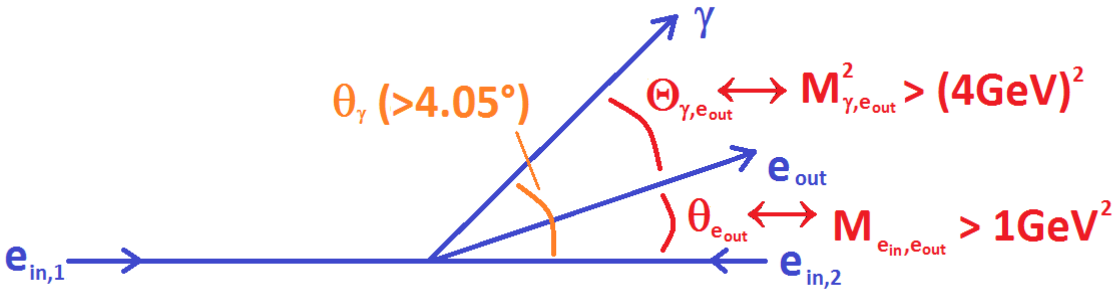

Figure 6.13: Visualisation of the angles between incoming and outgoing lepton (equation 6.1) and between outgoing lepton and photon (equation 6.2), which are restricted by the corresponding M cuts. Together with the minimal θ_γ a photon energy range around 15 GeV is favoured.

As can be seen in figure 6.7, at energies below this broad peak the distribution rises again. If the selected photon has a very low energy, the conditions from equations 6.1 and 6.2 can still be met either if the energy of the incoming lepton $E_{e_{in}}$ is low or if the energy of the outgoing lepton $E_{e_{out}}$ is lowered by the other ISR photons. The latter in turn can either be the energy correction of the ISR routine, which is restricted to zero polar angle, or one of the other matrix element photons, which carries away most of the energy but is not selected as signal photon because its transverse momentum is lower than of the signal photon. Additionally, objects mis-reconstructed as photons populate this energy range with a minor contribution.

This set of invariant mass cuts was applied to make a convergence of the matrix element calculation possible. In real data the rise in the distribution is expected to continue towards lower energies. An approach to generate these missing events is presented in the following section.

6.1.6.3 Alternative cut configuration in the generation of Bhabha scattering events

As discussed in the previous section 6.1.6.2, the reason of the apparantly missing Bhabha scattering events with low energetic photons are the cuts on invariant mass and four-momentum transfer in the event generation. In an alternative approach to generate Bhabha scattering events with one matrix element photon, the condition of a minimum invariant mass between photon and outgoing leptons is replaced by a minimum angle. In order to generate only phase space which is not covered by the main Bhabha scattering sample, the invariant mass cut is reversed ($M_{e^-_{out},\gamma_i}$ or $M_{e^+_{out},\gamma_i}$ smaller than 4 GeV) and all other cuts are the same as before (see table 5.2 on page 95). For simplicity no beam polarisation is assumed. The cross-section with this setup is 15 802 fb, compared to 116 146 fb of the standard sample (which is the average of the four polarisation combinations listed in table 5.4).

Also with the approach of an angular cut not the full phase space is generated. This means that only an estimate on the event number and distribution of the missing phase space can be given with this additional data set. Furthermore, the approach of a minimum angle only works for one photon, because the matrix element calculation is divergent, if the minimum invariant mass cut is translated into a minimum angular cut between several photons and the outgoing leptons. This means that the data set presented in chapter 5 is the best possible approach to cover the phase space with a matrix element generator with a focus on high-energetic electrons. The additional sample can help to give an estimate of the low-energetic electrons. For the WIMP study the selected events of both approaches are added up to obtain the Bhabha scattering background.

The shortcoming of the standard cuts was discovered after the reconstruction, which means that is was too late to perform a full detector simulation and reconstruction with the events from the alternative approach. So, the events are selected on generator level with a simplified signal definition and set of cuts.

The largest difference to the main analysis with fully reconstructed events is the assumed perfect tracking and photon reconstruction efficiency and 100% purity when taking the events from generator level. Additionally, no overlay particles are included. In the signal definition all cuts on the matrix element photon are applied as in the main analysis (see section 5.3.1), only the minimum transverse momentum is 1.92 GeV, independently of the azimuthal angle, i.e. the opening for the incoming beam pipe is ignored. The electrons are treated differently, depending on their polar angle. Above $\theta = 2.29°$ they are outside of BeamCal and are assumed to be identified as electrons. Both leptons are tested for the transverse momentum cut (see section 6.1.1), i.e. the event is discarded if $p_{T,e^-} > 0.5\,\mathrm{GeV}$ and/or $p_{T,e^+} > 0.5\,\mathrm{GeV}$. If the sum of their energies is above 10 GeV the event is rejected, according to the visible energy cut (see section 6.1.2). The BeamCal veto (see section 6.1.3) is implemented by requiring a minimum energy of the leptons to be identified, depending on the polar angle, to accound for the challenging overlay of beam-induced background in the inner part of BeamCal: Above $\theta = 0.32°$ the minimum energy is 10 GeV and below 175 GeV. Again the ϕ-dependent shape of the BeamCal opening is ignored. If both leptons are below all the thresholds and/or are within the beam pipe (i.e. $\theta < 0.32°$) the events are selected.

In order to test whether the event selection of the main analysis can be imitated with this procedure, the selection of the fully reconstructed Bhabha scattering events is repeated according to the simplified approach. The event number corresponding to $1\,\mathrm{fb}^{-1}$ for unpolarised beams and one matrix element photon is 110.9, i.e. only 0.1% larger than the 110.8 when applying all cuts a reconstruction level (see table 6.3). This means that the cuts on generator level result in a realistic event selection.

When applying this event selection to the new Bhabha scattering events, 56.9% fulfill the signal definition out of which 0.8% are selected. Both fractions are higher than for the main data set (compare with section 6.1.5 and table 6.3, respectively). The additional number of selected events from the new data set is 72.35 per fb^{-1}. In figure 6.14 the photon energy distributrion of signal-like and selected events show the same distributions as in figure 6.9, but with the additional events added in red. As can be seen in figure 6.14a, the additional events can partially fill the expected peak towards low values. The distribution shown in figures 6.14b and 6.14c serve as input to the limit calculation (explained in chapter 7).

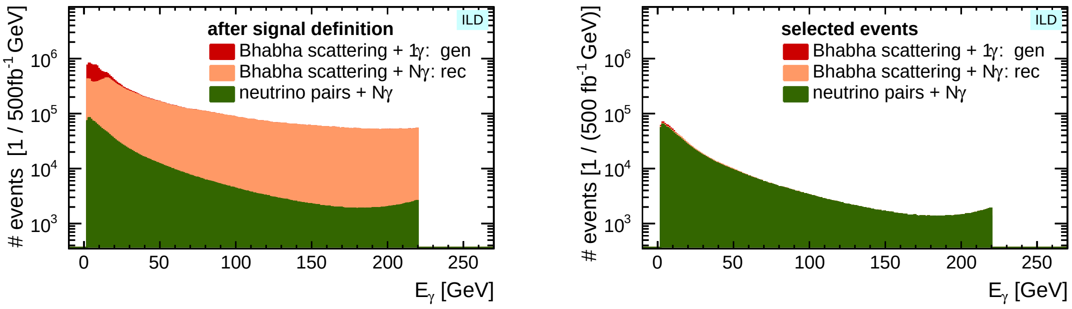

(a) (b)

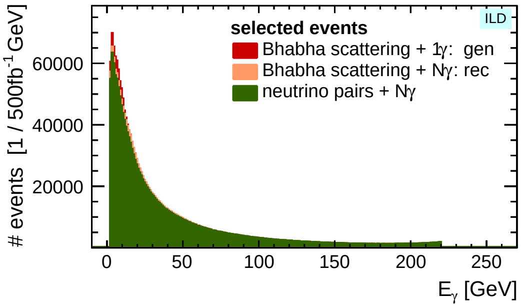

(c)

Figure 6.14: Photon energy distribution, including the additional Bhabha scattering events, (a) after the signal definition and (b,c) after the event selection.

With the additional events from the alternative approach to describe the Bhabha scattering phase space the reducible background is approximately 65% higher. But together with the neutrino events, the total background increases only by 2% for the unpolarised case and for $P(e^-, e^+)$ =(+80%,−30%) by 8%.

The phase space of the surviving events is shown in figure 6.15b in comparison to the main Bhabha scattering data set (figure 6.15a). The largest fraction of events contains a lepton in the central part of the detector. The typical lepton energies are very low (sub-GeV to GeV range) and hence the event is not rejected by the cuts.

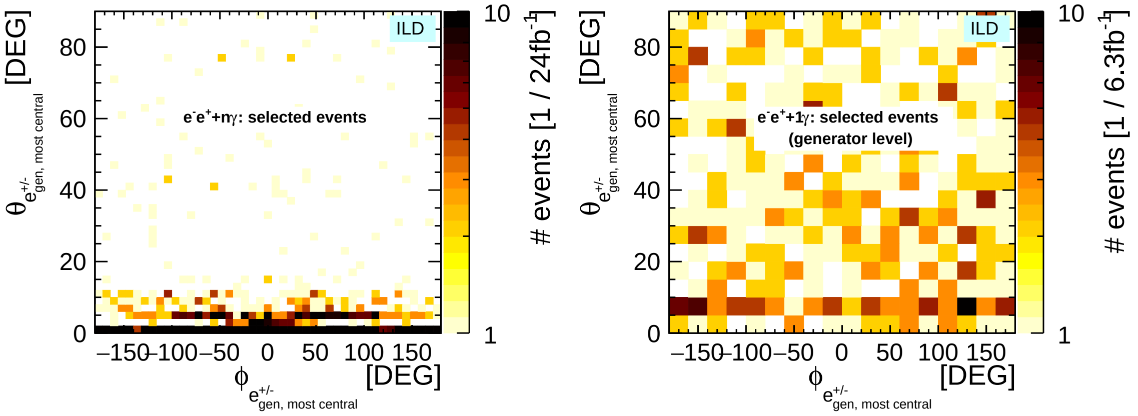

(a) (b)

Figure 6.15: The lepton phase space of events passing all selection criteria. (a) Events from the main data set (corresponding to figure 6.12) are highly concentrated in the forward region. (b) In the additional data sample most of the electrons have large polar angles.

The large fraction of low energetic leptons in these events triggered the separate transverse momentum cut on electrons (introduced in section 6.1.1). Before electrons were treated like the other charged particles and the threshold was 3 GeV. With the new cut $p_{T,e} < 0.5\,\text{GeV}$ a larger fraction of Bhabha scattering events can be suppressed.

As a conclusion of the study of the additional Bhabha scattering phase space detector requirements and generator requirements can be identified. A separate treatment of electrons requires a high tracking efficiency for low transverse momentum (GeV range) and good electron identification also at lowest energies and in the forward region, i.e. below 7° and especially the acceptance gap due to the LHCal could be closed with a better design. A suitable event generator to describe the complete phase space also has to allow electrons close to the photon.

6.1.7 Comparison to the selection efficiency of the previous analysis

In table 6.3 the selection efficiencies are compared to the previous analysis [1, 2]. A comparison of percentages is prefered over total numbers, because the signal definition is different (see section 5.3.1.4). Before addressing the selection efficiencies the different settings in WHIZARD and slightly modified selection criteria are presented.

WHIZARD settings: The differences in the event generation comprise the completely new setup of both the Bhabha scattering process (see section 5.3.2.2) and the modelling of ISR (see section 5.4.1). In [1, 2] the transverse momentum of the pseudo photons from the ISR routine were non-zero. As a consequence, an event with n matrix element photons contained $n + 2$ photons that potentially hit the detector. The effect of these additional pseudo photons is expected to be small, because they tend to be soft. Therefore, data sets with the same number of matrix element photons are compared in the table. Additionally, in the previous analysis the processes $\nu\bar{\nu}\gamma\gamma\gamma\gamma$, $e^+e^-\gamma\gamma$ and $e^+e^-\gamma\gamma\gamma$ were not considered.

Transverse momentum cut: As mentioned above in section 6.1.6.3, the separate cut on reconstructed electrons was introduced in this analysis and in [1, 2] they were treated like the other charged particles.

Visible energy cut: The visible energy criterion in [1, 2] differs from the one discussed above. No threshold was applied, the maximum allowed visible energy was lower (20 GeV) and the energies of all particle types were added up, i.e. neutrons and pions were not treated separately. These settings applied to the data sets produced in this analysis would reject many more neutrino (and hence also WIMP) events, because the low-p_T overlay (see section 3.5.3.2) is now more realistic and was underestimated in [1, 2].

A possible background to the mono-photon signal is the creation of several photons in the hard interaction ($e^+e^- \rightarrow \gamma\gamma$). In [1, 2] this background was included and the cut on the visible energy was crucial to suppress it. Most of the photon energies are high and hence the rejection is expected to be comparable with the new setup. With event numbers well below the other background types in [1, 2] the multi-photon processes can be safely neglected.

BeamCal veto: In [1,2] the BeamCal clusters were modeled using the previous standard BeamCal reconstruction [121]. The reconstruction efficiency was slightly lower than in the new approach (see figure 4.10 on page 83).

Despite all the differences the efficiencies are overall at comparable scales. The lower efficiency for neutrino events in this analysis can be explained by the introduction of the separate p_T cut on electrons and by the updated and more realistic overlay of low-p_T hadrons.

When applying the BeamCal veto slightly more events are kept: The efficiencies with respect to the number of events after the visible energy cut is 99.5% in this analysis and 98.1% in the previous one for neutrino pair production with one photon. Even though the improvement is not tremendous, it is worth highlighting that the BeamCalClusterReco algorithm performs a real reconstruction and also allows for fakes, but the performance is better.

For the Bhabha scattering samples the suppression efficiencies of the p_T and visible energy cuts differ significantly. The rate of events surviving the first cut is twice as high, because with the updated generator cuts a larger fraction of leptons have a lower polar angle (see figure 5.11b on page 98). The updated visible energy criteria however lead to a significantly better background rejection. After the BeamCal veto the final selection efficiencies are very close to each other, which shows that the updated reconstruction algorithms compensate the additional phase space in the very challenging forward region: More leptons are generated which deposit their energy in the polluted inner part of BeamCal or escape detection through the beam pipe.[iii]

6.2 Evaluation of the data quality

In the main analysis of this study the events with all the reconstruction imperfections (see section 5.5) are used. In the following, the influence of the data quality is evaluated using information from the generator level. The effect on the WIMP exclusion limits will be presented in section 7.3.2.

6.2.1 Event selection using generator information

The only difference to the event selection after reconstruction (as described above in section 6.1) is that the reconstructed photon energy is replaced by a smeared generated photon energy, i.e. events are not tested if they contain a *reconstructed*

[iii] Due to the different ISR modelling (see section 5.4.1) the overall Bhabha scattering cross-section and hence the number of surviving events in [1, 2] was higher.

signal-like photon, instead the signal defining cuts are applied on the *generated* photon with the highest transverse momentum.

Before applying the cuts, energy and transverse momentum distribution of all generated photons are randomly smeared according to a Gaussian distribution with the energy-dependent width from test beam data (equation 3.4). In this way the detector resolution is modelled.

The events are selected with the criteria of low detector activity using the *reconstructed* events, i.e. as described in section 6.1. It is worthwhile to mention that the approach of performing the selection based on the reconstructed events goes beyond a typical generator-level study without any realistic detector simulation.

6.2.2 Effect of the data quality on the photon observables

The number of selected events using the photons with generator information is 3607 for an integrated luminosity of $1\,\mathrm{fb}^{-1}$ which is only 1 event less than the 3608 events obtained with the reconstructed photons, where the latter corresponds to the sum of the event numbers for unpolarised beams in table 6.2. The ratio between the number of reconstructed photons N_{rec} and generated photons N_{gen} as a function of the energy and polar angles is shown in figures 6.16 and 6.17, respectively.

For energies up to 150 GeV the ratio N_{rec}/N_{gen} is close to one, but slightly bigger. For higher energies the reconstruction efficiency steadily decreases and falls below 80% for the maximum energy. At lowest energies there is a small dip in the distribution.

The deviations from 1 can be explained by the wrong calibration of the ECAL components and the non-linearity of the response. Around 3 GeV the average reconstructed energy corresponds to the generated energy, below the reconstructed energy is too small and above too high (see figure 5.17 on page 110). This leads to a migration of reconstructed photons away from the region around 3 GeV, leading to the dip.

As can be seen in figure 5.17, the ratio E_{rec}/E_{gen} increases with increasing energy. At the same time the photon spectrum is falling. Both effects together lead to an excess of N_{rec} over N_{gen} that increases with energy (see figure 6.16a). At even higher energies the number of photons increases (due to the Z return) which means that the migration out of the bins is not compensated by a migration from lower energies and the ratio of reconstructed to generated photons starts to go down. Photons close to the maximum energy of 220 GeV are likely to be reconstructed above the

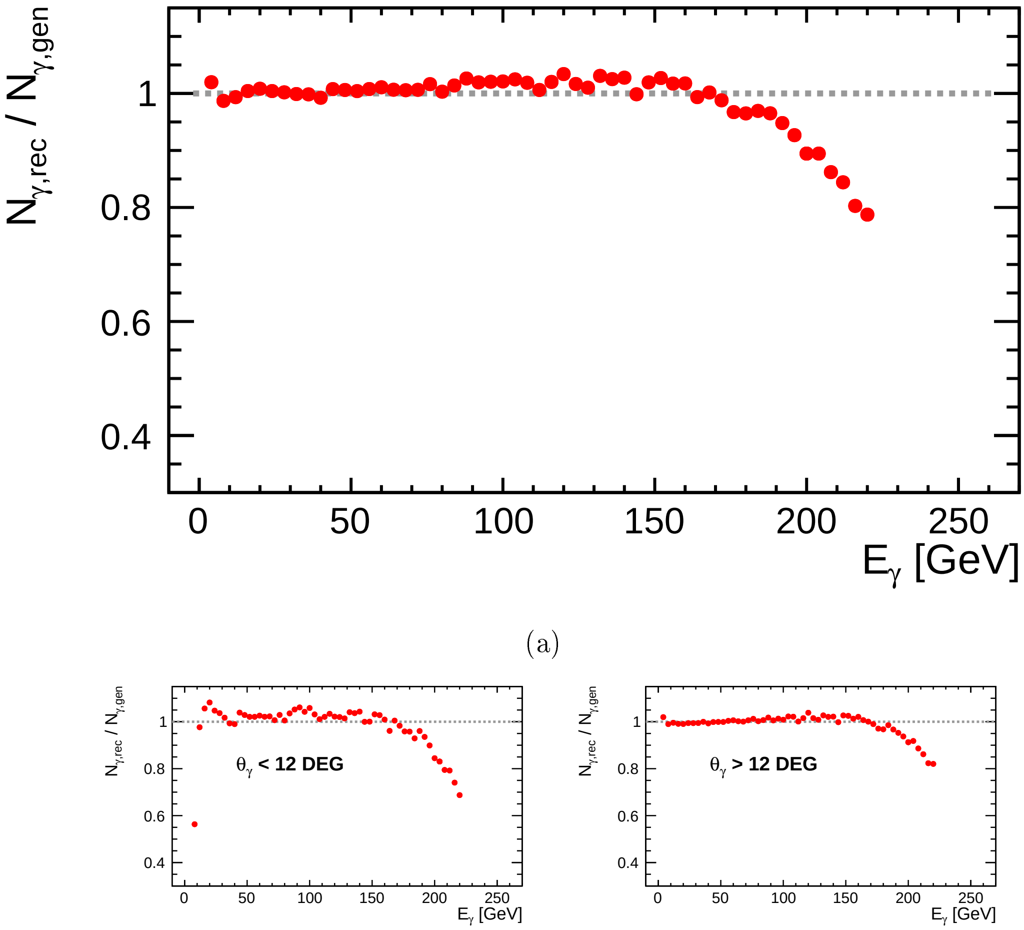

(a)

(b) (c)

Figure 6.16: Smeared acceptance as a function of the generated photon energy. (a) all photons, (b) polar angles corresponding to the ECAL ring, (c) all other detector parts.

cut and migrate out of the signal region, which leads to the drop by 20%.

The energy dependence is looked at for two polar angle ranges separately in figures 6.16b and 6.16c. With the wrong calibration in the ECAL ring and the reconstruction failure in the transition region (see section 5.5.3) the very forward region is a special case and the ratio of N_{rec} to N_{gen} for $\theta < 12°$ (and $\theta > 168°$) is displayed in figure 6.16b and the more central part of the detector is shown in figure 6.16c.

In the curve for the central angular range (figure 6.16c) the deviations from 1 are less pronounced. Analogously to the distribution in figure 6.16a, the values are slightly below 1 at very low energies, at medium energies there is an excess of reconstructed photons and at the highest values the decrease is also present.

In the ECAL ring region (figure 6.16b) the distribution below ~170 GeV is dominated by several wiggles and most of the values are clearly above 1. The wrong calibration to higher values than in the rest of the detector, leads to a migration of events to higher energies which is more pronounced. As a consequence, also the drop of the ratio of reconstructed to generated photons is more severe than in the central part of the detector, which reaches 60% at the maximum energy. In the ECAL ring energies below ~10 GeV are not reconstructed at all which leads to the significant drop of the reconstruction efficiency at low energies.

The angular dependence of the ratio of reconstructed and generated selected events shows several features, see figure 6.17. In the central part N_{rec}/N_{gen} is slightly above 100% and decreases steadily until it reaches 99% around the transition regions from barrel to endcaps (around 40° and 140°). In the endcaps it is slightly below 1. In the very forward regions the number of events from the full reconstruction is 2% higher than from the analysis using generator information.

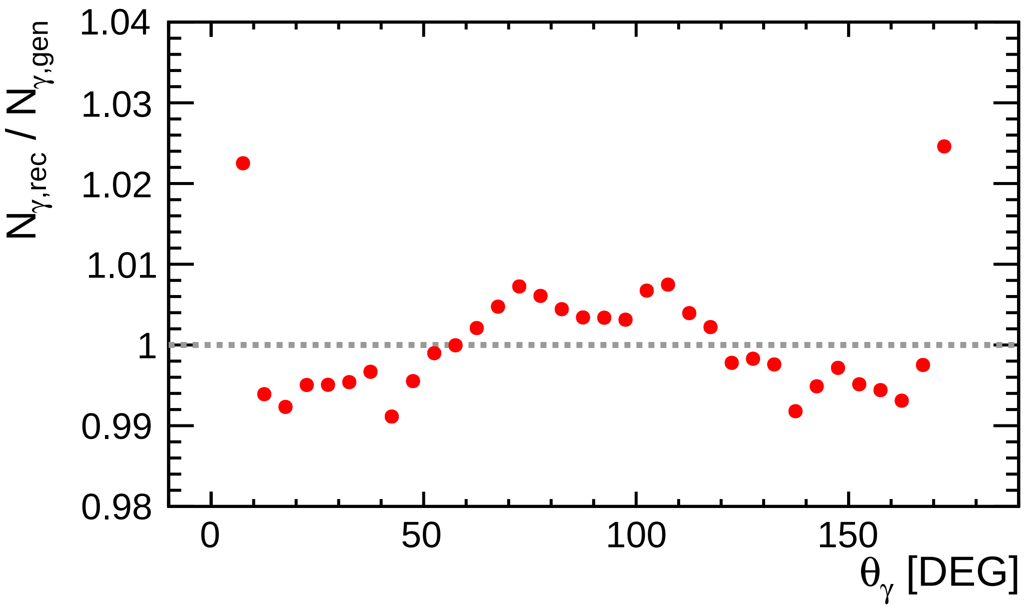

Figure 6.17: Smeared acceptance as a function of the generated polar angle θ.

The first and last entry in the angular distribution corresponds to the phase space drawn in figure 6.16b. The energy distribution peaks at low values and hence the part of the distribution with higher N_{rec} than N_{gen} dominates and leads to these outliers.

The photons at highest energies are mainly in the forward region and hence the deficit at highest energies has the largest contribution in the angular ranges corresponding to the endcaps. The fraction of high energetic photons decreases with increasing θ and hence the level rises towards the central angular range in figure 6.17. With the minimum transverse momentum cut in the signal definition, the lowest energies are possible around 90°. The deficit a lowest energies thus plays an increasing role, which leads to the decrease of the ratio towards 90°.

Overall the deviations in the polar angle distribution are at the level of a few per cent and can be neglected. The effect seen in the energy distribution is up to 40%. How these reconstruction deficits influence the WIMP exclusion limits will be evaluated in section 7.3.2. It will be shown that the differences in the photon observables only have a minor effect on the WIMP exclusion limits. This means that the impact of the mis-calibration can be neglected in the main analysis.

Chapter 7

Impact of Operating Scenario and Systematic Uncertainties

In this chapter the approach to quantify the expected sensitivity of the ILC to WIMP production is presented. The underlying mathematical formalism and the software are addressed in section 7.1. With a first set of expected exclusion limits the effect of beam polarisation and integrated luminosity is presented in section 7.2 and the influence of detector effects is evaluated in section 7.3.

The systematic uncertainties on luminosity, beam polarisation, event selection and the theory are presented in section 7.4. In the previous studies [1–3] the luminosity spectrum was the main source of systematic uncertainties. An improved approach for its evaluation is shown in section 7.5. How alternative assumptions on the systematic uncertainties would modify the sensitivity reach is discussed in section 7.6. Finally, the results are compared to the previous study in section 7.7.

The potential to discover a signal and expected exclusion limits for the complete programme of the ILC will be presented in the following chapter 8.

7.1 Calculation of confidence levels

The presented sensitivity to WIMPs are results of hypothesis tests. The null hypothesis is that there is no WIMP signal in the data. Even though a discovery is hoped for, most of the results will be quantified in terms of expected exclusion limits, in order to be comparable with many other studies.

With a test statistic a value can be assigned to a measurement or a toy experiment according to its compatibility to be signal-like. For a counting experiment the test statistic X is calculated as [168]

$$X = \sum_{\text{events } l} w_{k(l)} \tag{7.1}$$

with weight w_k for *channel*, i.e. separate measurement, k [168]

$$w_{ki} = \frac{s_k}{s_k + 2b_k} \tag{7.2}$$

where s_k and b_k are the number of signal and background events, respectively.

In order to assign a confidence level to the test statistic calculated for an experiment with real data, the underlying probability density functions (P_{s+b} for the *signal plus background* hypothesis and P_b for the *background only* hypothesis) have to be identified by performing toy Monte Carlo experiments.

P_{s+b} and P_b are used to form confidence levels CL_{s+b} and CL_b for the assumptions *signal plus background* and *background only*, respectively. The confidence level of an experiment is calculated as the integral over the probability density functions up to the observed test statistic X_{obs} [168]

$$CL_{s+b} = \int_0^{X_{obs}} P_{s+b}(X)dX \tag{7.3}$$

and

$$CL_b = \int_0^{X_{obs}} P_b(X)dX \tag{7.4}$$

A value of $CL_b = 0.5$ is expected for data which agrees perfectly with the *background only* hypothesis. Due to statistical fluctuations the value can be smaller or larger, even if the data only contains background events. A significantly larger value corresponds to an excess, which could mean that the *signal plus background* hypothesis is favoured. A deficit with respect to the *signal plus background* hypothesis, on the other hand, is reflected in a small value of CL_{s+b}.

The underlying method of the sensitivity calculation follows a modified frequentist approach [169, 170]. In this "CL_s method" the confidence levels of exclusion limits are calculated according to

$$CL_{\text{exclusion}} = 1 - CL_{s+b}/CL_b \tag{7.5}$$

By taking the ratios of the confidence in the *signal plus background* hypothesis and the *background only* hypothesis, exclusion limits can be set in conservative manner. In this way an exclusion of a signal to which the search is not sensitive to is avoided, especially for small signal rates, i.e. when the signal is very small and hence CL_{s+b} and CL_b are close together.

The sensitivity to detect a signal can be studied by testing the *backgroud only* hypothesis and the probability for the discovery reach is [168]

$$CL_{\text{discovery}} = 1 - CL_b \tag{7.6}$$

corresponding to a clear excess over the background expectation.

In order to estimate the expected sensitivity of an experiment or an analysis prior to real data, like in this study, toy experiments can be carried out. The input, i.e. number of events in a counting experiment, is modelled according to one hypothesis (e.g. *background only*) and randomly varied. Many toy experiments are performed, resulting in a distribution of the test statistic, which is used to calculate the expectation value of the confidence level $\langle CL \rangle$ according to the opposite hypothesis (e.g. *signal plus background*). In the software (which will be introduced in section 7.1.1) this option to calculate the confidence level according to *signal plus background* for input according to *background only*, i.e. $\langle CL_{s+b} \rangle_b$, was already implemented. The opposite case $\langle CL_b \rangle_{s+b}$ was added to also study the potential of a discovery.

In order to discriminate between the two hypotheses that the data either consists of *signal plus background* or *background only*, an observable can be chosen, which looks different for background and signal. In the WIMP study the photon energy distribution is taken as discriminating variable. The test statistic X is hence calculated as [168]

$$X = \sum_{\text{events } l} w_{k(l)i(l)} \tag{7.7}$$

with weight w_{ki} for photon energy bin i and *channel* k [168]

$$w_{ki} = \frac{s_{ki}}{s_{ki} + 2b_{ki}} \tag{7.8}$$

where s_{ki} and b_{ki} are the photon energy histograms for signal and background, respectively. The test statistic is thus a weighted sum over the photon energy bins, according to the approach of fractional event counting [168]. Additionally, weights of bins with large systematic uncertainties are downgraded, following [168]. The sources of systematic uncertainties will be presented in section 7.4.

In the following, 2σ expected exclusion regions will be presented, which correspond to phase space points where the confidence in the *signal plus background* hypothesis is small, i.e. the probability that the observed data is caused by a fluctuation is smaller than $1 - 2\sigma = 0.05$. In section 8.2 3σ and 5σ confidence levels disfavouring the *background only* hypothesis, i.e. the sensitivity to a discovery, will be presented.

7.1.1 Implementation of the sensitivity calculation in TSysLimit

For the calculation of the sensitivity the package TSysLimit is used, which was originally written for a leptoquark analysis at HERA [171]. The basic concept is to read in a signal and a background photon energy spectrum and calculate the confidence levels in terms of the energy scale Λ of the tested effective operators, which were introduced in section 2.4.1.1. The background corresponds to the distribution shown in figure 6.14b, i.e. the photon energy spectrum of the selected neutrino and Bhabha scattering events. The WIMP photon energy spectra are reweighted using the neutrino events (see section 7.1.2 for more details). Different WIMP masses are tested in steps of 1 GeV, up to half the centre-of-mass energy, i.e. 250 GeV. In the case of data sets with different polarisation configurations and centre-of-mass energies the individual sets of signal and background form separate *channels*.

The photon energy, i.e. the discriminating variable, is binned in 1 GeV intervals. In figure 7.1a examples for signal and background input histograms are shown. The vector operator and a WIMP mass of 150 GeV are assumed for the signal distribution. The result of the sensitivity calculation is a Λ_{95} which corresponds to a signal strength for an exclusion with a 2σ confidence level, according to equation 7.5.

During the calculation different signal heights are tested by varying the value of Λ until the calculated confidence limit corresponds to 2σ (or the desired value). The procedure is repeated with a smaller step size in the variation of Λ and the calculation is terminated once the Λ range is smaller than $\frac{1}{128}$ GeV to allow for a 10 MeV precision. The signal distribution in figure 7.1a is shown for $\Lambda = 1542$ GeV, i.e. the value found by TSysLimit for the expected exclusion limit for this toy experiment.

In figure 7.1b the expected exclusion limits for the WIMP mass scan is presented. All Λ values below the curve are excluded at the respective WIMP mass. The shape of the curve comprises a plateau at lower masses and the sensitivity decreases

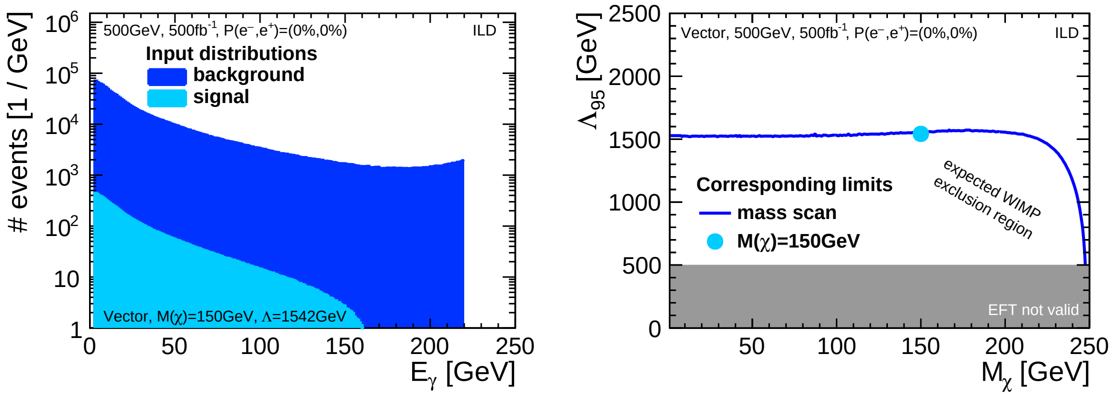

(a)

(b)

Figure 7.1: (a) The signal and background input histograms of the photon energy distributions with $\Lambda = 1542\,\text{GeV}$ corresponding to the exclusion limit. (b) Example for expected 2σ exclusion limits.

towards masses just below half the centre-of-mass energy, because the cross-section (equation 2.28) gets smaller with higher WIMP masses which will also be visualised in section 7.1.2.1.

The grey band at low energy scales shows the region which is unsuitable for the approach of effective operators, i.e. $\Lambda \leq \sqrt{s}$ (see section 2.4.1).

The input histograms are chosen according to the desired polarisation configuration. This means that individual signal and background photon energy spectra are required for the different tested combinations of electron and positron polarisation. In total, eight background templates are created with the polarisation combinations $P(e^-, e^+) = (0, 0)$, (−80%,0), (+80%,0), (−80%,−30%), (−80%,+30%), (+80%,−30%), (+80%,+30%) and (+80%,−60%). For the signal those cases are created for 250 WIMP masses and the three operators vector, axial-vector and scalar, resulting in a total number of $8 \times 250 \times 3 = 6000$ templates.

As described in section 5.2.1, the WIMP photon spectrum is obtained by reweighting neutrino events, which are are also a background process. In order to obtain statistically independent distributions, the neutrino data set is split into two parts to create the signal and background templates. The latter is added to the Bhabha scattering events.

7.1.2 The signal events

The signal cross-sections (equations 2.28, 2.29 and 2.30) are given for WIMP production with a single ISR photon. This means that the weight has to be the ratio of the WIMP and neutrino cross-sections with *one* ISR photon at the centre-of-mass energy of the process $e^+e^- \to \nu\bar{\nu} + 1\gamma$ (or $e^+e^- \to \chi\chi + 1\gamma$).

The Monte Carlo neutrino events, on the other hand, are generated with luminosity spectrum, the soft/collinear ISR photons and up to four matrix element photons (see section 5.4), meaning that the process of neutrino pair production with one ISR photon is convoluted with a function Φ, describing the additional photons and the luminosity spectrum:

$$\Phi(n\gamma, E_{beam}) \times \sigma(\nu\bar{\nu}\gamma) \tag{7.9}$$

It is assumed that the effect of Φ can be transfered to the WIMP events in the reweighting process. In this way, WIMP events with the effects of luminosity spectrum and the full description of the ISR spectrum can be obtained by applying the ratio of the cross-sections as weight according to equation 5.2

$$\text{“WIMP events”} = \text{“neutrino events”} \times \frac{\sigma(\chi\chi\gamma, E_\gamma^*, \sqrt{s^*}, M_\chi, \text{operator})}{\sigma(\nu\bar{\nu}\gamma, E_\gamma^*, \sqrt{s^*})} \tag{7.10}$$

where E_γ^* is the photon energy (of the photon with the highest transverse momentum) and $\sqrt{s^*}$ the centre-of-mass energy, in the frame of the $\nu\bar{\nu}\gamma$ or $\chi\chi\gamma$ system. E^* and $\sqrt{s^*}$ are calculated with the generator-level four-momenta of the neutrinos and the photon with the highest transverse momentum, which are boosted into the centre-of-mass frame of the three particles.

7.1.2.1 The WIMP cross-section

The WIMP cross-sections are computed prior to the event reweighting using the double-differential cross-sections for the three effective operators (equations 2.28, 2.29 and 2.30). The cross-sections are calculated as a function of WIMP mass, E^* and $\sqrt{s^*}$, each in steps of 1 GeV. The polar angle is integrated over, because the angular distributions of the photons from the two processes $\nu\bar{\nu}\gamma$ and $\chi\chi\gamma$ are almost identical, as depicted in figure 7.2. Only in the very forward region the distributions differ. Therefore, the cross-section values depend on the integration borders, if they are very close to -1 and 1.

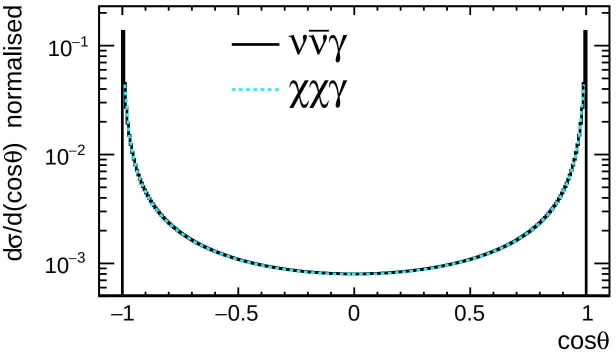

Figure 7.2: The normalised polar angle distributions of the ISR photons from neutrino pair production (black solid line) and WIMP pair production (cyan dashed line) are very similar.

Some events contain photon with very low polar angles. If the integral is solved over the full range, it would thus extend to the region where the dependence of neutrino and WIMP cross-section differ. As the neutrino cross-section rises more steeply towards values of -1 or 1, the weights would be pessimistic.

In the ILD reference frame the polar angle range is given by the signal definition (see below). In the frame of the $\nu\bar{\nu}\gamma$ system only 2% of the boosted polar angles θ^* are outside of this range. These events are reweighted using a cross-section map with a larger theta integral range covering all the occuring values, i.e. with somewhat pessimistic weights. In most cases the boost due to the luminosity spectrum and the additional ISR photons leaves the polar angle within the range allowed by the signal definition. These events are reweighted using two additional cross-section maps.

The polar angle range allowed by the signal definition depends on the photon energy. Due to the minimum transverse momentum condition (see section 5.3.1) the integration borders are dependent on the photon energy: $\theta_{\gamma,min} = \sin^{-1}(p_{T,\gamma,min}/E)$. In addition, the $p_{T,\gamma,min}$ cut has different values depending on the azimuthal angle of the photon (1.92 GeV or 5.65 GeV), which results in the two different cross-section sets.

Above $E_\gamma = 15.8\,\text{GeV}$ for $p_{T,min} = 1.92\,\text{GeV}$ (and $E_\gamma = 46.4\,\text{GeV}$ for $p_{T,min} = 5.65\,\text{GeV}$) the minimum polar angle, as calculated above, is smaller than the minimum angle of 7° of the signal definition and hence the integration range is given by the angular cut in the signal definition: $7° - 173°$, meaning that the two cross-section maps are identical above 46.4 GeV.

In figure 7.3 cross-section maps for $\Lambda = 1580\,\text{GeV}$ and two different WIMP masses are shown for the example of the vector operator. The differences between the three maps with different polar angle ranges are small and hence only the sets for $p_{T,\gamma,min} = 1.92\,\text{GeV}$ are shown.

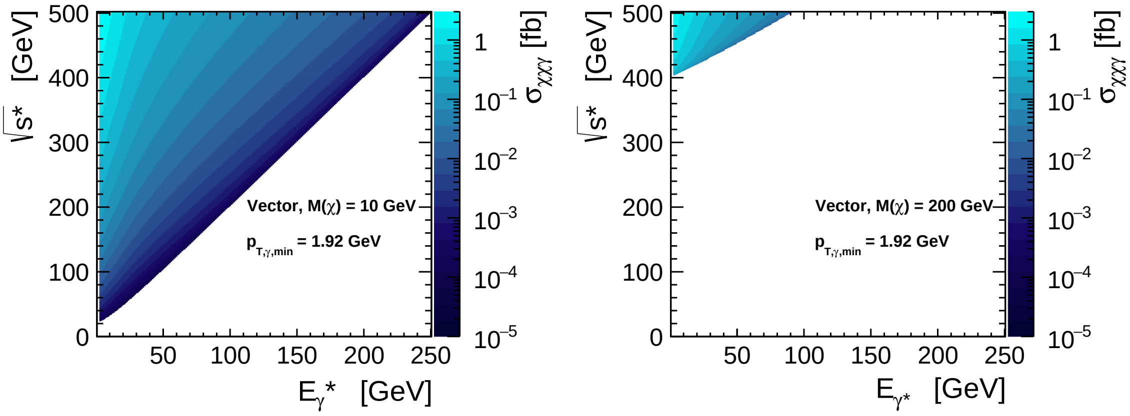

(a) (b)

Figure 7.3: WIMP cross-section for the vector operator as a function of photon energy and centre-of-mass energy for $\Lambda = 1580\,\text{GeV}$ and different WIMP masses: (a) $M_\chi = 10\,\text{GeV}$, (b) $M_\chi = 200\,\text{GeV}$.

The values rise towards low photon energies and high centre-of-mass energies. The ISR energy cannot exceed the energy of one incoming particle meaning that the centre-of-mass energy has to be at least twice the photon energy. The photon energy (and hence also the centre-of-mass energy) is constrained by the WIMP mass. The maximum photon energy is given by equation 5.1 on page 87. Whereas with $M_\chi = 10\,\text{GeV}$ almost the full range of photon energy E_γ^* and centre-of-mass energy $\sqrt{s^*}$ is kinematically possible, the phase space is considerably constrained for the higher mass of 200 GeV, which leads to the typical shape of the exclusion limit which decreases for higher masses (compare figure 7.1b).

7.1.2.2 The neutrino cross-section

In figure 7.4 the generator-level photon energy in the $\nu\bar{\nu}\gamma$ system E_γ^* is shown in comparison with the distribution of the reconstructed photon energies in the lab frame. The distributions clearly differ, because of the different reference frame and because in some cases the generated photon with the highest transverse momentum is not selected as signal photon, due to mis-reconstruction. Whereas the peak corresponding to the radiative return to the Z boson is broadened due to detector resolution and reconstruction effects in the reconstructed events and lead to a clearly visible rise towards the maximum energy of 220 GeV, the E_γ^* distribution for left-handed electrons and right-handed positrons is significantly lower and also in the other polarisation combination the feature is less pronounced.

Above the maximum energy cut the distributions of the generator-level photons continues at a significantly lower level and at the radiative return energy a small and sharp peak can be seen. In these events either the wrong reconstructed photon was selected or the energy was reconstructed far to low, as expected for a sizeable fraction of photons in the transition region of ECAL barrel and ring, because of the reconstruction failure which is visualised in figure 5.19a on page 112.

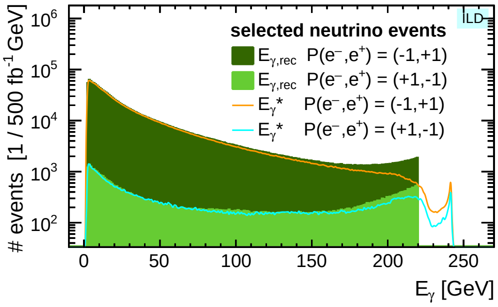

Figure 7.4: The energy distribution of the selected neutrino events in the ILD frame (solid, same as figure 6.7d) is compared to the E_γ^* distribution for the two polarisation configurations.

The distribution of E_γ^* versus $\sqrt{s^*}$ of the selected neutrino Monte Carlo events is shown in figures 7.5a and 7.5b for the two data sets corresponding to the different polarisation configurations. As opposed to the WIMP cross-section, the distribution of neutrino events varies significantly as a function of E^* and $\sqrt{s^*}$ and hence, for the cross-section calculation the bin size is adapted, as explained below.

Two regions with high populations can be identified. The radiative return to the Z boson is clearly visible as a band slightly above $\sqrt{s^*} = 2E_\gamma^*$. Whereas this feature is similar for both polarisation combinations, the remaining phase space differs. In the case of left-handed electrons and right-handed positrons (figure 7.5a) the process can also be mediated by a W in the t-channel which leads to numerous events in the upper left corner of the graph, i.e. around the nominal centre-of-mass energy and at low photon energies. This region is only sparsely populated in the data set with opposite polarisation (figure 7.5b). This, together with the band at soft photon energies, is expected for initial state radiation. The second band at highest centre-of-mass energies reflects the effect that the other ISR photons in the event tend to be soft, and that the luminosity spectrum peaks at 500 GeV, i.e. that most of the energy is carried away by the system $\nu\bar{\nu}\gamma$.

The cross-sections for the different values of E_γ^* and $\sqrt{s^*}$ are calculated with the matrix element calculator O'MEGA [152] by running WHIZARD [139] (see section 4.4). As opposed to the analytical calculation of the WIMP cross-section discussed above, this procedure is a lot more CPU-intensive and hence larger bin sizes are chosen in regions of the phase space with little variation of the cross-section. In

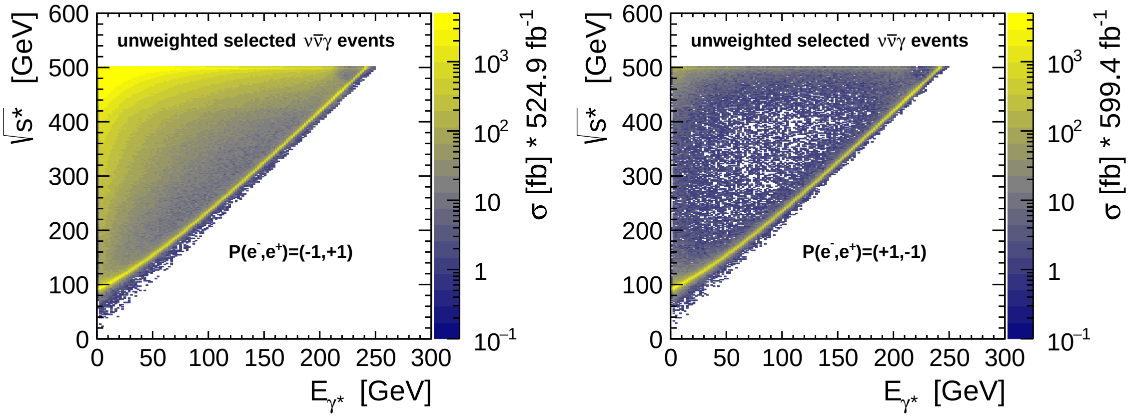

(a)

(b)

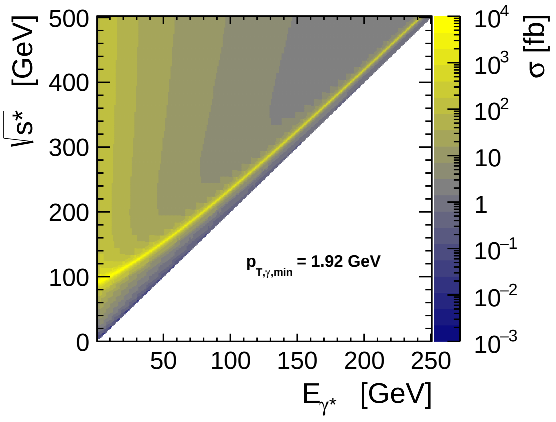

(c)

Figure 7.5: (a) and (b) Distribution of the photon energy and centre-of-mass energy of the system $\nu\bar{\nu}\gamma$ in the selected neutrino events. (c) Unpolarised cross-sections of the process $e^+e^- \to \nu\bar{\nu} + 1\gamma$ at a fixed centre-of-mass energy (i.e. without luminosity spectrum) and without additional ISR emission for $p_{T,\gamma,min} = 1.92\,\text{GeV}$.

a loop over E^*_γ in steps of 1 GeV and $\sqrt{s^*}$ with differing step sizes, approximately 12,000 values are calculated (see appendix E for an example steering file).

The step size of $\sqrt{s^*}$ is adapted to how strongly the cross-section varies with the centre-of-mass energy: Around the radiative return to the Z boson the bin size is 1 GeV to get a better description of the peak. For high values of $\sqrt{s^*}$ the dependence on the centre-of-mass energy is small and the bin size is 10 GeV and for centre-of-mass energies below the radiative return it is 5 GeV.

As the neutrino events are combined to an unpolarised data set, the cross-sections are calculated without beam polarisation. Analogously to the WIMP cross-section, three maps with different θ ranges are calculated. As the cross-sections maps look similar, only the cross-section map for the example with $p_{T,\gamma,min} = 1.92\,\text{GeV}$ is shown figure 7.5c. Whereas the sharp band of the radiative return is very similar, the remaining phase space differs with respect to the Monte-Carlo events in figures 7.5a and 7.5b. The cross-section map is flatter and especially the rise towards $\sqrt{s} =$

500 GeV is absent. This difference is expected because the cross-section is folded with Φ (see equation 7.9) in the case of the events. This also explains why the overall scale is different.

7.2 Effect of polarisation and luminosity on the sensitivity

In this section the role of beam polarisation and integrated luminosity for the expected WIMP exclusion limits is presented. In order to study the effect of the individual parameters, simplified setups are used in sections 7.2.1, 7.2.2 and 7.2.3 where it is assumed that the complete data set is taken at a certain polarisation combination, whereas in a realisic operation scenario the integrated luminosity is expected to be split over all possible polarisation combinations. For this simplified setup, the full integrated luminosity of the ILC 20 years programme is not suitable and hence only 500 fb^{-1} are assumed, corresponding to the first 4 years of the H20 scenario (see section 3.4).

First, the sensitivity to the different effective operators is presented for the simple setup of unpolarised beams (see section 7.2.1). In the following, the role of beam polarisation is evaluated: In section 7.2.2 different *values* of polarisation are assumed and in section 7.2.3 all possible polarisation *combinations* are studied. In section 7.2.4 it is assumed that the data is collected with several polarisation combinations. Finally, the effect of the integrated luminosity is shown (see section 7.2.5).

All results are for $\sqrt{s} = 500\,\text{GeV}$, i.e. the centre-of-mass energy of the full simulation. The effect of systematic uncertainties, which will be introduced in section 7.4, are taken into account.

7.2.1 Vector, axial-vector and scalar operators

The expected 2σ exclusion limits for different effective operators (introduced in section 2.4.1.1) are compared in figure 7.6. At a centre-of-mass energy of 500 GeV and an integrated luminosity of 500 fb^{-1} with unpolarised beams the reachable energy scales are in the range of $\Lambda = 1.4 - 1.5\,\text{TeV}$. WIMP masses up to almost half the centre-of-mass energy can be tested. For low WIMP masses the sensitivity for a vector and axial-vector operator is the same and higher than for the scalar operator. Towards higher WIMP masses the sensitivity decreases. In the case of the vector operator the plateau with constant testable energy scales continues to significantly higher WIMP masses than for the other operators, because of the different mass dependence of the cross-section formula (equation 2.28).

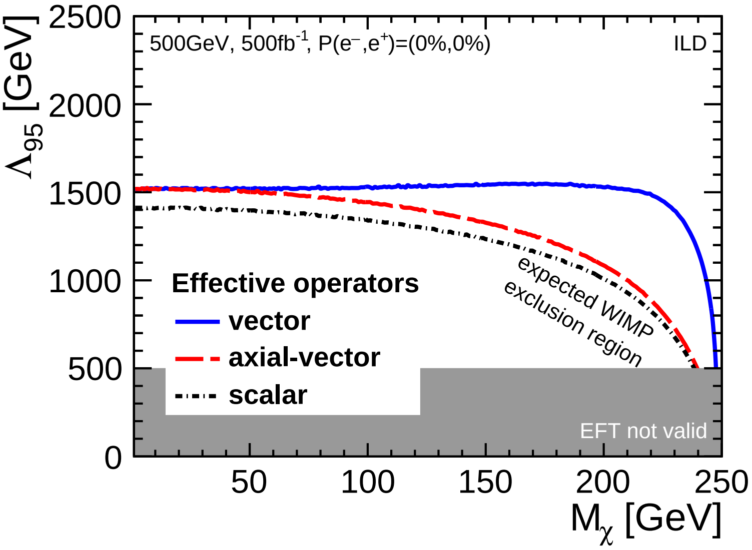

Figure 7.6: Comparison of the expected 2σ exclusion limits for different effective operators, for the example of a centre-of-mass energy of 500 GeV, an integrated luminosity of 500 fb^{-1} and unpolarised beams.

7.2.2 Impact of beam polarisation

In order to study the effect of beam polarisation, four cases are compared: (1) both beams unpolarised, (2) only polarised electrons with +80% and additional positron polarisation with (3) −30% and (4) −60%.

In figure 7.7a the background photon spectra for the different polarisation combinations are shown. As expected from the numbers of selected events in table 6.2 on page 124, the electron beam polarisation helps to reduce the background considerably. For unpolarised beams the number of neutrino background events surviving all selection criteria is 3495 per fb^{-1}. For 80% right-handed electrons and 30% left-handed positrons the number can be reduced by a factor of ∼5 to 762 events. Taking the Bhabha scattering events into account, which are 113 for both cases, the number of background events can be reduced by a factor of ∼4.

With left-handed positrons the total number of background events can be further reduced, especially at lower energies. At the highest energies the background rises instead, because the contribution of events mediated by a Z boson increases for which energies around the radiative return are favoured (see also figure 5.8).

If only the electrons are polarised, the photon energy spectrum of the signal remains unchanged, because the considered processes have the same cross-sections

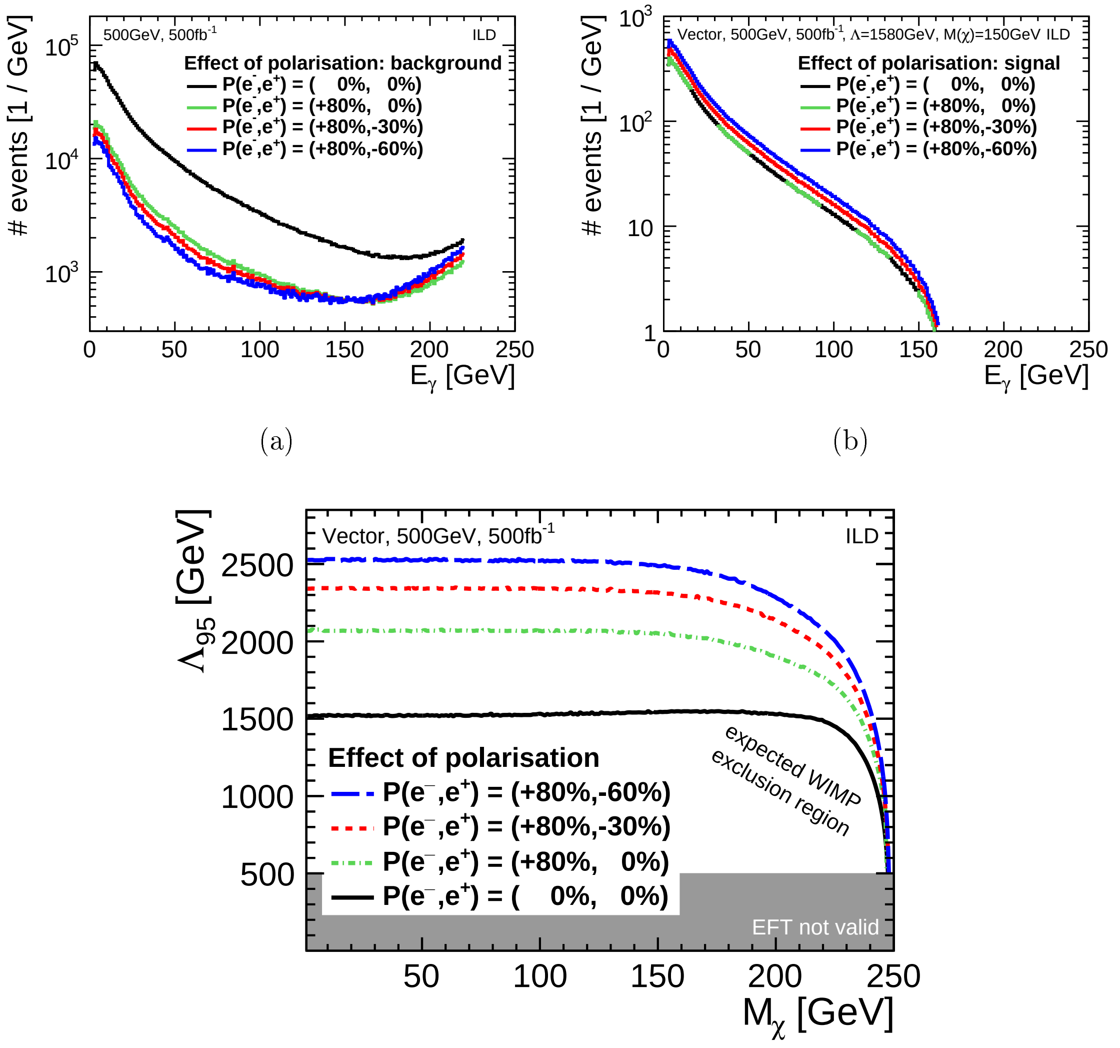

(a) (b)

(c)

Figure 7.7: Effect of the beam polarisation on the photon spectra of background (a) and signal (b) and the corresponding sensitivity for the example of the vector operator at 500 fb^{-1}.

for either both opposite polarisation combinations and cannot be produced with like-sign polarisation (vector) or the other way around (axial-vector and scalar). Only if both beams are polarised, the signal cross-section is modified. In figure 7.7b the case of a vector operator for an assumed WIMP mass of 150 GeV is shown, where the signal increases with the fraction of positrons with the opposite helicity than the electrons.

As shown in figure 7.7c the sensitivity for a vector operator increases significantly for polarised beams. Here, the role of the polarisation of both beams is more pronounced than in figures 7.7a and 7.7b, because the signal increases at the same time as the background decreases. At an integrated luminosity of 500 fb^{-1} the expected exclusion limit is up to 60% improved by beam polarisation.

Also the shape of the excluded region changes with polarisation. For unpolarised beams the flat part of the curve extends to almost the highest WIMP masses and the reachable Λ even increases slightly with mass, whereas with higher polarisation values the decrease of the sensitivity starts at lower WIMP masses.

Even though the kinematically maximum possible photon energy (see equation 5.1) cannot be resolved because of the high background level (see figure 7.1a), the constraint range of the signal photon energy is important because at higher energies there is a signal-free control region. In the unpolarised case the sensitivity to higher WIMP masses is therefore better than to low masses. With polarisation the background at highest energies rises and hence the effect of the control region is diminished. The influence of the systematics is further discussed in section 7.6.

7.2.3 Different helicity combinations

Wheareas the combination of right-handed electrons and left-handed positrons is the optimal case to suppress the background, it depends also on the chirality of the assumed signal process which setting leads to the best exclusion limits. In figures 7.8a, 7.8b and 7.8c sensitivities for all possible helicity combinations are shown for the vector, axial-vector and scalar operators, respectively. For each curve the full data, corresponding to an integrated luminosity of 500 fb^{-1}, is assumed to be taken with the same polarisation setting, which is not a realistic running scenario. The purpose of this study is to identify suitable setups for the different operators.

In the case of the vector operator the sensitivity can be improved for right-handed electrons compared to unpolarised beams, because the neutrino background can be suppressed. The optimal case is (+80,−30) which is favoured over (+80,+30) because the WIMP production cross-section vanishes for like-sign polarisation (see equation 2.28). In the case of left-handed electrons the positron polarisation only has a minor effect on the result because the improved neutrino suppression for (−80,−30) is balanced out by a higher signal cross-section at (−80,+30).

Both axial-vector and scalar mediators can only be produced for like-sign polarisations (see equations 2.29 and 2.30), consequently the preferences of beam polarisation are the same for the two operators. Also here right-handed electrons are

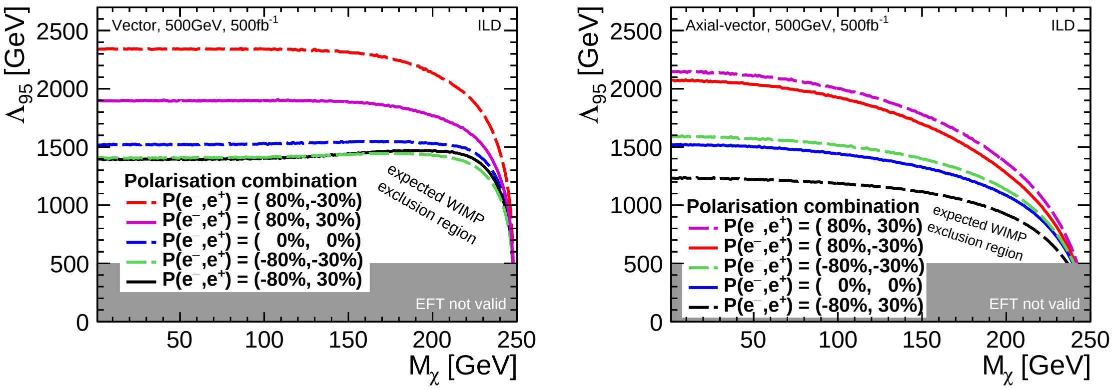

(a) Vector

(b) Axial-vector

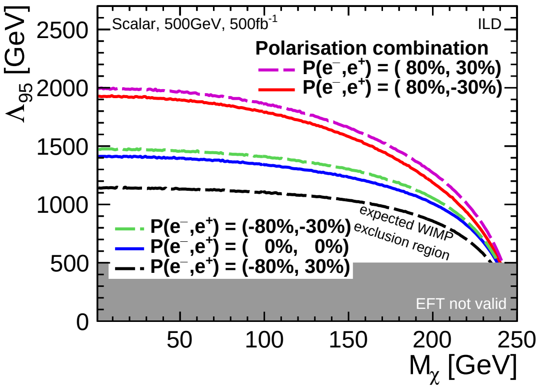

(c) Scalar

Figure 7.8: Effect of different polarisation combinations of $P(e^-) = \pm 80\%$ and $P(e^+) = \pm 30\%$ on the expected exclusion limits at $500\,\text{fb}^{-1}$ for different operators: (a) vector, (b) axial-vector and (c) scalar.

prefered because of background suppression. The optimal case is (+80,+30) where the signal cross-section is enhanced. For (−80,−30) on the other hand the higher signal production is compensated by the moderate neutrino background level and the limits are at a comparable level as for unpolarised beams. The worst scenario is (−80,+30) with high neutrino background and suppressed signal production.

For every polarisation combination higher Λ values can be tested for the axial-vector than for the scalar operator. The overall highest scales can be probed in case of the vector operator with a polarisation combination of (+80,−30).

In the case of the vector operator the same polarisation-dependent shape of the curve can be seen as discussed in section 7.2.2. The larger the share of left-handed electrons and right-handed positrons, the smaller the background at highest photon energies and hence the larger the advantage of the signal-free control region. In the case of axial-vector and scalar operator the cross-section to produce high WIMP masses is so small that no effect can be seen.

7.2.4 Polarisation combinations in an ILC running scenario

To fully exploit the potential of the beam polarisation at the ILC, the machine will switch between the polarisation combinations rather than collecting data at only one configuration as assumed so far. With a realistic polarisation sharing, the initial 500 fb^{-1} could be distributed according to the running scenario H20 (see table 3.1 on page 52): 200 fb^{-1} each with the opposite sign polarisation combinations $P(e^-, e^+) = (\pm 80\%, \mp 30\%)$ and 50 fb^{-1} each for the same sign combinations $(\pm 80\%, \pm 30\%)$ or in a short notation, which is used throughout this and the next chapter: $(--, -+, +-, ++)$ = (10%,40%,40%,10%). The corresponding exclusion limits can seen in figure 7.9. A comparison with the unpolarised case (figure 7.6) shows that all sensitivities can be significantly improved with a combination of polarisation combinations. With $\Delta\Lambda \approx 800$ GeV at low WIMP masses the improvement is largest in the case of the vector operator, which profits from the large data sets of opposite polarisation, where its cross-section is enhanced. The testable energy of axial-vector and scalar operators is enlarged by more than 600 GeV.

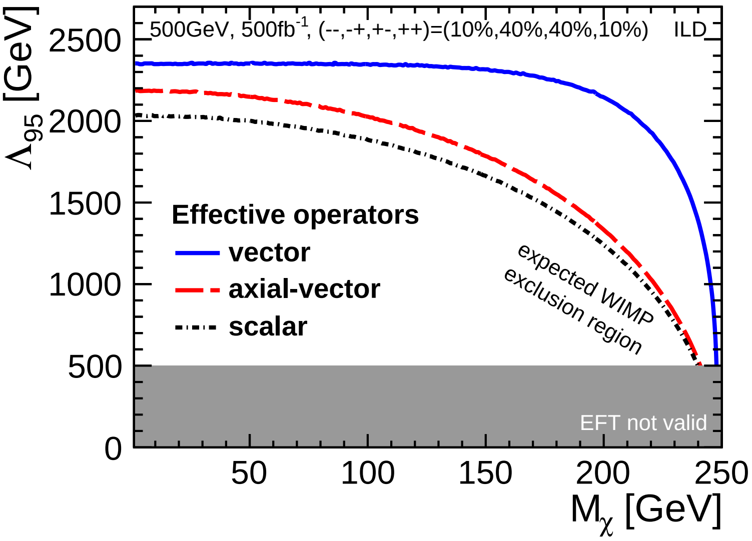

Figure 7.9: Comparison of the sensitivity to different operators for a realistic sharing of the polarisation at 500 fb^{-1}, corresponding to the first four years of the H20 scenario.

For all three operators the expected exclusion limits with a mix of polarisation configurations are better than the results with only one data set at the optimal polarisation combination, as shown in figure 7.8. This can be explained by polarisation-independend systematic uncertainties, which can be partially compensated with the combinations of data sets (see section 7.6.2 for a detailed discussion).

7.2.5 Effect of the integrated luminosity

In figure 7.10 the evolution of the reachable energy scale Λ with the integrated luminosity in the range of $50\,\mathrm{fb}^{-1}$ to $5\,\mathrm{ab}^{-1}$ is shown. How the sensitivity increases with the amount of collected data depends on the WIMP mass and the polarisation combination. For the three operators, the WIMP masses 1 GeV and 200 GeV are tested with unpolarised beams, $P(e^-,e^+)$=(+80%,−30%) and the mixing of the H20 scenario (−−,−+,+−,++)=(10%,40%,40%,10%).

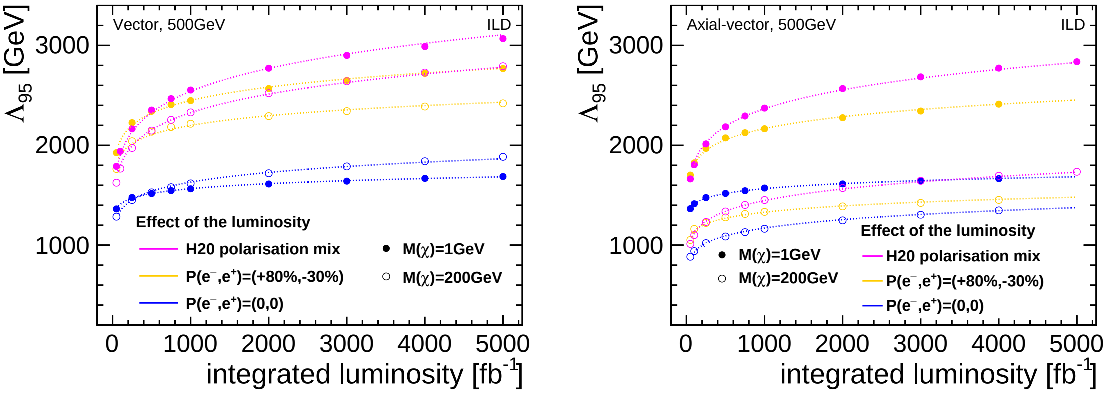

(a) Vector (b) Axial-vector

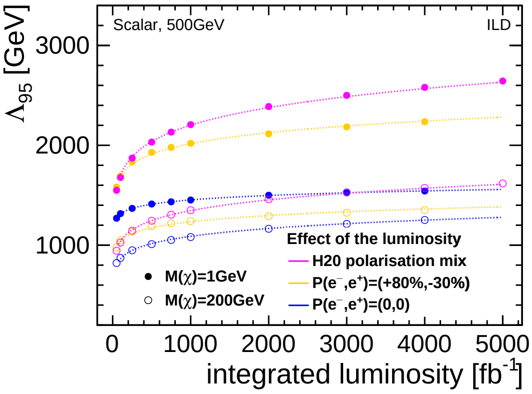

(c) Scalar

Figure 7.10: Scan of the expected exclusion limits over different values of the integrated luminosity for different WIMP masses, polarisation configurations and operators.

In the beginning, the rise is steeper in all cases and around $500 - 1000\,\mathrm{fb}^{-1}$ the curve starts to flatten. The exact slope is quite different from case to case. In table 7.1 the fitted proportionalities are shown. For the respective polarisation configuration the slopes for $M_\chi = 1\,\mathrm{GeV}$ are similar for all operators. The slopes for $M_\chi = 200\,\mathrm{GeV}$ are also similar in the cases of axial-vector and scalar operator.

If the limits are based on several input parameters (like in the H20 scenario) the rise is significantly steeper and almost independent of WIMP mass and operator.

	vector		axial-vector		scalar	
$P(e^-, e^+)$	$M_\chi = 1\,\mathrm{GeV}$	200 GeV	1 GeV	200 GeV	1 GeV	200 GeV
$(0\%, 0\%)$	$\Lambda \propto \mathcal{L}^{1/22}$	$\mathcal{L}^{1/12}$	$\mathcal{L}^{1/22}$	$\mathcal{L}^{1/10}$	$\mathcal{L}^{1/23}$	$\mathcal{L}^{1/10}$
$(+80\%, -30\%)$	$\Lambda \propto \mathcal{L}^{1/13}$	$\mathcal{L}^{1/16}$	$\mathcal{L}^{1/13}$	$\mathcal{L}^{1/15}$	$\mathcal{L}^{1/13}$	$\mathcal{L}^{1/14}$
H20	$\Lambda \propto \mathcal{L}^{1/8}$	$\mathcal{L}^{1/9}$	$\mathcal{L}^{1/9}$	$\mathcal{L}^{1/9}$	$\mathcal{L}^{1/9}$	$\mathcal{L}^{1/9}$

Table 7.1: Proportionalities of the sensitivity Λ to the integrated luminosity $\mathcal{L}$ for the different operators, WIMP masses and polarisation configurations.

Here the effect of the systematic uncertainties is significantly smaller (which will be further discussed in section 7.6.2) and in section 8.4.4 it will be shown that these proportionalities are close to the expectations for statistical uncertainties only ($\Lambda \propto \mathcal{L}^{1/8}$).

In addition to this scan over different values of the integrated luminosity, the full WIMP mass range is compared for two cases corresponding to the first 4 years of operation and the full 20 years assuming the running scenario H20 (see section 3.4). In figure 7.11 the 2σ exclusion limits are shown for the example of the vector operator. With an eight times larger data set the exclusion limit improves by 25%, i.e. from ~2400 GeV to ~3000 GeV in the plateau region.[i]

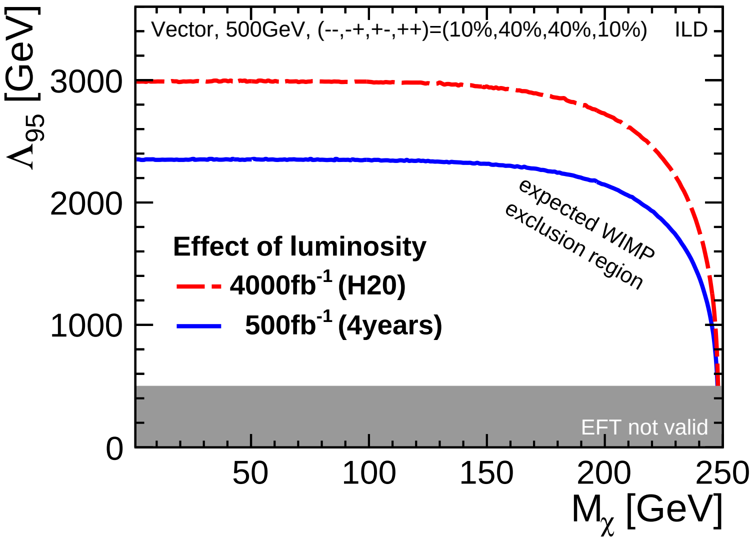

Figure 7.11: Comparison of the sensitivity after 4 years and 20 years of operation for the example of the vector operator.

---

[i] The corresponding limits for the other operators are shown figures 7.9 ($500\,\mathrm{fb}^{-1}$) and 8.1 ($4\,\mathrm{ab}^{-1}$).

7.3 Detector effects

Within the WIMP analysis several requirements on the detector design and the reconstruction could be identified, which serves as important feedback in the ongoing planning phase of the ILD experiment. Three crucial aspects of the detector design are studied in the following: The importance of the hermiticity in the forward region to identify Bhabha scattering is addressed in section 7.3.1. The effect of the imperfections of the photon reconstruction is investigated in section 7.3.2. And the energy resolution is varied to understand its importance (see 7.3.3).

7.3.1 Importance of the suppression of the reducible background

Bhabha scattering is the main source of reducible background. At least one lepton needs to be identified to distinguish Bhabha scattering from signal event. The suppression of the background hence strongly depends on the hermeticity in the forward region of the detector. Due to the high numbers of electron-positron pairs created from beamstrahlung which hit the inner part of BeamCal, the reconstruction efficiency of particles coming from the hard interaction decreases dramatically at very low polar angles θ (see section 4.6.2).

7.3.1.1 Dependence of Λ on the Bhabha scattering background

In order to give a quantitative estimate on how the Bhabha background influences the reachable sensitivity, the number of background events is scaled up or down in the limit calculation. How the expected exclusion limit changes as a function of this modified background level is shown in figure 7.12a. With a better background rejection the improvement would be moderate, i.e. below 10% for 10 times more identified Bhabha scattering events. If, on the other hand, more background events survived the event selection the testable energy scale would drop by several hundred GeV for a 10 times higher reducible background. For even higher background levels the slope of the curve starts to flatten.

7.3.1.2 Influence of the redesign of the forward region

As discussed in section 3.6.5.1, the design of the forward region has been modified since the detector simulation for this analysis was carried out. While a detailed study of the redesign and the implementation in the ILD simulation is ongoing,

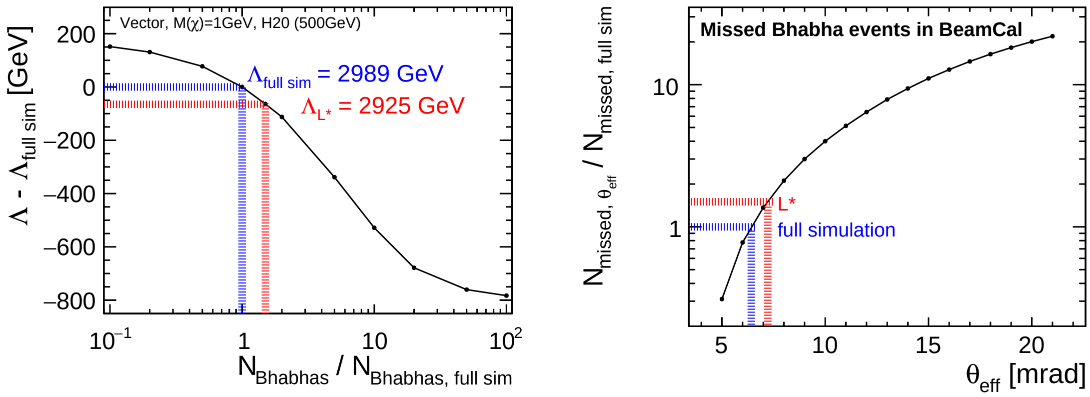

(a) (b)

Figure 7.12: (a) Dependence of the reachable energy scale on the reducible Bhabha scattering background, for the example of a vector operator and a WIMP mass of 1 GeV for the H20 luminosity and polarisation combination. (b) Number of Bhabha scattering events with both leptons below a certain polar angle.

the impact is estimated in the following way: First, it is assumed that the area in BeamCal polluted by the pairs is the same for all considered distances. Second, the lepton reconstruction efficiency is approximated to be 100% for polar angles above an effective angle θ_{eff} and 0% below, instead of the smooth transition as visible in figure 4.10 on page 83. With these simplifications, the hermeticity in the forward region depends purely geometrically on the distance of BeamCal to the interaction point. This means that the effective polar angle grows linearly with the distance by which BeamCal is moved in towards the interaction point, as shown in the sketch in figure 7.13.

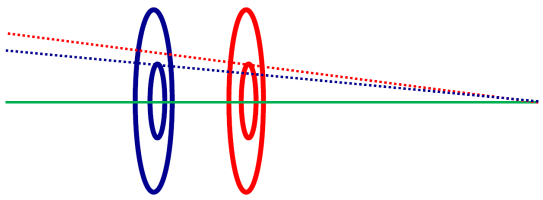

Figure 7.13: Sketch to visualise the effect of a smaller distance of BeamCal to the interaction point.

Figure 7.12b shows the number of Bhabha scattering events with both leptons not being reconstructed, i.e. lying within an effective polar angle, normalised to the number of events with both leptons not being reconstructed using the full detector simulation, which corresponds to $\theta_{eff} \approx 6.42$ mrad. The blue bands show the situation for the detector design of the Technical Design Report [99] and the red bands indicate the BeamCal which is moved 40 cm closer to the interaction point, which results in $\theta_{eff} = 6.42\,\text{mrad} \cdot \frac{z+40\,\text{cm}}{z} = 7.22\,\text{mrad}$, where $z = 359.5\,\text{cm}$ is the distance of BeamCal to the interaction point in the full simulation.

With the new position of the subdetector, the Bhabha background is estimated to be 50% higher. As shown in figure 7.12a the reachable energy scale Λ would only be about 2% lower. This means that the redesign of the forward region has no significant impact on the WIMP study. If however the blind region became even larger, the background would increase drastically.

7.3.2 Impact of the photon reconstruction imperfections

The imperfections of the photon reconstruction (discussed in section 5.5) lead to significant deviations in the photon distributions (presented in section 6.2). The influence on the effective operator limits is studied by comparing the limits of the full simulation to those obtained using information from the generator level, smeared with the energy resolution of the electromagnetic calorimeter, as described in section 6.2.

The resulting Λ values differ by a few per cent from the corresponding results using the reconstructed photons. For the example of unpolarised beams, $500\,\text{fb}^{-1}$ and the vector operator, the expected exclusion limits are up to 3% higher, as shown in table 7.2. This difference is at an acceptable level and hence the reconstructed events can be used to obtain sensible values of the testable energy reach, despite the reconstruction imperfections.

7.3.3 Testing the impact of the ECAL resolution

The importance of the ECAL energy resolution can be studied by modifying the Gaussian σ when the events from generator level are smeared. As discussed in section 3.6.6, the energy resolution of the electromagnetic calorimeter in the ILD detector design is limited because of its high granularity.

The assumed optimal energy resolution is $\sigma_E/E = 1\%/\sqrt{E}$, where the constant term is assumed to be absent. This is significantly better than the resolution at CMS ($2.8\%/\sqrt{E} \oplus 0.3\%$ [133]). As shown in table 7.2, the effect of the different energy resolution can be neglected. It can be concluded that the foreseen energy resolution is sufficient for the WIMP search.

	Λ_{95} [GeV] (vector, H20)			
	$M_\chi = 1\,\text{GeV}$		$M_\chi = 200\,\text{GeV}$	
full simulation	2989		2728	
MC true energies smeared	3076	(+3.0%)	2792	(+2.3%)
optimal ECAL σ_E/E	3074	(+2.9%)	2804	(+2.8%)

Table 7.2: Impact of the photon reconstruction and ECAL energy resolution on the expected exclusion limits for the vector operator, assumed WIMP masses of 1 GeV and 250 GeV at $\sqrt{s} = 500\,\text{GeV}$ with integrated luminosity and polarisation mixing of the H20 running scenario.

7.4 Sources of systematic uncertainties

Five different sources of systematic uncertainties are taken into account: luminosity spectrum, luminosity, beam polarisation, event selection and the cross-section (theory). The largest uncertainties are those of the luminosity spectrum, which are hence treated in more detail (see section 7.5).

In most cases the uncertainty is implemented as a global relative uncertainty with values in the per mill range. Only in the case of the luminosity spectrum the systematics are calculated for different photon energies, i.e. they are fed in as histograms with different values for the upper and lower uncertainty.

The considered systematic uncertainties are supposed to be examples to study the effect. More sources, like the detector effects (section 7.3) could be included as well, but from a technical point of view the source of the uncertainties is irrelevant. Different setups are implemented, like polarisation-dependent and E_γ-dependent systematic uncertainties. In section 7.6.4 it will be shown that additional uncertainties would modify the sensitivity only slightly, as long as they are at the same order of magnitude.

7.4.1 Luminosity

The luminosity of the ILC is planned to be measured by counting Bhabha scattering events, reconstructed as coincident showers in the forward detectors LumiCal, one on each side [121, 172]. With GuineaPig [137] and Bhlumi [163, 164] simulations, the different sources of uncertainty were investigated. The largest individual uncertainties, coming from the luminosity spectrum, the physics background of four fermion processes and beam-induced effects, are in the per mill range, adding up to a total systematic uncertainty of 2.6‰ [121, 172].

7.4.2 Beam polarisation

The beam polarisation can be measured directly via laser-Compton polarimeters, 1.65 km upstream and 150 m downstream of the interaction point [173,174]. In order to obtain the polarisation at the interaction point, spin tracking is used, resulting in a systematic uncertainty of 2.5‰ [175].

These measurements can be combined with collision data, i.e. with measurements from the interaction point directly [176]. This leads to significantly better precisions for the nominal polarisation values of $P(e^-) = \pm 80\%$ and $P(e^+) = \pm 30\%$, as shown in table 7.3.

$\Delta P^-_{e^-}/P = 0.8‰$	$\Delta P^+_{e^-}/P = 0.2‰$	[176]
$\Delta P^-_{e^+}/P = 0.4‰$	$\Delta P^+_{e^+}/P = 0.8‰$	
other polarisation values: 2.5‰		[175]

Table 7.3: Relative polarisation uncertainties for $\sqrt{s}$=500 GeV and 3.5 ab^{-1}.

For unpolarised positron beams it could be shown, that the systematics cannot be lowered with respect to the polarimetry measurements by using collision data [177]. As a consequence, for this case the systematic uncertainty of the polarimetry measurement (2.5‰) is taken, neglecting effects from spin precession and depolarisation in collision. Without any detailed studies for other polarisation values (like $P(e^-) = 0\%$ or $P(e^+) = 60\%$) also here 2.5‰ is taken[ii].

In the exclusion limit calculation, the uncertainty on each beam is given individually, according to the respective polarisation of the beam.

7.4.3 Event selection

A theoretically well known Standard Model process with a low uncertainty on the cross-section, like the photon energy peak at the radiative return to the Z boson can be used to estimate the signal efficiency ϵ_{sig}, i.e. the product of reconstruction and selection efficiency. In the previous analyses [1–3], the uncertainty on the efficiency was taken from a fit of a Gaussian distribution to the peak. This gave a relative uncertainty of $\delta\epsilon_{sig}/\epsilon_{sig} = 0.43\%$ for $\mathcal{L} = 500\,\mathrm{fb}^{-1}$ [1, 2].

The uncertainty is assumed to scale with the integrated luminosity. By assuming

---

[ii] For $P(e^+) = 60\%$ this is a conservative estimate because a higher polarisation is expected to improve the uncertainty.

$4\,\mathrm{fb}^{-1}$, corresponding to the full running scenario (see section 3.4) this is reduced to

$$\sigma_{\epsilon_{sig},4\,\mathrm{ab}^{-1}} = \sqrt{500\,\mathrm{fb}^{-1}/4\,\mathrm{ab}^{-1}} = 0.2\%. \tag{7.11}$$

7.4.4 Cross-section and number of photons

The ambiguity of the minimum transverse momentum cut on additional photons in the case of more than one matrix element photon leads to a large uncertainty on the cross-section calculation of 3.5% (see section 5.4.1.2).

The uncertainty is expected to be significantly smaller, because initial state radiation is in principle calculable and a better treatment in the event generator WHIZARD is under development. By the time the ILC is operating a theory uncertainty in the range of the value calculated for the individual generated processes can be expected, as shown in table 5.4 on page 104. In order to give a more realistic estimate a typical value from the matrix element calculation O'MEGA of 1.3‰ is hence assumed as theory uncertainty in the sensitivity calculation. The effect of the larger value of 3.5% is evaluated in section 7.6.4.

7.4.5 Systematic uncertainties used in the standard sensitivity calculation

In table 7.4 the set of systematic uncertainties is summarised, which is used in the calculation of the results presented in this and the following chapter, with the exception of section 7.6, where alternative settings are tested. The largest values come from the uncertainty on the luminosity spectrum shape. All other systematics are one order of magnitude smaller. Even though high integrated luminosities are assumed for some of the values (polarisation and selection), the same settings are taken for setups with smaller integrated luminosities. This simplification can be justified, because the determination of the dominating uncertainty on the luminosity spectrum is independent of the integrated luminosity.

The fraction of correlation f_{corr} between the individual bins of the input distributions can be set in TSYSLIMIT. Uncorrelated uncertainties can be addressed with the parameter f_{uncorr}, where $\sqrt{f^2_{\mathrm{uncorr}} + f^2_{\mathrm{corr}}} = 1$. The uncorrelated part of the uncertainties are added in quadrature to the statistical uncertainty. For the standard exclusion limits, the variations of each systematic uncertainty are assumed to be fully correlated from bin to bin of the background and signal histograms and also

source of systematics	range of values in standard setting	see section
luminosity spectrum	$\leq 3\%$ (dependend on E_γ, M_χ and polarisation)	7.5
luminosity	2.6‰	7.4.1
polarisation	$0.2 - 2.5$‰ (see table 7.3)	7.4.2
event selection	2.0‰	7.4.3
theory	1.3‰	7.4.4

Table 7.4: The systematic uncertainties included in the WIMP exclusion limit calculation.

fully correlated between signal and background. The impact of alternative values will be discussed in section 7.6.

7.5 Evaluation of the uncertainties induced by the luminosity spectrum

In the previous WIMP searches [1–3] the description of the uncertainty of the luminosity spectrum was incomplete. At the same time it was assumed to be the largest source of systematic uncertainties. Therefore, a new approach was developed in the context of this thesis.

In order to measure the luminosity spectrum and hence obtain the systematic uncertainty, the distribution of centre-of-mass energies must be determined, for example by using Bhabha scattering [178]. Alternatively, the beam parameters can be extracted from measurements of beam-induced background processes [130]. And with the paramaters the beam energy spectrum can be predicted by modelling the beam-beam interactions (see section 4.2).

In this study the beam parameter measurements are used as input to simulations of the beam-beam interactions. As the determination of beam parameters is performed during run time, the presented approach is expected to be conservative compared to [178], where event numbers corresponding to a significantly higher integrated luminosity are used.

Depending on the relative height and shape of peak and tail of the luminosity spectrum, the cross-section to produce different photon energies varies. Therefore, the uncertainties are included in the limit calculation as a histogram with values for different photon energy bins.

7.5.1 Approach in the previous studies

The values for the systematic uncertainties implemented in the limit calculation in [3] were based on a simplistic estimate performed in [1,2]. The signal photon spectrum was compared for data sets with two different luminosity spectra, RDR [179] and SB-2009 [180]. The relative difference (shown in figure 7.14) was simply taken as uncertainty. Therefore, the uncertainty was implemented in the limit calculation in the shown 10 GeV bins from 10 (the minimum photon energy in [1–3]) to 110 GeV. Higher energies were not taken into account, because with the choice of a high WIMP mass of 150 GeV the statistics above $E_\gamma = 110\,\text{GeV}$ were too low.

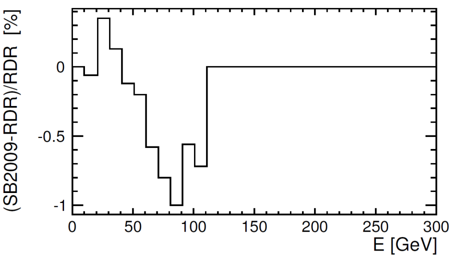

Figure 7.14: The relative difference of photon energies in WIMP events assuming $M_\chi = 150\,\text{GeV}$ for two different luminosity spectra was used as an estimate of the uncertainty on the luminosity spectrum in the previous WIMP studies. Taken from [3].

In the range of 10-20 GeV, which dominates the photon energy spectrum (see figure 7.1a), the deviation is very small. The cross-section of photons between 20 and 40 GeV is larger for the SB-2009 setup, whereas higher energetic photons occur more often for the RDR beam energy spectrum. The largest uncertainties are up to 1%.

In conclusion, this approach was not suitable for a realistic estimate of the luminosity spectrum systematic for two reasons. On one hand, the comparison of different beam configurations cannot give a clear answer to the uncertainty within one configuration. On the other hand, the considered energy range is too small. The cut on higher energies can be justified for massive WIMPs but simply translating the uncertainties to the background spectrum (or to photon spectra of ligher WIMPs) is not feasible, because they have a substantial fraction of photons with higher energies. Additionally, energies below 10 GeV, which are allowed in the updated signal definition (see section 5.3), are not included.

7.5.2 New approach using run time information

The idea of the new approach is to obtain the uncertainties from the determination of the luminosity spectrum using measurements of beam-induced pair background and beamstrahlung photons (introduced in sections 3.5.3.1 and 3.5.2, respectively) during run time. The energy depositions of beam-induced background in the forward region can be used to determine the beam parameters in a multi-parameter fit [130], see section 7.5.4 for more details. The uncertainties on the individual parameters are used as a conservative estimate of the uncertainty on the shape of the luminosity spectrum.

Two sets of simulations of the beam-beam interactions using GuineaPig [137] (see section 4.2) are run. As a first step, the beam parameters, which have a significant influence on the shape of the luminosity spectrum, are identified (see section 7.5.3).

In the second step 200 beam-beam interaction are simulated (see section 7.5.5) with different values of the identified relevant beam parameters, varied within the fit uncertainties. In this way the fit uncertainties are translated into a variation of the luminosity spectra.

Finally, the photons of the background data sets are reweighted according to these varying spectra (see section 7.5.6). The strategy to get the uncertainties on the signal is explained in section 7.5.7 and the polarisation-depended values of the uncertainties are presented in section 7.5.8.

7.5.3 Influence of the beam parameters on the luminosity spectrum

In order to focus on the crucial parameters, the influence of the individual beam parameters on the luminosity spectrum is evaluated, by simulating the beam-beam interaction in GuineaPig runs with one beam parameter modified at a time and all other parameters at their nomial values according to the Technical Design Report [98]. In this preparational step both beams are assumed to be fully correlated, meaning that the modification of a beam parameter is applied on both beams simultaneously. As a measure for the influence on the shape, the average energy losses of the electron and positron bunches are compared to the nominal values. Parameters only modifying the luminosity but not the shape of the spectrum are not considered, because the luminosity is measured independently of this fit by counting Bhabha scattering events in LumiCal in the forward region of ILD [172].

The nominal energy loss is determined by running GuineaPig with the default values. On average the electrons lose $\delta E_{nominal} = 11.70\,\text{GeV}$ and the positrons $\delta E_{nominal} = 11.67\,\text{GeV}$, or 4.7% in both cases, which is very close to the value of 4.5% given in the Technical Design Report [98].

In table 7.5 the beam parameters (introduced in section 3.5.1) are shown with their nominal value and a 10% higher value which was used to test its influence. In the case of the waist the value is modified by 250 μm. The horizontal beam size σ_x was not modified itself but relates to horizontal beta function β^*_x and emittance ϵ_x as $\sigma = \sqrt{\epsilon\beta^*}$. In GuineaPig an equivalent setting of two of the three parameters leads to the same description. In [130] σ_x and ϵ_x were fitted and hence β^*_x is not considered in the following.

The parameters causing a significantly different energy loss are the number of particles in the bunches N, the horizontal beam size σ_x and emittance ϵ_x. These three parameters are varied together in the following GuineaPig runs (see section 7.5.5).

beam parameter	nominal value	modified value	unit	δE/δE$_{nominal}$	
				e^-	e^+
N	2	2.2	10^{10}	**1.186**	**1.180**
$\gamma\epsilon_x$	10	11	10^{-6} m rad	**0.882**	**0.892**
σ_x	474	497	nm	**0.885**	**0.891**
β^*_x	11	12.1	mm	0.885	0.891
β^*_y	5.9	6.2	nm	1.003	1.000
$\gamma\epsilon_y$	0.035	0.039	10^{-6} m rad	1.002	0.991
σ_z	300	330	μm	0.965	0.959
waist$_x$	0	250	μm	0.987	0.991
waist$_y$	250	500	μm	0.988	0.981
E spread e^-	0.24	0.136	%	0.999	1.020
E spread e^+	0.070	0.077	%	0.999	1.020

Table 7.5: Influence of beam parameters on the average energy loss per particle. The change in δE in comparison to the value for nominal beam parameters $\delta E_{nominal,e^-} =$ 11.70 GeV and $\delta E_{nominal,e^+} =$ 11.67 GeV is given for GuineaPig runs where the modified values were used individually.

7.5.4 Fitting beam parameters to measurements

In [130] different observables are used to fit the beam parameters. The measurements of the beam-induced pair background measured in BeamCal and, optionally, the beamstrahlung photons measured in GamCal[iii] serve as input to the beam parameter determination. Observables comprise for example the total energy, spatial

---

[iii] GamCal is a very forward detector, at a distance of 180 m from the main detector.

distributions of the energy depositions, and to imitate input from GamCal the total energy of beamstrahlung photons is taken from Monte Carlo information. A multi-parameter analysis can be performed where these observables are fitted to a function of the beam parameters [130].

In table 7.6 the resulting reconstructed values for the relevant beam parameters (number of particles N, horizontal beam size σ_x and horizontal emittance ϵ_x) are shown for the fits performed in [130]. As the forward detector GamCal is not included in the Technical Design Report nor in the general detector simulation, two data sets, with and without the measurement of the photon energy are used to determine the systematic uncertainty of the luminosity spectrum. For the default settings in the limit calculation the realisation of GamCal is assumed. The importance of this sub-detector is evaluated with the second set (see section 7.6.4).

beam parameter		nominal value	reconstructed value without GamCal		reconstructed value with GamCal		unit
number of	N	2.0	2.001	± 0.004	2.002	± 0.003	10^{10}
particles	ΔN	0	0.000	± 0.011	0.000	± 0.011	
horizontal	σ_x	474	473.8	± 2.0	473.1	± 0.9	nm
beam size	$\Delta\sigma_x$	0	2.8	± 4.2	-0.6	± 1.5	
horizontal	$\gamma\epsilon_x$	10	9.8	± 1.9	9.8	± 1.9	10^{-6} m rad
emittance	$\Delta\epsilon_x$	0	0.6	± 1.2	0.6	± 1.2	

Table 7.6: Nominal and reconstructed values for beam parameters. Excerpt of table 1 in [130].

7.5.5 Impact of the beam parameter uncertainties on the beam energy spectrum

In a second set of 200 GuineaPig runs the three beam parameters N, σ_x and ϵ_x are varied simultaneously within the uncertainties from the fit in [130] (see table 7.6). The values are picked randomly from a normal distribution around the nominal value with the fit uncertainty as Gaussian standard deviation. The parameters of the electron and positron beams are changed individually according to the fitted ΔN, $\Delta\sigma_x$ and $\Delta\epsilon_x$. This results in variations of the luminosity spectrum in height and shape. In figure 7.15 the average spectrum of the 200 beam energy spectra is shown, where the uncertainties indicate the size of variation.

The 200 beam energy spectra also have different integrals, i.e. different integrated

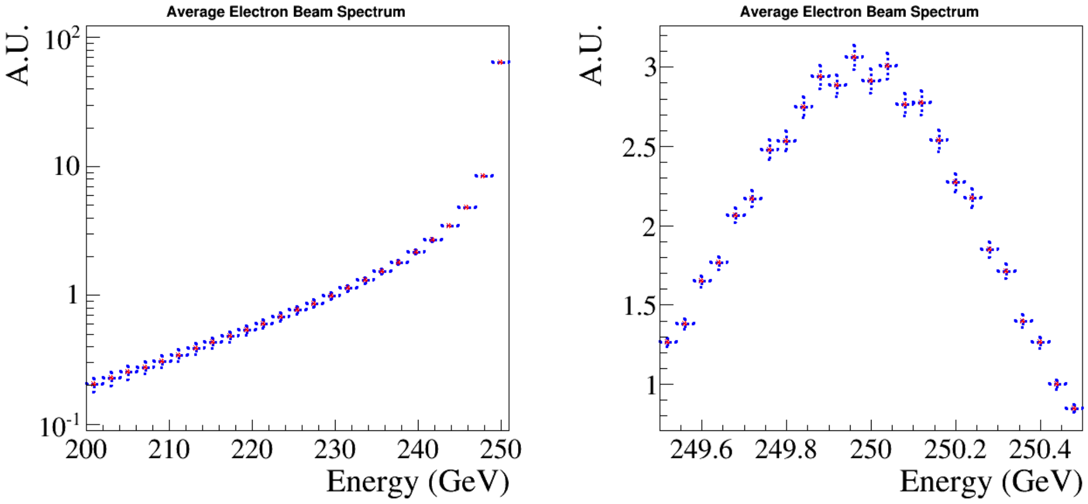

(a)

(b)

Figure 7.15: Average of the electron beam energy spectrum obtained by varying the beam parameters N, σ_x and ϵ_x within the uncertainties from the fit.

luminosities. The average is $2.61 \cdot 10^{34}\,\mathrm{m}^{-2}$ per bunch crossing and the standard deviation is $1.28 \cdot 10^{33}\,\mathrm{m}^{-2}$ per bunch crossing. As the luminosity will be measured independently, the individual spectra from each beam-beam interaction simulation are normalised to obtain solely the information on the shape. In figure 7.16a the bin-wise variation of the normalised luminosity spectra is shown. The bins cover the full range of centre-of-mass energies in the event samples and the bin sizes are adapted to the height of the values.

In order to study the effect of different shapes of the luminosity spectrum within the 1σ uncertainty band, two new distributions are used, refered to as *upper* and *lower envelope* in the following. The upper envelope is constructed by taking the central value plus the 1σ uncertainty in each bin and the lower envelope with the 1σ uncertainty substracted.

Clearly, the integral of the upper (lower) envelope is larger (smaller) than the mean. Again, the height of the different tested luminosity spectra should not vary because the total luminosity is determined independently and hence the envelopes are normalised.

The normalised envelopes are shown in figure 7.16b. The deviation from the average rises with falling centre-of-mass energy. Below 350 GeV the relative difference is about 35%, whereas the statistically more important values closer to the nominal centre-of-mass energy of 500 GeV are in the range of a few per cent. Around 475 GeV the curves intersect and above the normalised lower envelope leads to higher values.

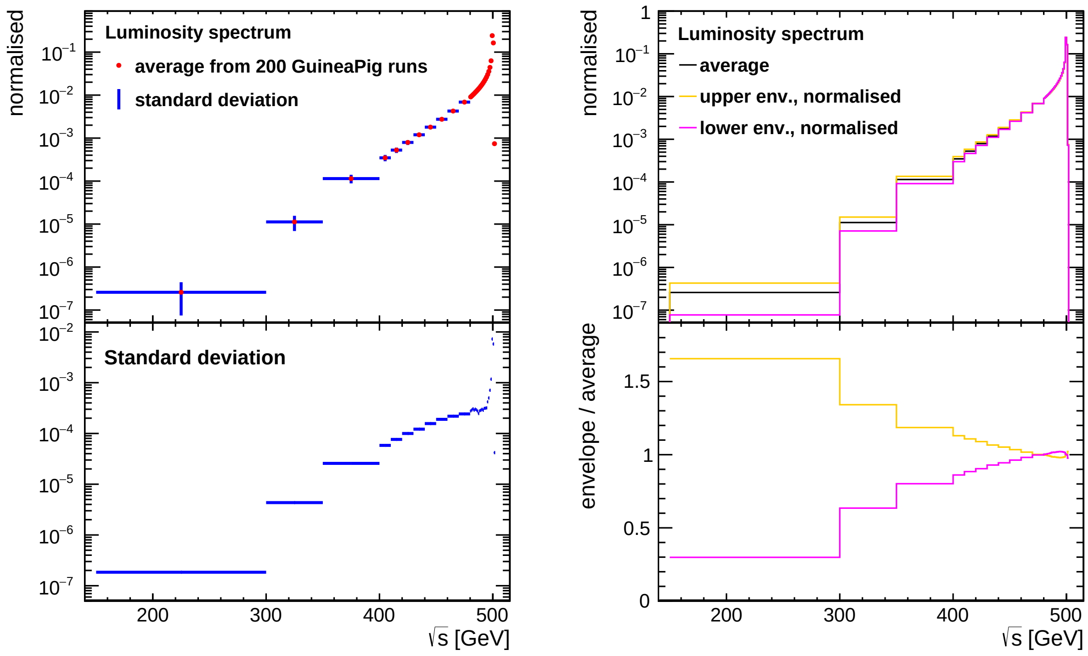

(a)

(b)

Figure 7.16: (a) Average luminosity spectrum shape obtained with 200 simulations where the beam parameters N, σ_x and ϵ_x are varied within the uncertainties from the fit in [130]. (b) Nominal luminosity spectrum and the normalised upper and lower envelopes of the 1σ uncertainties shown in (a).

7.5.6 Uncertainty on the background photon energy spectra

In order to evaluate the influence of the luminosity spectrum uncertainties on the background of the WIMP study, the photon spectrum of the neutrino and Bhabha scattering events is produced using the envelopes shown in the lower part of figure 7.16b. The centre-of-mass energy of the individual selected events is calculated with the energies of the incoming particles taken from Monte Carlo truth information and the event obtains two weights given by the ratio of the normalised upper and lower envelopes to the nominal value in the corresponding bin of the luminosity spectrum. In this way two new photon spectra are created, shown as blue and red curves in figure 7.17.

The deviations are energy-dependent, because different photon energies are sensitive to different ranges of the luminosity spectrum. The higher the photon energy the larger the centre-of-mass energy must be, whereas only the smallest photon energies can be produced with the tails of the luminosity spectrum. This means that higher photon energies are only sensitive to the uncertainties around the nominal centre-of-mass energy, whereas low photon energies are sensitive to the entire luminosity spectrum.

In order to examine the full photon spectrum, the cut on the maximum photon energies of 220 GeV is not applied in the neutrino data sets in the graphs in figure 7.17. In the case of Bhabha scattering the event number decreases rapidly with rising photon energy and thus, the bin sizes are adapted and the very few events above the maximum energy cut are not plotted.

The statistically dominant neutrino data set with left-handed electrons and right-handed positrons (figure 7.17a) has the smallest deviations. The uncertainty increases towards higher energies with maximum values of $\leq$1% around the maximum photon energy of 220 GeV.

In the case of opposite polarisation (figure 7.17b) a stronger dependence can be seen. The central part has the highest deviations, due to photons corresponding to the radiative return to the Z boson, which are shifted to lower energies because of a lower effective centre-of-mass energy in the event. Either the energy is lowered due to the luminosity spectrum, or by the additional ISR photons, or a combination of both effects.

In both neutrino samples, a swap of the dependence can be seen around the Z return. Producing these high photon energies is kinematically possible only with the highest centre-of-mass energies, where (due to the normalisation) the “lower” curve is higher (see figure 7.16b).

In the limit calculation more realistic polarisation fractions below 100% are assumed. For the different polarisation combinations separate sets of values are calculated. In the different photon energy bins j the systematics of the data sets i (as shown in figures 7.17a-c) are reweighting with the corresponding polarisation weights w_{pol} (equation 5.7):

$$\sigma_j^{\text{up/down}} = \sum_i \left(\frac{w_{pol} \cdot N_{i,j}^{\text{upper/lower env.}}}{\mathcal{L}_{MC,i}} \right) \Big/ \sum_i \left(\frac{w_{pol} \cdot N_{i,j}^{\text{nominal}}}{\mathcal{L}_{MC,i}} \right) \tag{7.12}$$

with the integrated luminosities of the data sets $\mathcal{L}_{MC,i}$. The result for unpolarised beams is shown in figure 7.17d and for the other cases in figure 7.20.

7.5.7 Uncertainty on the WIMP photon energy spectra

The systematic uncertainty on the photon spectrum of the signal is obtained by applying the weights according to the normalised envelopes of the individual neutrino

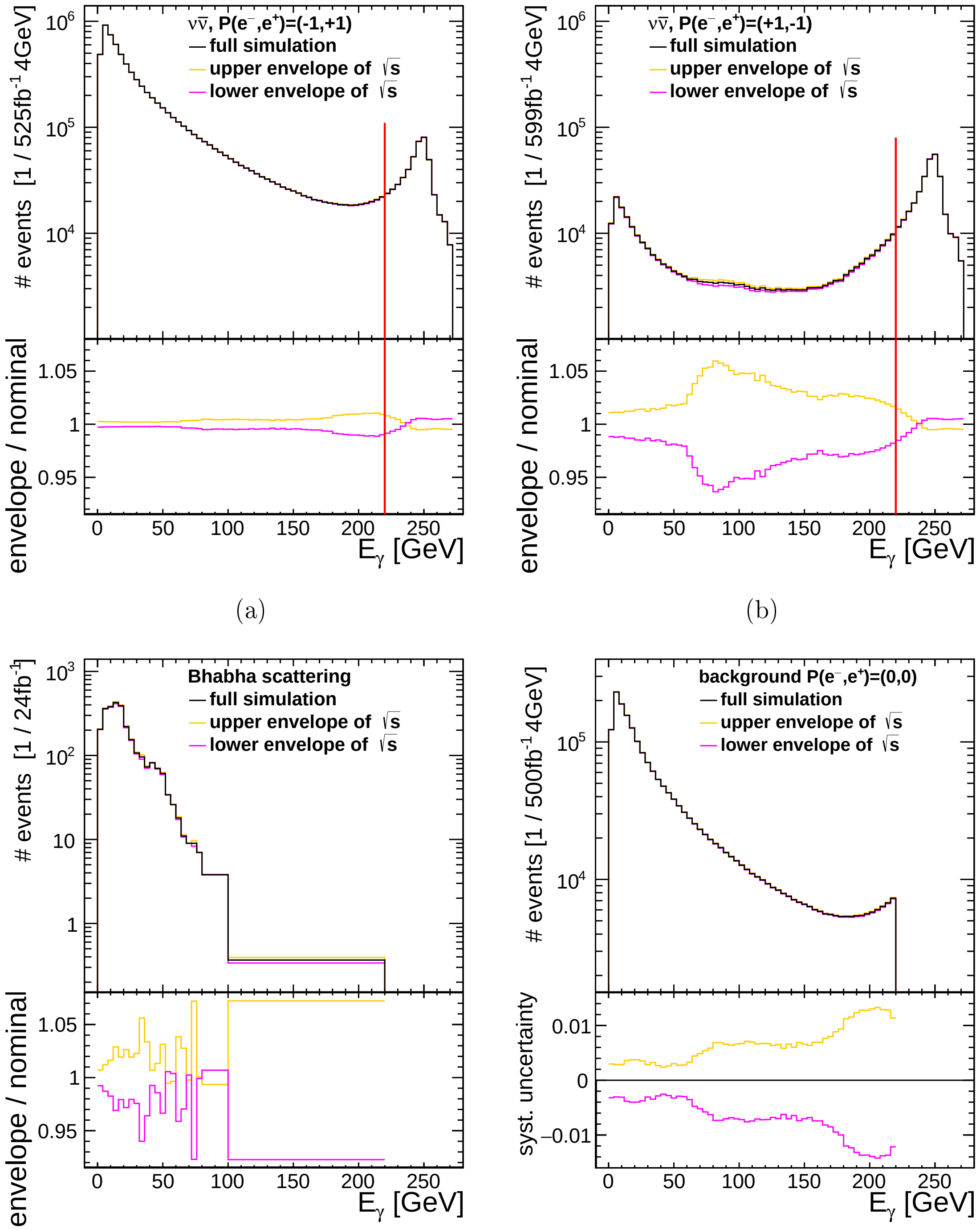

(a)

(b)

(c)

(d)

Figure 7.17: Photon spectrum for the nominal luminosity spectrum and weighted according to the two envelopes, for neutrino events with (a) left-handed electrons and right-handed positrons, (b) right-handed electrons and left-handed positrons and (c) for Bhabha scattering events. The red curves visualise the maximum energy cut of 220 GeV. (d) Total background for unpolarised beams. Statistical fluctuations at the same level as in (d) are also present in (a), but not visible because of different vertical scales.

events, as shown in the lower graphs of figures 7.17a and 7.17b, in the step of reweighting the neutrino events to WIMP events. In this way, also three signal photon distributions are obtained: the nominal and one for the lower and upper envelopes. In figure 7.18 the photon spectra for different WIMP masses are shown. In the central graphs the ratios of the spectra corresponding to the envelopes and the nominal spectra are shown.

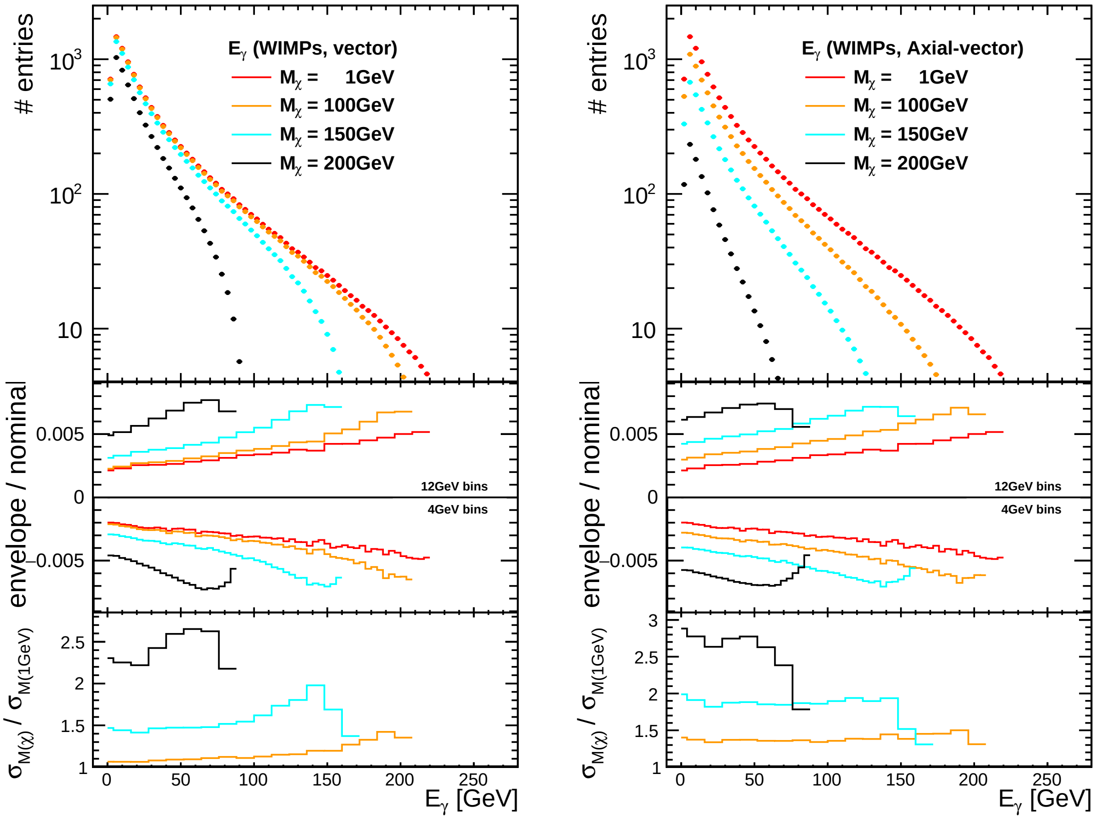

(a) (b)

Figure 7.18: Systematic uncertainty of the luminosity spectrum on the signal as a function of the photon energy, for several WIMP masses and the different operators: (a) vector, (b) axial-vector and scalar.

The systematic uncertainties rise with photon energy, from about 2% to 5% for $M_\chi = 1$. The higher the WIMP mass, the larger the values. In the region below the maximum photon energy, which is kinematically possible for the corresponding WIMP mass, the uncertainties decrease again.

The values for $M_\chi = 1\,\text{GeV}$ are almost the same for all three operators. Also for higher masses the curves for axial-vector and scalar operator are the same, because of the similar shape of the exclusion limit curves, meaning that a similar fraction of events survive at a certain WIMP mass. Only the vector operator has a different dependence on the mass.

The different values are implemented in a simplified way, where the systematics of the lowest WIMP mass of 1 GeV are taken as a reference. In order to describe the case of higher WIMP masses in a conservative manner, the highest value for each WIMP mass is taken and a fit is performed (see figure 7.19). The whole curve is then weighted up according to the ratio of the maximum value and the uncertainties at the same photon energy for $M_\chi = 1\,\text{GeV}$. The fit function for the vector operator is $0.997 + 4.3 \times 10^{-5} \cdot M_\chi^2$ and for the axial-vector and scalar operators $0.756 + \exp(-1.382 + 0.0106 \cdot M_\chi)$.

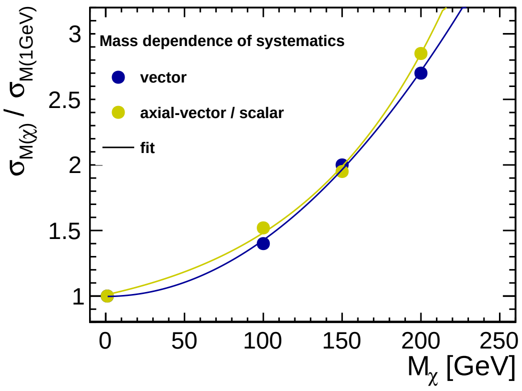

Figure 7.19: Maximum systematic uncertainty for different WIMP masses fitted with different functions for the vector and the axial-vector operators.

The uncertainty on the signal distribution is the same for all polarisation combinations. The height, i.e. overall cross-section varies but the shape is invariant, as opposed to the Standard Model background processes, which are produced involving several mediators with different differential cross-sections $\partial\sigma/\partial E_\gamma$. Depending on the polarisation the process consists of different channels and hence the shape varies.

7.5.8 Implementation of uncertainties in the limit calculation

The relative deviations of the photon energy corresponding to the two envelopes of the luminosity spectra are implemented in the limit calculation as upper and lower systematic uncertainty. In order to reflect the dependence on the photon energy, the values are read-in as a histogram. Statistical fluctuations are eliminated by rebinning the histograms from 4 GeV bins to 8 GeV bins in the case of the background and 12 GeV bins in the case of the signal curves. In figure 7.20 distributions for different polarisation combinations and for different WIMP masses are shown. The shown values are included in the limit calculation script. The respective upper and lower

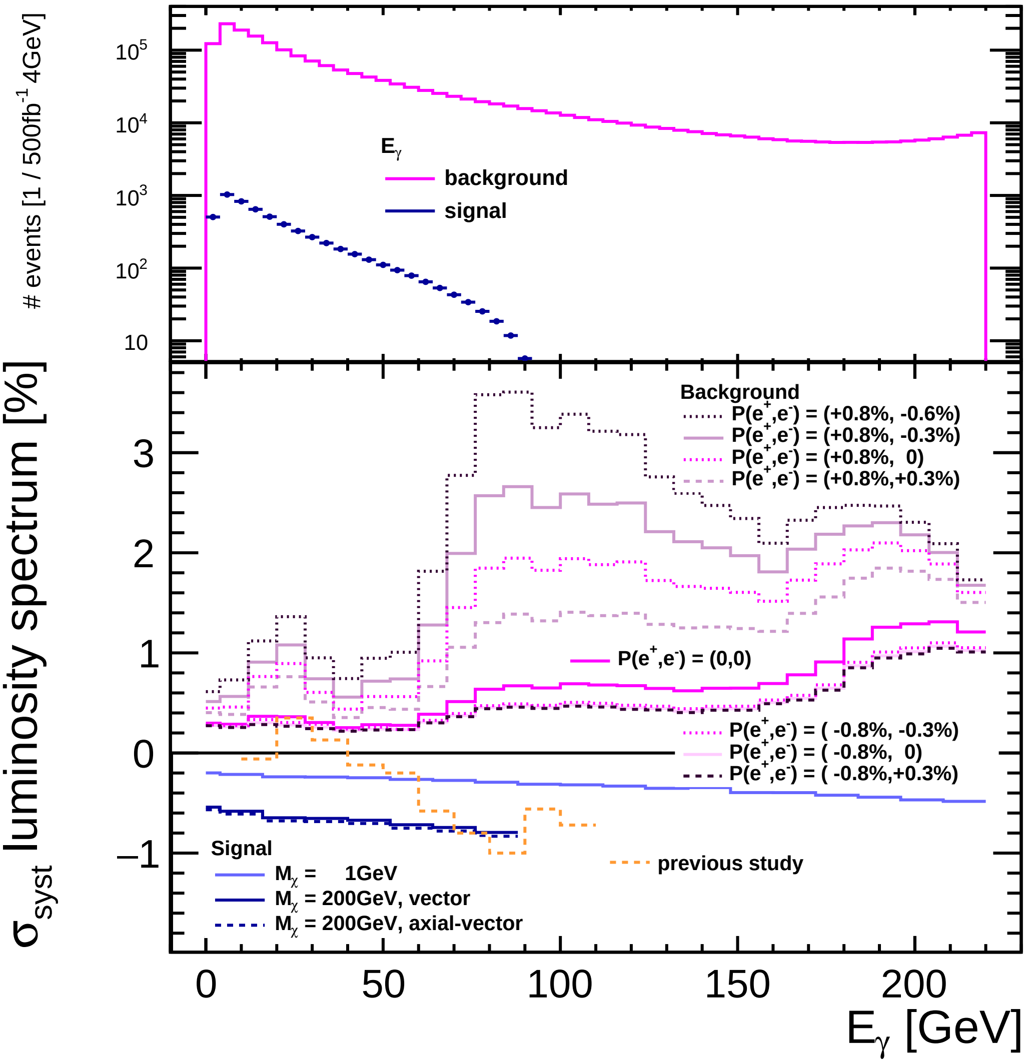

Figure 7.20: Systematic uncertainties induced by the luminosity spectrum as a function of the photon energy. These values are used in the limit calculation. Background sets for different beam polarisation configurations and signal curves for two M_χ are shown. For better visibility only one side of the uncertainties is shown. The values of the previous study are included to highlight the differences.

uncertainties have an almost identical absolute value, which allows to increase the visibility by only showing the upper (background) or the lower (signal) curve for each case.

The distributions of the background uncertainty for the different polarisation combinations differ in height but have a similar shape. The larger the contribution of the neutrino sample with right-handed electrons and left-handed positrons (i.e. the one with the larger deviations, shown in figure 7.17b) the larger the uncertainties.

All the curves of the background systematics rise with photon energy. For energies up to approximately 70 GeV the uncertainties are around $0.2 - 1\%$. For higher energies, the deviations in the neutrino sample with $P(e^-, e^+) = (+80\%, -30\%)$ (figure 7.17b) start to rise, and also the uncertainties increase to around 3 times higher values. At the highest energies the deviations of the neutrino sample with $P(e^-, e^+) = (-80\%, +30\%)$ (figure 7.17a) are highest, which leads to higher uncertainties for the cases of unpolarised beams and left-handed electrons.

When these uncertainties are compared to the values of the previous study (introduced in section 7.5.1 and shown as the dashed orange line in figure 7.20) the most prominent difference is the covered range of photon energies. Whereas previously only photon energies in the range $10 - 110$ GeV had an uncertainty assigned, the realism has been increased with the new setup, where the full spectrum is taken into account. This means that even though the scale of values are in a similar range the overall uncertainty is higher than in [3], because there are no longer photon energies with zero uncertainty.

Also the shape is different. In the old approach the sign of the uncertainty in the range $20 - 40$ GeV is opposite. In the central part, the uncertainties rise with photon energy, analogously to the new values. At energies around 100 GeV the tendency is however inverted and the uncertainties slightly decrease.

When data sets taken with different polarisation combinations are combined, the different data sets give redundancy and polarisation-independent systematic effects are reduced, see further section 7.6.2.

7.6 Study of systematic uncertainties

Whereas in all other parts of this thesis the sensitivites are calculated with the settings introduced in section 7.4.5, in this section the effect of alternative settings are discussed.

7.6.1 Effect of the information on the photon spectrum shape

In order to identify the best approach, the exclusion limits obtained with a counting experiment are compared to those using different photon energy bins. In figure 7.21 exclusion limits for the vector operator with an integrated luminosity of $500\,\mathrm{fb}^{-1}$ and unpolarised beams are shown.

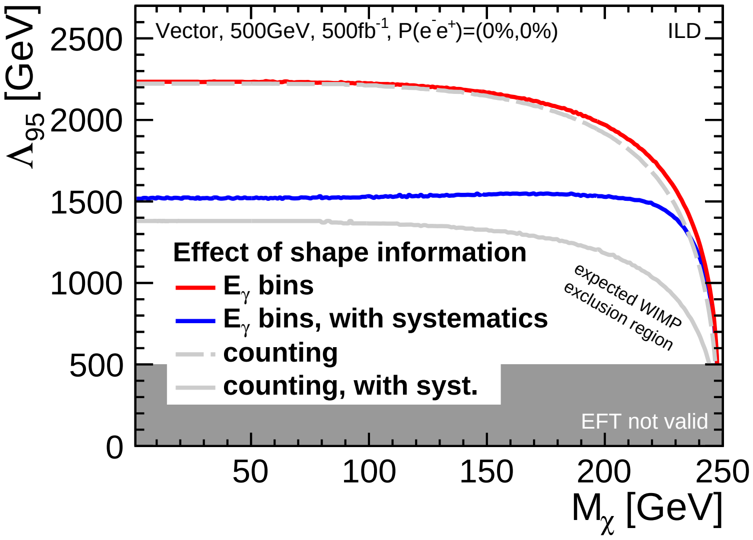

Figure 7.21: Comparison of exclusion limits with and without taking the shape information of the photon spectrum into account. Without systematic uncertainties the difference is negligible, but with the full set of uncertainties the performance of a counting experiment is worse.

Without any systematic uncertainties the difference between the two approaches is negligible. After including the systematic uncertainties in the limit calculation the performance is worse in both cases. Whereas the value of the counting experiment drops by approximately 700 GeV, it is only 600 GeV worse in the approach with photon energy bins. The difference is even larger for high WIMP masses. This means that in the presence of the systematic uncertainties it is beneficial to split the photon energy over several bins.

7.6.2 Reduction of the systematic uncertainties using several data sets

The shape of the blue curve in figure 7.21 is flatter than the others, because the signal-free control region at highest photon energies helps to constrain the systematic uncertainties partially. In the absence of systematic effects the uncertainties are purely statistical and the improvement for lower masses are better because of the larger allowed phase space (see figure 7.3). A pure counting experiment does not allow control regions and hence the sensitivity for larger masses is also decreased.

In figure 7.22 the cases with and without systematic uncertainties are compared for the full H20 data sets. The different polarisation combinations help to constrain systematic uncertainties and hence the effect of the systematics is weaker, also for lower WIMP masses, which explains why there is no increase of the sensitivity at higher masses. With nominal settings the testable energy scales are up to ~350 GeV

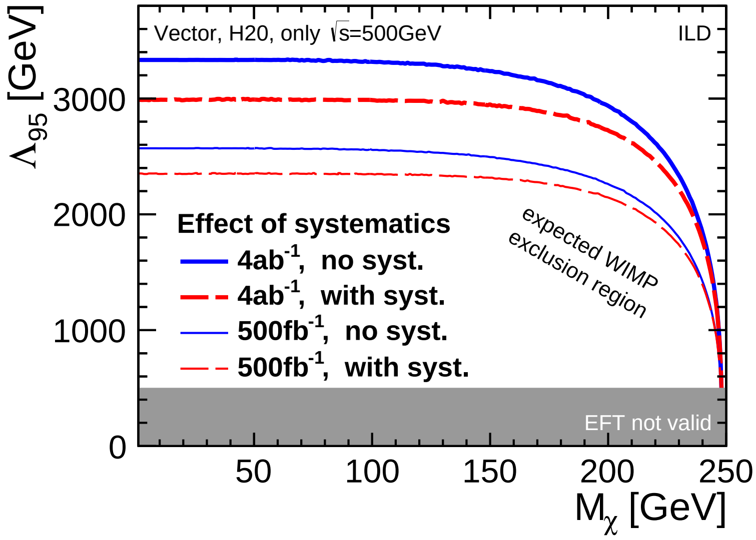

Figure 7.22: Effect of systematic uncertainties on the expected exclusion limits for the running scenario H20.

worse than without systematics, corresponding to around 10% which is significantly less than the ~30% for the unpolarised case (figure 7.21).

The importance of using several data sets can also be seen by comparing the exclusion limits for 500 fb^{-1} shown in figure 7.22 to those in figure 7.21. Even though the full integrated luminosity is the same in both cases, the results in figure 7.22 are up to 840 GeV better.

The results with several data sets are even comparable to the best case in figure 7.8a. The red dashed curve shows the case where the full data is taken with right-handed electrons and left-handed positrons, i.e. where the background is suppressed and the signal enhanced. Even though the optimal polarisation combination only contributes 40% of the data, the results in figure 7.22 are 13 GeV better because the systematic uncertainties are constrained by the other data sets with a smaller signal-to-noise ratio, which act as control samples.

7.6.3 Role of individual sources of systematic uncertainties

The effect of the individual sources of systematic uncertainties on the sensitivity is studied by switching the sources in the limit calculation on one-by-one. In figure 7.23 the difference in Λ_{95} is visualised for the vector operator, a WIMP mass of 1 GeV and 4 ab^{-1} taken with the polarisation sharing (10%,40%,40%,10%) without systematic uncertainties, i.e. corresponding to the thick blue line in figure 7.22.

To a first order, the individual differences in sensitivity reflect the sizes of the values in table 7.4. With a difference of almost 100 GeV, the smallest effect comes

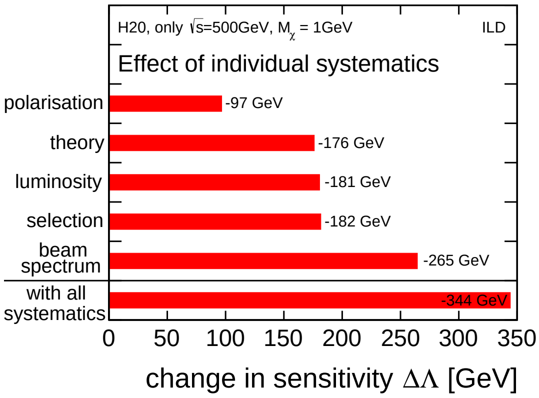

Figure 7.23: Effect of different systematic uncertainties on the sensitivity. Change of the expected exclusion limit with respect to the case without any systematic uncertainties for each source individually.

from the polarisation uncertainties. As the uncertainties are polarisation-dependent, the samples with different polarisation combinations and hence different signal-to-background ratios help to partially cancel the systematic uncertainties.

For the different kinds of systematic uncertainties, which are assumed to have one global value, the effect is similar, even though the size of the uncertainties of the theory (1.3‰), the event selection (2.0‰) and the luminosity (2.6‰) differ. The largest sensitivity loss comes from the uncertainty on the luminosity spectrum, which is almost at the scale of the decrease with all effects together.

7.6.4 Impact of larger uncertainties and potential reduction of the values

In the current planning phase of the ILC the systematic effects can only be estimated and the exact values change when new studies are conducted and when the accelerator and detector design are modified. The effect of alternative values for the systematic uncertainties is tested which can help to define targets for future efforts to improve the systematic uncertainties.

Five different modifications are tested and compared to the case with the nominal settings for H20 integrated luminosity and polarisation, the vector operator and a WIMP mass of 1 GeV. In figure 7.24 the increase or decrease of the expected exclusion limit with respect to the nominal case, i.e. 2989 GeV (thick red dashed line in 7.22), is shown.

In the first two test runs the uncertainty on the luminosity is reduced and all other values are left at the nominal settings. If there was no uncertainty on the luminosity, the expected exclusion limit would be 10 GeV (or 3‰) better. If on the other hand more sources of systematic uncertainties in the same range were added,

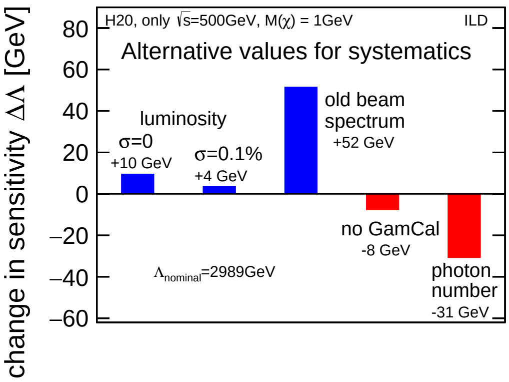

Figure 7.24: Effect of alternative values of the systematic uncertainties.

the decrease of the sensitivity is expected to be similar. This rather small change shows that more sources of systematics would not worsen the results significantly, as long as the uncertainties are not larger than the considered effects.

If the luminosity measurement could be improved to yield the anticipated uncertainty of 1‰ instead of 2.6‰, the improvement would only be 4 GeV, meaning that an update of the uncertainty study would not lead to a measurable effect.

Also for the beam energy spectrum two alternative settings are tested, the values from the previous study [3] and the case without the forward detector GamCal. If the smaller uncertainties on the luminosity spectrum of the previous study are used, the expected exclusion limit would be 52 GeV better, meaning that the old approach was 1.7% too optimistic.

If GamCal is not installed, beamstrahlung photons could not be measured and the fit values would be significantly worse (see table 7.6). Nevertheless, the expected exclusion limits would only be 8 GeV worse. Whether GamCal will be installed or not is hence not crucial for the WIMP study.

In the last test run the theory uncertainty is modified. If the current value with the lack of clarity on the minimum transverse momentum on the additional photons (see section 5.4.1.2) would be taken into accout, the exclusion limits would be 31 GeV (or 1%) worse.

Overall the effect of alternative settings of the systematic uncertainties is in the per cent range and thus the reachable energy scales of this study are expected to hold.

7.6.5 Influence of correlations

In the standard settings of this analysis the systematic uncertainties are assumed to be fully correlated between different photon bins, between signal and background and between the different sources of systematics, which is realised by setting the parameter f_{uncorr} in TSysLimit to 0.

The role of the correlation is tested by setting f_{uncorr} to different values for all sources at once. In figure 7.25 the corresponding exclusion limits are shown for two different WIMP masses (1 GeV and 200 GeV) for the vector operator and the integrated luminosity and polarisation sharing from the H20 scenario. As expected, the sensitivity decreases for smaller fractions of correlation. If f_{uncorr} is set to 0.9, the limit is approximately 150 GeV lower.

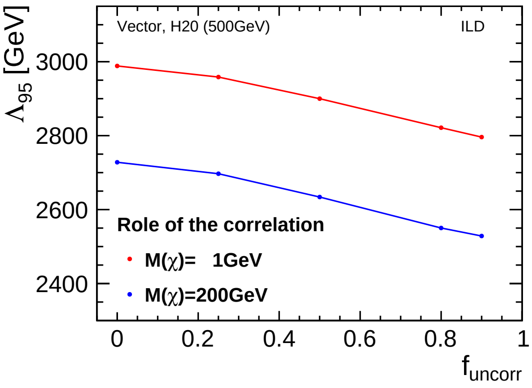

Figure 7.25: Impact of the fraction of correlation on the expected exclusion limit.

If f_{uncorr} is set to exactly 1, the complete systematic uncertainties are treated like statistical uncertainties, which is not a meaningful approach. This setup was used in [3] (see next section) and gives questionable results.

With $f_{\mathrm{uncorr}} = 1$ an unexpected increase of the sensitivity is observed. For the H20 setup and $M_\chi = 1\,\mathrm{GeV}$ the limit increases to 2992 GeV, i.e. to a value similar as for $f_{\mathrm{uncorr}} = 0$ (2989 GeV). Without polarisation mixing the effect is even more pronounced. For $M_\chi = 1\,\mathrm{GeV}$, $500\,\mathrm{fb}^{-1}$ and unpolarised beams the value is 2060 GeV for $f_{\mathrm{uncorr}} = 1$ and 1516.72 GeV for 0.

7.7 Comparison to previous ILC results

In figure 7.26a results of the previous WIMP study using effective operators [3] are reproduced. The shown expected exclusion limits are for the example of the vector operator with an integrated luminosity of $500\,\text{fb}^{-1}$ collected with unpolarised beams and $P(e^-, e^+) = (+80\%, -30\%)$.

For a comparison of the curves to the new limits, it is worthwhile to summarise the differences in both the input photon energy distributions and the limit calculation. The signal and background distributions are based on new Monte Carlo data sets (see section 5.4), the signal definition differs (see section 5.3.1.4) and the approach to reweigh the neutrino events to signal events has been updated by using E^*_γ and $\sqrt{s^*}$ instead of $E_{\gamma,\text{ILD}}$ and $\sqrt{s} = 500\,\text{GeV}$ (see section 7.1.2). In [3] the systematic uncertainties in TSysLimit were different. Especially the values for the for the luminosity spectrum has been revisited (see section 7.5) and instead of assuming a full correlation, f_{uncorr} was set to 1, where the behaviour is unexpected (see section 7.6.5).

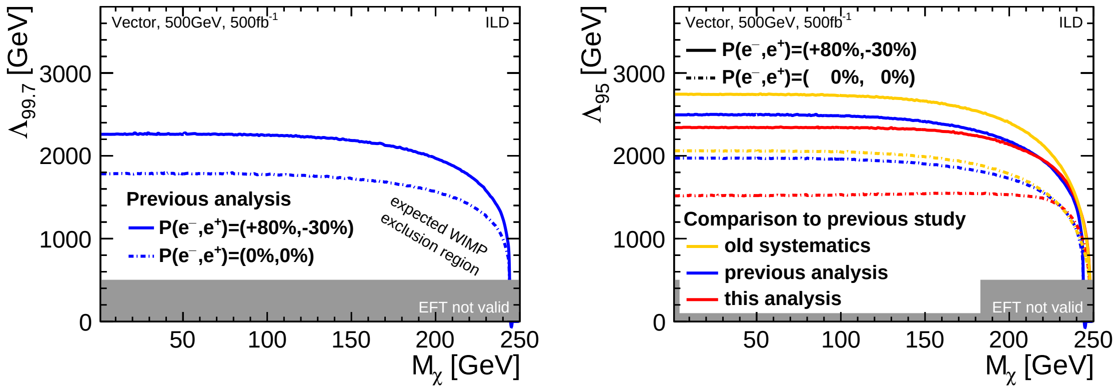

(a)

(b)

Figure 7.26: (a) Reproduction of the 3σ exclusion limits of [3] for the vector operator at $500\,\text{fb}^{-1}$ with and $P(e^-, e^+) = (+80\%, -30\%)$. (b) Comparison of the exclusion limits of [3] (blue) with this analysis (red). For the orange lines the new signal and background input with the old setup of the systematics uncertainties was used.

An additional difference is that in [3] 3σ instead of 2σ confidence levels were presented. Thus, the calculation with the old input data and settings is repeated to obtain 2σ exclusion curves, shown as the blue lines in figure 7.26b. The corresponding lines from this study are shown in red.

The previous results for polarised beams are up to 150 GeV better and for unpolarised beams even up to 450 GeV better. In order to understand whether the different input or the settings in the limit calculation lead to the worse results than in [3], in a third setup the new data is used as input to the limit calculation which is run with the old settings of the systematics. The reachable energy scales, shown by the orange lines, are better than in the other cases with the corresponding polarisation. Consequently, the optimistic treatment of systematic effects in [3] can be identified as the reason for the better results.

In this study also higher masses can be tested: Due to the smaller minimum photon energy of 2 GeV in the signal definition (see section 5.3.1.3) compared to 10 GeV in [3], the testable range of WIMP masses is slightly increased to ~245 GeV.

The effect of the improved signal definition on lower WIMP masses can also be tested by re-running the analysis with new Monte Carlo data sets and systematic uncertainties, but with the old signal definition (see section 5.3.1.4) and event selection (see section 6.1.7). The maximum testable Λ would only be 16 GeV or 1% worse for unpolarised beams and 25 GeV or also 1% for $P(e^-, e^+) = (+80\%, -30\%)$ with the smaller signal region from [3].

When the analysis was first re-visited [177, 181], the signal definition and the cuts on invariant mass and four-momentum transfer at the generation of the Bhabha scattering events were the same as in [1–3]. Unfortunately, also the same settings in TSysLimit were used, which led to too optimistic results. In [181] the expected exclusion limit for the vector operator at 500 fb^{-1} with $P(e^-, e^+) = (+80\%, -30\%)$ was ~2600 GeV at low WIMP mass, which is now about 250 GeV lower (as shown in figure 7.8a). An update to the role of positron polarisation at 250 GeV (presented in [177]) can be found in section 8.3.3.

Chapter 8

Sensitivity of the Full ILC Programme

In this chapter the sensivity to WIMPs for the complete ILC programme is presented. First, expected exclusion limits (section 8.1) and the potential for the observation of a WIMP signal (section 8.2) at a centre-of-mass energy of 500 GeV are discussed. Even though the full simulation study is performed at $\sqrt{s} = 500\,\text{GeV}$, approximations for other centre-of-mass energies can also be obtained in two different ways, which are subject of sections 8.3 and 8.4. In the first study the input data to the limit calculation is scaled to the desired centre-of-mass energy. The second approach comprises an extrapolation framework which allows to give results for different centre-of-mass energies and luminosities without CPU-intensive calculations. In section 8.6 the ILC exclusion limits are compared to prospects of other planned lepton colliders and to results from LEP and LHC.

8.1 Expected exclusion limits at 500 GeV

After studying the impact of detector and systematic effects in chapter 7, the standard settings for the systematic uncertainties, as presented in section 7.4.5, are well justified and the results for the full ILC sensitivity can be presented. The results for the centre-of-mass energy of the full simulation of 500 GeV are based on a running scenario for 20 years of operation. As presented in section 3.4, data corresponding to $4\,\text{ab}^{-1}$ is supposed to be taken at 500 GeV with a polarisation sharing of $(--, -+, +-, ++) = (10\%,40\%,40\%,10\%)$, according to the H20 scenario [114].

In figure 8.1 the resulting 2σ expected exclusion limits for the three effective

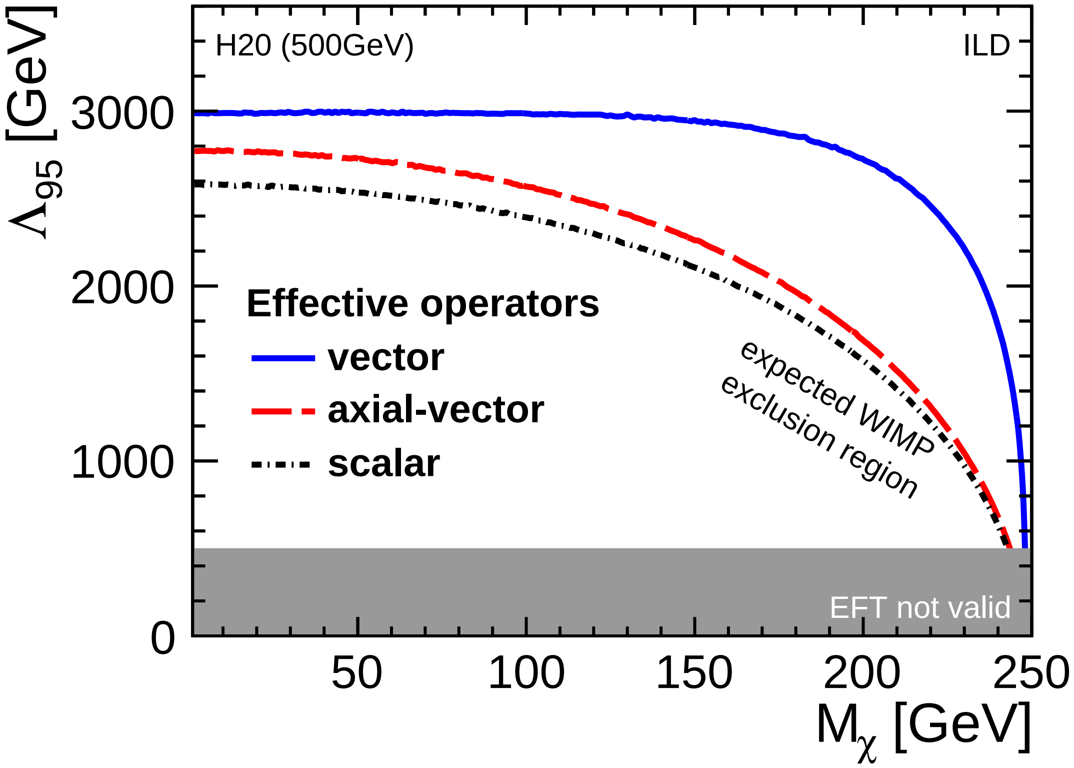

Figure 8.1: Expected exclusion limits for the different effective operators for $\sqrt{s} = 500\,\text{GeV}$ assuming the running scenario H20.

operators (vector, axial-vector scalar) are shown. The pattern is similar to the curves for the initial four years of operation (figure 7.9), but the reach for low WIMP masses is ∼27% better for all operators. Energy scales up to 2.6, 2.8 and 3 TeV can be probed for the scalar, axial-vector and vector operators, respectively. For higher WIMP masses the reach is lower, but still in the TeV range. For the example of $M_\chi = 150\,\text{GeV}$ the limits are 2250 GeV for the axial-vector and 2100 GeV for the scalar operator. For the vector operator the same sensitivity can be reached as for low masses.

If the $4\,\text{ab}^{-1}$ are collected with a lower fraction of the like-sign polarisation combinations, which would increase the cross-section of many Standard Model processes, the effect on the WIMP sensitivity would be negligible. For a sharing of $(--, -+, +-, ++) = (5\%, 45\%, 45\%, 5\%)$ the expected exclusion limits are shown as the thick lines in figure 8.2. The difference to the limits of the standard H20 configurations is at the per cent level. The effect of the polarisation sharing is small, because all considered scenarios have small contributions with like-sign polarisa-

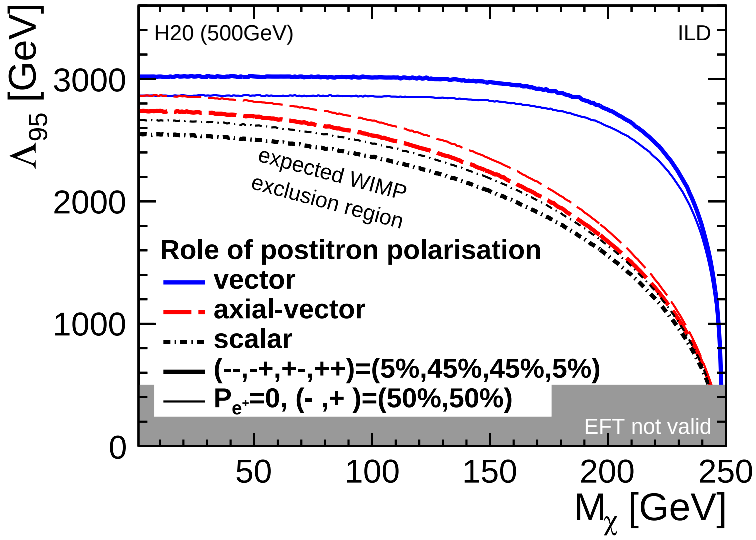

Figure 8.2: Expected exclusion limits for the different effective operators and for different polarisation configurations with an integrated luminosity of $4\,\mathrm{ab}^{-1}$.

tion due to the preference of opposite polarisation configurations for most Standard Model studies.

If the positron beam was unpolarised, the sensitivity would be affected. The thin lines in figure 8.2 visualise the expected exclusion limits assuming two data sets taken with +80% and −80% polarised electrons with integrated luminosities of $2\,\mathrm{fb}^{-1}$ each. Wheareas the sensitivity in case of the vector would drop by up to 160 GeV, the limits for the other operators would *improve* by up to 100 GeV. The reason for the increase of the sensitivity to axial-vector and scalar operators is the large contribution of opposite helicity in the common scenarios with positron polarisation, where the production of axial-vector and scalar operators is suppressed.

At low WIMP masses the expected limits for the vector and axial-vector operators are identical, like in the case without any polarisation (see figure 7.6), because if only the electron beam is polarised, the first two terms and the last two terms in equation 5.8 on page 105 are identical and hence, despite the opposite helicity dependence of the operators, the polarisation weights are equal.

Whereas positron polarisation has no big effect on the reachable energy, it is essential to have polarisation of both beams to test the chirality of the new interaction in case a signal is observed [177].

8.2 Discovery potential

So far all presented results have been expected exclusion limits. Without a clear prediction from theoretical models for a WIMP that the ILC could be sensitive to, the studies on how beam polarisation, integrated luminosity and systematic effects influence the sensitivity were performed assuming the absence of a signal. With the final setup (discussed above in section 8.1) also the optimistic assumption of a signal detection is tested.

In figure 8.3 the energy scales corresponding to an exclusion of the *background only* hypothesis with confidence levels of 3σ and 5σ (i.e. 0.997 and 0.9999994) are shown. A 3σ excess over the background is usually referred to as an *observation* of a signal and above 5σ the excess is called *discovery*.

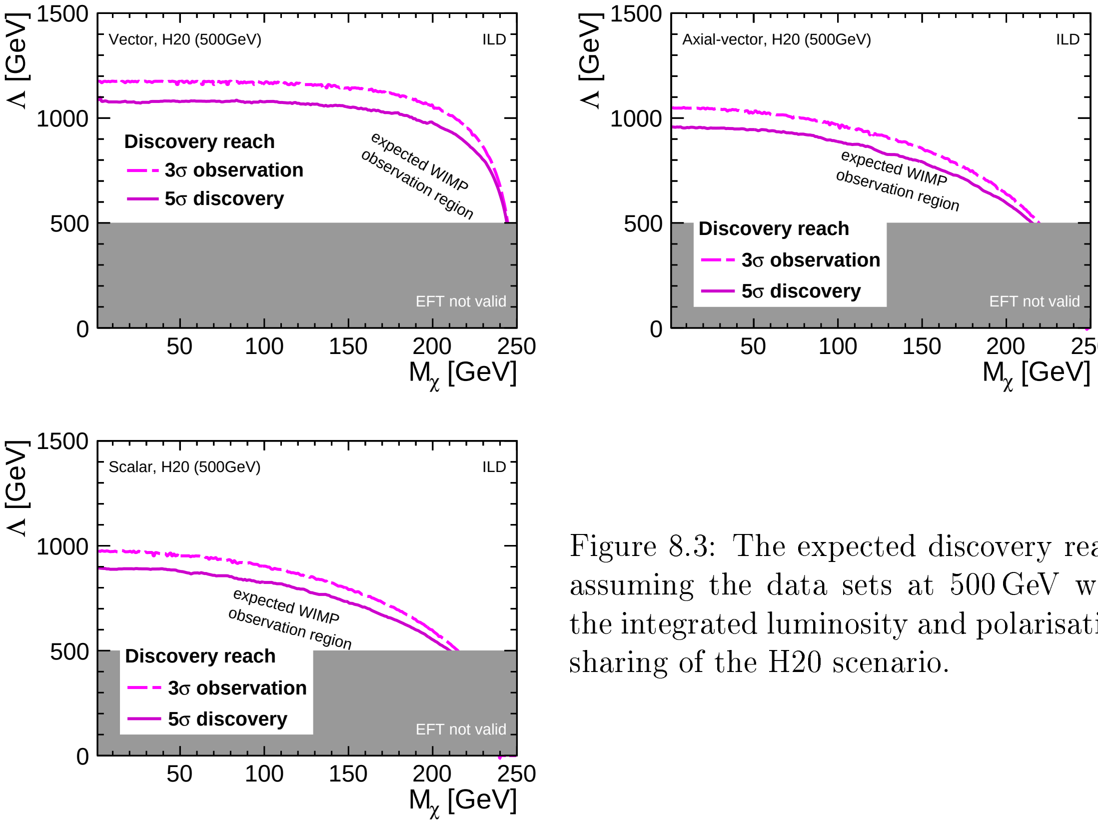

Figure 8.3: The expected discovery reach assuming the data sets at 500 GeV with the integrated luminosity and polarisation sharing of the H20 scenario.

The region corresponding to combinations of WIMP mass and energy scales Λ that would lead to an observation, has the same shape as the exclusion regions, but the overall scale is lower, because of the higher values of the confidence level. The reachable energy scale for low WIMP masses is about 1 TeV. In the case of the vector operator energy scales up to 1200 GeV, assuming a 3σ observation, and 1100 GeV, assuming a 5σ discovery, can be tested. For the other operators the sensitivity is about 15% smaller.

In order to quantify what Λ values in the 1 TeV range mean in practice, the corresponding number of signal events is calculated for the example of the vector operator, a WIMP mass in the plateau region of the curve and the discovery case with $\Lambda_{5\sigma} \approx 1.1\,\text{TeV}$. The total number of WIMP events that would be necessary for a 5σ discovery is about 400,000.

8.3 Limit calculation for lower centre-of-mass energies

As discussed in section 5.2.2, higher centre-of-mass energies are favoured for the WIMP search, but the mono-photon signal can be looked for at any centre-of-mass energy. Exploring the potential of the ILC below 500 GeV is of special importance, if the experiment starts operation at lower centre-of-mass energies, e.g. at 250 GeV [111].

Instead of producing new Monte Carlo data sets, which would be very CPU-intensive, the data from the full analysis at $\sqrt{s} = 500\,\text{GeV}$ can be used as a basis to calculate limits at the lower centre-of-mass energies of the ILC. In the following, an approach is described, where the signal and background photon energy spectra are modified to give an approximative description for the centre-of-mass energy of interest. In section 8.4 a second strategy is presented.

8.3.1 Obtaining the signal photon energy distribution

The way to reweigh neutrino events to WIMP events, as described in section 7.1.2 is independent of the centre-of-mass energies of the two cross-sections and hence also WIMP events for other energies can be obtained in the same way. The only requirement is the availability of neutrino events with photons in the energy range expected for the WIMPs. The operation scenarios described in section 3.4 comprise runs at $\sqrt{s} = 250\,\text{GeV}$, 350 GeV and 500 GeV and with an upgrade also $\sqrt{s} = 1\,\text{TeV}$ is expected to be reached.

For 250 GeV and 350 GeV the full kinematically reachable range of signal photon events is below 220 GeV, the maximum energy of the full simulation, but at 1 TeV WIMP events can contain photons with higher energies. This means that the presented approach is restricted to centre-of-mass energies below the value of the full simulation, i.e. $\sqrt{s} < 500\,\mathrm{GeV}$.

In order to adapt the reweighting procedure, the WIMP cross-section is evaluated at the centre-of-mass energy in the frame of the $\chi\chi\gamma$ system ($\sqrt{s^*}$), which is scaled with the centre-of-mass energy.[i] In this way, events which are kinematically not reachable for a given WIMP mass at the new centre-of-mass energy will obtain zero as weight. The neutrino cross-section, on the other hand, is unmodified, i.e. calculated with the original value of $\sqrt{s^*}$. Also the photon energy in the frame of the $\chi\chi\gamma$ system (E^*) is kept at its original value.

8.3.2 Scaling the background photon energy distribution

The overall number of background events at a lower centre-of-mass energy can be obtained from cross-section calculations. The shape of the photon spectrum on the other hand is approximated by compressing the photon energy spectrum from the full simulation. This means that the background photon energy spectrum is modified in two ways. First, all entries are rescaled according to the ratio $\sqrt{s}$ / $500\,\mathrm{GeV}$, e.g. for $\sqrt{s} = 250\,\mathrm{GeV}$ the spectrum is compressed by a factor of 2. Second, the entire histogram is weighted according to the total cross-sections of the background processes at the different centre-of-mass energies.

The cross-sections of the two background processes (neutrino pair production and Bhabha scattering) are calculated for $\sqrt{s} = 250\,\mathrm{GeV}$, $350\,\mathrm{GeV}$ and $500\,\mathrm{GeV}$ and for the four possible polarisation configurations with ($|P_{e^-}|, |P_{e^+}|$)=(100%,100%) using WHIZARD [139] and O'MEGA [152]. A less detailed setup than in the full simulation is applied in order to save CPU time: No luminosity spectrum is included and one order of ISR less is considered ($\nu\bar{\nu} + 1, 2, 3\ \gamma$, $e^+e^- + 1, 2\ \gamma$).[ii] Additionally, the signal definition is simplified (as shown in table 8.1) and applied directly during the generation of the events. Instead of a ϕ-dependent cut on the transverse momentum, $p_{T,\gamma} > 1.97\,\mathrm{GeV}$ is taken for all ϕ. All cuts are applied in the frame where electron and positron collide head-on. This allows to omit the minimum energy cut.

The maximum energy cut corresponds to the radiative return to the Z boson minus ~10%. E_{return} depends on the considered centre-of-mass energy and the different values of $E_{max,\gamma}$ are shown in table 8.2.

---

[i] Thus, the different shape of the luminosity spectrum at different centre-of-mass energies is neglected.

[ii] As indicated by the cross-section values (shown in table 6.3) the influence of $\nu\bar{\nu} + 4\ \gamma$ and $e^+e^- + 3\ \gamma$ is negligible.

full simulation		**approximation**
$\nu\bar{\nu} + 1,2,3,4\ \gamma$ $e^+e^- + 1,2,3\ \gamma$		$\nu\bar{\nu} + 1,2,3\ \gamma$ $e^+e^- + 1,2\ \gamma$
$7° < \theta_\gamma < 173°$		$7° < \theta_\gamma < 173°$
$p_{T,\gamma} > 1.92\,\mathrm{GeV}$	for $\lvert\phi_\gamma\rvert > 35°$	$p_{T,\gamma} > 1.97\,\mathrm{GeV}$
$p_{T,\gamma} > 5.65\,\mathrm{GeV}$	for $\lvert\phi_\gamma\rvert \leq 35°$	
$E_\gamma > 2\,\mathrm{GeV}$		-
$E_\gamma < 220\,\mathrm{GeV}$		$\sqrt{s}$-dependent, see table 8.2

Table 8.1: Comparison of the signal definition in the full simulation and the approximation used for the calculation of the cross-sections at other centre-of-mass energies.

$\sqrt{s}$ [GeV]	250	350	500
E_{return} [GeV]	108.37	163.12	241.68
E_{max} [GeV]	100	150	220

Table 8.2: Energy of the radiative return to the Z boson at the different centre-of-mass energies. The maximum energy cut is at ~90% of E_{return}.

The calculated cross-sections are shown in table 8.3. Whereas the value for neutrino pair production with left-handed electrons and right-handed positrons increases with centre-of-mass energy, the cross-sections of all other processes decrease. The ratio of cross-sections at the respective centre-of-mass energy to $\sqrt{s} = 500\,\mathrm{GeV}$ (shown in the last column) is the weight by which the photon spectrum is scaled. For the additional Bhabha scattering data set (which was introduced in section 6.1.6.3) the weight is assumed to be similar to the other Bhabha scattering weights and is approximated by 500 GeV / $\sqrt{s}$.

Because of the non-linearity of the maximum energy cut, the background histograms will have entries above the maximum energy, when they are rescaled from 500 GeV to a lower centre-of-mass energy. In order to obtain the correct range, those events are cut away. The complete integral over the events is retained by multiplying the ratio of number of entries before and after the cut to the weight.

The number of background events is given by $B = \epsilon\sigma\mathcal{L}$. Reliable values for the selection efficiencies ϵ can only be given by a full detector simulation, hence for $\sqrt{s} = 500$ GeV. At lower centre-of-mass energies the Bhabha scattering events have lower lepton energies. In principle this leads to a worse detection capability in the forward calorimeters and less events could be rejected. On the other hand,

$\sqrt{s}$	process	σ [fb]	weight
250 GeV	$\nu\bar{\nu}_{LR}$	16557.7	0.86
	$\nu\bar{\nu}_{RL}$	2955.4	4.06
	$e^+e^-_{LL}$	104495	2.25
	$e^+e^-_{LR}$	104051	1.94
	$e^+e^-_{RL}$	103038	2.04
	$e^+e^-_{RR}$	104095	2.21
	additional e^+e^-		2.00
350 GeV	$\nu\bar{\nu}_{LR}$	17161.6	0.89
	$\nu\bar{\nu}_{RL}$	1456.8	2.00
	$e^+e^-_{LL}$	71553	1.54
	$e^+e^-_{LR}$	76913	1.44
	$e^+e^-_{RL}$	74258	1.47
	$e^+e^-_{RR}$	71936	1.53
	additional e^+e^-		1.43
500 GeV	$\nu\bar{\nu}_{LR}$	19177.4	-
	$\nu\bar{\nu}_{RL}$	728.0	
	$e^+e^-_{LL}$	46504	
	$e^+e^-_{LR}$	53570	
	$e^+e^-_{RL}$	50574	
	$e^+e^-_{RR}$	47058	

Table 8.3: Cross-sections of the background processes at different centre-of-mass energies with the signal definition presented in table 8.1.

a lower centre-of-mass energy also leads to a lower amount of energy deposited by e^+e^- pairs from beamstrahlung. For simplicity a similar scale of these counteracting effects is assumed, which allows to consider the efficiencies to be independent of $\sqrt{s}$. Consequently, they cancel in the calculation of the weights.

In figure 8.4 the background photon energy spectrum at the different centre-of-mass energies is compared for unpolarised beams. The height of the peak towards lower photon energies increases with decreasing centre-of-mass energy, because the overall background cross-sections are at a similar level (as shown in table 8.3), but the spectrum is more and more compressed. Even though the energy rise below the maximum energy of the respective curve is the result of the simple compression of the distribution for 500 GeV, its position is compatible with the rise towards the radiative return for the different centre-of-mass energies.

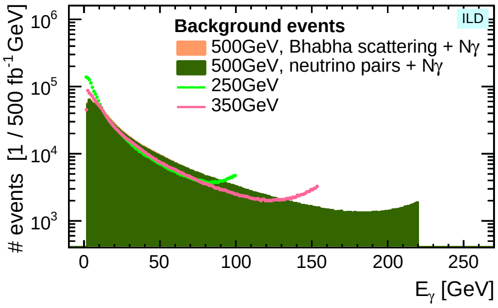

Figure 8.4: Background photon energy spectrum at different centre-of-mass energies for unpolarised beams.

8.3.3 Expected exclusion limits for lower centre-of-mass energies

With the signal and background scaled and reweighted according to sections 8.3.1 and 8.3.2, the sensitivity for centre-of-mass energies of 250 and 350 GeV can be calculated. The same systematic uncertainties as for 500 GeV are taken, even though especially the dominating luminosity spectrum is different at lower centre-of-mass energies. The effect on the sensitivity is however assumed to be smaller than the accuracy of this study.

In figures 8.5, 8.6 and 8.7 the 2σ expected exclusion limits for the three operators are shown assuming different running scenarios for a 20 years programme. The results for 500 GeV (shown in figure 8.1) are drawn for comparison. For 350 GeV the integrated luminosity in the H20 scenario is only 200 fb^{-1}. The sensitivity for the more optimistic scenario I20 with 1700 fb^{-1} (see section 3.4) is also calculated. In both cases the polarisation sharing is $(--, -+, +-, ++) = (5\%, 67.5\%, 22.5\%, 5\%)$. For 250 GeV the integrated luminosity fo the scenario H20 (2 ab^{-1}) and three different polarisation configurations are assumed: the originally proposed option in the H20 scenario $(--, -+, +-, ++) = (5\%, 67.5\%, 22.5\%, 5\%)$ [114], the new standard setting with (5%,45%,45%,5%) [111] and a setup without positron polarisation, where the integrated luminosity is equaly split over +80% and −80% electron polarisation.

At lower energies the testable WIMP mass range is smaller than at 500 GeV, with a maximum mass of almost half of the respective centre-of-mass energy. Also the reachable energy scales are smaller at lower centre-of-mass energies. All exclusion limits are however in the TeV range and hence above the region which is not suitable for effective operators. This region, where Λ is smaller than the centre-of-mass energy, is indicated by the grey region for 250 GeV and the two lines for $\sqrt{s} =$ 350 GeV and 500 GeV.

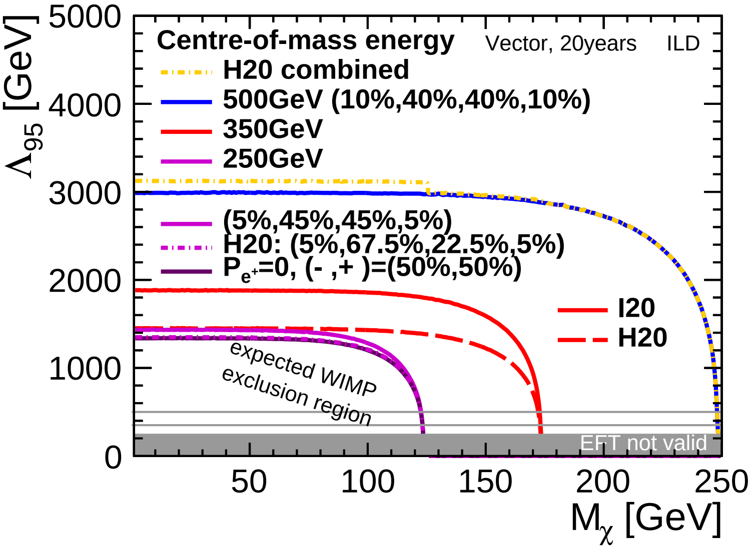

Figure 8.5: Expected exclusion limits for centre-of-mass energies of 250, 350 and 500 GeV for the vector operator, assuming various running scenarios for a 20 years programme.

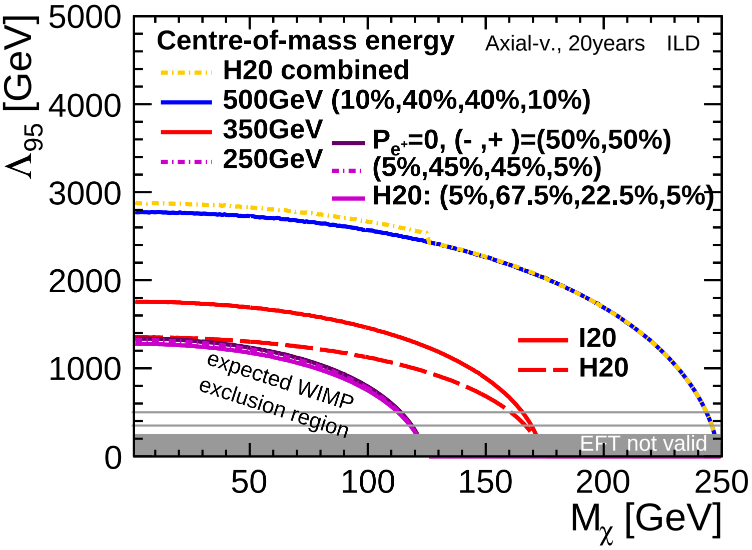

Figure 8.6: Expected exclusion limits for centre-of-mass energies of 250, 350 and 500 GeV for the axial-vector operator, assuming various running scenarios for a 20 years programme.

For low WIMP masses the sensitivity with 250 GeV and $2\,\mathrm{ab}^{-1}$ and with 350 GeV and $200\,\mathrm{fb}^{-1}$ are almost identical, which shows that higher centre-of-mass energies are favoured over higher integrated luminosities.

In [177] the role of positron polarisation for the physics programme of the ILC at a centre-of-mass energy of 250 GeV is discussed. For the WIMP study exclusion limits with and without positron polarisation were compared in [177]. The luminosity sharing (5%,45%,45%,5%) was found to be beneficial.

With the updated settings for the systematic uncertainties with larger values and the assumption of full correlation, the conclusion is slightly different and depends

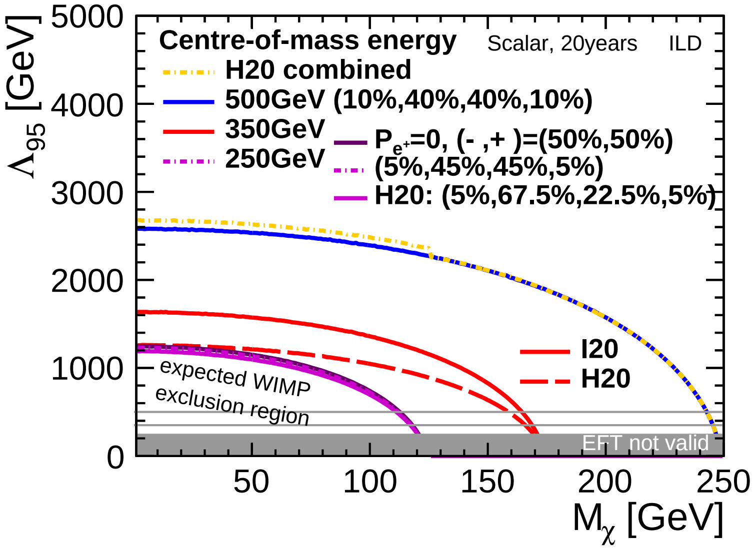

Figure 8.7: Expected exclusion limits for centre-of-mass energies of 250, 350 and 500 GeV for the scalar operator, assuming various running scenarios for a 20 years programme.

on the operator. In general, the polarisation sharing only has a small effect. In the case of the vector operator (5%,45%,45%,5%) is still the favoured case and is up to ∼85 GeV or 6% better than the original polarisation configuration of the H20 scenario (5%,67.5%,22.5%,5%), which in turn only offers negligible improvement compared to the case without positron polarisation. For the other two operators the three curves are even closer together. Here, the cases with positron polarisation are slightly worse, analogously to the case at $\sqrt{s} = 500$ GeV, as shown if figure 8.2.

8.3.4 Expected exclusion limits for full running scenarios

The orange dotted lines in figures 8.5, 8.6 and 8.7 show the exclusion limits for a combination of the data sets of all centre-of-mass energies for the H20 scenario. The overall improvement with respect to the results at 500 GeV is small. For masses which are accessible at both lower centre-of-mass energies, the maximum improvement is about 150 GeV or 5% for the vector operator. For the scalar and axial-vector operators the improvement is about 100 GeV or 4%. Above $M_\chi = 125$ GeV only the small data set at 350 GeV contributes, which leads to a negligible improvement with respect to the results at 500 GeV. Masses above 175 GeV can only be tested at 500 GeV, so the exclusion limits of the full H20 are given by the data sets from 500 GeV alone.

8.4 Extrapolation to other centre-of-mass energies and integrated luminosities

Up to now expected limits calculated for specific centre-of-mass energies and integrated luminosities were presented. The approach to create histograms for the signal and background expectations (presented in section 8.3) works well for a small number of scenarios. In order to calculate WIMP exclusion limits for many different setups, an extrapolation formalism is developed.

The approach is to find an approximative formula that depends on the centre-of-mass energy $\sqrt{s}$ and the integrated luminosity $\mathcal{L}$ which is proportional to the reachable energy scale with a certain confidence level Λ^{CL}:

$$\Lambda^{CL} \propto F(\sqrt{s}, \mathcal{L}) \tag{8.1}$$

This allows to relate Λ^{CL} at arbitrary $\sqrt{s}$ and $\mathcal{L}$ to a value Λ_0^{CL} calculated using the procedure explained in section 7.1 at $\sqrt{s_0} = 500\,\text{GeV}$ and a specific integrated luminosity $\mathcal{L}_0$ from the full analysis in the following way:

$$\Lambda^{CL}(\sqrt{s}, \mathcal{L}) = \Lambda_0^{CL}(\sqrt{s_0}, \mathcal{L}_0)\frac{F(\sqrt{s}, \mathcal{L})}{F(\sqrt{s_0}, \mathcal{L}_0)} \tag{8.2}$$

For this approach to hold, it has to be assumed that the polarisation dependence, the effects of systematic uncertainties and the photon energy spectrum factorise with the dependence on the centre-of-mass energy.

The decrease of the sensitivity around the kinematically maximum testable WIMP mass cannot be modelled in this approximation. Thus, the extrapolation only gives reasonable results for assumed WIMP masses which are low compared to the tested range of centre-of-mass energies, i.e. the plateau region of the exclusion curves.

The relation between the exclusion limit and parameters like $\sqrt{s}$, $\mathcal{L}$ and the polarisation is not directly given. It is more obvious that the exclusion limit depends on the number of signal (S) and background (B) events. Hence, as a starting point to find the relation of equation 8.2 the relation

$$\Lambda^{CL} \propto F'(S, B) \rightarrow \Lambda^{CL} = \Lambda_0^{CL}\frac{F'(S, B)}{F'(S_0, B_0)} \tag{8.3}$$

can be used, where S_0 and B_0 are the corresponding values from the full analysis.

In order to rewrite equation 8.3 as equation 8.2 three relations have to be determined:

1. a formula for the signal events: $S \propto f(\sqrt{s}, \mathcal{L}, \Lambda)$ (see section 8.4.1)
2. a formula for the background events: $B \propto g(\sqrt{s}, \mathcal{L}, P)$ (see section 8.4.2)
3. and the relation between signal and background events (see section 8.4.3).

The background events depend on the polarisation P and formulas for different polarisation splittings $P(e^-, e^+)$=(0,0),(+80%,0) and (+80%,−30%) will be derived, allowing to use exclusion limits corresponding to these polarisation combinations as starting points in the extrapolation. An extrapolation from one polarisation combination to a different setting goes beyond the scope of this formalism.

8.4.1 Formula for the signal events

The number of signal events is given by $S = \epsilon\sigma\mathcal{L}$, where σ is the cross-section of the respective effective operator (equations 2.28, 2.29 or 2.30 on page 41) and ϵ is the selection efficiency.

In the limit of small WIMP masses ($M_\chi \ll \sqrt{s}$ and hence $\mu \ll 1$) the double-differential cross-sections for both vector and axial-vector operator can be approximated by

$$\sigma_{M_\chi \ll \sqrt{s}} \approx \int dz \int d\cos\theta \frac{\alpha}{12\pi^2} \frac{(\sqrt{s})^2}{\Lambda^4} \frac{1}{z \sin^2\theta} (1-z)[4(1-z) + z^2(1+\cos^2\theta)] \quad (8.4)$$

In order to find an approximative description of the cross-section, the dependence on the centre-of-mass energy is studied by explicitely calculating $\partial\sigma/\partial E_\gamma$ for $\sqrt{s} =$ 250 GeV, 500 GeV and 1 TeV in the limit of small photon energies, which dominate the spectrum. The values are shown in table 8.4. As the cross-section depends on the value of Λ, all values are given relative to the one at 500 GeV. As a consequence of considering only the ratio, the term $\sin^2\theta$ in equation 8.4 cancels. The effect of the term $\cos\theta$ was found to be irrelevant, by testing the two different values $\cos\theta = 0$ and $\cos\theta = 1$, which only showed a negligible deviation.

The values in table 8.4 indicate that the cross-section increases by a factor of ∼8 when the centre-of-mass energy is doubled. Hence, the relation can be approximated by $\sigma \propto (\sqrt{s})^3$.[iii]

[iii] This dependence can also be derived from equation 8.4. The dimensionless quantity $z = \frac{2E_\gamma}{\sqrt{s}}$ is

centre-of-mass energy	$\sigma(\sqrt{s})/\sigma(500\,\mathrm{GeV})$
1 TeV	8.332
500 GeV	1
250 GeV	0.115

Table 8.4: WIMP cross-section for small WIMP masses and small photon energies at different centre-of-mass energies, relative to the value at $\sqrt{s} = 500\,\mathrm{GeV}$.

For the extrapolation the constants can be dropped and the cross-section as a function of centre-of-mass energy and energy scale Λ is approximated by

$$\sigma \propto (\sqrt{s})^3/\Lambda^4 \tag{8.5}$$

and finally the formula for the number of signal events is obtained

$$S \propto \epsilon\mathcal{L}(\sqrt{s})^3/\Lambda^4 \tag{8.6}$$

As described in section 7.1.1, data collected with different polarisation combinations are treated as separate channels. The presented formalism is resctricted to single channels, which means that only limits based on data with one polarisation combination can be extrapolated. In this case, the polarisation weight in the number of signal events is the same for S and S_0 and hence cancels out.

8.4.2 Centre-of-mass energy dependence of the background

Similarly to the procedure described in section 8.3.2 to apply weights to the background photon spectrum, also here weights are applied to the number of background events. Therefore, WHIZARD [139] and O'MEGA [152] are again used to calculate cross-sections of Bhabha scattering and neutrino pair production. In order to extrapolate limits with a realistic polarisation combination, the cross-sections are calculated with polarisation combinations foreseen in the experiment, rather than 100% polarised beams like in section 8.3.2. The same simplified signal definition is applied (see table 8.1). For the polarisation combinations $(P_{e^-}, P_{e^+}) = (0\%, 0\%)$, $(+80\%, 0\%)$ and $(+80\%, -30\%)$ the cross-sections are calculated at 250 GeV, 350 GeV, 500 GeV and 1 TeV.

---

small compared to 1 at the dominating low photon energies. This means that they can be neglected in the terms $(1-z)$ and $4(1-z)+z^2(1+\cos^2\theta)$. Thus, the only dependence on the centre-of-mass energy is given in the term $\frac{(\sqrt{s})^2}{z} = \frac{(\sqrt{s})^3}{2E_\gamma}$.

As discussed in section 8.3.2, the selection efficiency is assumed to be independent of the centre-of-mass energy. This means that the values for the different polarisation combinations at $\sqrt{s} = 500\,\text{GeV}$, as shown in table 6.2 on page 124, can be taken.

In order to obtain a relation between B and $\sqrt{s}$ the event numbers after event selection for $\mathcal{L} = 1\text{fb}^{-1}$ ($B_{P_{e^-}P_{e^+}}$) are plotted as a function of $\sqrt{s}$ and the slope is fitted. In figure 8.8 it can be clearly seen that $e^+e^-\gamma$ and $\nu\bar{\nu}\gamma$ depend differently on $\sqrt{s}$: the neutrino background increases with $\sqrt{s}$, while the $e^+e^-\gamma$ background decreases. As expected, the size of the Bhabha cross-section is almost independent of the helicity configuration, whereas the $\nu\bar{\nu}\gamma$ background depends strongly on the polarisation.

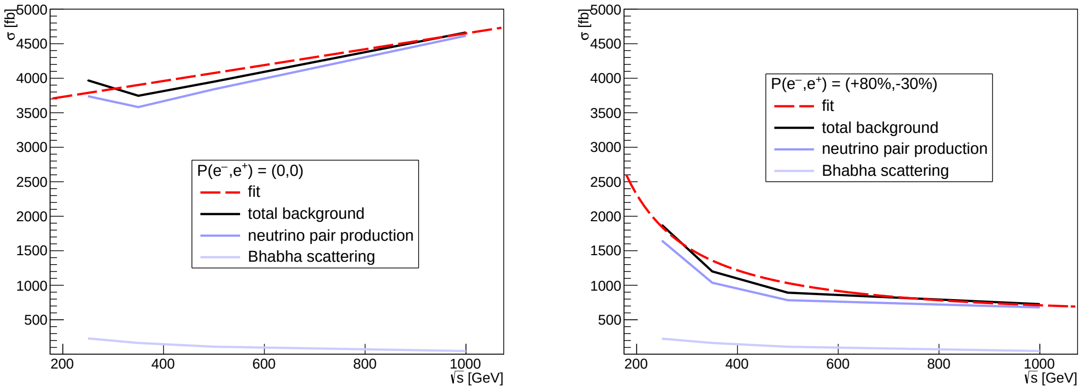

(a)

(b)

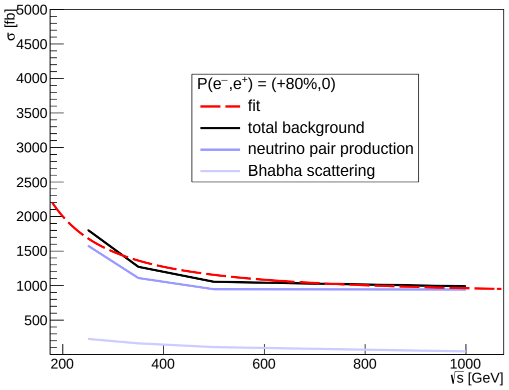

(c)

Figure 8.8: Fiducial background cross-section after the event selection as function of centre-of-mass energy. The fit functions (dashed lines) are listed in table 8.5.

The approximative descriptions of the background events as a function of $\sqrt{s}$ are summarised in table 8.5. As the number of background events is proportional to the integrated luminosity, the dependence on $\sqrt{s}$ is given by a function b, which relates to the number of background events as $b = B/\mathcal{L}$.

P_{e^-}	P_{e^+}	$b \propto$
0%	0%	$3500 + 1.15\sqrt{s}$
+80%	0%	$850 + 2.5 \cdot 10^6(\sqrt{s})^{-1.45}$
+80%	−30%	$500 + 2.2 \cdot 10^6(\sqrt{s})^{-1.34}$

Table 8.5: Approximative dependence of the number of background events ($e^+e^-\gamma$ and $\nu\nu\gamma$) on $\sqrt{s}$ with $b = B/\mathcal{L}$.

8.4.3 Relation between signal and background events

Whereas Λ could be expressed as a function of the number of signal events S, a relation to the number of background events B still has to be found. As a starting point the number of signal events is assumed to be proportional to the square root of the number of background events, which holds if only statistical errors are assumed. Thus, for a sensitivity reach Λ^{CL} with a certain confidence level k the relation is given by

$$S^{CL} = k\sqrt{B} \tag{8.7}$$

8.4.4 Formula for the extrapolation

With the formula for the signal events (equation 8.6) equation 8.3 can be rewritten:

$$\Lambda^{CL} \propto (\sqrt{s})^{\frac{3}{4}} \sqrt[4]{\frac{\epsilon\mathcal{L}}{S^{CL}}} \tag{8.8}$$

and

$$\Lambda^{CL} = \Lambda_0^{CL} \left(\frac{\sqrt{s}}{\sqrt{s}_0}\right)^{\frac{3}{4}} \sqrt[4]{\frac{\mathcal{L}}{\mathcal{L}_0}} \sqrt[4]{\frac{S_0^{CL}}{S^{CL}}} \tag{8.9}$$

where the constant selection efficiency cancels out.

With the relation between number of signal and background events (equation 8.7) and $B = \mathcal{L}b$ this is

$$\Lambda^{CL} = \Lambda_0^{CL} \left(\frac{\sqrt{s}}{\sqrt{s}_0}\right)^{\frac{3}{4}} \sqrt[8]{\frac{\mathcal{L}}{\mathcal{L}_0}} \sqrt[8]{\frac{b_{0,P}}{b_P}} \tag{8.10}$$

Assuming the relation between number of signal and background events for statistical uncertainties only (see section 8.4.3) the sensitivity scales with the integrated luminosity to the power of 1/8. In a more realistic setting, where also systematic effects are taken into account, a slower increase of the sensitivity is expected. The scans with different values for the integrated luminosity (presented in section 7.2.5) show that the proportionalities of 1/8−1/9 are close the expectations for sensitivities calculated with *several* data sets with different polarisation configurations.

This extrapolation formalism is however restricted to single data sets. For these cases the proportionalities have different powers between $1/23$ and $1/10$, depending on operator and polarisation configuration. These empirical values will be used for the different polarisation configurations instead of $\Lambda \propto \mathcal{L}^{1/8}$. As the extrapolation is only suitable for low WIMP masses, the values for $M_\chi = 1\,\text{GeV}$ of table 7.1 will be plugged into formula 8.10.

This means that the extrapolation formula depends on the operator and polarisation configuration. Also how the number of background events depends on $\sqrt{s}$ varies with the polarisation (compare with table 8.5). For the example of unpolarised beams and the vector or axial-vector operator the final formula is

$$\Lambda^{CL} = \Lambda_0^{CL} \left(\frac{\sqrt{s}}{\sqrt{s_0}}\right)^{\frac{3}{4}} \left(\frac{\mathcal{L}}{\mathcal{L}_0}\right)^{1/22} \sqrt[8]{\frac{3500 + 1.15\sqrt{s_0}}{3500 + 1.15\sqrt{s}}} \tag{8.11}$$

8.4.5 Accuracy of the extrapolation

In order to test the accuracy of the extrapolation formalism, the results are compared to the expected exclusion limits for different centre-of-mass energies calculated with the approach presented in section 8.3. The example of unpolarised beams and the vector operator is shown in figure 8.9. The values of the two approaches are in very good agreement. At $\sqrt{s} = 250\,\text{GeV}$ the extrapolated energy reach is 910 GeV, which is $\leq 1\%$ smaller than the value at $M_\chi = 1\,\text{GeV}$ of the exclusion curve (918 GeV). At 350 GeV the difference is also slightly smaller with $\Lambda = 1167\,\text{GeV}$ from the extrapolation and 1174 GeV from the full limit calculation.

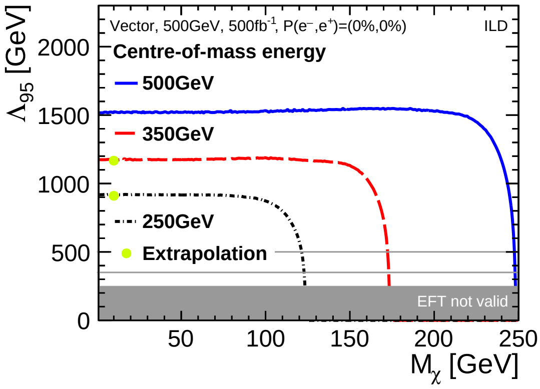

Figure 8.9: Comparison of the two approaches to calculate the sensitivity at other centre-of-mass energies: 2σ exclusion limits for unpolarised beams. The solid lines follow the approach in section 8.3 and the dots are obtained with the extrapolation.

8.4.6 Expected exclusion limits obtained with the extrapolation formalism

The results of the extrapolation for the full centre-of-mass range of the ILC and integrated luminosities of up to 5 ab^{-1} are presented in figures 8.10 and 8.11 for the vector and axial-vector operators, respectively. In figures 8.10a and 8.11a exclusion limits for unpolarised beams are shown and in figures 8.10b and 8.11b for $P(e^-, e^+) = (+80\%, -30\%)$. The input values from the full simulation are the energy scales Λ_{95} shown in figure 7.6 (unpolarised) and shown as the red curves in figure 7.8 ($P(e^-, e^+) = (+80\%, -30\%)$).

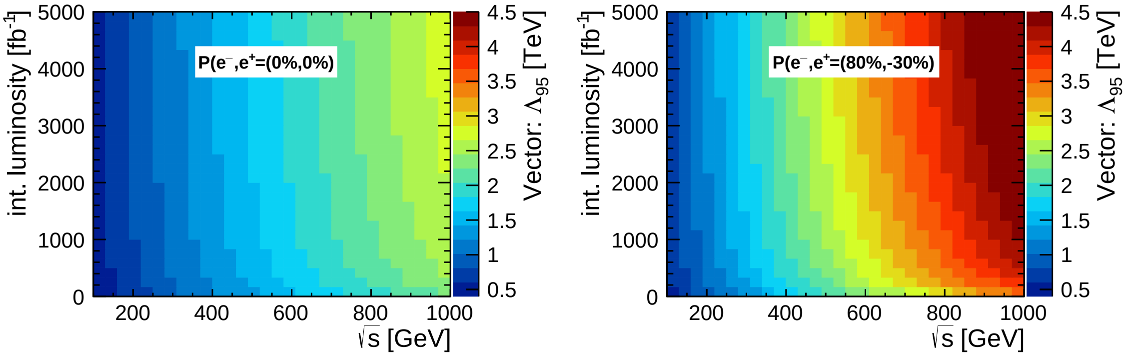

(a)

(b)

Figure 8.10: Expected 2σ exclusion limits obtained with the extrapolation formalism for the vector operator assuming (a) unpolarised beams and (b) $P(e^-, e^+) = (+80\%, -30\%)$.

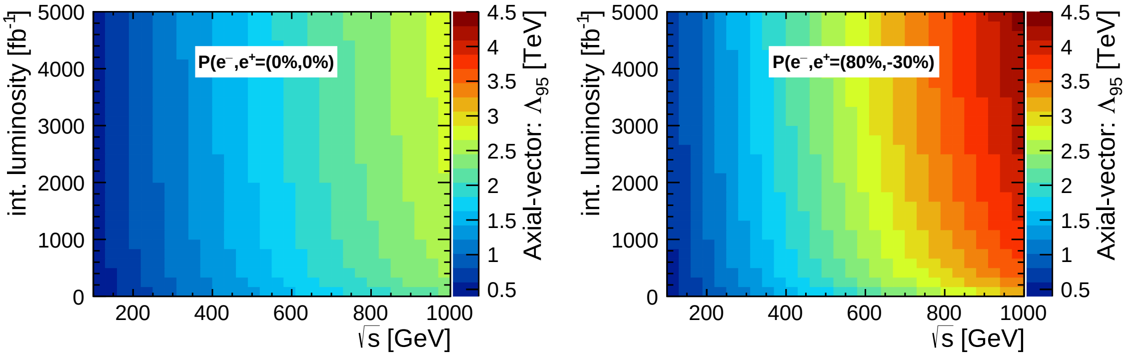

(a)

(b)

Figure 8.11: Results from the extrapolation formalism for the axial-vector operator assuming (a) unpolarised beams and (b) $P(e^-, e^+) = (+80\%, -30\%)$.

In this two-dimensional presentation, the effect of centre-of-mass energy and integrated luminosity can be easily visualised and compared. One of the key conclusions of this study is that a higher centre-of-mass energy is more beneficial than collecting large amounts of data at a lower centre-of-mass energy. This can be shown for the example of the vector operator, where the improvement with integrated luminosity at $\sqrt{s} = 250\,\mathrm{GeV}$ is small (the reachable energy is $\leq 1300\,\mathrm{GeV}$ with $500\,\mathrm{fb}^{-1}$ and $\Lambda \leq 1550$ with $5\,\mathrm{ab}^{-1}$), but at $\sqrt{s} = 500\,\mathrm{GeV}$ and $500\,\mathrm{fb}^{-1}$ already energy scales up to 2350 GeV can be probed.

With the extrapolation formalism approximative results for a centre-of-mass of 1 TeV can be given for the first time. For the vector operator the expected exclusion limits assuming an integrated luminosity of $1\,\mathrm{ab}^{-1}$ are $\Lambda = 2590\,\mathrm{GeV}$ for unpolarised beams and 4350 GeV for $P(e^-, e^+) = (+80\%, -30\%)$. For the axial-vector operator the corresponding values are 2590 GeV and 3860 GeV, which shows again the potential of polarised beams.

In [114] the proposed full integrated luminosity for the ILC at $\sqrt{s} = 1\,\mathrm{TeV}$ is $8\,\mathrm{ab}^{-1}$ [114]. As the extrapolation formalism does not allow to give results for data sets with different polarisation sharings, the 40% or $3200\,\mathrm{fb}^{-1}$ collected with $P(e^-, e^+) = (+80\%, -30\%)$ are taken to give a conservative estimate for the full potential at 1 TeV. The exclusion limits for the vector operator and axial-vector operator are 4760 GeV and 4220 GeV, respectively, which corresponds to an increase of ~50% compared to the results obtained in 20 years of operation at lower centre-of-mass energies.

8.5 Comparison of the different approaches

As shown in section 8.4.5, the results of the two different approaches presented in sections 8.3 and 8.4 are very similar.

With the different ways to calculate the sensitivity a variety of configurations can be tested. The biggest advantage of the extrapolation formalism over the full calculation of limits is a high flexibility. Without any CPU-intensive calculations, limits can be obtained for arbitrary integrated luminosities and centre-of-mass energies, including higher energies than the 500 GeV of the full simulation.

The full sensitivity calculation with TSysLimit, on the other hand, allows a proper treatment of the systematic effects and allows to calculate the sensitivity for data sets taken with different polarisation combinations and centre-of-mass energies. Additionally, it is not restricted to a certain WIMP mass range

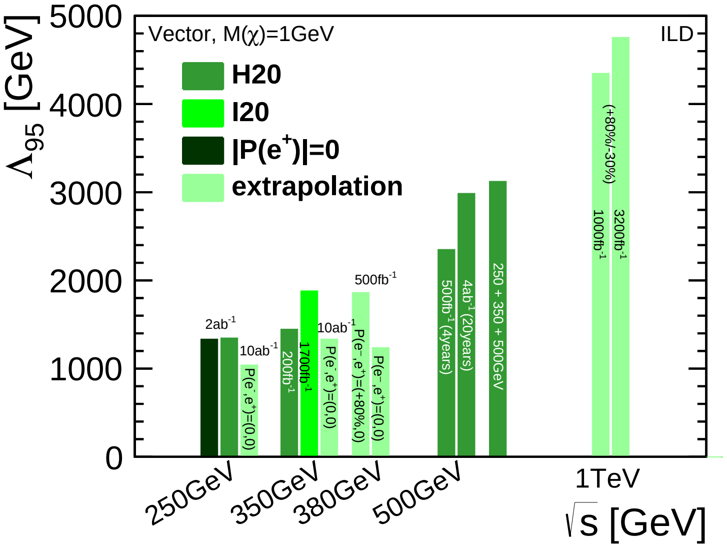

Figure 8.12: Expected exclusion limits for the vector operator assuming a WIMP mass of 1 GeV.

In order to compare the results obtained with the different approaches, a selection of expected exclusion limits for $M_\chi = 1\,\text{GeV}$ is assembled in figures 8.12 and 8.13 for the vector and axial-vector operator, respectively.

The results at 500 GeV are based on the full simulation. The other values for the H20 and I20 scenarios are those from figures 8.5 and 8.6 and the polarisation sharing can be seen in table 3.1. With the extrapolation formalism the sensitivities for different integrated luminosities and polarisation configurations at $\sqrt{s} = 250\,\text{GeV}$, 350 GeV, 380 GeV and 1 TeV are calculated.

The first two bars at $\sqrt{s} = 250\,\text{GeV}$ show once again that the exact sharing of the polarisation combination has a minor effect on the expected sensivity for $\mathcal{L} = 2\,\text{ab}^{-1}$. As discussed in section 8.3.3, the result for the vector operator is somewhat better with positron polarisation, but slightly worse for the axial-vector operator. Even though the exact mixing of the polarisation configurations is not important for the reachable energy scales, the drastic effect of polarisation can be seen, when the results are compared to the third case at $\sqrt{s} = 250\,\text{GeV}$, where electron and positron are both assumed to be unpolarised. Even with a five times higher integrated luminosity of $10\,\text{ab}^{-1}$ the lack of polarisation cannot be compensated.

For $\sqrt{s} = 350\,\text{GeV}$ two different values of integrated luminosity are compared assuming a polarisation sharing of $(--, -+, +-, ++) = (5\%, 67.5\%, 22.5\%, 5\%)$. With the larger data sets with $1700\,\text{fb}^{-1}$ proposed to be taken in the I20 scenario about 30% higher energy scales can be tested than with the $\mathcal{L} = 200\,\text{fb}^{-1}$ of the H20 scenario. The comparison with the third case (no polarisation, $\mathcal{L} = 10\,\text{ab}^{-1}$) shows that

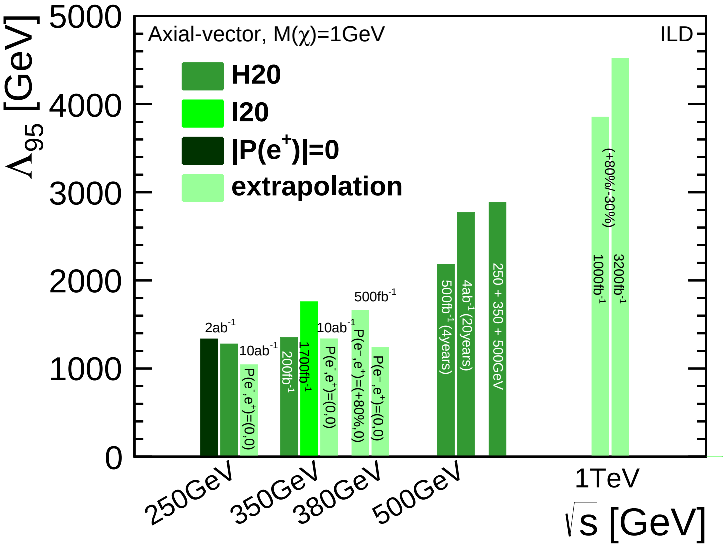

Figure 8.13: Expected exclusion limits for the axial-vector operator and a WIMP mass of 1 GeV.

the effect of the integrated luminosity is significantly smaller than the importance to have beam polarisation.

With the extrapolation formalism also additional centre-of-mass energies, which are not foreseen in the ILC running scenarios, can be tested without CPU-intensive calculations. For $\sqrt{s} = 380\,\mathrm{GeV}$ and $\mathcal{L} = 500\,\mathrm{fb}^{-1}$ two exclusion limits are shown. The scenario that the complete data set is taken with predominantly right-handed electrons and unpolarised positrons is assumed to show the optimal case for the studied operators, even though it is an unlikely setup, because many Standard Model processes would be suppressed. It can be seen that with this optimistic case the result is significantly better than for unpolarised beams. With electron polarisation the higher centre-of-mass energy can even compensate for the lack of positron polarisation and the lower integrated luminosity, indicated by the limit which is very close to the result for $\sqrt{s} = 350\,\mathrm{GeV}$ assuming the I20 scenario.

At $\sqrt{s} = 500\,\mathrm{GeV}$ results for integrated luminosities corresponding to the first four years of the H20 scenario and the full programme are assumed. These results are based on the full simulation and have been shown in figures 7.9 and 8.1. If the H20 data sets for the lower centre-of-mass energies of 250 GeV and 350 GeV are added, the improvement is only in the per cent range.

In section 7.6.2 it was discussed that exclusion limits calculated with several data sets with different polarisation combinations are very close to those assuming only one data set with the optimal polarisation configuration. With the assumption that this also holds for $\sqrt{s} = 1\,\mathrm{TeV}$, the results can be compared to those at other centre-of-mass energies. This clearly shows that the sensitivity calculation profits more from higher centre-of-mass energies than from integrated luminosities. For example the expected exclusion limit for $\sqrt{s} = 1\,\text{TeV}$ and $1\,\text{ab}^{-1}$ is almost 50% higher than the value for $\sqrt{s} = 500\,\text{GeV}$ and $4\,\text{ab}^{-1}$.

8.6 Comparison with other colliders

After the presentation of results for the complete ILC programme the potential is compared to other colliders. In section 8.6.1 it will be discussed how the framework for the calculation of the ILC sensitivity can be used to give estimates for the potential of other planned electron-positron colliders. In section 8.6.2 and 8.6.3 the ILC reach is compared to the LEP results obtained with the same framework of effective operators and selected exclusion limits of the LHC.

8.6.1 Other planned lepton colliders

With detector effects at the per cent scale (see section 7.3) and a small influence of different values of the systematic uncertainties (see section 7.6.4), the overall scale of the exclusion limits calculated for the ILC is expected to be independent of the exact design of machine and detector. Different machine designs will result in different beam parameters and hence the luminosity spectrum varies from accelerator to accelerator. The approach in the previous WIMP search to compare different ILC beam energy spectra showed that the effect on the reachable energy is at the per cent level.

This means that the extrapolation formalism can be used to calculate approximative results for the other planned lepton colliders CLIC, CepC and FCC-ee (introduced in section 3.1), based on their standard assumptions on centre-of-mass energy, integrated luminosity and polarisation.

8.6.1.1 Prospects for the first stage of CLIC

The centre-of-mass energy of the first stage of CLIC [100] is supposed to be 380 GeV and no positron polarisation is foreseen. As results from a combination of data sets with different polarisation configurations cannot be given in the extrapolation formalism, expected exclusion limits are calculated for the pessimistic case of unpolarised beams and for the optimistic (but unrealistic) case of right-handed electrons, where the background is reduced in the latter case. For the shown results in figures 8.12 and 8.13 500 fb^{-1} are assumed. The expected exclusion limits are also given in table 8.6. As can be seen, the limits obtained with polarised beams are close to the results at 350 GeV assuming the I20 scenario. If a lepton collider was operated at $\sqrt{s} = 380$ GeV without electron polarisation the reach of a machine with polarisation would be better already at 250 GeV.

operator	vector	axial-vector
no polarisation	1240	1240
+80% electron polarisation	1870	1660

Table 8.6: Approximative exclusion limits for the first stage of CLIC at 380 GeV for the vector and axial-vector operators. The integrated luminosity of 500 fb^{-1} is assumed to be either taken with unpolarised beams or with 80% right-handed electrons.

8.6.1.2 Circular colliders

As stated in section 3.1, both CEPC [103, 104] and FCC-ee [101, 102] are supposed to have an energy in the range of the lower ILC centre-of-mass energies. In order to study the potential of circular machines the results at 250 GeV and 350 GeV are extrapolated to a very large integrated luminosity of 10 ab^{-1}, which is twice the expected value for CEPC operating for 10 years with two detectors [182]. At CEPC and FCC-ee no polarisation is foreseen and hence the sensitivity is calculated for unpolarised beams.

The exclusion limits are shown in figures 8.12 and 8.13 as the third bar at $\sqrt{s} = 250$ GeV and $\sqrt{s} = 350$ GeV. For both the vector and axial-vector operators the exclusion limits are estimated to be 1040 GeV for CEPC at $\sqrt{s} = 250$ GeV and 1340 GeV for FCC-ee at $\sqrt{s} = 350$ GeV, which is significantly lower than the level of more than 2 TeV after 4 years in the H20 scenario (shown as the first bars in the figures).

This shows that the impact of the high luminosity of circular colliders at low centre-of-mass energies is very limited due to the absence of beam polarisation. The polarisation is not only essential to reduce SM backgrounds, but also (as disucssed in section 7.6.2) to control systematic uncertainties, which becomes more and more important with increasing size of the data set.

8.6.2 Comparison to LEP results

A comparison of the LEP results [72] (figure 2.10 on page 43) and the ILC results for $\sqrt{s} = 500\,\mathrm{GeV}$ (figure 8.1) shows that the testable WIMP mass range is more than doubled at the ILC due to the higher centre-of-mass energy. The shape of the exclusion regions obtained for LEP are similar to the ones for ILC.

The LEP exclusion curves are calculated for a confidence level of 90%. In order to allow a comparison, the ILC limit calculation is repeated for a WIMP mass of 1 GeV with the same confidence level. As examples the expected exclusion limits for the lowest centre-of-mass energy of the ILC of 250 GeV and for 500 GeV are calculated. In both cases the integrated luminosities and polarisation sharings from the H20 scenario are assumed. In table 8.7 the ILC results are compared to the LEP values which are shown in figure 2.10.

$\Lambda_{90\%}$ [GeV]		LEP	ILC	
	$\sqrt{s}$	~200 GeV	250 GeV	500 GeV
vector		480	1410	3140
axial-vector		480	1340	2920
scalar		440	1250	2710

Table 8.7: Comparison of LEP and ILC exclusion limits with a 90% confidence level for an assumed WIMP mass of 1 GeV. The LEP values are read off from figure 2.10 [72].

Already at its lowest foreseen centre-of-mass energy of 250 GeV the ILC can explore new phase space. The limits are improved by a factor of 3 or 1 TeV absolute. With the slightly higher centre-of-mass energy alone the sensitivity limits are not expected to increase much, though a tremendous improvement can be reached with the substantially higher integrated luminosity and due to beam polarisation.

With the expected exclusion limits of the complete ILC programme, which can be estimated by the results for $\sqrt{s} = 500\,\mathrm{GeV}$, the improvement corresponds to a factor of 6.

8.6.3 Comparison to LHC exclusion limits

The exclusion curve for LHC obtained with CMS data at 13 TeV [89] (section 2.4.2.1) can be compared to ILC results even though in [89] simplified models are assumed.

Exclusion limits in effective field theory can be converted to simplified models, as long as the mediator mass is significantly larger than the centre-of-mass energy.

In order to make a comparison between hadron and lepton collider exclusion limits, assumptions have to be made on the coupling of WIMPs to different Standard Model particles. Here, a simple example is given by assuming the same coupling to leptons for the case of the ILC as for the coupling to hadrons in the case of the LHC. With a coupling to dark matter of 1 and a coupling to Standard Model particles of 0.25 the mediator mass corresponding to a certain energy scale Λ can be calculated

$$M_{\text{mediator}} = \sqrt{q_\chi q_{SM}}\ \Lambda_{95} = \sqrt{1 \cdot 0.25}\ \Lambda_{95} \tag{8.12}$$

In figure 8.14 the LHC exclusion curve for the vector operator (shown in figure 2.11) is compared to the ILC results for a centre-of-mass of 500 GeV, assuming the polarisation sharing of the H20 scenario and two different integrated luminosities, 500 fb^{-1} and 4 ab^{-1}. The corresponding ILC sensitivity calculated with effective operators is shown in figure 7.11. In comparison to the presentation of results in the framework of effective operators, the axes in figure 8.14 are inverted, following the standard presentation of LHC results [88].

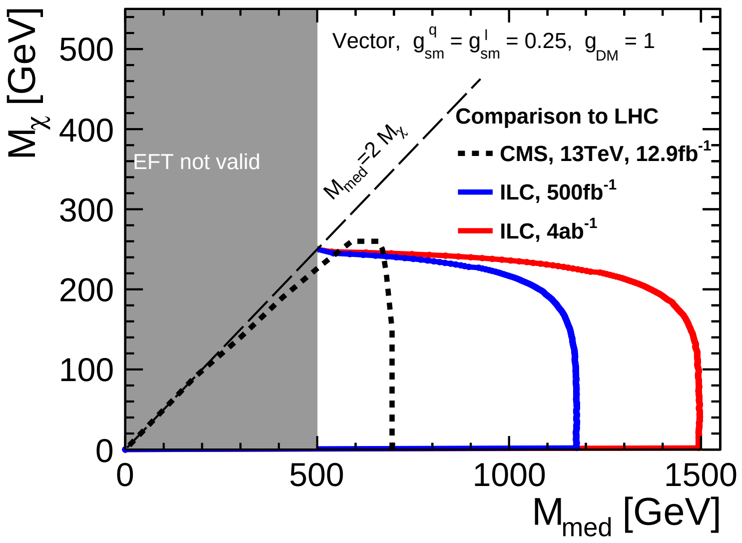

Figure 8.14: Comparison of LHC and expected ILC exclusion limits for the vector operator. The ILC sensitivity is converted to the framework of simplified models.

The grey region indicates that at low mediator masses the approach of effective operators cannot be applied. The testable WIMP mass range is almost identical, but at the ILC the excluded mediator mass range is about two times larger than at LHC. This is a striking demonstration of the power to conduct precision measurements in the clean environment of lepton colliders, which was discussed in section 2.5.

The presented LHC results show the current status of a particular analysis. With increasing integrated luminosity the exclusion limits will improve and may well reach the level of a few TeV, both in terms of mediator and WIMP mass. Here, as also shown in this study, it is very crucial to understand the systematic uncertainties. For different assumptions made in extrapolation studies to higher integrated luminosities the LHC sensitivity is expected to either increase very slowly [183] or the projections are more optimistic [84].

Chapter 9

Conclusion

In this thesis, the expected sensitivity of the future electron-positron collider ILC to WIMP dark matter was evaluated. With a Monte Carlo study of the ILD detector concept the expected discovery reach and the expected exclusion limits were calculated for WIMP masses in the range $1 - 250\,\text{GeV}$, assuming pair production of WIMPs in association with an ISR photon.

For a centre-of-mass energy of $500\,\text{GeV}$ dedicated data sets of the most important Standard Model background processes, namely neutrino pair production and Bhabha scattering, were produced with up to 4 detectable photons. The setup provides for the first time a modelling of ISR, which was constructed in a way that double-counting of the photons is avoided, in combination with a detailed description of the lepton collider environment provided by the event generator WHIZARD [139].

A shortcoming of WHIZARD encountered during this work is the necessity of cuts to avoid divergences of the Bhabha scattering process leading to an underestimation of this background. Whereas the developed setup gives a sufficient description, in the presence of real data a dedicated programme to generate Bhabha scattering, which allows to control the number of photons as well as the phase space of the signal-like photon, would be required in order to model the background more precisely.

In comparison to previous studies [1–3] the description of the Bhabha scattering phase space has been nevertheless improved, which allowed to study the lepton identification down to the smallest polar angles. For the forward detector BeamCal a new reconstruction programme [129] was tuned to the ILD setup, which provides high efficiencies to reconstruct Bhabha leptons in the challenging environment of high rates of beam-induced background. Despite the possibility to reconstruct fakes, which adds more realism to the reconstruction, the number of lost signal-like events is low.

With an event selection allowing only little detector activity besides the signal photon, the Bhabha scattering background could be suppressed to the per mille level, whereas 60−70% of the signal-like neutrino events were kept. The effect of a redesign of the forward region with a smaller L* was estimated to lead to an increase of the Bhabha scattering background by 50%. Other detector effects like the impact of the observed photon reconstruction deficits or the potential improvement with a better resolution of the electromagnetic calorimeter were studied by smearing the Monte Carlo true photon energy instead of using the reconstructed photons. All of these detector effects were estimated to influence the sensitivity only at the level of a few per cent.

The expected sensitivity was calculated using a frequentist approach with fractional event counting. The description of the WIMP production is based on effective operators [70]. Instead of full models the signal is described by simplified setups with only one free parameter Λ, which is the energy scale of the new physics. It could be shown that the testable energy scales are well above the centre-of-mass energy and hence effective operators are a suitable approach. Three different operators (vector, axial-vector and scalar) were tested. The main results of this study are expected exclusion limits and the potential discovery reach, both expressed in terms of the energy scale of the new interaction Λ.

Assuming data corresponding to 20 years of operation, up to $\Lambda_{95} \approx 3\,\mathrm{TeV}$ can be excluded and a signal with $\Lambda_{5\sigma} \approx 1\,\mathrm{TeV}$ could be discovered with a confidence level corresponding to 5σ. Polarised beams are essential to reduce the Standard Model background and, depending on the tested effective operator, can increase the signal, which leads to an improved sensitivity of 50% or more.

This is the first WIMP study at the ILC with a thorough treatment of the systematic uncertainties and their correlations. The largest source of systematic uncertainties is the one on the shape of the luminosity spectrum. The uncertainties were determined from beam monitoring measurements by varying the beam parameters within the uncertainties of the fit in the simulation of beam-beam interactions. The uncertainties are in the per cent range and depend on the photon energy and the polarisation configuration and, in the case of the signal, on the WIMP mass.

Together with additional systematic effects in the per mille range the sensitivity drops by ∼25% compared to a test run without systematic uncertainties. If on the other hand events taken with different polarisation combinations are treated as separate data sets, the decrease is only ∼10%. Thus, beam polarisation is important to provide independent data sets with different helicity combinations resulting in different signal-to-noise ratios, where data sets with a suppressed signal production act as control sample to cross-calibrate the systematic uncertainties.

The effect of improved values for the systematic uncertainties as well as more pessimistic assumptions were tested and found to be at the per cent level. Also if more systematic effects are included, the effect is expected to be small as long as the values are at the per mille level.

The full simulation was performed at 500 GeV, but approximated results can be given for other energies in two ways. The signal and background photon spectra can be reweighted to other ILC energies, which allows to calculate the sensitivity for different WIMP masses with the full treatment of systematic uncertainties. Alternatively, the reachable energy scales Λ of the full simulation can be extrapolated to other centre-of-mass energies, which provides a simple tool to calculate estimates for arbitrary centre-of-mass energies and integrated luminosities and hence also approximative results for other planned electron-positron colliders can be given. With the latter approach expected exclusion limits for $\sqrt{s} = 1\,\text{TeV}$ were estimated to be up to 4.5 TeV.

A comparison to LEP results showed that new phase space in the search for dark matter can be explored already at the lowest centre-of-mass energies of the ILC (250 GeV), where higher luminosity and beam polarisation can improve the exclusion limits to 1.4 TeV (or could lead to the discovery of a new particle). Also the complementarity to LHC results was tested in a comparison using the framework of simplified models, where the expected exclusion limits of the ILC are significantly better if the WIMP couplings to leptons are assumed to be the same as to hadrons.

This study has shown that the ILD detector concept meets the key requirements of a WIMP search and the identification of the decisive role of beam polarisation and the preference of higher centre-of-mass energies are important conclusions for future lepton colliders. With the results presented in this thesis the basis for comparison studies is provided, e.g. to assess if the surving phase space, identified by combining results from several search channels [78], can be probed with a lepton collider. If a signal is discovered in a direct or indirect detection experiment, measurements at a collider will have a central role to test proposed underlying models. But if no sign of dark matter can be seen in direct detection experiments nor at the LHC, WIMPs that couple preferentially to leptons could still be discovered at the ILC.

Appendix A

GuineaPig output file

The GuineaPig output file *lumi.dat* contains the energies of the colliding electrons and positrons in the first two columns. The quantities in the other columns of the shown snippet of the file are the horizontal x, vertical y and longitudinal z position of the particles in the bunch. x and y are given in nm and z in μm.

```
250.196 249.959 169.11 3.32221 49.1316
250.059 250.287 -769.834 3.2866 -157.144
249.972 249.94 -539.705 -7.85066 -61.2875
249.997 250.022 245.934 -1.70537 16.6295
249.915 250.044 -535.721 -7.99731 -139.934
250.475 249.97 502.44 -4.2972 -62.0753
250.103 250.113 -491.531 -0.718363 -109.257
250.529 249.807 302.742 6.61742 39.8287
249.875 249.945 -109.681 2.70163 219.092
249.907 249.961 788.413 -1.73183 191.288
250.102 249.85 -194.842 2.1879 -24.3691
249.867 249.95 -128.99 4.35144 -4.6716
249.996 249.843 59.2172 8.11148 -43.0604
250.274 250.105 164.955 5.92601 81.1485
250.158 249.971 565.401 -1.84355 -65.7293
250.301 250.342 -230.281 2.58403 -206.373

...
```

Appendix B

GUINEAPIG steering file

This is the steering file to simulate the beam-beam interaction with GUINEAPIG (see section 4.2) for baseline beam parameters (see section 3.5.1) at $\sqrt{s} = 500\,\text{GeV}$. For the evaluation of the systematic uncertainties several beam parameters, which are set in the `accelerator` section, were varied (see section 7.5.5). The `parameters` section contains settings for the simulation and the output files.

```
$ACCELERATOR::  Waisty_opt_Jan2012_500GeV
   {trav_focus=0;espread.1=0.00125;espread.2=0.0007;energy=250;
   particles=2;beta_x=11;beta_y=0.48;emitt_x=10.0;emitt_y=0.035;
   sigma_x=474;sigma_y=5.9;sigma_z=300;offset_y=0;offset_x=00.0;
   waist_x=0000;waist_y=250;f_rep=1.0;n_b=1;espread.1=0.00125;
   espread.2=0.0007;which_espread=3;charge_sign=-1;scale_step=1.0;
   angle_y=0.0000;angle_phi=-00.00000;}
$PARAMETERS::  par
   {n_x=16*4;n_y=16*4;n_z=64;n_t=10;n_m=80000;cut_x=4*sigma_x.1;
   cut_y=6*sigma_y.1+6*0;cut_z=3*sigma_z.1;hist_ee_bins=50;
   hist_ee_min=405;hist_ee_max=505;track_pairs=1;store_pairs=1;
   do_coherent=1;do_compt=1;grids=7;beam_size=1;rndm_seed=1;
   rndm_load=0;rndm_save=0;force_symmetric=0;integration_method=2;
   do_eloss=1;electron_ratio=1;do_pairs=1;pair_ratio=1.0;
   pair_ecut=0.0005;pair_q2=2;do_photons=1;store_photons=1;
   photon_ratio=0.1;do_hadrons=1;store_hadrons=1;hadron_ratio=10000;
   do_lumi=1;num_lumi=500000;lumi_p=1e-29;do_jets=1;store_jets=1;
   jet_ratio=10000;do_isr=0;do_espread=0;load_beam=3;do_dump=0;
   dump_step=1;dump_particle=1;electron_ratio=0.1;store_beam=1;}
```

Appendix C

CIRCE2 steering files

Steering file for the parametrisation giving the best description of the peak region, used for the event generation in this analysis.

```
{ file="/nfs/dust/ilc/user/haberm/mc_generated/E500-TRD_ws.circe"
  { design="ILC" roots=500 bins=100 scale=250
    { pid/1=electron pid/2=positron pol=0
    events="/afs/desy.de/group/flc/pool/haberm/beams/guineapig_beamspectra/
          existingGPoutput/WAISTY_250/lumi_1-20.dat"
    columns=2
    histogram="/nfs/dust/ilc/user/haberm/mc_generated/E500-TRD_ws.histogram"
    lumi = 8.00802e33
    iterations = 10
    min = 0 max = 1.05 bins = 100
    smooth = 5 [0.00,1.05] [0.00,1.05]
} } }
```

The CIRCE2 steering file for a parametrisation giving a more realistic description of the tails towards lower centre-of-mass energies differs in the following lines:

iterations = 2
min = 0 max = 1.05 bins = 100
smooth = 1 [0.00,1.05] [0.00,1.05]

Appendix D

Whizard steering files for the event generation

The Whizard steering files for radiative neutrino pair production and Bhabha scattering. The command language of Whizard version 2 is called Sindarin (Scripting INtegration, Data Analysis, Results display and INterfaces).

At the beginning the `process` is defined, which is a combination of neutrino pair production (or Bhabha scattering) with 1,2,3,4 (1,2,3) photons. With the help of aliases all three neutrino generations are adressed together.

In the `cuts` section the preselection from section 5.3.2 is defined, followed by the settings for the ISR, as described in section 5.4.1. Beam polarisation and centre-of-mass energy are defined and the Circe2 beam energy spectrum parametrisation (see section 4.3) is called.

Neutrino pair production:

```
model = SM
alias nu = ve:vm:vt
alias anu = "ve~":"vm~":"vt~"
process vv_LR = "e-", "e+" => ("nu", "anu", "A") + ("nu", "anu", "A", "A")
+ ("nu", "anu", "A", "A", "A") + ("nu", "anu", "A", "A", "A", "A")
compile
cuts =
   let subevt @meA = select if Index > 2 [A]
   in
   let subevt @trackA = select if abs (cos(Theta)) < 0.998 [@meA]
   in
```

```
   any Pt > 1 GeV [@trackA] ! 2nd sigdef pre-cut
   and all Pt > 0.1 GeV [@meA]
   and all abs(cos(Theta)) < 0.9999755 [@meA] ! all photons
   outside beam pipe
   and all Theta > 0.15 degree [@meA,@meA]
?isr_recoil = false
?isr_keep_energy = true
isr_order = 3
beams_pol_density = @(-1),@(+1)
beams_pol_fraction = 1.0,1.0
sqrts = 500 GeV
beams = e1,E1 => circe2 => isr
$circe2_file = "E500-TRD_ws.circe"
$circe2_design = "ILC"
?circe2_polarized = false
integrate (vv_LR)  iterations = 10:100000, 5:100000
luminosity = 600
sample_format = stdhep_ev4
$extension_stdhep_ev4 = "stdhep"
sample_split_n_kbytes=500000
?write_raw = false
?keep_remnants = true
?keep_beams = true
simulate (vv_LR)
```

Bhabha scattering:

```
model = SM
alias visible = e1:E1
process bhabha_LL = e1,E1 => (e1,E1,A)+(e1,E1,A,A)+(e1,E1,A,A,A)
compile
cuts =
   let subevt @meA = select if Index > 2 [A]
   in
   let subevt @trackA = select if abs (cos(Theta)) < 0.9975 [@meA]
   in
   any Pt > 1 GeV [@trackA] ! 2nd sigdef pre-cut
```

```
   and all Pt > 0.1 GeV [@meA]
   and all abs(cos(Theta)) < 0.9999755 [@meA] ! all photons
   outside beam pipe
   and all M > 1 GeV [visible,visible]
   and all M < -1 GeV [incoming particle, visible]
   and all M > 1 GeV [visible, @meA]
   and all M > 4 GeV [visible, @trackA]
   and all Theta > 0.15 degree [@meA,@meA]
?isr_recoil = false
?isr_keep_energy = true
isr_order = 3
beams_pol_density = @(-1),@(-1)
beams_pol_fraction = 1.0,1.0
sqrts = 500 GeV
beams = e1,E1 => circe2 => isr
$circe2_file = "E500-TRD_ws.circe"
$circe2_design = "ILC"
?circe2_polarized = false
integrate (bhabha_LL)  iterations = 10:1000000, 5:1000000
n_events = 3000000
sample_format = stdhep_ev4
$extension_stdhep_ev4 = "stdhep"
sample_split_n_kbytes=500000
?write_raw = false
?keep_remnants = true
?keep_beams = true
simulate (bhabha_LL)
```

Appendix E

Whizard steering file for the cross-section calculation

In this example WHIZARD steering file for the cross-section calculation scan over photon energy and cross-section (see section 7.1.2.2) the cross-section is 180 GeV, the photon energy $7.5\,\text{GeV} < E_\gamma < 8.5\,\text{GeV}$ and the resulting polar angle range $|\cos\theta| < 0.71$.

```
model = SM
alias nu = ve:vm:vt
alias anu = "ve ":"vm ":"vt "
process vvA = "e-", "e+" => ("nu", "anu", "A")
compile
cuts = all E > 7.5 [A]
    and all E < 8.5 [A]
    and all abs(cos(Theta)) < 0.707963 [A]
   sqrts = 180 GeV
integrate (vvA) { iterations = 10:1000000, 5:1000000 }
```

List of Figures

List of Tables

Bibliography

[1] C. Bartels, M. Berggren, and J. List, “Characterising WIMPs at a future e^+e^- linear collider,” *EPJ C* **72** no. 11, (2012) 2213. `https://doi.org/10.1140/epjc/s10052-012-2213-9`.

[2] C. Bartels, *WIMP search and a Cherenkov detector prototype for ILC polarimetry*. PhD thesis, University of Hamburg, 2011. `http://www-library.desy.de/cgi-bin/showprep.pl?desy-thesis-11-034`.

[3] A. Chaus, *Searches for Dark Matter particles and development of a pixellized readout of the Time Projection Chamber for the International Linear Collider (ILC)*. PhD thesis, Paris 11, 2014. `http://www.theses.fr/2014PA112300`.

[4] D. Larson, J. Dunkley, G. Hinshaw, *et al.*, “Seven-year Wilkinson Microwave Anisotropy Probe (WMAP*) observations: power spectra and WMAP-derived parameters,” *The Astrophysical Journal Supplement Series* **192** no. 2, (2011) 16. `http://stacks.iop.org/0067-0049/192/i=2/a=15`.

[5] **Planck** Collaboration, R. Adam *et al.*, “Planck 2015 results - I. Overview of products and scientific results,” *Astronomy & Astrophysics* **594** (2016) A1. `http://dx.doi.org/10.1051/0004-6361/201527101`.

[6] J. H. Oort, “The force exerted by the stellar system in the direction perpendicular to the galactic plane and some related problems,” *Bulletin of the Astronomical Institutes of the Netherlands* **6** (1932) 249. `http://cds.cern.ch/record/436532`.

[7] F. Zwicky, “On the masses of nebulae and of clusters of nebulae,” *The Astrophysical Journal* **86** (1937) 217. `http://adsabs.harvard.edu/doi/10.1086/143864`.

[8] V. C. Rubin and W. K. Ford Jr, "Rotation of the Andromeda nebula from a spectroscopic survey of emission regions," *The Astrophysical Journal* **159** (1970) 379. `http://adsabs.harvard.edu/doi/10.1086/150317`.

[9] A. Bosma, *The distribution and kinematics of neutral hydrogen in spiral galaxies of various morphological types.* PhD thesis, Rijksuniversiteit te Groningen, 1978. `http://hdl.handle.net/11370/9490a028-214d-4eb3-974d-3cedcfde44f2`.

[10] T. S. van Albada, J. N. Bahcall, K. Begeman, and R. Sanscisi, "Distribution of dark matter in the spiral galaxy NGC 3198," *The Astrophysical Journal* **295** (1985) 305–313. `http://adsabs.harvard.edu/doi/10.1086/163375`.

[11] D. Clowe, M. Bradač, A. H. Gonzalez, *et al.*, "A direct empirical proof of the existence of dark matter," *The Astrophysical Journal Letters* **648** no. 2, (2006) L109. `https://doi.org/10.1086/508162`.

[12] **Planck** Collaboration, "Planck 2015 results - XIII. Cosmological parameters," *Astronomy & Astrophysics* **594** (2016) A13. `dx.doi.org/10.1051/0004-6361/201525830`.

[13] P. Tisserand, "Constraints on Machos with the EROS-2 project," in *Dark Matter In Astroparticle And Particle Physics*, pp. 142–149. World Scientific, 2008. `https://doi.org/10.1142/9789812814357_0015`.

[14] H. Niikura, M. Takada, N. Yasuda, *et al.*, "Microlensing constraints on primordial black holes with the Subaru/HSC Andromeda observation," *arXiv:1701.02151* (2017) .

[15] S. L. Glashow, "Partial-symmetries of weak interactions," *Nuclear Physics* **22** no. 4, (1961) 579–588. `https://doi.org/10.1016/0029-5582(61)90469-2`.

[16] A. Salam and J. Ward, "Electromagnetic and weak interactions," *Physics Letters* **13** no. 2, (1964) 168 – 171.

[17] S. Weinberg, "A model of leptons," *Phys. Rev. Lett.* **19** (Nov, 1967) 1264–1266. `https://link.aps.org/doi/10.1103/PhysRevLett.19.1264`.

[18] H. Fritzsch, M. Gell-Mann, and H. Leutwyler, "Advantages of the color octet gluon picture," *Physics Letters B* **47** no. 4, (1973) 365 – 368. `http://www.sciencedirect.com/science/article/pii/0370269373906254`.

[19] Particle Data Group, C. Patrignani, *et al.*, “Review of particle physics,” *Chinese physics C* **40** no. 10, (2016) 100001 and 2017 update. `https://doi.org/10.1088/1674-1137/40/10/100001`.

[20] U. Mosel, *Fields, Symmetries, and Quarks.* Springer, 1999.

[21] D. Griffiths, *Introduction to elementary particles.* John Wiley & Sons, 2008.

[22] E. Noether, “Invariant variation problems,” *Transport Theory and Statistical Physics* **1** no. 3, (1971) 186–207. `https://doi.org/10.1080/00411457108231446`.

[23] P. Higgs, “Broken symmetries, massless particles and gauge fields,” *Physics Letters* **12** no. 2, (1964) 132 – 133.

[24] F. Englert and R. Brout, “Broken symmetry and the mass of gauge vector mesons,” *Phys. Rev. Lett.* **13** (Aug, 1964) 321–323.

[25] A. Strumia and F. Vissani, “Neutrino masses and mixings and...,” *arXiv hep-ph/0606054* (2006) .

[26] **AMS** Collaboration, T. Kobayashi *et al.*, “Lyman-α constraints on ultralight scalar dark matter: Implications for the early and late universe,” *Physical Review D* **96** no. 12, (2017) 123514.

[27] **MACHO** Collaboration, C. Alcock *et al.*, “The macho project: microlensing results from 5.7 years of large magellanic cloud observations,” *The Astrophysical Journal* **542** no. 1, (2000) 281. 7.

[28] D. J. Chung, P. Crotty, E. W. Kolb, and A. Riotto, “Gravitational production of superheavy dark matter,” *Physical Review D* **64** no. 4, (2001) 043503. `https://doi.org/10.1103/PhysRevD.64.043503`.

[29] G. Bertone, *Particle dark matter: observations, models and searches.* Cambridge University Press, 2010.

[30] A. Ringwald, “Exploring the role of axions and other wisps in the dark universe,” *Physics of the Dark Universe* **1** no. 1-2, (2012) 116–135. `https://doi.org/10.1016/j.dark.2012.10.008`.

[31] B. W. Lee and S. Weinberg, "Cosmological lower bound on heavy-neutrino masses," *Phys. Rev. Lett.* **39** (Jul, 1977) 165–168. `https://link.aps.org/doi/10.1103/PhysRevLett.39.165`.

[32] D. Dicus, E. Kolb, and V. Teplitz, "Cosmological upper bound on heavy-neutrino lifetimes," *Phys. Rev. Lett.;* **39** no. 168, (7, 1977) .

[33] P. Hut, "Limits on masses and number of neutral weakly interacting particles," *Physics Letters B* **69** no. 1, (1977) 85 – 88.

[34] J. Gunn, B. Lee, I. Lerche, *et al.*, "Some astrophysical consequences of the existence of a heavy stable neutral lepton," *The Astrophysical Journal* **223** (1978) 1015–1031. `http://adsabs.harvard.edu/doi/10.1086/156335`.

[35] G. Steigman, C. L. Sarazin, H. Quintana, and J. Faulkner, "Dynamical interactions and astrophysical effects of stable heavy neutrinos," *The Astronomical Journal* **83** (1978) 1050–1061. `http://adsabs.harvard.edu/abs/1978AJ.....83.1050S`.

[36] H. Goldberg, "Constraint on the photino mass from cosmology," *Phys. Rev. Lett* **50** (1983) 1419. `https://doi.org/10.1103/PhysRevLett.50.1419`.

[37] J. Ellis, J. S. Hagelin, D. V. Nanopoulos, *et al.*, "Supersymmetric relics from the big bang," *Nuclear Physics B* **238** no. 2, (1984) 453–476. `https://doi.org/10.1016/0550-3213(84)90461-9`.

[38] H.-C. Cheng and I. Low, "TeV symmetry and the little hierarchy problem," *Journal of high energy physics* **2003** no. 09, (2003) 051. `https://doi.org/10.1088/1126-6708/2003/09/051`.

[39] H.-C. Cheng and I. Low, "Little hierarchy, little higgses, and a little symmetry," *Journal of High Energy Physics* **2004** no. 08, (2004) 061. `https://doi.org/10.1088/1126-6708/2004/08/061`.

[40] T. Kaluza, "Zum Unitätsproblem der Physik," *Sitzungsber. Preuss. Akad. Wiss. Berlin.(Math. Phys.)* **1921** (1921) 966–972, `1803.08616`.

[41] O. Klein, "Quantum theory and five-dimensional theory of relativity.," *Surveys High Energ. Phys.* **5** (1926) 895–906. `https://link.springer.com/article/10.1007%2FBF01397481`.

[42] T. Appelquist, H.-C. Cheng, and B. A. Dobrescu, “Bounds on universal extra dimensions,” *Physical Review D* **64** no. 3, (2001) 035002.

[43] G. Jungman, M. Kamionkowski, and K. Griest, “Supersymmetric dark matter,” *Physics Reports* **267** no. 5-6, (1996) 195–373. `https://doi.org/10.1016/0370-1573(95)00058-5`.

[44] E. W. Kolb and M. S. Turner, “The early universe,” *Front. Phys.* **69** (1990) 1–547.

[45] M. Milgrom, “A modification of the Newtonian dynamics as a possible alternative to the hidden mass hypothesis,” *The Astrophysical Journal* **270** (1983) 365–370. `http://adsabs.harvard.edu/doi/10.1086/161130`.

[46] J. D. Bekenstein, “Relativistic gravitation theory for the modified Newtonian dynamics paradigm,” *Physical Review D* **70** no. 8, (2004) 083509.

[47] D. Hooper and E. A. Baltz, “Strategies for determining the nature of dark matter,” *Annual Review of Nuclear and Particle Science* **58** (2008) 293–314. `https://doi.org/10.1146/annurev.nucl.58.110707.171217`.

[48] T. M. Undagoitia and L. Rauch, “Dark matter direct-detection experiments,” *Journal of Physics G: Nuclear and Particle Physics* **43** no. 1, (2015) 013001. `https://doi.org/10.1088/0954-3899/43/1/013001`.

[49] **XENON** Collaboration, E. Aprile *et al.*, “Dark matter search results from a one tonne × year exposure of XENON1T,” *arXiv:1805.12562* (2018) .

[50] **LUX** Collaboration, D. Akerib *et al.*, “Results from a search for dark matter in the complete LUX exposure,” *Physical review letters* **118** no. 2, (2017) 021303.

[51] **PandaX-II** Collaboration, X. Cui *et al.*, “Dark matter results from 54-ton-day exposure of PandaX-II experiment,” *Physical review letters* **119** no. 18, (2017) 181302.

[52] W. Atwood, A. A. Abdo, M. Ackermann, *et al.*, “The Large Area Telescope on the Fermi gamma-ray space telescope mission,” *The Astrophysical Journal* **697** no. 2, (2009) 1071. `https://doi.org/10.1088/0004-637X/697/2/1071`.

[53] M. Doro, “A decade of dark matter searches with ground-based Cherenkov telescopes,” *Nucl. Instrum. Methods Phys. Res. Section A: Accelerators, Spectrometers, Detectors and Associated Equipment* **742** (2014) 99–106. `https://doi.org/10.1016/j.nima.2013.12.010`.

[54] M. Leventhal, “Positronium-formation redshift of the 511-keV annihilation line,” *The Astrophysical Journal* **183** (1973) L147.

[55] **AMS** Collaboration, M. Aguilar *et al.*, “First result from the Alpha Magnetic Spectrometer on the International Space Station: precision measurement of the positron fraction in primary cosmic rays of 0.5–350 GeV,” *Physical Review Letters* **110** no. 14, (2013) 141102.

[56] L. Accardo, M. Aguilar, *et al.*, “High statistics measurement of the positron fraction in primary cosmic rays of 0.5–500 GeV with the Alpha Magnetic Spectrometer on the International Space Station,” *Physical review letters* **113** no. 12, (2014) 121101.

[57] M. Boezio, G. Barbiellini, V. Bonvicini, *et al.*, “Measurements of cosmic-ray electrons and positrons by the Wizard/CAPRICE collaboration,” *Advances in Space Research* **27** no. 4, (2001) 669–674. `https://doi.org/10.1016/S0273-1177(01)00108-9`.

[58] J. Beatty, A. Bhattacharyya, C. Bower, *et al.*, “New measurement of the cosmic-ray positron fraction from 5 to 15 GeV,” *Physical Review Letters* **93** no. 24, (2004) 241102.

[59] M. DuVernois, S. Barwick, J. Beatty, *et al.*, “Cosmic-ray electrons and positrons from 1 to 100 GeV: measurements with HEAT and their interpretation,” *The Astrophysical Journal* **559** no. 1, (2001) 296. `https://doi.org/10.1086/322324`.

[60] M. Aguilar, J. Alcaraz, J. Allaby, *et al.*, “Cosmic-ray positron fraction measurement from 1 to 30 GeV with AMS-01,” *Physics Letters B* **646** no. 4, (2007) 145–154. `https://doi.org/10.1016/j.physletb.2007.01.024`.

[61] O. Adriani, G. Barbarino, G. Bazilevskaya, *et al.*, “Cosmic-ray positron energy spectrum measured by PAMELA,” *Physical review letters* **111** no. 8, (2013) 081102.

[62] M. Ackermann, M. Ajello, A. Allafort, *et al.*, "Measurement of separate cosmic-ray electron and positron spectra with the Fermi Large Area Telescope," *Physical Review Letters* **108** no. 1, (2012) 011103.

[63] V. Barger, F. Halzen, D. Hooper, and C. Kao, "Indirect search for neutralino dark matter with high energy neutrinos," *Phys. Rev. D* **65** (Apr, 2002) 075022. `https://link.aps.org/doi/10.1103/PhysRevD.65.075022`.

[64] F. Kahlhoefer, "Review of LHC dark matter searches," *International Journal of Modern Physics A* **32** no. 13, (2017) 1730006.

[65] M. Berggren, A. Cakir, D. Krücker, *et al.*, "Non-simplified SUSY: $\widetilde{\tau}$-coannihilation at LHC and ILC," *EPJ C* **76** no. 4, (2016) 183. `https://doi.org/10.1140/epjc/s10052-016-3914-2`.

[66] D. Abercrombie, N. Akchurin, E. Akilli, *et al.*, "Dark matter benchmark models for early LHC run-2 searches: report of the ATLAS/CMS dark matter forum," *arXiv:1507.00966* (2015) .

[67] J. P. Ellis, "Tikz-feynman: Feynman diagrams with tikz," *Computer Physics Communications* **210** (2017) 103–123. `https://doi.org/10.1016/j.cpc.2016.08.019`.

[68] H. Dreiner, D. Schmeier, and J. Tattersall, "Contact interactions probe effective dark-matter models at the LHC," *EPL (Europhysics Letters)* **102** no. 5, (2013) 51001. `https://doi.org/10.1209/0295-5075/102/51001`.

[69] A. Birkedal, K. Matchev, and M. Perelstein, "Dark matter at colliders: A model-independent approach," *Physical Review D* **70** no. 7, (2004) 077701.

[70] Y. J. Chae and M. Perelstein, "Dark matter search at a linear collider: effective operator approach," *Journal of High Energy Physics* **2013** no. 5, (2013) 138, `1211.4008`.

[71] H. K. Dreiner, M. Huck, M. Krämer, *et al.*, "Illuminating dark matter at the ILC," *Physical Review D* **87** no. 7, (2013) 075015.

[72] P. J. Fox, R. Harnik, J. Kopp, and Y. Tsai, "LEP shines light on dark matter," *Physical Review D* **84** no. 1, (2011) 014028.

[73] M. Beltran, D. Hooper, E. W. Kolb, *et al.*, "Maverick dark matter at colliders," *Journal of High Energy Physics* **2010** no. 9, (2010) 37. `https://doi.org/10.1007/JHEP09(2010)037`.

[74] Y. Bai, P. J. Fox, and R. Harnik, "The Tevatron at the frontier of dark matter direct detection," *Journal of High Energy Physics* **2010** no. 12, (2010) 48. `https://doi.org/10.1007/JHEP12(2010)048`.

[75] J. Goodman, M. Ibe, A. Rajaraman, *et al.*, "Constraints on dark matter from colliders," *Physical Review D* **82** no. 11, (2010) 116010.

[76] J.-M. Zheng, Z.-H. Yu, J.-W. Shao, *et al.*, "Constraining the interaction strength between dark matter and visible matter: I. fermionic dark matter," *Nuclear Physics B* **854** no. 2, (2012) 350–374. `https://doi.org/10.1016/j.nuclphysb.2011.09.009`.

[77] Z.-H. Yu, J.-M. Zheng, X.-J. Bi, *et al.*, "Constraining the interaction strength between dark matter and visible matter: II. scalar, vector and spin-3/2 dark matter," *Nuclear Physics B* **860** no. 1, (2012) 115–151. `https://doi.org/10.1016/j.nuclphysb.2012.02.016`.

[78] S. Matsumoto, S. Mukhopadhyay, and Y.-L. S. Tsai, "Effective theory of WIMP dark matter supplemented by simplified models: singlet-like majorana fermion case," *Physical Review D* **94** no. 6, (2016) 065034.

[79] O. Buchmueller, M. J. Dolan, and C. McCabe, "Beyond effective field theory for dark matter searches at the LHC," *Journal of High Energy Physics* **2014** no. 1, (2014) 25. `https://doi.org/10.1007/JHEP01(2014)025`.

[80] **ATLAS** Collaboration, "Search for dark matter candidates and large extra dimensions in events with a jet and missing transverse momentum with the ATLAS detector," *Journal of High Energy Physics* **2013** no. 4, (2013) 75. `https://doi.org/10.1007/JHEP04(2013)075`.

[81] **CMS** Collaboration, S. Chatrchyan *et al.*, "Search for dark matter and large extra dimensions in monojet events in pp collisions at $\sqrt{s} = 7$ TeV," *Journal of High Energy Physics* **2012** no. 9, (2012) 94.

[82] **CMS** Collaboration, S. Chatrchyan *et al.*, "Search for dark matter and large extra dimensions in pp collisions yielding a photon and missing transverse energy," *Physical review letters* **108** no. 26, (2012) 261803.

[83] G. Busoni, A. De Simone, E. Morgante, and A. Riotto, “On the validity of the effective field theory for dark matter searches at the LHC,” *Physics Letters B* **728** (2014) 412–421. `https://doi.org/10.1016/j.physletb.2013.11.069`.

[84] S. A. Malik, C. McCabe, H. Araujo, *et al.*, “Interplay and characterization of dark matter searches at colliders and in direct detection experiments,” *Physics of the Dark Universe* **9** (2015) 51–58. `https://doi.org/10.1016/j.dark.2015.03.003`.

[85] J. Alwall, P. C. Schuster, and N. Toro, “Simplified models for a first characterization of new physics at the LHC,” *Physical Review D* **79** no. 7, (2009) 075020.

[86] D. Alves, N. Arkani-Hamed, S. Arora, *et al.*, “Simplified models for LHC new physics searches,” *Journal of Physics G: Nuclear and Particle Physics* **39** no. 10, (2012) 105005. `https://doi.org/10.1088/0954-3899/39/10/105005`.

[87] “Working group on dark matter searches at the LHC.” `https://lpcc.web.cern.ch/content/lhc-dm-wg-wg-dark-matter-searches-lhc`.

[88] A. Albert, M. Backovic, A. Boveia, *et al.*, “Recommendations of the LHC dark matter working group: comparing LHC searches for heavy mediators of dark matter production in visible and invisible decay channels,” *arXiv:1703.05703* (2017) .

[89] A. M. Sirunyan, A. Tumasyan, W. Adam, *et al.*, “Search for new physics in the monophoton final state in proton-proton collisions at $\sqrt{s} = 13$ TeV,” *Journal of High Energy Physics* **2017** no. 10, (2017) 73, `1706.03794`.

[90] **ATLAS** Collaboration, M. Aaboud *et al.*, “Search for new phenomena in final states with an energetic jet and large missing transverse momentum in pp collisions at $\sqrt{s} = 13$ TeV using the ATLAS detector,” *Physical Review D* **94** no. 3, (2016) 032005.

[91] A. Freitas and S. Westhoff, “Leptophilic dark matter in lepton interactions at LEP and ILC,” *Journal of High Energy Physics* **2014** no. 10, (2014) 116. `https://doi.org/10.1007/JHEP10(2014)116`.

[92] D. Dercks, N. Desai, J. S. Kim, *et al.*, "CheckMATE 2: From the model to the limit," *Computer Physics Communications* **221** (2017) 383–418. `https://doi.org/10.1016/j.cpc.2017.08.021`.

[93] D. Dercks and G. Moortgat-Pick, "Automatised ILC-bounds on dark matter models with CheckMATE," *arXiv:1801.08037* (2018) .

[94] B. Wang, "Searches for new physics at the Belle II experiment," *arXiv:1511.00373* (2015) .

[95] T. Behnke, J. E. Brau, B. Foster, *et al.*, "The International Linear Collider technical design report - volume 1: Executive summary," *arXiv:1306.6327* (2013) .

[96] H. Baer, T. Barklow, K. Fujii, *et al.*, "The International Linear Collider technical design report - volume 2: Physics," *arXiv:1306.6352* (2013) .

[97] C. Adolphsen, M. Barone, B. Barish, *et al.*, "The International Linear Collider Technical design report - volume 3. I: Accelerator in the technical design phase," *arXiv:1306.6353* (2013) .

[98] C. Adolphsen, M. Barone, B. Barish, *et al.*, "The International Linear Collider technical design report - volume 3. II: Accelerator baseline design," *arXiv:1306.6328* (2013) .

[99] T. Behnke, J. Brau, P. Burrows, *et al.*, "The International Linear Collider technical design report - volume 4: Detectors," *arXiv:1306.6329* (2013) .

[100] L. Linssen, A. Miyamoto, M. Stanitzki, and H. Weerts, "Physics and detectors at CLIC: CLIC conceptual design report," *arXiv:1202.5940* (2012) .

[101] "FCC-ee web page." `http://cern.ch/fcc`.

[102] D. d'Enterria, "Physics at the FCC-ee," in *Particle Physics at the Year of Light: Proceedings of the Seventeenth Lomonosov Conference on Elementary Particle Physics*, pp. 182–191, World Scientific. 2017.

[103] "CEPC web page." `http://cepc.ihep.ac.cn/`.

[104] J. Gao, "CEPC-SPPC accelerator status towards CDR," *International Journal of Modern Physics A* **32** no. 34, (2017) 1746003.

[105] J. D. Jackson, "Classical electrondynamics, third edition," *Wiley* (1998) .

[106] L. Evans and S. Michizono, "The International Linear Collider machine staging report 2017," *arXiv:1711.00568* (2017) .

[107] W. Glen and W. Mark, "Main linac extension: Implementation status." `http://ilcdoc.linearcollider.org/record/62926?ln=en`. ILC-CR-0004.

[108] B. List, L. Hagge, and M. Stanitzki, "EDMS user requirement list." `https://www.e-jade.eu/sites/sites_custom/site_e-jade/content/e49893/e65922/e65937/D17.WP3.EDMSUserReq.pdf`.

[109] G. Moortgat-Pick, H. Baer, M. Battaglia, *et al.*, "Physics at the e^+ e^- linear collider," *EPJ C* **75** no. 8, (2015) 371. `https://doi.org/10.1140/epjc/s10052-015-3511-9`.

[110] K. Fujii, C. Grojean, M. E. Peskin, *et al.*, "Physics case for the International Linear Collider," *arXiv:1506.05992* (2015) .

[111] K. Fujii, C. Grojean, M. E. Peskin, *et al.*, "Physics case for the 250 GeV stage of the International Linear Collider," *arXiv:1710.07621* (2017) .

[112] K. Fujii, C. Grojean, M. E. Peskin, *et al.*, "The potential of the ILC for discovering new particles," *arXiv:1702.05333* (2017) .

[113] A. Freitas, K. Hagiwara, S. Heinemeyer, *et al.*, "Exploring quantum physics at the ILC," *arXiv:1307.3962* (2013) .

[114] T. Barklow, J. Brau, K. Fujii, *et al.*, "ILC operating scenarios," *arXiv:1506.07830* (2015) .

[115] K. Wille, "Physik der Teilchenbeschleuniger und Synchrotronstrahlungsquellen, 2. überarbeitete Ausgabe," *Teubner Studienbücher* (1986) .

[116] W. Gai, "ILC positron source parameters," 2012. `https://edmsdirect.desy.de/item/D00000000943695`.

[117] A. Vogel, *Beam-induced backgrounds in detectors at the ILC*. PhD thesis, University of Hamburg, 2008. `http://inspirehep.net/record/802261/files/desy-thesis-08-036.pdf`.

[118] P. Chen, "Disruption, beamstrahlung, and beamstrahlung pair creation," tech. rep., Stanford Linear Accelerator Center, 1988. `https://inis.iaea.org/search/search.aspx?orig_q=RN:20037541`.

[119] G. Breit and J. A. Wheeler, "Collision of two light quanta," *Phys. Rev.* **46** (Dec, 1934) 1087–1091. `https://link.aps.org/doi/10.1103/PhysRev.46.1087`.

[120] H. Bethe and W. Heitler, "On the stopping of fast particles and on the creation of positive electrons," *Proc. R. Soc. Lond. A* **146** no. 856, (1934) 83–112.

[121] H. Abramowicz, A. Abusleme, K. Afanaciev, *et al.*, "Forward instrumentation for ILC detectors," *Journal of Instrumentation* **5** no. 12, (2010) P12002. `http://stacks.iop.org/1748-0221/5/i=12/a=P12002`.

[122] S. Sasikumar, "Hadron production in photon-photon processes at the ILC and the BSM signatures with small mass differences." `http://bib-pubdb1.desy.de/record/398111`. PUBDB-2017-13722.

[123] O. Napoly, "Collimation depth requirements for the TESLA interaction region," tech. rep., 2001.

[124] A. Drozhdin, N. Mokhov, N. Nakao, *et al.*, "Suppression of muon backgrounds generated in the ILC beam delivery system," in *Particle Accelerator Conference, 2007. PAC. IEEE*, pp. 2945–2947, IEEE. 2007.

[125] M. Thomson, "Particle flow calorimetry and the PandoraPFA algorithm," *Nucl. Instrum. Methods Phys. Res. Section A: Accelerators, Spectrometers, Detectors and Associated Equipment* **611** no. 1, (2009) 25–40. `https://doi.org/10.1016/j.nima.2009.09.009`.

[126] A. Vogel, "The coordinate system for LDC detector studies," *LC Notes. LC-DET-2005-009.* (2005) . `https://www.lctpc.org/e11/e72/`.

[127] B. Parker and A. Seryi, "Compensation of the effects of a detector solenoid on the vertical beam orbit in a linear collider," *Physical Review Special Topics-Accelerators and Beams* **8** no. 4, (2005) 041001.

[128] A. Seryi, T. Maruyama, B. Parker, *et al.*, "IR optimization, DID and anti-DID," tech. rep., Stanford Linear Accelerator Center (SLAC), 2006. `https://www.osti.gov/biblio/876041`.

[129] A. Sailer and A. Sapronov, "High energy electron reconstruction in the BeamCal," *arXiv:1702.06945* (2017) .

[130] C. Grah and A. Sapronov, "Beam parameter determination using beamstrahlung photons and incoherent pairs," *Journal of Instrumentation* **3** no. 10, (2008) P10004. `https://doi.org/10.1088/1748-0221/3/10/P10004`.

[131] B. List, "Change management at the International Linear Collider (ILC)," in *Proc. International Particle Accelerator Conference 2016 (IPAC, Busan, Korea, 2016)*. 2016. `http://accelconf.web.cern.ch/AccelConf/ipac2016/papers/thpor026.pdf`.

[132] A. Levy, "The design of the ILD forward region," *arXiv:1701.01923* (2017) .

[133] C. Biino, "The CMS electromagnetic calorimeter: overview, lessons learned during run 1 and future projections," in *Journal of Physics: Conference Series*, vol. 587, p. 012001, IOP Publishing. 2015. `https://doi.org/10.1088/1742-6596/587/1/012001`.

[134] **Belle II** Collaboration, T. Abe *et al.*, "Belle II technical design report," *arXiv:1011.0352* (2010) .

[135] J. Repond, L. Xia, G. Eigen, *et al.*, "Construction and response of a highly granular scintillator-based electromagnetic calorimeter," *Nucl. Instrum. Methods Phys. Res. Section A: Accelerators, Spectrometers, Detectors and Associated Equipment* **887** (2018) 150–168. `https://doi.org/10.1016/j.nima.2018.01.016`.

[136] C. Adloff, Y. Karyotakis, J. Repond, *et al.*, "Response of the CALICE Si-W electromagnetic calorimeter physics prototype to electrons," *Nucl. Instrum. Methods Phys. Res. Section A: Accelerators, Spectrometers, Detectors and Associated Equipment* **608** no. 3, (2009) 372–383. `https://doi.org/10.1016/j.nima.2009.07.026`.

[137] D. Schulte, "Beam-beam simulations with Guinea-Pig,". `http://cds.cern.ch/record/382453`.

[138] T. Ohl, "Circe2 manual: $\kappa\iota\rho\kappa\eta$ version 2.0: Beam spectra for simulating linear collider physics." `https://whizard.hepforge.org/circe2.pdf`.

[139] W. Kilian, T. Ohl, and J. Reuter, "WHIZARD - simulating multi-particle processes at LHC and ILC," *EPJ C-Particles and Fields* **71** no. 9, (2011) 1–29. `https://doi.org/10.1140/epjc/s10052-011-1742-y`.

[140] P. M. De Freitas and H. Videau, "Detector simulation with MOKKA/GEANT4: Present and future," in *International Workshop on Linear Colliders (LCWS 2002), Jeju Island, Korea*, pp. 26–30. 2002.

[141] "MARLIN - Modular Analysis and Reconstruction for the LINear collider." `http://ilcsoft.desy.de/portal/software_packages/marlin/index_eng.html`.

[142] "ILCSoft web page." `http://ilcsoft.desy.de/portal`.

[143] F. Gaede, T. Behnke, N. Graf, and T. Johnson, "LCIO - a persistency framework for linear collider simulation studies," *physics/0306114* (2003) .

[144] S. Aplin, J. Engels, F. Gaede, *et al.*, "LCIO: A persistency framework and event data model for HEP," in *Nuclear Science Symposium and Medical Imaging Conference (NSS/MIC), 2012 IEEE*, pp. 2075–2079, IEEE. 2012. `http://ieeexplore.ieee.org/document/6551478/`.

[145] "StdHep." `http://cepa.fnal.gov/psm/stdhep/`.

[146] B. Xu, "Improvement of photon reconstruction in PandoraPFA," *arXiv:1603.00013* (2016) .

[147] "GuineaPig simulations for the Detailed Baseline Design data sets." `http://ilcsoft.desy.de/dbd/generated/500/beamstr_production/`.

[148] "Lumi-linker." `https://confluence.slac.stanford.edu/display/ilc/Standard+Model+Data+Samples`.

[149] T. Ohl, "Circe1: Beam spectra for simulating linear collider physics." `https://whizard.hepforge.org/circe1.pdf`.

[150] T. Ohl, *Presentation at Whizard Workshop Würzburg*, 2015. `https://indico.desy.de/indico/event/10353/session/10/contribution/30/material/slides/2.pdf`.

[151] F. Simon, "Impact of theory uncertainties on the precision of the top quark mass in a threshold scan at future e^+e^- colliders," *arXiv:1611.03399* (2016) .

[152] M. Moretti, T. Ohl, and J. Reuter, "O'Mega: An optimizing matrix element generator," *arXiv preprint hep-ph/0102195* (2001) .

[153] T. Sjöstrand, "Monte Carlo generators," *arXiv hep-ph/0611247* (2006) .

[154] J. Allison, K. Amako, J. Apostolakis, *et al.*, "Geant4 developments and applications," *IEEE Transactions on Nuclear Science* **53** no. 1, (2006) 270–278.

[155] J. Allison, K. Amako, J. Apostolakis, *et al.*, "Recent developments in Geant4," *Nucl. Instrum. Methods Phys. Res. Section A: Accelerators, Spectrometers, Detectors and Associated Equipment* **835** (2016) 186–225. `https://doi.org/10.1016/j.nima.2016.06.125`.

[156] S. Agostinelli, J. Allison, K. a. Amako, *et al.*, "Geant4 - a simulation toolkit," *Nucl. Instrum. Methods Phys. Res. section A: Accelerators, Spectrometers, Detectors and Associated Equipment* **506** no. 3, (2003) 250–303. `https://doi.org/10.1016/S0168-9002(03)01368-8`.

[157] L. Garren, I. Knowles, T. Sjöstrand, and T. Trippe, "Monte Carlo particle numbering scheme," *EPJ C-Particles and Fields* **15** no. 1-4, (2000) 205–207. `https://doi.org/10.1007/BF02683426`.

[158] B. Xu, "Detectors and physics at a future linear collider." PhD thesis, King's College.

[159] F. A. Berends and R. Kleiss, "Distributions in the process $e^+e^- \to e^+e^-(\gamma)$," *Nuclear Physics B* **228** no. 3, (1983) 537–551. `https://doi.org/10.1016/0550-3213(83)90558-8`.

[160] K. Tobimatsu and Y. Shimizu, "Radiative correction to $e^+e^- \to e^+e^-$ in the electroweak theory. I: Cross sections for hard photon emission," *Progress of Theoretical Physics* **74** no. 3, (1985) 567–575. `https://doi.org/10.1143/PTP.74.567`.

[161] D. Karlen, "Radiative bhabha scattering for singly tagged and untagged configurations," *Nuclear Physics B* **289** (1987) 23 – 35. `http://www.sciencedirect.com/science/article/pii/0550321387903695`.

[162] S. Jadach, W. Płaczek, and B. Ward, “BHWIDE 1.00: $O(\alpha)$ YFS exponentiated Monte Carlo for Bhabha scattering at wide angles for LEP1/SLC and LEP2,” *Physics Letters B* **390** no. 1, (1997) 298 – 308.

[163] S. Jadach, E. Richter-Wąs, *et al.*, “Monte Carlo program BHLUMI 2.01 for Bhabha scattering at low angles with Yennie-Frautschi-Suura exponentiation,” *Computer Physics Communications* **70** no. 2, (1992) 305 – 344.

[164] S. Jadach, W. Płaczek, *et al.*, “Upgrade of the Monte Carlo program BHLUMI for Bhabha scattering at low angles to version 4.04,” *Computer Physics Communications* **102** no. 1, (1997) 229 – 251.

[165] J. Reuter, F. Bach, B. Chokoufe, *et al.*, “Modern particle physics event generation with WHIZARD,” *Journal of Physics: Conference Series* **608** no. 1, (2015) 012063. `http://stacks.iop.org/1742-6596/608/i=1/a=012063`.

[166] W. Kilian, T. Ohl, J. Reuter, and C. Speckner, “WHIZARD 1.97 manual.” `http://flc.desy.de/lcnotes/noteslist/index_eng.html`. LCNotes LC-TOOL-2001-039.

[167] S. Green, *Calorimetry at a Future Linear Collider*. PhD thesis, Cambridge U., 2017.

[168] P. Bock, “Computation of confidence levels for exclusion or discovery of a signal with the method of fractional event counting,” *JHEP* **01** (2007) 080, `arXiv:hep-ex/0405072 [hep-ex]`.

[169] A. L. Read, “Modified frequentist analysis of search results (the CL_S method),” tech. rep., Cern, 2000. `http://cds.cern.ch/record/451614/files/p81.pdf`.

[170] T. Junk, “Confidence level computation for combining searches with small statistics,” *Nucl. Instrum. Methods Phys. Res. Section A: Accelerators, Spectrometers, Detectors and Associated Equipment* **434** no. 2-3, (1999) 435–443. `https://doi.org/10.1016/S0168-9002(99)00498-2`.

[171] **H1** Collaboration, A. Aktas *et al.*, “Search for leptoquark bosons in ep collisions at HERA,”.

[172] I. B. Jelisavčić, S. Lukić, G. M. Dumbelović, *et al.*, “Luminosity measurement at ILC,” *Journal of Instrumentation* **8** no. 08, (2013) P08012. `https://doi.org/10.1088/1748-0221/8/08/P08012`.

[173] J. List, A. Vauth, and B. Vormwald, “A quartz Cherenkov detector for Compton-polarimetry at future e^+e^- colliders,” *Journal of Instrumentation* **10** no. 05, (2015) P05014. `https://doi.org/10.1088/1748-0221/10/05/P05014`.

[174] B. Vormwald, J. List, and A. Vauth, “A calibration system for Compton polarimetry at e^+e^- linear colliders,” *Journal of Instrumentation* **11** no. 01, (2016) P01014. `http://stacks.iop.org/1748-0221/11/i=01/a=P01014`.

[175] M. Beckmann, J. List, A. Vauth, and B. Vormwald, “Spin transport and polarimetry in the beam delivery system of the International Linear Collider,” *Journal of Instrumentation* **9** no. 07, (2014) P07003. `https://doi.org/10.1088/1748-0221/9/07/P07003`.

[176] R. Karl and J. List, “Polarimetry at the ILC,” *arXiv:1703.00214* (2017) .

[177] K. Fujii, C. Grojean, M. E. Peskin, *et al.*, “The role of positron polarization for the inital 250 GeV stage of the International Linear Collider,” *arXiv:1801.02840* (2018) .

[178] S. Poss and A. Sailer, “Luminosity spectrum reconstruction at linear colliders,” *EPJ C* **74** no. 4, (2014) 2833. `https://doi.org/10.1140/epjc/s10052-014-2833-3`.

[179] N. Phinney, N. Toge, and N. Walker, “ILC reference design report volume 3 - accelerator,” *arXiv:0712.2361* (2007) .

[180] M. Ross, N. Walker, A. Yamamoto, *et al.*, “SB2009 proposal document.” `https://ilc.kek.jp/SB2009/SB20091217B.pdf`.

[181] M. Habermehl, K. Fujii, J. List, *et al.*, “WIMP searches at the International Linear Collider,” in *38th International Conference on High Energy Physics, ICHEP, Chicago, USA*. 2016. `https://pos.sissa.it/282/155/pdf`.

[182] M. Ahmad *et al.*, “CEPC-SPPC preliminary conceptual design report. 1. physics and detector,” tech. rep., IHEP-CEPC-DR-2015-01, 2015.

[183] N. Zhou, D. Berge, T. M. Tait, *et al.*, "Sensitivity of future collider facilities to WIMP pair production via effective operators and light mediators," *arXiv:1307.5327* (2013) .

Acknowledgements

I would like to thank a few people who supported me during the time of my PhD project.

Jenny, thank you very much for supervising my PhD project. Thank you for your time, for giving clear guidance and for letting me develop my own ideas. I appreciate all the practial advice and your constant interest in staying up to date with my work. And also thanks for all the proofreading.

I know the second assessor of my thesis already from my Bachelor and Master's theses, which I made in Dieter's group for experimental astrophysics. Thank you for the interesting topics we worked on.

I'd like to thank my office mates for the nice atmosphere. Thank you, Hale and Madalina, for the warm welcome you gave me, when I was new in the group. Suvi, thank you for all the fruitful discussions we had. Shin-ichi, thank you for the delicious Japanese tea.

I also want to thank all FLC members for the good time I had. My first thank-you goes to Andrea, the soul of FLC. Thank you Coralie, for convincing me to ask for a PhD position in the group. Mikael, who has known the answer to every question I asked him, thank you for sharing your knowledge with me. Thank you Swathi for your positive attitude. Merci beaucoup, Eldwan.

And all the nice lunch appointments I had... Thank you, Eva, Coralie and Christian for establishing our weekly "Stammtisch". Ambra, grazie mille per avermi insegnato l'italiano.

I want to thank my family for the support throughout my studies and my PhD time. Thank you for always letting me chose what I wanted to do.

Juli, thank you for going through these exciting years together with me. Thank you for accepting that I would come home late so often and that I would talk about bizarre things, when we meet with my colleagues. Thank you for the pretty Higgs picture you gave me.

Eidesstattliche Versicherung

Hiermit versichere ich an Eides statt, die vorliegende Dissertationsschrift selbst verfasst und keine anderen als die angegebenen Hilfsmittel und Quellen benutzt zu haben.

Die eingereichte schriftliche Fassung entspricht der auf dem elektronischen Speichermedium.

Die Dissertation wurde in der vorgelegten oder einer ähnlichen Form nicht schon einmal in einem früheren Promotionsverfahren angenommen oder als ungenügend beurteilt.

Hamburg, den 19.12.2018

Unterschrift des Doktoranden